A Novel Synergetic Combined Modality of Nanotechnology, Chemotherapy, and Radiotherapy for the Treatment of Pancreatic Cancer

By

Abdulaziz Alhussan

B.Sc., Oregon State University, 2015
M.Sc., Oregon State University, 2017
M.Sc., Oregon Health & Science University, 2020

A Dissertation Submitted in Partial Fulfillment of
the Requirements for the Degree of

DOCTOR OF PHILOSOPHY

in the Department of Physics and Astronomy

We acknowledge and respect the Lək̓ʷəŋən (Songhees and Esquimalt) Peoples on whose territory the university stands, and the Lək̓ʷəŋən and W̱SÁNEĆ Peoples whose historical relationships with the land continue to this day.

A Novel Synergetic Combined Modality of Nanotechnology, Chemotherapy, and Radiotherapy for the Treatment of Pancreatic Cancer

By

Abdulaziz Alhussan

B.Sc., Oregon State University, 2015
M.Sc., Oregon State University, 2017
M.Sc., Oregon Health & Science University, 2020

Supervisory Committee

Dr. Devika Chithrani, Supervisor
Department of Physics and Astronomy

Dr. Wayne Beckham, Departmental Member
Department of Physics and Astronomy

Dr. Stephanie Willerth, Outside Member
Department of Mechanical Engineering

Dr. Abraham Alexander, Outside Member
Department of Surgery, University of British Columbia

ABSTRACT

Pancreatic cancer is one of the deadliest types of cancer, with a five-year survival rate of less than 8%. Despite the current advances in medicine, innovative treatment options are needed. Nanotechnology offers a novel perspective to treat such deadly cancers through their incorporation into radiotherapy (RT), as radiosensitizers, and chemotherapy, as drug carriers, for the goal of having better therapeutic efficacy and reducing normal tissue toxicity. However, the interaction of nanoparticles (NPs) with major cells of the tumor microenvironment (TME) is yet to be understood. Therefore, our first goal was to shed light on the dynamics of NPs within a TME of pancreatic origin. In addition to cancer cells, normal fibroblasts (NFs) and cancer-associated fibroblasts (CAFs) were examined due to their important yet opposite roles of suppressing tumor growth and promoting tumor growth, respectively. Gold nanoparticles (GNPs) were used as promising radiosensitizers due to their biocompatibility and physical and chemical proprieties. Our *in vitro* 2D monocultures studies revealed that NFs take up less than 50% of GNPs compared to cancer cells, while CAFs had over 300% increase in GNPs uptake compared to cancer cells. Cancer cells, CAFs, and NFs lost ~ 25% of GNPs 24 h post-dosing. We were able to significantly enhance the uptake and retention using the radiosensitizing drug docetaxel (DTX). GNP uptake was improved by a factor of three in cancer cells and a factor of two in CAFs. Both cell lines were able to retain ~ 70% of GNPs even 72 h post-treatment with DTX.

Drawing on these encouraging findings, our second goal was to create a 2D co-culture of CAFs and cancer cells to model the interaction between cancer and stromal cells in the TME and allow for better testing of therapeutic combinations. To test the proposed co-culture model, cells were grown in co-culture with different ratios of CAFs to cancer cells. Co-cultured cells were treated with 2 Gy of radiation following GNP incubation. DNA damage and cell proliferation were examined to assess the combined effect of radiation and GNPs. Cancer cells in co-culture exhibited up to a 23% decrease in DNA double strand breaks (DSB) and up to a 35% increase in proliferation compared to monocultures. GNP/RT induced up to a 25% increase in DNA DSBs and up to a 15% decrease in proliferation compared to RT alone in both monocultured and co-cultured cells. The observed resistance in the co-culture system may be attributed to the role of CAFs in supporting cancer cells. In parallel, our third goal was to explore encapsulating the toxic DTX prodrug in lipid nanoparticles ($LNP_{DTX\text{-}P}$) and how that affect GNP uptake *in vitro* and *in vivo* in NRG mice. The

results show that LNP_{DTX-P} treated tumor samples have double the amount GNPs compared to control samples in both *in vitro* and *in vivo*.

Based on the outcomes of the preceding studies, we aimed to evaluate the anti-cancer efficacy of GNPs and LNP_{DTX-P} in combination with RT on a 3D co-culture spheroid model. GNPs/RT and RT/LNP_{DTX-P} showed a significant reduction in the spheroid size of 7% and 33%, respectively, and an increase in DNA DSB damage of 20% for RT/GNPs. However, the combination of the two nanoparticles with RT significantly enhanced the anti-cancer efficacy resulting in a 46% decrease in spheroid size and a 39% increase in DNA DSB. The combination of GNPs and LNP_{DTX-P} with RT showed a synergistic effect due to their radiosensitizing properties improving the therapeutic efficacy of each treatment modality alone even in the more treatment-resistant co-culture spheroid model. This triple modality presents a promising approach for enhancing cancer treatment while reducing side effects, and ongoing research in this area holds great promise for improving outcomes for cancer patients.

TABLE OF CONTENTS

LIST OF FIGURES

ACKNOWLEDGEMENTS

I would like to express my heartfelt gratitude to my parents. Without their invaluable contribution, I would not have had the privilege of presenting this dissertation. I extend my sincere appreciation to my supervisor Dr. Devika Chithrani for her unbelievable support throughout my journey in pursuing my PhD. She is the most devoted and committed scientist I have ever encountered. She is a beast of a professor and a true role model. It has been a great privilege to work with her and benefit from her guidance as my mentor.

Yo, my boy Nolan Jackson, you are one trustworthy madafaka, a lifelong friend and a brother. It has been a great honor to work alongside you, you fake Filipino. Many thanks to all my committee members, colleagues, mentors, mentees, co-authors, collaborators, and everyone I have had the pleasure of interacting with during my time at UVic. I would also like to thank the Kuwait Foundation for the Advancement of Sciences (KFAS) and the NanoMedicines Innovation Network (NMIN) for their financial support of this work.

My family, my friends, my supervisors, the respected scientific community, and everybody else…. humanity is engaged in a difficult battle against an opponent of unparalleled strength—cancer. This enemy surpasses any other challenge we face. Its magnitude is such that no individual can single-handedly defeat it. Life is the love we share and the impact we make…and I want to leave this earth a better place than what I found it. Listen, I tried my best, but I am not a science nerd like you, I am not a physics geek like my colleagues, I stop being a "scientist" at 5 o'clock, I have so many other passions in life. I am not a genius either, there are millions of scientists out there that are way smarter than me. If each one of you tap into your fullest potential, I truly believe that you collectively can overcome cancer. By cooperatively utilizing your skills, knowledge, and resources, you possess the ability to be victorious over this vicious disease. I encourage you all to keep pressing forward and wish each and every one of you the best of luck in this battle. Now that I got this off my chest, I would like to take this opportunity to apologize, from the bottom of my heart to…ABSOLUTELY NOBODY! The HERO does what the fuck he wants! I am one resolute, persistent, fearless, versatile, badass, HUNGRY SAVAGE who cannot comprehend the concept of giving up. There exists a will within me that far surpasses mere intelligence—a burning flame, FIRE. I am not here to play by the rules, I am here to CREATE new rules and CHANGE the game forever. I am here to CONQUER and build a LEGACY. ~~Cancer~~ will be defeated!

ABBREVIATIONS

α-SMA: Alpha Smooth Muscle Actin

ARC: Animal Resource Centre

ATCC: American Type Culture Collection

BLM: Bleomycin

BSA: Bovine Serum Albumin

CAFs: Cancer Associated Fibroblasts

CAF-98: Patient-Derived Pancreatic Cancer Associated Fibroblasts

CBC: Complete Blood Count

CEA: Carcinoembryonic Antigen

CPIs: Checkpoint Inhibitors

CTAs: Cancer-Testis Antigens

CTRL: Control

DF: Darkfield

DLS: Dynamic Light Scattering

DMEM: Dulbecco's Modified Eagle Medium

DMSO: Dimethyl Sulfoxide

DNA: DeoxyriboNucleic Acid

DSB: Double-Strand Break

DTX: Docetaxel

EBRT: External Beam Radiotherapy

ECM: Extracellular Matrix

EGFR: Epidermal Growth Factor Receptor

EMT: Epithelial-Mesenchymal Transition

EPR: Enhanced Permeability and Retention

FAP- α: Fibroblast Activation Protein Alpha

FBS: Fetal Bovine Serum

G1: Gap 1

G2: Gap 2

GI: Gastrointestinal

GNPs: Gold Nanoparticles

$GNP_{PEG-RGD}$: Gold Nanoparticles Functionalized with Polyethylene Glycol and RGD Peptide.

$GNP_{PEG-CY5-RGD}$: Gold Nanoparticles Functionalized with PEG-thiol-CY5 and RGD Peptide.

Gy: Gray

H&E: Haematoxylin and Eosin

HAADF: High-Angle Annular Darkfield

HGF: Hepatocyte Growth Factor

HR: Homologous Recombination

HSI: Hyperspectral Imaging

IC-50: Half Maximal Inhibitory Concentration

ICD: Immunogenic Cell Death

ICL: Interstrand Crosslink

ICP-MS: Inductively Coupled Plasmon Mass Spectroscopy

IFP: Interstitial Fluid Pressure

IMRT: Intensity-Modulated Radiation Therapy

IRDS: Interferon-Related DNA Damage Resistance Gene Signature

keV: Kilo Electron Volts

kVp: Kilovoltage-Peak

LET: Linear Energy Transfer

LNPs: Lipid Nanoparticles

LNP_{DTX-1}: 5% Docetaxel Prodrug Encapsulated in Lipid Nanoparticles

LNP_{DTX-2}: 10% Docetaxel Prodrug Encapsulated in Lipid Nanoparticles

LNP_{DTX-P}: DTX Prodrug Encapsulated in Lipid Nanoparticles

M: Mitosis

mAbs: Monoclonal Antibodies

MeV: Mega Electron Volts

MT: Microtubules

MTAs: Microtubules Targeting Agents

MTOC: Microtubule-Organizing Center

MV: Mega Volt

nab: Nanoparticle Albumin-Bound

NHEJ: Non-Homologous End Joining

NER: Nucleotide Excision Repair

NF: Normal Fibroblasts

NP: Nanoparticle

NPF-98: Normal Pancreas Fibroblasts

NTCP: Normal Tissue Complication Probability

O_2^-: Superoxide

PARP: Poly(ADP-ribose) Polymerase

PEG: Polyethylene Glycol

PBS: Phosphate-Buffered Saline

PCWC: Probability of Cure Without Complication

PDAC: Pancreatic Ductal Adenocarcinoma

PDX: Patient-Derived Xenograft

PFA: Paraformaldehyde

ppb: part per billion

PYD: Pyronaridine

RDR: Reference Dose Rate

RGD: Arginine-Glycine-Aspartic Peptide

RIT: Radioimmunotherapy

RME: Receptor-Mediated Endocytosis

ROS: Reactive Oxygen Species

RT: Radiotherapy

S: Synthesis

SBRT: Stereotactic Body Radiation Therapy

STEM: Scanning Transmission Electron Microscopy

TCP: Tumor Control Probability

TGF-β: Transforming Growth Factor Beta

TME: Tumor Microenvironment

TMR: Tissue Maximum Ratio

TNF-α: Tumor Necrosis Factor-Alpha

UPLC: Ultra-Performance Liquid Chromatography

UV-VIS: Ultraviolet Visible

VPC: Vancouver Prostate Centre

WHO: World Health Organization

Z: Atomic Number

CHAPTER 1

INTRODUCTION

This chapter aims to deliver an overview of the research, including the underlying motivation, rationale, and hypothesis.

1.1 The Challenge and Inspiration

It is commonly believed that given a long enough lifespan, the likelihood of developing cancer becomes almost inevitable for all humans. According to the World Health Organization (WHO), the global estimated lifetime risk of developing cancer is around 33% for men and 25% for women [1]. WHO estimates that cancer is responsible for about 1 in 6 deaths globally [1]. In 2020 alone, there were approximately 19.3 million new cancer cases and 10 million recorded cancer-related deaths worldwide [2]. Cancer rates in North America are among the highest in the world. Cancer is the currently the leading cause of death in Canada where 33% of all deaths is attributed to cancer [3]. In 2022, an estimated 233,900 new cancer cases and 85,100 cancer-related deaths were recorded [3]. Even worse, the Canadian Cancer Society projects that 43% of Canadians will develop cancer during their lifetime [3]. The case is not much better in the United States where 1.9 million new cancer cases and 609,360 cancer-related deaths were recorded in 2022 [4]. The American Cancer Society estimates the lifetime risk of developing cancer in the United States to be 39.5% for men and 38.5% for women [4]. While the lifetime risk of dying from cancer in the United States is 20% for both sexes [4].

Of all cancer types, pancreatic cancer has one of the lowest survival rates of all types of cancer. The five-year survival rate for pancreatic cancer is less than 6% [2]. In 2020, there were 495,773 new cases of pancreatic cancer and 466,003 deaths globally related to pancreatic cancer

[2]. In 2022 in Canada, an estimated 6,000 new cases of pancreatic cancer were diagnosed, and approximately 5,700 deaths were attributed to this disease [3]. The American Cancer Society reported that in 2022, there were an estimated 62,210 new cases of pancreatic cancer in the United States, and about 49,830 deaths were attributed to this disease [4]. Pancreatic cancer poses a critical global health challenge due to its aggressive nature and devastating impact. Urgent action is necessary to address this hazard and improve outcomes for patients affected by this disease.

1.2 Limitations in Current Treatment Modalities

Current treatment regimens of pancreatic cancer are highly dependent on the cancer stage and location, and include surgery, chemotherapy, and radiotherapy (RT) each with their own shortcomings [5–8]. At present, surgical resection followed by adjuvant chemotherapy is the most favorable therapy for early-stage pancreatic cancer [5]. Nevertheless, pancreatic cancer is locally invasive and highly metastatic, rendering most patients not suitable for surgery [5]. One of the challenges in chemotherapy is the limited amount of the drug that reaches the tumor site when a free drug is used with no appreciable variation in drug concentrations between the tumor and healthy organs [9–11]. This is attributed to several factors, including systemic distribution and clearance of the drug, as well as the presence of the tumor microenvironment (TME) which prevents the propagation of chemotherapeutic drugs to the tumor site denying the delivery of the necessary doses [9]. Alternatively, RT is an essential element of curative treatment for many locally advanced non-metastatic cancers, including breast, prostate, cervix, head and neck, lung, and brain. It is estimated that ~ 50% of current cancer patients receive RT [13]. However, RT has limitations in safely targeting pancreatic cancer. The location of the pancreas in the vicinity of multiple organs at risk (**Fig. 1.1**) for RT-associated toxicity limits the desired radiation dose needed for local control [7].

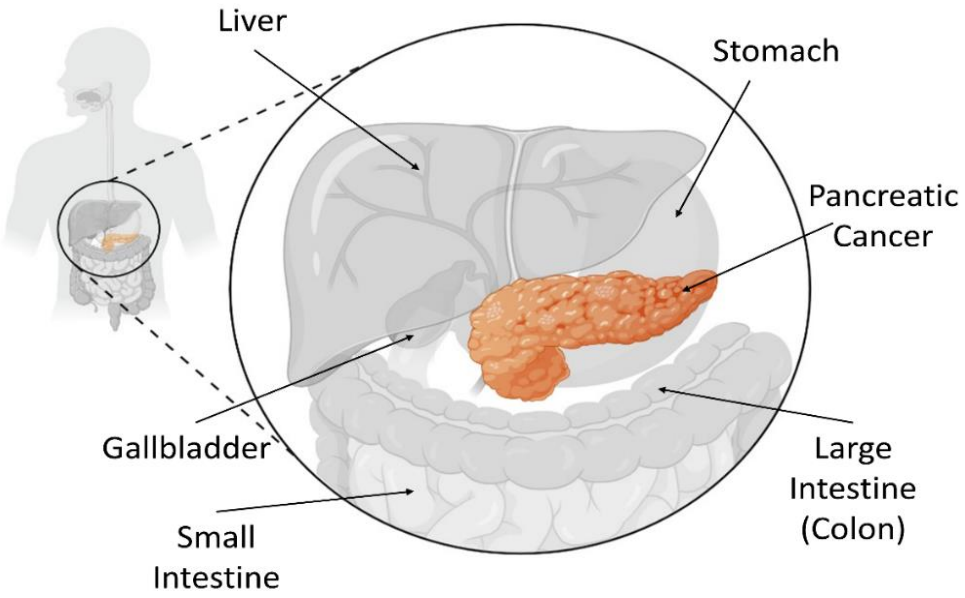

Figure 1.1 Illustration demonstrating the location of the pancreas next to vital organs. Created with BioRender.com.

Newley emerging treatment modalities such as immunotherapy are slowly developing as alternatives to treat such patients [5, 13]. However, it is still in its early stages to treat a large number of patients [14, 15]. Another alternative treatment of non-metastatic pancreatic cancer is chemoradiation therapy where the addition of radiosensitizing chemotherapy to RT has marginally improved survival [16]. Nonetheless, most patients surrender to their illness within the first year [17, 18]. Regrettably, the safe delivery of effective doses of radiation and chemotherapy is often hindered by limitations in minimizing normal tissue toxicity and preventing complications to vital organs. We are approaching the maximum dosage limit of RT and chemotherapy administered to patients, highlighting the need for innovative techniques that can enhance the effectiveness of RT and chemotherapy doses to the tumor while minimizing potential side effects.

1.3 Nanotechnology as the Answer

Nanotechnology has shown remarkable potential in addressing numerous challenges associated with traditional cancer treatments. Nanoparticles (NPs) have shown promising results as radiosensitizer agents in RT and as vectors for targeted-drug delivery in chemotherapy [19–22]. For example, high atomic number (Z) material, like gold nanoparticles (GNPs), are a powerful tool for maximizing radiation doses to tumors while significantly reducing the exposure of normal tissue to radiation [23–29]. Similarly, the utilization of lipid nanoparticles (LNPs) has emerged as

a promising solution as drug carriers to address challenges associated with chemotherapy. LNPs have been demonstrated to increase the injection dose of chemotherapeutic drugs within tumors many folds [30–35]. Utilizing their small size, NPs can effectively leverage the enhanced permeability and retention (EPR) effect, enabling them to penetrate tumors by utilizing their leaky blood vessels [36–40]. Moreover, NPs can be customized and equipped with specific targeting properties, allowing them to selectively bind with tumor cells [27, 31, 36]. This highly promising characteristic makes NPs a valuable tool that can enhance the effectiveness of existing cancer treatments.

1.3.1 Gold Nanoparticles (GNPs) Radiosensitizers

The use of GNPs as radiosensitizers in RT is an emerging field that has shown great potential to improve the effectiveness of radiation treatment for cancer [23–29]. GNPs are nanometer-sized gold particles, typically between 1-100 nm in diameter, which can be easily engineered to bind selectively to cancer cells in the body. GNPs can be functionalized with polyethylene glycol (PEG) and the integrin binding peptide RGD as shown in **Fig. 1.2** [19]. The former works as a protective coating that prevents protein adsorption on the surface of the nanoparticle (opsonization) and clearance by the reticuloendothelial system, thereby allowing for longer circulation time [41]. The latter is used due to the high expression of integrin dimers on pancreatic cancer cells, which can recognize the RGD motif allowing for improved cancer cell targeting [42].

The size of GNPs is a critical factor that influences their behavior *in vivo*, including blood circulation, tumor accumulation, penetration, and cellular uptake. In the extracellular matrix (ECM), where collagen fibrils are spaced approximately 20-40 nm apart, NP size becomes significant as it sets the upper limit for effective penetration [43]. Despite GNPs smaller than 13 nm possessing better capabilities to penetrate deeper into cells they tend to have higher accumulation in kidneys *in vivo* [44]. Therefore, achieving an optimal balance between optimized cellular uptake, circulation time, and GNP size selection is crucial for effective outcomes. When GNPs are exposed to radiation, they can absorb the energy from the radiation and locally deposit it to the tumor site, thus requiring less total RT dose [25, 29]. By selectively delivering GNPs to tumor sites, radiation doses can be increased to cancer cells while minimizing damage to normal cells [20, 21]. GNPs are particularly promising due to their simple surface chemistry,

biocompatibility, low toxicity, and ease of manufacturing [21, 29, 45–48]. Recent *in vivo* and *in vitro* studies have shown promising results in using GNPs with RT for various types of cancer, such as prostate, breast, and lung cancer [45, 49, 50]. However, further studies are needed to optimize these approaches and determine the best dosing, administration, and safety considerations for patients.

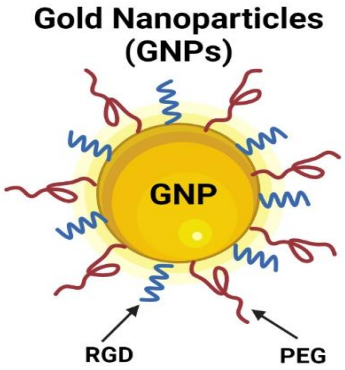

Figure 1.2 Illustration of a GNP functionalized with PEG and RGD. Created with BioRender.com.

1.3.2 Lipid Nanoparticles (LNPs) Drug Delivery Vehicles

LNPs are nanoscale structures made up of lipids such as phospholipids and cholesterol that can effectively encapsulate and deliver various types of drugs [30, 31]. They can be utilized as drug delivery vectors and functionalized to specifically target tumors with controlled delivery, thus significantly decreasing the dose delivered to healthy organs [30, 31]. Additionally, LNPs' long circulation time results in an increase of up to 2-5% of the injected dose within the tumor compared to 0.1% of the free-form drug that has a short half-life [51]. Assuming only 1% of the LNP drug reaches the target site, this still results in over 10 times the intra-tumoral concentration of the drug compared to the free-form drug [52]. In addition to these advantages, the small size of the NPs allows them to reach the tumor via the EPR effect due to the leaky tumor vasculatures [53].

In cancer therapy, LNPs have been used in combination with the chemotherapy drug docetaxel (DTX) to improve treatment efficacy [31, 53]. DTX is an FDA-approved chemotherapy drug that is used to treat various types of cancers, including breast, lung, and prostate cancer [54]. However, it has poor solubility in water, making its delivery to cancer cells in the body difficult [55]. Moreover, DTX in its free form is considerably compromised due to its toxicity to normal tissues [56]. These challenges can be resolved by encapsulating DTX prodrugs within LNPs ($LNP_{DTX\text{-}P}$), **Fig. 1.3**, which can improve its delivery to cancer cells, increase its effectiveness, and

reduce its side effects [57–60]. Additional advantages of using LNP_{DTX-P} in cancer therapy include increased drug stability, which allows for longer circulation periods, thus, improving overall tumor accumulation and efficacy [58, 59]. Furthermore, there is an opportunity to improve drug delivery by engineering the LNPs to selectively target cancer cells, enhancing the delivery of DTX directly into cancer cells [59, 60]. This targeted delivery reduces the risk of toxicity to healthy cells, thereby reducing side effects.

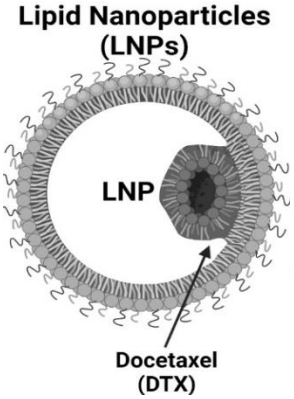

Figure 1.3 Illustration of a DTX prodrug encapsulated in lipid nanoparticle. Created with BioRender.com.

1.3.3 The Synergy of GNPs/ LNP_{DTX-P}/RT

GNPs and low concentrations of DTX have been shown to sensitize cancer cells to RT *in vitro* [61–63]. GNPs can sensitize tumor cells to radiation by enhancing the cell-damaging species such as free radicals and low-energy electrons [64, 65]. DTX, on the other hand, is an antimitotic agent that interferes with the formation of microtubules (MTs) [66–68]. Due to the role of MTs in cell division, DTX impedes the cell division cycle and traps cells in the most radiosensitive phase of mitosis, the G2/M phase [69–72]. Because of this, DTX has been used as a radiosensitizer in several clinical trials [73–77]. Moreover, the defect in the function of MTs leads to a significant accumulation of GNPs within cells over time [62]. Hence, the coupling of GNPs and LNP_{DTX-P} with RT could result in a synergistic therapeutic outcome due to their complementary mechanism of action. Therefore, the approach is to fight the disease using a combined modality treatment that not only involves RT but also nanotechnology and chemotherapy as radiosensitizers. This could be accomplished at clinically safe concentrations, using clinically relevant ionizing radiation energies, and with administration schedules of NPs, chemotherapeutics, and RT that are practical for clinical settings.

1.4 Upgraded *in vitro* Tumor Modelling

To best examine the combined effects of GNPs, LNP_{DTX-P}, and RT, *in vitro*, it is important to understand the TME. The TME refers to the surrounding environment in which a tumor exists, which contains a heterogenous mix of cancer associated fibroblasts (CAFs), immune cells, macrophages, vasculatures, the ECM, and signaling molecules, **Fig. 1.4** [78]. The TME is complex and dynamic, consisting of both pro-tumorigenic and anti-tumorigenic factors that influence tumor growth and progression [78]. The ECM acts as a framework that aids in the growth of cells by controlling different cellular activities within the tissue, such as cells intercommunication [18]. It is made up of an intricate arrangement of large molecules created by neighboring cells. These large molecules mainly consist of complex sugars called glycosaminoglycans, adhesive proteins like fibronectin, and structural proteins like collagen [18]. Pancreatic cancer is characterized by the presence of an ECM that exhibits a dense fibrotic stroma [17, 18]. This stroma, with its high proportion of activated CAFs, creates an environment that hinders blood vessel formation, resulting in limited drug delivery and tissue hypoxia. Consequently, the efficacy of RT is diminished [16]. CAFs play a crucial role within the TME. Activated by cancer cells, CAFs secrete various proteins and growth factors that facilitate tumor growth and invasion [6]. CAFs also contribute to the remodeling of the ECM, thereby promoting the migration and invasion of cancer cells [6, 18]. This intercommunication between cancer cells and CAFs fosters the ideal niche for tumors to develop. Hence, there is a critical need to target both cancer cells and CAFs in a co-culture model in order to effectively combat pancreatic cancer.

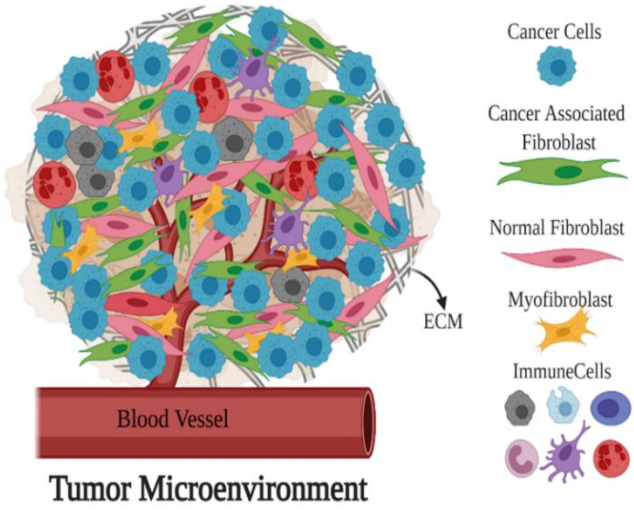

Figure 1.4 This schematic demonstrates the complexity of TME of pancreatic origin. Created with BioRender.com.

Furthermore, the interactions of NPs with the ECM through physical or hydrodynamic interactions impose limitations on NP diffusion [79]. Therefore, for successful translation of our experimental results it is important to develop a more realistic model to test our treatment modality. Unlike the traditional 2D cell culture model, a 3D spheroid mimics the conditions of the TME more accurately since it introduces both the ECM and cell-to-cell interaction of cells of different cell lines similar to that found in tumors [80, 81]. Spheroidal models have demonstrated increased physiological similarity to tumors in similar drug concentration gradients, growth patterns, and metabolic rates compared to traditional 2D cell cultures [82–84]. This allows for more accurate testing of drug efficacy and improved *in vivo* predictive outcomes compared to 2D cell culture models [80, 82]. By controlling the number of seeded cells, the size of the spheroid at the initiation of the experiment could be controlled not to introduce confounding factors such as hypoxia as illustrated in **Fig. 1.5**. This 3D spheroidal co-culture *in vitro* tumor model is a step closer to mimicking the *in vivo* TME and will help analyze the effectiveness of such targeted nanoparticle-chemotherapy-radiotherapy treatment for successful clinical translation.

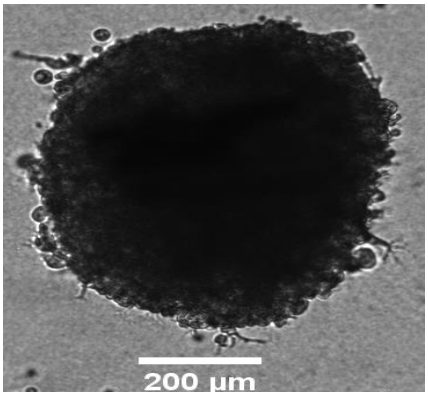

Figure 1.5 Bright-Field image of co-culture spheroid of MIA PaCa-2 and CAF-98 pancreatic cancer cell lines. Scale bar: 200 µm.

1.5 The Hypothesis

LNPs are drug delivery systems that can improve the effectiveness and safety of cancer treatments. DTX prodrug is a chemotherapy drug that is known to have radiosensitizing properties and can be encapsulated in LNPs ($LNP_{DTX\text{-}P}$) to enhance its delivery to cancer cells. LNPs can accumulate in cancer cells and release their payload of DTX directly into the cancer cells, leading to greater efficacy and reduced toxicity compared to traditional chemotherapy. GNPs are used as radiosensitizers. When exposed to radiation doses they can amplify the effect of RT to the tumor.

When NPs are injected into the bloodstream, they can travel through the body and accumulate in tumors due to the leaky vasculature of the tumor and NPs' targeting properties. The window where the tumor retains the highest number of NPs could be used to deliver specified doses of ionizing radiation to reach a higher therapeutic index. Using pancreatic cancer as a model system, this project aims to test the efficacy of our novel therapy of RT combined with 2 radiosensitizers, i.e., GNPs and LNP_{DTX-P}, in a 3D co-culture spheroid made of cancer cells and CAFs derived from the TME of pancreatic cancer patients (**Fig. 1.6**). In the presence of DTX, it is anticipated that GNPs will be trapped within cells close to the nucleus and promote increased DNA damage during RT. Therefore, with the triple combination, a significant shrinkage in the 3D tumor size is expected as compared to RT alone. The translation of the GNP-RT-LNP_{DTX-P} combined modality to the clinic is expected to yield synergistic therapeutic effect allowing us to decrease both RT and chemotherapy doses. This has the potential to significantly minimize damage to healthy tissues while maintaining the therapeutic effectiveness of the treatment, ultimately leading to improved survival rates for cancer patients.

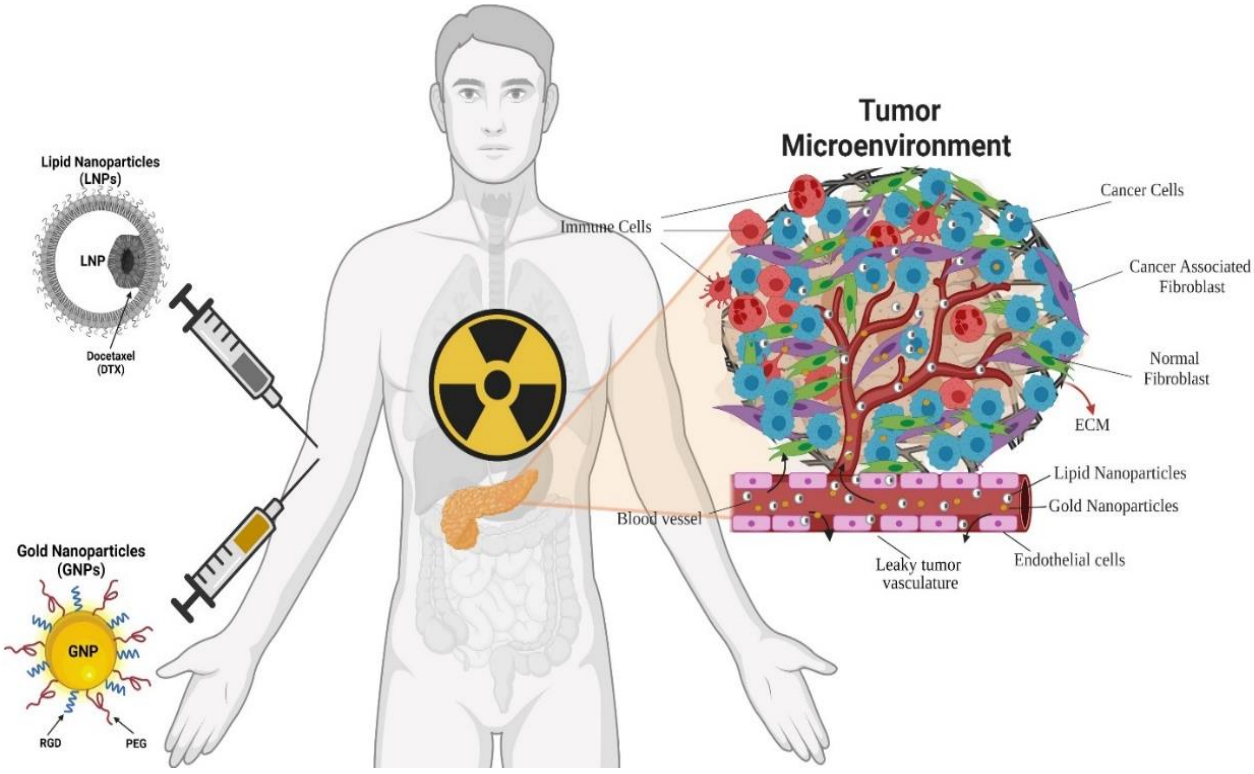

Figure 1.6 Schematic showing the combined modality of nanotechnology, chemotherapy, and RT for the treatment of pancreatic cancer. Created with BioRender.com.

1.6 Dissertation Outline

Chapter 1 is an introductory chapter that contained a broad overview of the problem of cancer, the motivation, the limitations of current cancer treatments, the gaps that nanotechnology could exploit, the rational of improved *in vitro* testing environment, the hypothesis & the anticipated outcome, and the project significance.

Chapter 2 serves as a comprehensive background and theoretical framework, providing a deeper understanding of cancer biology, the tumor microenvironment, various treatment approaches for pancreatic cancer, radiation biology, radiophysics, and the potential role of LNPs and GNPs as radiosensitizers.

Chapter 3 explores how GNPs are internalized and retained by various cell types within the TME when cultured in 2D monoculture models and *in vivo*. Additionally, it discusses the impact of DTX on the accumulation of GNPs in these cell lines.

Chapter 4 demonstrates the potential of using GNPs as radiosensitizers in the present of radiation in 2D and 3D monoculture and coculture models. It also discusses the added resistance presented by CAFs in co-culture cell models.

Chapter 5 presents the impact of $LNP_{DTX\text{-}P}$ on the behavior of GNPs in both *in vitro* and *in vivo*. We further demonstrate the enhanced efficacy of merging GNPs and $LNP_{DTX\text{-}P}$ with RT, as tested in a 3D co-culture model of pancreatic cancer cells.

Chapter 6 summarizes the dissertations' findings and outlines prospective future research.

CHAPTER 2

BACKROUND & THEORY

This chapter will present essential background material and expand upon the underlying theory.

2.1 Cancer Biology

It is crucial to have a comprehensive understanding of cancer to have a better chance of successful treatment. Understanding the cellular and molecular processes involved in the development and progression of cancer is critical for developing effective strategies for treatment of cancer. The following sections will provide information about cancer relevant to this project.

2.1.1 Cancer Initiation, Growth and Metastasis

Cancer is a disease that involves an unregulated and uncontrollable cell division that has the ability to invade and spread to other organs in the body. There are over hundred types of cancer, most of which can be grouped into one of three groups: carcinomas (malignancies of epithelial cells; most common ~ 90%), sarcomas (rare; solid tumors of connective tissues, such as muscle, bone, fat and cartilage), and leukemias (blood-forming cells) / lymphomas (immune system cells) [85]. An accumulation of gene mutations, particularly in genes that control proliferation, apoptosis, immortalization, and genetic stability, is thought to cause tumor development [86]. These genes fall into one of three main groups: proto-oncogenes, tumor suppressor genes and DNA stability genes. Examples of mutations that affect the function of these genes are gain-of-function mutations to proto-oncogenes that activate oncogenes (growth stimulators), loss-of-function mutations that inactivate tumor suppressor genes (growth inhibitors and apoptosis promoters), and loss of activity of genome stability genes (repairers, e.g. DNA repair genes and mismatch repair genes) that

increases the probability for genomic instability [86]. It is thought that carcinogenesis is likely to start from a mutation in one of the genome stability gene families, which then may lead to an increase in genetic mutation rates possibly in both oncogenes and tumor suppressor genes, which then leads to a sequence of events such as cell immortalization and transformation, ending with the growth of an invasive (attacking surrounding normal tissues), metastatic (spreading throughout the body via blood, lymph system or other body fluids such as peritoneal fluid and cerebrospinal fluid) cancer [86]. This whole multistep process, from the moment the mutation occurs in these genes in the cell nucleus to the progression of the neoplasm from normal tissue to malignant tumor to metastasis cancer, may take up to decades [86].

Once the tumor is formed, it will start growing by seeking oxygen and essential nutrients through the process of angiogenesis or formation of a network of blood vessels driven by signals sent from cancer cells [85]. This process also helps cancer cells navigate their way to other tissues by getting into the blood and spreading to other organs in a process known as metastasis. As cancer cells reach nearby normal tissue, they can take over by producing enzymes that eliminate normal cells and they start locally invading these healthy tissues [85]. Cancer cells manifest distinct characteristics compared to normal cells, primarily due to their consistent immaturity and lack of differentiation. Their capacity to evade immune surveillance by originating from the host's own cells further sets them apart [85]. Additionally, these cells are equipped with the ability to disseminate to nearby organs through the circulatory or lymphatic systems, ignore growth regulatory signals, experience unchecked proliferation, infiltrate organs, disrupt their normal functions, and eventually lead to the individual's demise [85]. Consequently, some cancer cells can escape therapeutic interventions, establishing new cancer foci in the same or different regions of the body shortly after treatment. To counter this, adjuvant therapy, involving sequential treatments, is frequently employed to avert cancer recurrence [87, 88]. In certain scenarios, cancer cells develop resistance to specific treatments, necessitating the implementation of alternative therapeutic approaches [87, 88]. Given the undeniable role of cancer cells in tumor initiation and progression, the precise targeting of these aberrant cells remains a fundamental aspect in the development of novel cancer treatments.

In his work "Hallmarks of Cancer", Douglas Hanahan masterfully offered a thorough and enlightening overview of cancer mechanisms (**Fig. 2.1**) [89–91]. Cancer encompasses a framework consisting of eight hallmark capabilities and two enabling characteristics. Beyond the

initial six acquired capabilities originally proposed in 2000 (evading growth suppressors, enabling replicative immortality, resisting cell death, sustaining proliferative signaling, accessing vasculature, and activating invasion and metastasis) the two "emerging hallmarks" introduced in 2011, namely "deregulation cellular metabolism" and "avoiding immune destruction," have gained enough validation to be integrated into the core set [89–90]. The 2011 follow-up also introduced "tumor-promoting inflammation" as a supplementary enabling characteristic, synergizing with the overarching role of "genome instability and mutation" in activating the eight functional hallmark capabilities essential for tumor advancement [90]. On the other side, the newest review article published in 2022 introduces further proposed emerging hallmarks and enabling characteristics, encompassing "unlocking phenotypic plasticity," "nonmutational epigenetic reprogramming," "polymorphic microbiomes," and "senescent cells" [91].

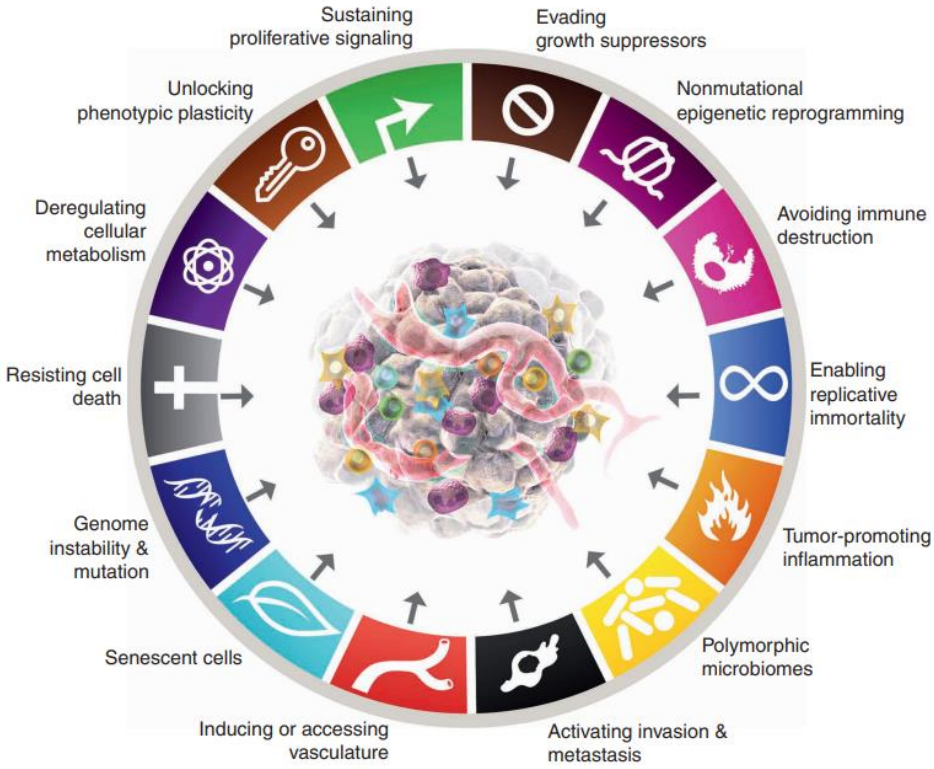

Figure 2.1 The hallmarks of cancer circa. Reproduced with permission from open access Creative Common license [91].

2.1.2 Cancer Stages

Cancer staging is a standardized system used by medical professionals to describe the extent and progression of cancer within the body [92, 93]. Cance stage defines the point in the natural history of an individual's cancer and provides crucial information about the size of the

tumor, its location, whether it has spread to nearby lymph nodes, and whether it has metastasized to other distant parts of the body [92, 93]. The information gathered through staging helps doctors plan appropriate treatment strategies and predict the patient's prognosis. The most common cancer staging system is the TNM system, which stands for Tumor, Node, and Metastasis [92, 93]. It classifies cancers into stages based on these three key factors:

1. **Tumor (T):** This category describes the size and extent of the primary tumor. It's usually categorized numerically, with higher numbers indicating larger tumors or more extensive involvement [92].
2. **Lymph Nodes (N):** This category indicates whether the cancer has spread to nearby lymph nodes. The higher the number, the greater the number of nodes affected [92].
3. **Metastasis (M):** This category shows whether the cancer has spread to distant organs or tissues. M0 indicates no distant spread, while M1 indicates the presence of distant metastases [92].

Combining the T, N, and M categories results in a specific stage, denoted by Roman numerals I to IV, with additional subdivisions denoted by lowercase letters. The stages are defined differently for each type of cancer based on its unique characteristics [94]. For instance, for Pancreatic ductal adenocarcinoma (PDAC), the stages are defined as follows:

- **Stage 0:** This stage indicates that abnormal cells are present only in the innermost lining of the pancreas [94]. It's also called carcinoma *in situ*.
- **Stage I:** The cancer is confined to the pancreas and is localized to a specific area [94].
- **Stage II:** The tumor might be larger and involve nearby structures, but it hasn't spread to nearby lymph nodes or distant sites [94].
- **Stage III:** The cancer has spread to nearby lymph nodes but not to distant sites [94].
- **Stage IV:** The cancer has metastasized to distant organs or tissues [94].

2.1.3 Tumor Control

Tumor control is a comprehensive approach with a goal of effectively manage and mitigate the impact of cancer to reduce the burden of cancer on individuals and societies [95, 96]. This requires multidisciplinary collaboration among healthcare professionals, researchers, policymakers, and communities to address the challenges posed by cancer. It involves cancer prevention by promoting healthy behaviors to reducing risk factors, early detection and screening,

ensuring timely and accurate diagnosis and treatment, improving access to palliative care for patients, developing programs to support cancer survivors, encouraging cancer research, providing access to quality care for all individuals affected by cancer, and develop better international collaboration for the one goal of defeating cancer [95, 96]. This will reduce the incidence, morbidity, and mortality associated with cancer and improve the quality of life for individuals affected by it.

2.1.4 Pancreatic Ductal Adeno Carcinoma (PDAC)

PDAC ranks as one of the deadliest cancers, holding the third position in terms of mortality rates [3]. Its 5-year survival rate is less than 6%, and a significant number of patients succumb within the initial year of diagnosis [3]. PDAC is the most common type of pancreatic cancer, accounting for about 90% of all pancreatic malignancies. PDAC originates in the cells lining the ducts of the pancreas, which are responsible for producing digestive enzymes that aid in food digestion and hormones that regulate blood sugar levels [17]. Several risk factors are associated with the development of PDAC. These include age (usually diagnosed in people over 65), smoking, obesity, chronic pancreatitis (inflammation of the pancreas), diabetes, family history of pancreatic cancer or certain genetic syndromes, and certain inherited gene mutations [17, 18].

PDAC is known for its aggressive behavior. It has a generally poor prognosis, mainly due to the fact that it's often diagnosed at advanced stages when surgical intervention is no longer an option [5–8, 16–18]. Early-stage PDAC often doesn't show specific symptoms, which makes early detection challenging. As the cancer progresses, common symptoms may include jaundice (yellowing of the skin and eyes), abdominal pain, unexplained weight loss, digestive problems, and new-onset diabetes [16, 17]. Diagnosing PDAC involves a combination of imaging tests like CT scans, MRI, and endoscopic ultrasound, along with biopsy to confirm the presence of cancer cells [17]. Depending on the stage and location of the cancer, surgical removal of the tumor, known as a Whipple procedure, is considered for localized cancers in the head of the pancreas. While, a tumor in the body or tail of the pancreas may need a different procedure, like a subtotal pancreatic left resection. However, because of the invasive metastatic nature of pancreatic cancer, over 80% of patients are not eligible for surgery [17, 18]. Adjuvant chemotherapy and RT are also common treatment approaches [16]. Nevertheless, the resistance of PDAC to existing chemotherapy and RT regimens poses significant challenges to these treatment approaches [16]. One of the major

issues in RT in treating pancreatic cancer is the proximity of adjacent organs at risk especially the proximity of the small bowel (**Fig. 2.2**), resulting in treatment doses being limited by these organs, preventing dose escalation needed for local control [6–8]. With chemotherapy, the presence of the TME, including CAFs, stroma cells and ECM, prevents propagation of chemotherapeutic drugs denying the delivery of the necessary doses [5]. Despite the emergence of new immunotherapies for cancer therapy, these treatments are not suitable for PDAC due to its immunosuppressive and immunotherapy resistant dense TME [17, 18]. The cancer's resistance to conventional treatments and its ability to rapidly metastasize present significant obstacles in treatment development.

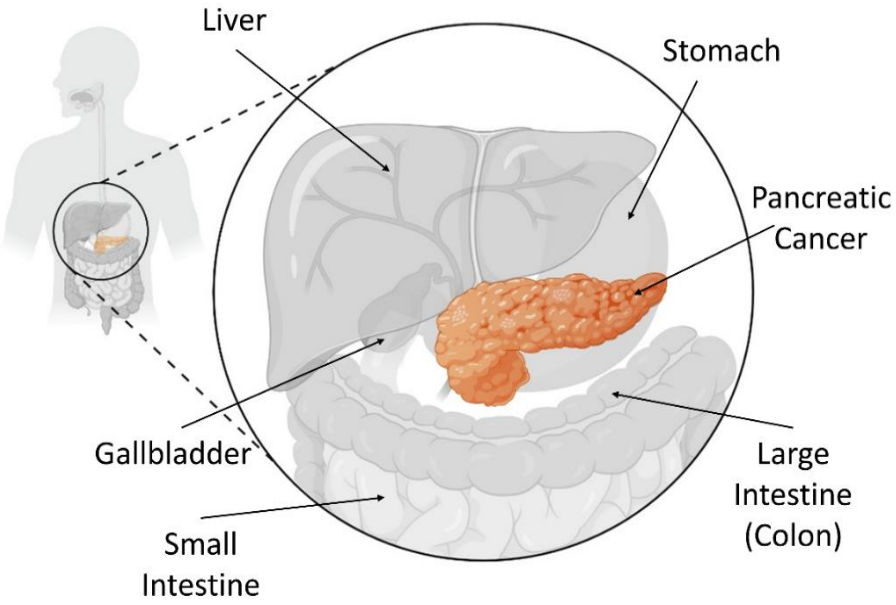

Figure 2.2 Illustration demonstrating the location of the pancreas next to vital organs. Created with BioRender.com.

2.1.5 Tumor Microenvironment (TME)

To design successful novel therapeutic approaches, it is very important to recognize the role of the TME in cancer development. As illustrated in **Fig. 2.3**, the TME is composed of cells, such as normal fibroblasts (NFs), cancer-associated fibroblasts (CAFs), endothelial cells, pericytes, macrophages, lymphocytes, and other immune cells, as well as an acellular compartment comprising the ECM soluble factors, and signaling molecules, all of which interact with the cancer cells and play a crucial role in tumor progression, invasion, and metastasis [78, 97, 98]. PDAC TME is very heterogeneous among different patients making it very immunosuppressive. It is made of a condensed desmoplasia and stroma that account for most of the tumor mass which results

in reduced vascularization, elevated hypoxia, thus hindering drug activity and increasing radio- and chemo-resistance effects [97, 98]. Therefore, understanding the TME and its interactions with treatment modalities is critical in reaping the benefits of nanotechnology particularly in pancreatic cancer where tumor stroma acts as a barrier.

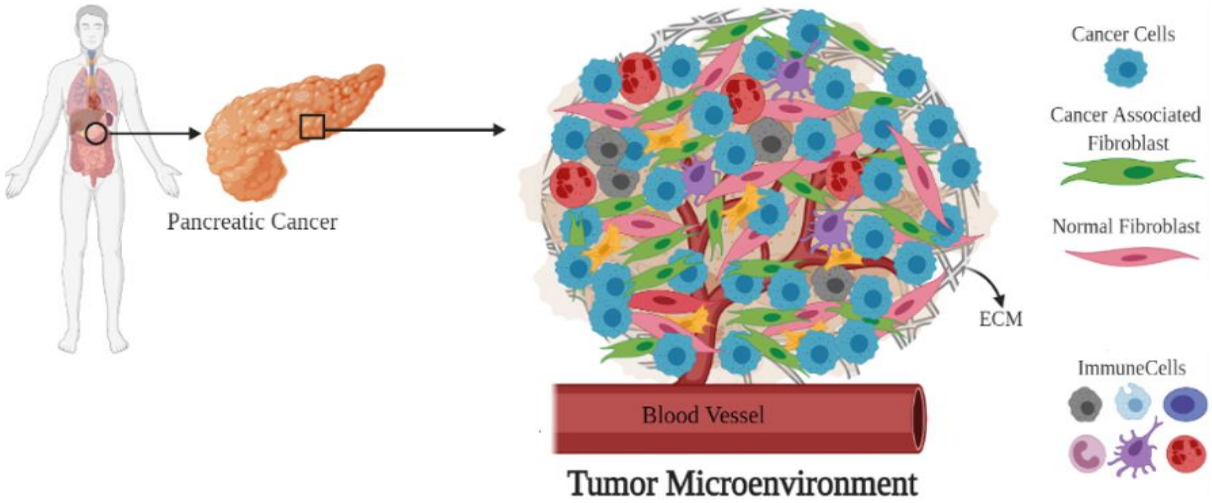

Figure 2.3 A schematic picturing the complexity of a TME for PDAC. Created with BioRender.com.

Among the diverse cell types within the TME, CAFs stimulate tumor growth, whereas NFs inhibit tumor growth [99–101]. NFs are a cell type that produces various essential proteins in the extracellular matrix, are associated with wound healing, and support normal tissue functioning. Unlike NFs, CAFs stimulates tumor growth, support angiogenesis, promote metastasis, play a negative role in tumor surgical excision, and are radio- and chemo-resistant [99–101]. Depending on the cancer type and individual human variations, CAFs comprise between 15% and 85% of the total stromal cell population, with roughly 10% of cells being cancer cells [6, 102]. Specifically, pancreatic TME undergoes desmoplasia, resulting in the formation of a fibrotic stroma. This process involves the accumulation of ECM components and the activation of CAFs, which subsequently lead to reduced vasculature patency, limited drug accessibility, and modifications in the anti-tumor immune reaction [97, 98]. Despite that, the current interest in use of new therapeutics in cancer therapy is mainly focused on pancreatic cancer cells rather than the TME.

2.1.6 The role of Cancer Associated Fibroblasts (CAFs)

It has been hypothesized that CAFs either originate from cells within the TME or from the recruitment of circulating cells that differentiate into CAFs once they arrive to the TME [103]. *In*

vivo mice experiments suggests that CAFs differentiate from NFs, mesenchymal stem cells, endothelial cells, and smooth muscle cells [103]. They are activated by cancer cells and can be identified by certain markers such as fibroblast activation protein alpha (FAP- α) and alpha smooth muscle actin (α-SMA) [104–107]. Once activated, they play an integral rule in cancer progression by helping with the deposition of the ECM which supports the development and expansion of fibrotic PDAC desmoplastic stroma and accounts for the majority of the tumor volume. Not only do CAFs encompass up to 85% of the overall stromal cell population, but they also promote tumor growth, angiogenesis, metastasis, and resistance to chemotherapy and RT [105–107]. Cancer cells and CAFs often work in tandem, wherein cancer cells stimulate the activation of CAFs to encourage the growth of the tumor, CAFs secret several growth factors, enzymes and cytokines that promote the proliferation of the tumor, help with metastasis of tumor cells, and weaken the impact of the immune system on tumor cells (**Fig. 2.4**) [103]. This intercommunication between cancer cells and CAFs fosters the ideal niche for tumor to develop. It is also worth mentioning that tumor cells are considerably smaller in size compared to CAFs, as illustrated in the two confocal images in **Fig. 2.4**.

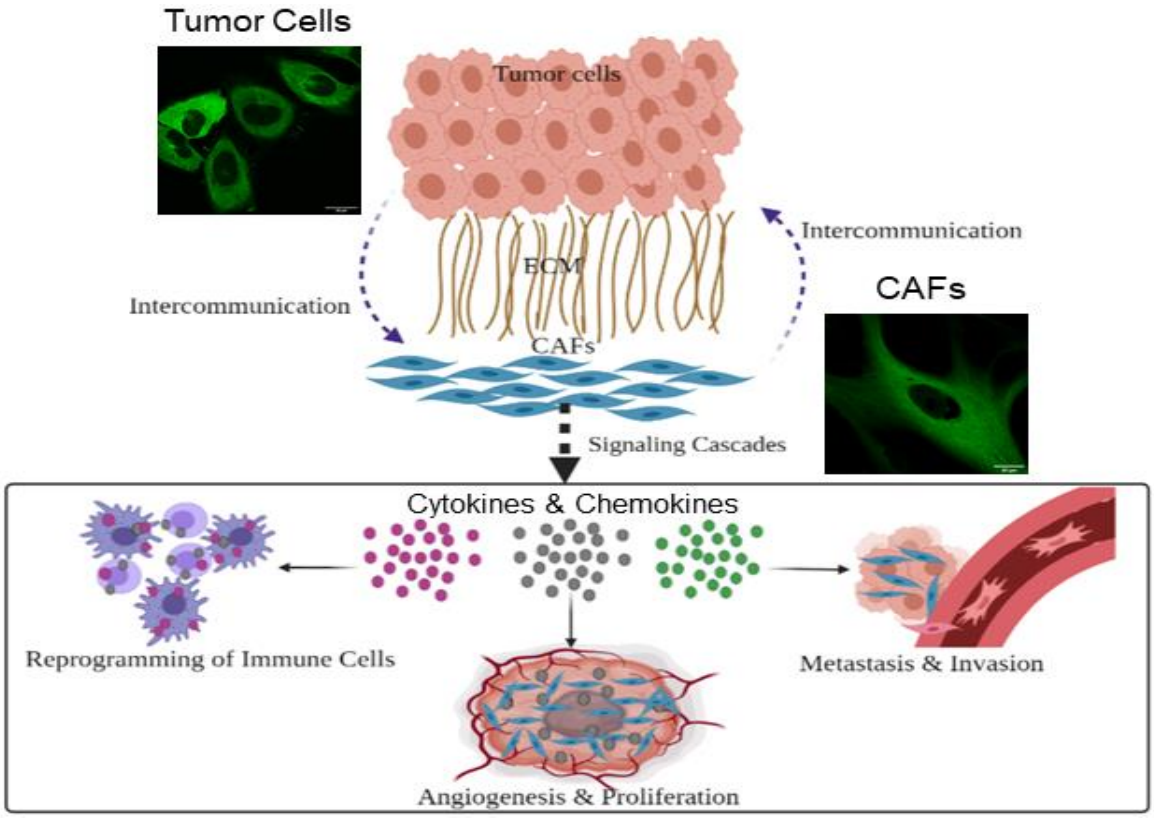

Figure 2.4 Schematic showing the role CAFs in tumor progression. Scale bar = 20 μm. Created with BioRender.com.

CAFs promote tumor growth and proliferation by multiple pathways including the recruitment of stromal cells, increasing the stem cell-like properties of cancer cells through the secretion of growth factors such as hepatocyte growth factor (HGF) and transforming growth factor beta (TGF-β), modifying the ECM, and encouraging angiogenesis by recruitment of endothelial [104]. CAFs can also enable cancer invasiveness by creating routes in the stroma for cancer cells to travel through to other sites, and by secretion of host-derived cytokines, chemokines, and inflammatory mediators that promote growth and attenuate apoptosis [104]. Moreover, CAFs facilitate metastasis by producing TGF-β signaling which encourage cancerous cells colonization of distant organs [104, 105]. CAFs also play an integral role in the immunomodulation of tumor tissue. CAFs release pro-inflammatory cytokines that recruit certain immune cells to the tumor stroma which then differentiate into tumor-associated immune cells and release several important endothelial and growth factors that promote the occurrence and progression of tumors, contribute to chemotherapeutic resistance, and engage in immunosuppression activities [104, 105].

It is indisputable that CAFs are involved in numerous phases of cancer development and are an essential component of the ECM of PDAC TME. CAFs are a predominant component of the stroma and represent an under-explored potential therapeutic target. Developing a new cancer treating modality requires co-targeting cancer cells and CAFs for its successful incorporation into cancer therapy. This could potentially reduce tumor growth and proliferation, lessen tumor invasion, inhibit metastatic dissemination, and disturb the tumor-associated immune response.

2.1.7 In vitro Co-Culture Models

In vitro co-culture cancer models involve growing different types of cells together in a controlled environment, mimicking the interactions that occur in the complex TME. These models provide a valuable tool for studying cell-cell interactions, cellular responses to various stimuli, and the influence of neighboring cell types on each other [80]. These models are widely used to study tumor-stroma interactions, which play a crucial role in cancer progression and treatment response [108, 109]. While not as complex as *in vivo* models, *in vitro* co-culture systems still provide a more realistic representation of cellular interactions than single-cell cultures. These models typically involve culturing cancer cells alongside other cell types found in the TME, such as fibroblasts,

immune cells, endothelial cells, and more [80, 82, 108, 109]. Such models offer several advantages including precisely controlling the cell types, their ratios, and the experimental conditions, allowing for detailed investigations into specific interactions [110]. These models also enable dissecting the mechanisms underlying cell-cell communication, signaling pathways, and molecular changes in response to various stimuli [110]. When it comes to ethical considerations, *in vitro* co-culture models are more ethical and cost-effective compared to animal models [110]. Furthermore, *in vitro* models can be standardized more easily, leading to reproducible results across different research groups [110].

In PDAC co-culture models, researchers often include different cell types such as cancer cells which are the driving force behind tumor growth and progression, CAFs which promote tumor growth, invasion, and metastasis, immune cells which inhibit tumor growth, endothelial cells which form blood vessels and are essential for supplying nutrients and oxygen to the tumor, and other stromal cells, to study their contributions to tumor progression [111–113]. Co-culturing cancer cells with CAFs (**Fig. 2.5**) can help uncover the role of CAFs in tumor growth, invasion, and drug resistance [112]. This is going to provide a platform for various studies such as studying the efficacy of potential anti-cancer drugs or combination therapies, exploring how the CAFs influences cancer cell behavior, and developing strategies to target specific interactions within the TME to improve treatment outcomes [112, 113].

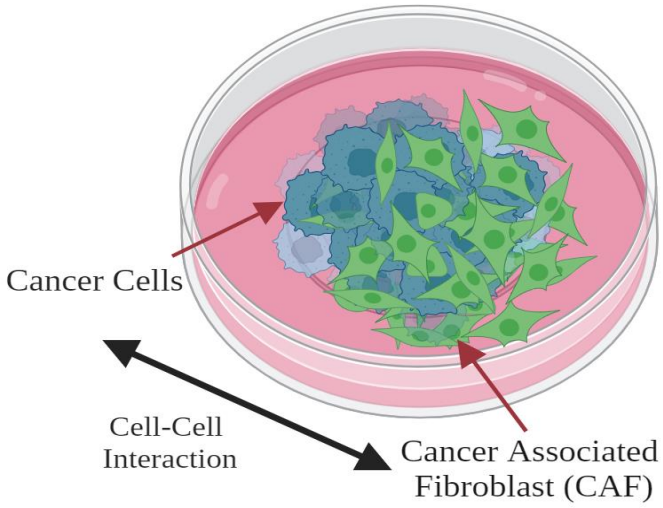

Figure 2.5 Cancer cells and CAFs 2D co-culture. Created with BioRender.com.

2.1.8 3D Spheroidal Model

Moving beyond 2D co-culture models, the adoption of 3D co-culture spheroids represents a realistic and simplified advancement. They offer several advantages studies over traditional 2D cell culture systems. 3D co-culture spheroids better mimic the complex three-dimensional architecture and cellular interactions found in living tissues. This physiological relevance provides a more accurate representation of *in vivo* conditions, allowing for more reliable and predictive experimental results [80]. 3D co-culture spheroids better predict drug responses and toxicity compared to 2D cultures. The 3D culture models better represent the diffusion gradients, nutrient availability, and oxygenation levels observed in tissues, resulting in more reliable assessments of drug efficacy and toxicity [82]. 3D co-culture spheroids allow for better screening approaches to evaluate the effects of various compounds, drug combinations, or novel therapeutics [112]. This allows for a more efficient and cost-effective evaluation of potential treatments than *in vivo*.

While 3D spheroid models have gained popularity as *in vitro* tools for studying various aspects of cell biology, disease, and drug responses, they also come with certain disadvantages. 3D spheroids lack the full complexity of *in vivo* environments [114]. Spheroids lack a functional vascular network, which is crucial for delivering nutrients and oxygen and removing waste products. This limitation hinders the study of interactions between cells and blood vessels, which are essential in many physiological processes [114]. Furthermore, the ECM in 3D spheroids might not fully replicate the ECM found *in vivo* which can influence cell behavior and drug responses [114, 115]. Also, the absence of immune cells in 3D spheroids, may limit the study of immune-tumor interactions. Larger spheroids can face another problem where cells at the core may experience limited access to nutrients, oxygen, and drugs due to diffusion limitations. This can create gradients of cellular responses within the spheroid, affecting the overall interpretation of experimental results [116]. It is also important to note that certain cell types may not form well-defined spheroids, and the mechanical properties of the spheroids may differ from those of native tissues [114, 115]. Despite being simplified representations of the complex *in vivo* environment, 3D spheroid models (**Fig. 2.6**) remain valuable tools for studying cell behavior in a more physiologically relevant context and predictive manner than 2D cultures helping to bridge the gap between traditional cell cultures and *in vivo* studies.

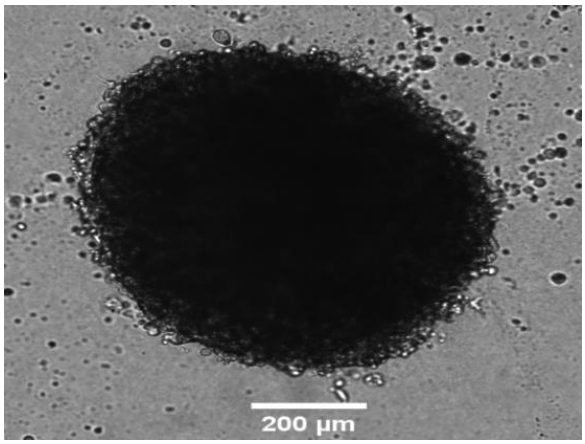

Figure 2.6 Bright-Field of 3D co-culture spheroid of cancer cells and CAFs. Scale bar: 200 µm.

2.2 Treatment Modalities

As a result of the various challenges posed by the intricate TME of PDAC, its current survival rate is a single digit, classifying it among the most unfavorable scenarios across all forms of cancer. To enhance the effectiveness and survival rates of clinical PDAC therapy, developing novel therapeutic modalities which combine various curative strategies to accomplish synergistic effect is inevitable. The reason for using a combined modality is to overcome therapy resistance, however the main problem in combined modality treatments is higher toxicity levels. Therefore, the proposal is to use a smart combination of RT and two radiosensitizer NPs that would have lower toxicity levels than current treatment methods. Here we explore the mechanism behind the three components to be used in our combined modality, namely RT, the relevant chemotherapeutic drug, and NPs as radiosensitizers.

2.2.1 Radiotherapy (RT)

RT is widely used in the treatment of various types of cancer. It is an important component of cancer treatment strategies and can be used alone or in combination with other treatments, such as surgery, chemotherapy, and targeted therapies. The specific use of RT depends on factors such as the type of cancer, its stage, the patient's overall health, and treatment goals.

2.2.1.1 Ionizing Radiation & DNA Damage

Ionizing radiation, radiation that has enough energy to free electrons from molecules, is proven to be damaging to living cells at high energies. Ionizing radiation can be divided based on

the rate of energy transfer, better known as linear energy transfer (LET). Neutrons, protons, α-particles, and heavy charged particles are high LET particles meaning that they are densely ionizing since they transfer more energy per unit length along their path [86]. In contrast, X- and γ-rays radiation produce low LET electrons that are sparsely ionizing because they deposit less energy per unit length along their tracks [86]. Both low LET and high LET radiation can interact 'directly' with the DNA (the critical target) in the cell nucleus causing damage, or 'indirectly' by ionizing atoms, i.e. knocking electrons out of the atoms that then start interacting with other molecules (mostly water since 80% of cell is water) which produce free radicals or reactive oxygen species (ROS) — an atom or molecule with an unpaired electron such as the highly reactive hydroxyl radical OH·— that can then damage the DNA [86]. The path of the direct damage by charged particles or by the products of neutrons and photons, i.e., electrons, and the indirect damage by ROS is comparable to the diameter of the DNA double helix of ~2 nm resulting is severe damage [86]. Indirect action through free radicals is dominant for low LET radiation and can be chemically modified by free radicals' scavengers, whereas high LET radiations produce most biological damage by direct action which cannot be chemically modified [86].

The DNA damage of most concern is the double-strand break (DSB) which can be formed by single tracks of ionizing radiation, in a single nucleus, in a single cell, and may result in cell death [86]. DNA damage can be recognized by enzymes where DSBs are repaired mainly by homologous recombination (HR) and non-homologous end joining (NHEJ) which are error-prone. Unrepaired or misrepaired damages to genes that control growth and proliferation will disable the cell to multiply and primarily result in cell death [117]. Cell deaths happens in different forms; apoptosis a.k.a. programmed cell death due to serious damage, mitotic catastrophe due to aberrant mitosis when cells enter mitosis with damaged DNA, necrosis which is an accidental unregulated cell death due to stress, or autophagy where the cell digests itself in desperation [86]. This destructive and distinctive characteristic of ionizing radiation is utilized in RT to damage cancer cells [118].

2.2.1.2 The Cell Cycle

The cell cycle and DNA repair are intimately connected processes within a cell's lifecycle. As illustrated in **Fig. 2.7**, the cell cycle is the process by which cells reproduce and can be divided into four major phases: G1 a first gap, S corresponding to DNA duplication and synthesis, G2 a

gap for mitosis preparation, and mitosis (M) where the cell divides into two daughter cells. Under normal circumstances, mitotic spindles form normally out of microtubules, stretching between two ‘asters’ originating at centrosomes at either pole at mitosis. The DNA is arranged at a metaphase plate between the asters before the chromosomes are evenly separated into daughter cells. Cellular progression is controlled by checkpoint genes that get activated when DNA damage occurs [86]. They ensure proper completion of events prior to progression through cell cycle. For example, at G2 cells are halted to inventory and for damage repair before mitosis. Cells where checkpoint genes are inactivated move directly to mitosis with damaged chromosomes and tend to be more sensitive to radiation or any DNA damaging agent [86]. The cell cycle phase also determines a cell’s relative radiosensitivity, with cells being most radiosensitive in the M and G2 phases, and most radioresistant in late S phase [86].

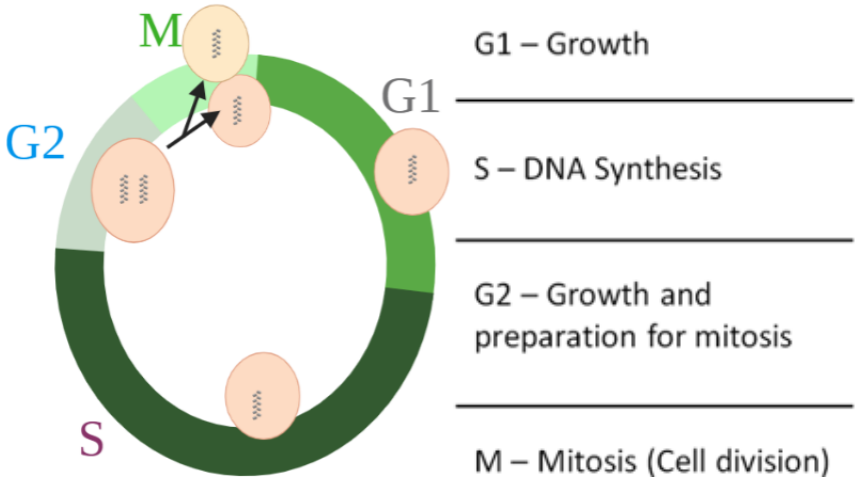

Figure 2.7 Cell cycle phases. In division preparation the cell goes through three different phases: G1 gap phase between M and S phases, S phase where DNA replication occurs and G2 where the cell prepares for mitosis. Created with BioRender.com.

2.2.1.3 RT Options

The most common type of RT treatment is using external beam of ionizing radiation where beam energy of up to ~ 25 MeV is used [119–121]. The two types of external beam ionizing radiation used in cancer treatment are: 1) photon beams (x-rays and gamma rays), 2) particle beams (electrons, neutrons, protons, and other heavy charged particles) [120, 122]. Because these beam types behave differently in terms of penetration depth and energy deposition (**Fig. 2.8**), they are used to treat different cancer types based on the tumor location [121]. For example, electrons have

very interesting dosimetric properties in which they deposit most of their energy early in their tracks compared to other charged particles and have a sharp dose fall-off compared to photons, thus they do not penetrate deep into the body [123, 124]. Therefore, electron beam is mainly used to treat skin cancers and cancers that are close to the surface of the body while sparring deep critical structures [120]. On the other hand, proton and other heavy charged particles can deliver high-dose to the tumor while sparing most of nearby healthy tissues providing dose distributions with excellent tumor control that are superior to photons. However, proton therapy is sparse worldwide, and the technology is not available for the vast majority of patients, not to mention the very expensive cost of such treatment [125]. In contrast, high energy beams of photons in the MV range are readily available in any cancer clinic with a linear accelerator. They have been used to treat most types of cancer effectively since the last century and they are currently the most used RT treatment worldwide [120]. Therefore, the goal is to utilize what is widely available for most pancreatic cancer patients.

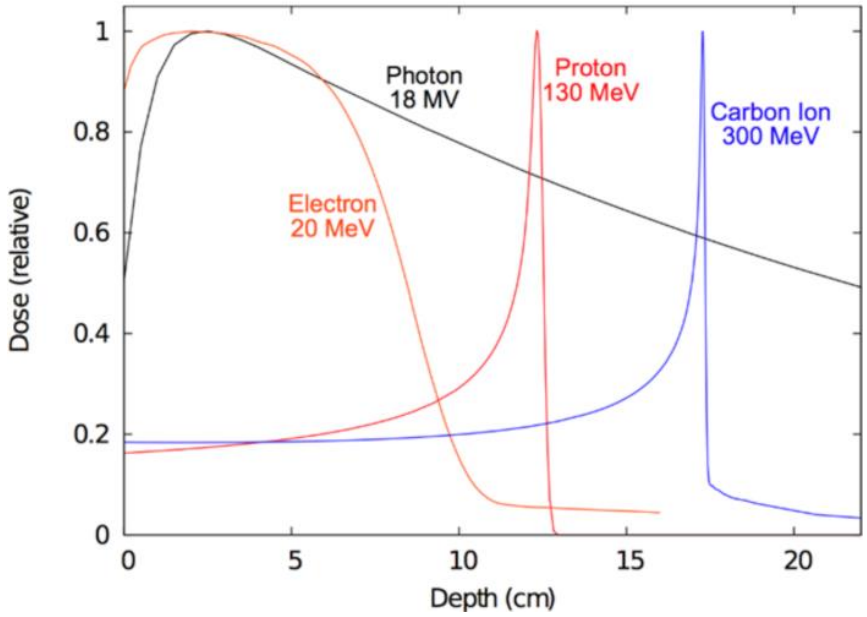

Figure 2.8 Depth dose distribution of different ionization radiation. Reproduced with permission from open access Creative Common license [123].

2.2.1.4 RT for PDAC

The commonly used doses for PDAC are 45-50.4 *Gy* in 25-30 fractions (1.8 *Gy* per fraction) for conventional external beam radiotherapy (EBRT), 50-54 *Gy* in 25-30 fractions (1.8-2 *Gy* per fraction) for intensity-modulated radiation therapy (IMRT), or stereotactic body radiation

therapy (SBRT) given as 25-33 *Gy* in 3-5 fractions (5-10 *Gy* per fraction) [126–133]. In IMRT, radiation beams are conformed to the treatment area, and the beam strength is altered across the area being treated. Thus, IMRT conforms the radiation dose more closely to the target, reducing the dose to the nearby organs at risk. (**Fig. 2.9**). On the other hand, SBRT precise higher single doses of RT are delivered to the tumor in fewer sessions to effectively spare adjacent organs at risk resulting in relatively lower toxicity. However, the use of RT alone for the treatment of PDAC has been infrequent due to PDAC high degree of radioresistance and the location of pancreas being hard-to-reach because of its proximity to many other vital organs [17].

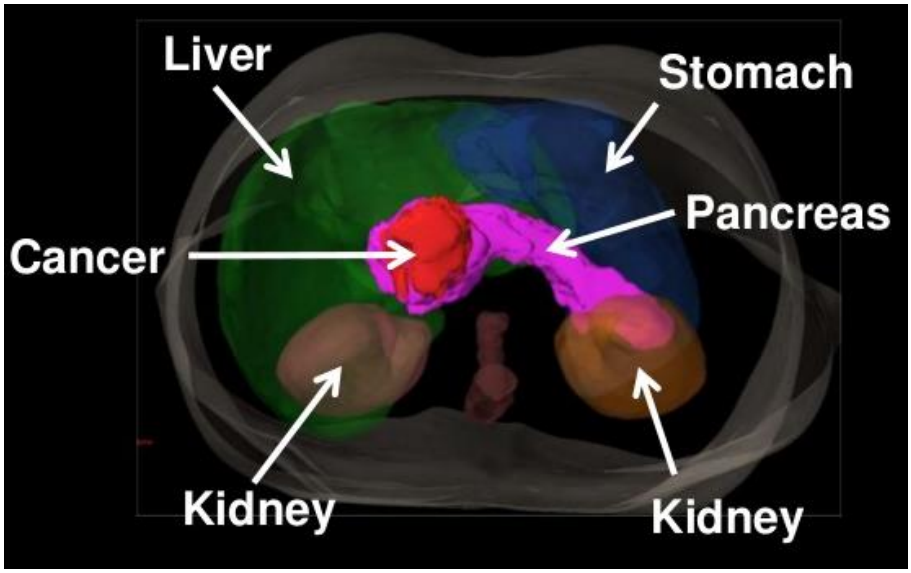

Figure 2.9 Illustration of deep-seated tumor in the pancreas. Transverse view.

There have been some attempts to enhance the efficiency of RT in PDAC treatment when surgery is not feasible. Studies have suggested that PDAC patients may survive longer with the use of SBRT [130–133]. One novel approach that is still being studied is the use of SBRT, for better local control, in combination with immunotherapy to further help break the immunosuppressive milieu of PDAC [17]. Another approach is to combine local RT with systemic chemotherapy. Researchers looked at the use of IMRT along with chemotherapy for the treatment of advanced or locally advanced PDAC. Results show that IMRT combined with chemotherapy increased survival rates and had better tumor control [127, 128]. When combined with gemcitabine, IMRT was found to improve survival [127]. Another study showed that administering chemotherapy before IMRT improved survival in people with locally advanced PDAC [128]. On

a different study, it has been found that the combination of chemotherapy and IMRT post-surgery improves survival, compared to just chemotherapy alone [129]. While the combination of chemotherapy and RT has shown some improvements compared to chemotherapy alone, best improvements in PDAC local control, patient quality of life and overall survival were credited for concurrent chemoradiotherapy using either IMRT or SBRT [126–132]. However, it is important to note that these improvements were only able to prolong patients' survival a few extra months. The outcome is still very poor for PDAC compared to other cancer types and a new treatment approach is desperately needed.

2.2.1.5 RT & Surgery for PDAC

RT combined with surgery is a treatment approach commonly used for PDAC. This combined treatment strategy is known as adjuvant RT and is aimed at improving treatment outcomes in patients who have undergone surgical removal of the tumor, also known as resection. Surgery is the primary treatment for PDAC if the tumor is localized and has not spread to distant sites [5]. A surgical procedure, called a pancreaticoduodenectomy or Whipple procedure, involves removing the head of the pancreas, part of the small intestine, the gallbladder, and sometimes a portion of the stomach and lymph nodes [134]. After surgery, adjuvant RT is often used to target the area where the tumor was removed, which may harbor residual disease, with or without irradiation of the draining lymph node regions. This helps reducing the risk of cancer recurrence in the surgical site [135]. This combined treatment can have better local cancer control and improved survival [135]. RT can also be used prior to surgery (neoadjuvant therapy**)** which is often considered for tumors that are initially deemed unresectable [136]. Neoadjuvant therapy helps shrink the tumor size, making it easier to remove and have better odds that the resection will have negative margins [136]. However, it's important to note that the decision to use RT with surgery for PDAC depends on various factors, including the stage of the cancer, the patient's overall health, and the extent of the surgical resection. In some desperate cases RT could be used as a palliative option to shrink the tumor and slow down its growth without aiming to cure it. This is typically used for patients with advanced PDAC that has spread to other parts of the body [137]. It could also be used to palliate symptoms from the primary tumor, such as pain. Although RT in combination with surgery has proven to be effective in many cases, survival rates are still extremely low.

2.2.1.6 The "6 Rs" of Radiobiology

The "6 Rs" of radiobiology are a framework that describes the fundamental principles governing the response of cells and tissues to radiation [86]. These principles help in understanding the interactions between radiation and living organisms. The 6 Rs stand for:

1. **Repair:** Cells possess mechanisms to mend damage caused by radiation. This repair mechanism can operate both during and subsequent to radiation exposure. Cells endowed with more proficient repair capabilities have a higher likelihood of enduring radiation exposure [86, 138].
2. **Reassortment:** Cell cycle redistribution indicates the reorganization of cells within their cycle after radiation exposure. Radiation's impact on distinct phases of the cell cycle can result in reshuffling, causing fluctuations in cellular vulnerability to radiation at various time intervals [86, 138].
3. **Repopulation:** Following radiation exposure, surviving cells may undergo repopulation to replenish damaged or deceased cells. This regrowth process involves cell division and can be influenced by factors such as the rate of cellular proliferation and the availability of necessary nutrients [86, 138].
4. **Reoxygenation:** The presence of oxygen plays a vital role in augmenting the effects of radiation by contributing to the production of ROS that induce cellular damage. Hypoxic cells, which experience low oxygen levels, tend to exhibit greater radioresistance. Conversely, tumors can be sensitized to RT by increasing oxygen levels, thereby enhancing the effectiveness of the treatment [86, 138].
5. **Radiosensitivity:** The response of cells and tissues to radiation varies based on their inherent sensitivity. This sensitivity is influenced by several factors, including the cell type, its differentiation status, and its genetic characteristics. Cells with higher radiosensitivity are more prone to damage or elimination upon exposure to radiation [86, 138].
6. **Reactivation of anti-tumor immune response:** This refers to the phenomenon where RT can trigger or enhance the body's immune system to recognize and target cancer cells. Radiation can cause cancer cells to release specific antigens or signals that alert the immune system to their presence [139]. This process can help immune cells, such as T cells, recognize cancer cells as abnormal and mount an attack against them. In some cases,

radiation can also suppress the immunosuppressive components of the tumor microenvironment, allowing the immune system to function more effectively [139]. This can turn "cold" tumors (those that have been less responsive to the immune system) into "hot" tumors that are more susceptible to immune attack.

Understanding these principles is crucial for comprehending the consequences of RT and enhancing its efficacy in cancer treatment. For example, fractionated RT is used because it helps synchronizing cells in the more radiosensitive phases of mitosis G2/M. Fractionation helps to re-oxygenate tumors for subsequent fractions. Fractionation helps to overcome DNA repair in tumor cells while allowing for repair in normal cells (because of the different shape of cell survival curves between tumor cells and normal cells) [86]. The 6 Rs framework provides guidance for making educated choices regarding treatment strategies, dosages, and timing, aiming to attain the intended therapeutic results while mitigating harm to healthy tissues.

2.2.2 Chemotherapeutic Drugs

Even though chemotherapy is typically used for treatment of PDAC, their uses are associated with high level of toxicity, thus often preventing their application in many PDAC patients [17]. Therefore, a combination of chemotherapy along with RT is a more attractive option for unresectable PDAC. Chemotherapy with RT can have an advantage where some chemotherapeutic drugs are not only good radiosensitizers, but also have different mechanisms of cell killing, thus, chemotherapy can eliminate cells that withstand RT, and vice versa [126]. Currently, the standard treatment of locally advanced unresectable PDAC involves either palliative chemotherapy (designed for incurable cancers to prolong survival and ease symptoms but not cure disease), adjuvant sequential chemoradiation (chemotherapy administered in cycles prior to RT), chemotherapy followed by concurrent chemoradiotherapy (chemotherapy administered with RT on the same day), and concurrent chemoradiotherapy [126–129]. In PDAC's case, chemotherapeutic drugs that can work synergically such as gemcitabine and nanoparticle albumin-bound paclitaxel (nab-paclitaxel) are often used in Canada [140–144].

2.2.2.1 Gemcitabine and Nab-Paclitaxel

Gemcitabine ($C_9H_{11}F_2N_3O_4$) is an FDA approved anticancer drug used alone or as an adjunct therapy in the treatment of several types of cancer such as ovarian cancer, non-small cell

lung carcinoma, metastatic breast cancer, and PDAC [145–147]. It is chemotherapeutic agent classified as a nucleoside metabolic inhibitor where it exerts its anticancer effects by interfering with the DNA (deoxyribonucleic acid) synthesis. The two fluorine atoms of the drug replace the hydroxyl on the ribose sugar of the DNA nucleotide nullifying effective DNA synthesis in malignant cells, thus halting tumor growth and encouraging apoptosis of cancer cells [148]. Generally, gemcitabine is the first-line treatment for PDAC [145]. However, due to the chemoresistance of pancreatic cancer cells and CAFs to gemcitabine, it has been complemented by another FDA approved drug, nab-paclitaxel ($C_{47}H_{51}NO_{14}$), which works as an antimicrotubular agent thus working in synergy with the DNA affecting gemcitabine [148]. This treatment is now used as the new first-line treatment of metastatic PDAC is many countries around the world including Canada, the US and the European Union [145, 146, 149–151]. Paclitaxel, the active ingredient in nab-paclitaxel, is a taxane that has been used to treat many different types of cancers such as breast cancer, lung cancer and pancreatic cancer [146]. As an antimicrotubular drug, it kills cancer cells by stimulating the assembly of MTs and stabilizes them by preventing depolymerization during cell division. This causes defects in the mitotic spindles' assembly of Paclitaxel-treated cells, thus preventing chromosome segregation. This in return blocks the progression of mitosis and prolongs the activation of the mitotic checkpoint, thus triggering apoptosis or return to the G0 phase of the cell cycle without division [152]. As a result of cancer cell resistance to taxanes, hypersensitivity, high toxicity and low solubility, many different synthetic by-products of taxanes have been developed to try to overcome these challenges such as the development nab-paclitaxel which is an injectable formula of paclitaxel that uses nanoparticle technology to increase the concentration of drug in the tumor [153, 154]. In this formula, paclitaxel is bonded to albumin, which is a protein, as a drug carrier. The typical administered dose of gemcitabine and nab-paclitaxel are, 1000 mg/m^2 and 50-150 mg/m^2, respectively, once a week over 4 weeks cycles, where the body surface area (m^2) is calculated as: $\sqrt{\frac{height(cm)\times weight(kg)}{3600}}$ [146, 147, 149–151].

2.2.2.2 Docetaxel (DTX)

Docetaxel (DTX; $C_{43}H_{53}NO_{14}$) is a paclitaxel semisynthetic analogue that is also an antimicrotubular anticancer agent that is FDA-approved to treat plenty of solid cancers such as

head & neck, ovarian, breast, prostate and lung cancers in combination with RT or other chemotherapeutics such as cisplatin [155–157]. The typical dose of the drug used is 75 mg/m^2 [158]. DTX mechanism of action is similar to that of paclitaxel where it is an MT stabilizing agent [155]. DTX stabilizes MTs against depolymerization, while also lowering the critical concentration of tubulin necessary to form new MTs [159]. This would lead to unregulated formation of MTs, without regard to the microtubule-organizing center (MTOC), resulting in bundles hindering the formation of mitotic spindles which are necessary for a proper cell division (**Fig. 2.10 (i-iii)**) [160–162]. Under regular M phase conditions, normal cells use the MTOC and microtubules to form mitotic spindle (**Fig. 2.10 a(ii)**) where chromosomes are then segregated equally between two daughter cells (**Fig. 2.10 a(iii)**). However, with DTX treatment, microtubules will be stabilized, and the cell will no longer be able to divide properly. This results in asters and bundles forming independently of centrosomes, creating multiple cleavage planes. Doses as low as 50 nM of DTX is sufficient to cause a "mitotic catastrophe" *in vitro* where the cell is unable to enter anaphase and remains locked in mitosis or becomes multinucleate as the nuclear envelope reforms around the multiple asters (**Fig. 2.10 b(i-iii)**) [61]. This results in blocking the cell cycle at the G2/M phases the most radiosensitive phases of mitosis. This is why DTX has shown remarkable radiosensitization effects at low doses both *in vitro* and *in vivo* despite higher doses being associated with toxicity [163–166]. This encouraged its use with RT in several Phase II clinical trials [167–171]. Although DTX is not currently being used to treat pancreatic cancer, given that the mechanism of action of DTX is like nab-paclitaxel, combined with its radiosensitizing effects *in vivo* and *in vitro*, and its tolerable usage with RT in multiple phase II studies, DTX is a good candidate for this project. However, the free form of DTX have limitations such as poor solubility, limited targeting ability, and high normal tissue toxicity [172].

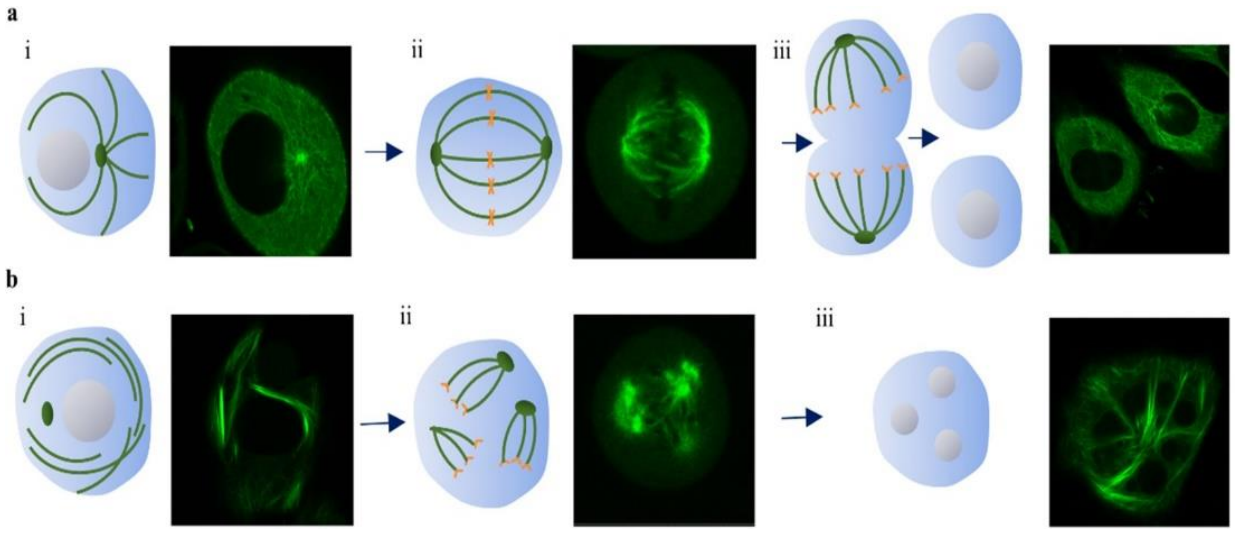

Figure 2.10 Schematic diagram and confocal images of cell division showing microtubules under normal conditions (a) and 50nM DTX (b). a) i) Quiescent normal cell, ii) normal mitotic spindle, iii) normal pair of daughter cells. b) i) Aster formation in non-dividing cell with DTX, ii) fragmentary division with 10nM DTX, and iii) mitotic arrest with multinucleation under 50nM DTX Reproduced with permission from open access Creative Common license [61].

2.2.2.3 Lipid Nanoparticles (LNPs)

Pharmaceutical drugs in their free form are administered to the body without any specific carriers or delivery systems. These drugs are often in their simplest and unaltered chemical state, and are not bound to any other molecules, which allows them to exert their therapeutic effects directly upon administration. When a free drug is administered, it circulates throughout the body via the bloodstream and can potentially be cleared by organs such as the liver and kidneys. Additionally, tumors can have irregular blood vessels and abnormal TME, making it difficult for drugs to adequately penetrate and reach the tumor cells. As a result, only a small fraction of the total dose administered actually reaches the tumor site [51–53]. Studies have estimated that this amount can be as low as approximately 0.1% or even less [51]. This limited delivery to the tumor contributes to the challenges faced in achieving optimal therapeutic efficacy and reducing side effects.

To improve drug delivery to tumors, various strategies are being explored, such as using drug carriers or delivery systems that can enhance selective accumulation in the tumor site while minimizing exposure to healthy tissues [173]. LNPs, which have gained a huge success during the current pandemic delivering mRNA vaccines against COVID-19, are nanoscale structures made up of lipids such as phospholipids and cholesterol that can effectively encapsulate and deliver

various types of drugs [174]. LNPs can be utilized as drug delivery vectors and functionalized to specifically target tumours with controlled delivery, thus significantly decreasing the dose delivered to healthy organs [175]. Moreover, the extended circulation time of LNPs leads to an uptick, with 2–5% of the administered dose accumulating in the tumor. This is in contrast to a mere 0.1% for the unencapsulated drug [52]. Even if we consider that only 1% of the drug from LNPs reaches the target, it still signifies a more than tenfold increase in the drug concentration within the tumor compared to its free form [53]. In addition to these advantages, the small size of the NPs allows them to reach the tumour via the EPR effect due to the leaky tumour vasculatures [176].

In cancer therapy, LNPs have been used in combination with DTX to improve treatment efficacy [31]. However, not only is DTX very toxic to normal tissues but it has poor solubility in water, making its delivery to cancer cells in the body difficult [172]. This solubility issue can be resolved by encapsulating DTX prodrugs within LNPs, which can enhance the solubility of the drug and improve its delivery to cancer cells, thus, increasing its effectiveness [56]. To further to improve DTX therapeutic efficacy and reduce its side effects, we have successfully developed an inactive prodrug version of DTX and encapsulated it into LNPs ($LNP_{DTX\text{-}P}$) (**Fig. 2.11**). The prodrug DTX contains ester bonds which is hydrolyzed by the esterases enzyme found on cancer cells and CAFs. This enzymatic hydrolysis leads to the activation of DTX [177]. This can lead to improved patient tolerability and compliance with the treatment regimen.

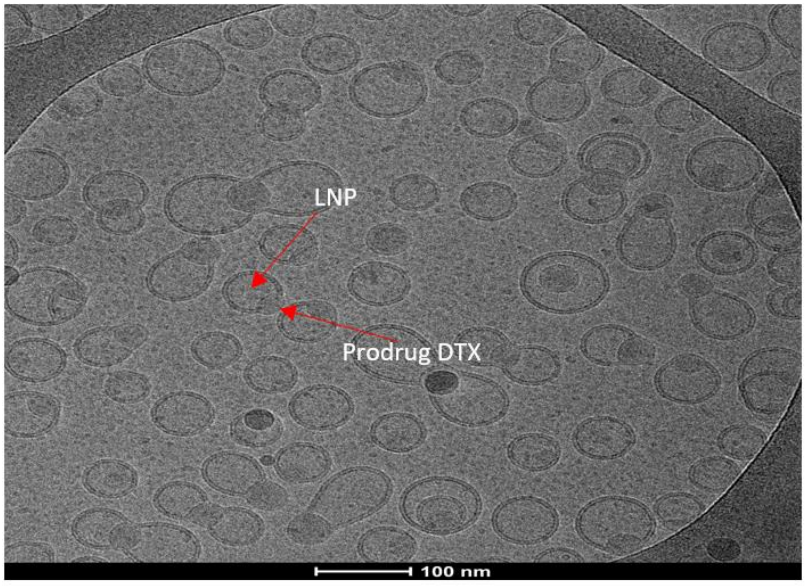

Figure 2.11 Cryogenic Transmission Electron Microscopy image of $LNP_{DTX\text{-}P}$. Scale bar = 100 nm.

Additional advantages of using $LNP_{DTX\text{-}P}$ include increased drug stability, which allows for longer circulation periods, thus, improving overall tumor accumulation and efficacy [177]. Moreover, there's potential to enhance drug delivery by customizing LNPs with specific ligands or antibodies that target receptors predominantly expressed on cancer cells. This paves the way for more individualized and pinpointed therapy [175]. Such targeted delivery diminishes the likelihood of affecting healthy cells, thus minimizing side effects. The combination of LNPs with DTX prodrugs has demonstrated a reduction in the systemic toxicity commonly linked with DTX [59]. This is attributed to the precise delivery of the drug to the tumor, limiting the impact on normal organs. Research further indicates that employing LNPs with DTX prodrugs amplifies the drug's potency against cancer cells, leading to enhanced treatment results [60].

2.3 Radiosensitizers

2.3.1 Radiosensitization

Delivering doses that would eradicate tumor tissue without disrupting surrounding healthy tissues is very challenging. The ideal goal of cancer treatment is 100% tumor control, i.e., to halt all division of cancerous tissues by cell death or sufficient damage [178]. Unfortunately, due to the difficulties encountered in targeted cancer therapies, this is often not practically possible as the collateral damage to the patient would cause death or unacceptable side-effects. The probability for a tumor to be controlled is referred to as the tumor control probability (TCP), while the probability for healthy tissue side effect is referred to as normal tissue complication probability (NTCP), and the probability of cure without complication (PCWC) refers to the likelihood of treating the tumor with minimal side effects (**Fig. 2.12**) [178]. Under normal circumstances, the dose that would be associated with for example %80 tumor control would be associated with considerable damage to normal tissue (**Fig. 2.12**). In other words, the borderline between TCP and NTCP is small, hence the small PCWC window. In general, physicians in clinical radiotherapy, prescribe doses that would be associated with a 5% or less probability of significant long-term complications as the typical cutoff, this could limit the achievable tumor response [178]. Therefore, it is critical to explore other possibilities that improve the PCWC. Reaching the optimal balance is still being studied extensively [178].

One common strategy in cancer therapy is to combine anticancer drugs with non-overlapping mechanisms and profiles of side effects. This would cause maximum damage to the

cancer due to the combined effects of the drugs while keeping the side effects more “spread out” over different organs and tissues [178]. Although recent advances in RT improved the dose conformity and the clinical outcome, additional therapeutic benefit may be gained by using chemotherapeutic radiosensitizers in RT for different cancers such as cervix, head & neck, rectal, and higher grade gliomas [178]. The benefit of using radiosensitizers is to expand the therapeutic window by increasing the maximum and width of the PCWC distribution. This shifts the TCP curve towards the left and creates a larger margin sparing healthy tissues. Radiosensitization mechanisms vary from directly amplifying the radiation dose or creating additional ROS to making the cell ignore DNA damage [179].

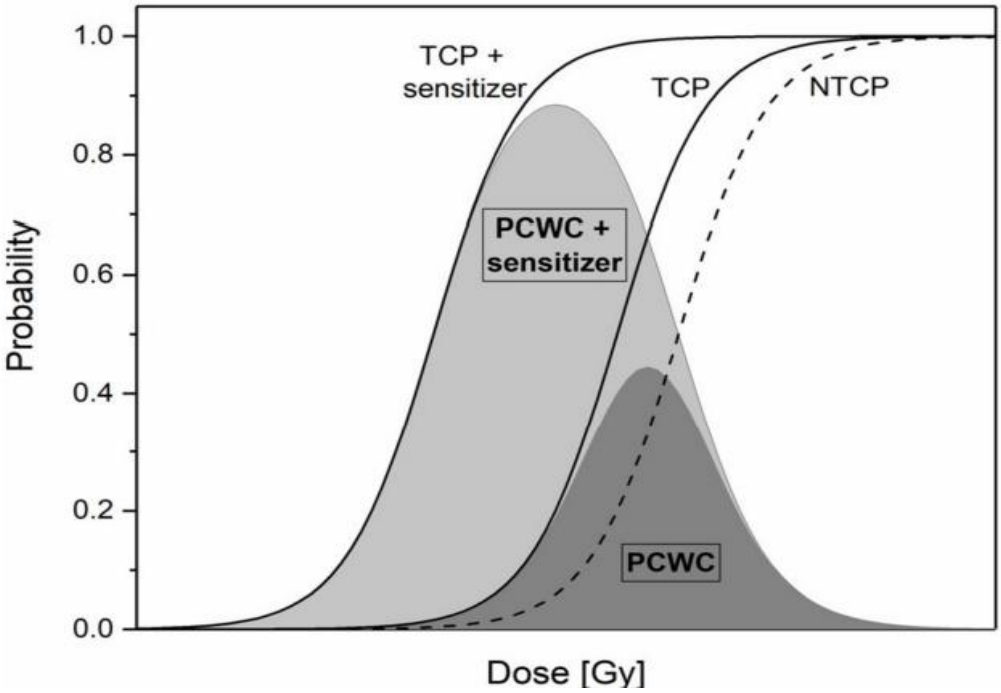

Figure 2.12 An illustration schematic showing the effect of tumor-targeted radiosensitizer on the PCWC. The TCP (solid line) and NTCP (dashed line) are shown as a function of the dose delivered to the patient. Two scenarios are illustrated with or without the use of a radiosensitizer and the associated PCWC is shown by the surface in each case. Reproduced with permission from open access Creative Common license [178].

2.3.2 Photons Interaction with Matter

The three fundamental processes that occur when photons interact with matter relevant to RT are photoelectric effect, Compton scattering and pair production [120]. Their probability of occurrence depends on the incident energy of the photon and the Z number of the material as shown in **Fig. 2.13**. In the photoelectric effect, a photon interacts with an atom, typically an inner-

shell electron, and transfers all its energy to that electron. This results in the ejection of the electron from the atom, creating an ionized atom and a free electron [120]. In Compton scattering a photon collides with an electron, the photon transfers some of its energy to the electron, causing it to recoil. As a result, the photon's energy decreases due to this energy transfer [120]. The Compton effect is dominant at clinically utilized radiotherapeutic energies (**Fig. 2.13**). In pair production, a high-energy photon interacts with a nucleus or an electron in the vicinity of a nucleus [120]. The photon transforms its energy into the mass of an electron-positron pair. This process requires a minimum energy threshold, usually well above 1.02 MeV, due to the rest mass of the electron and positron [120].

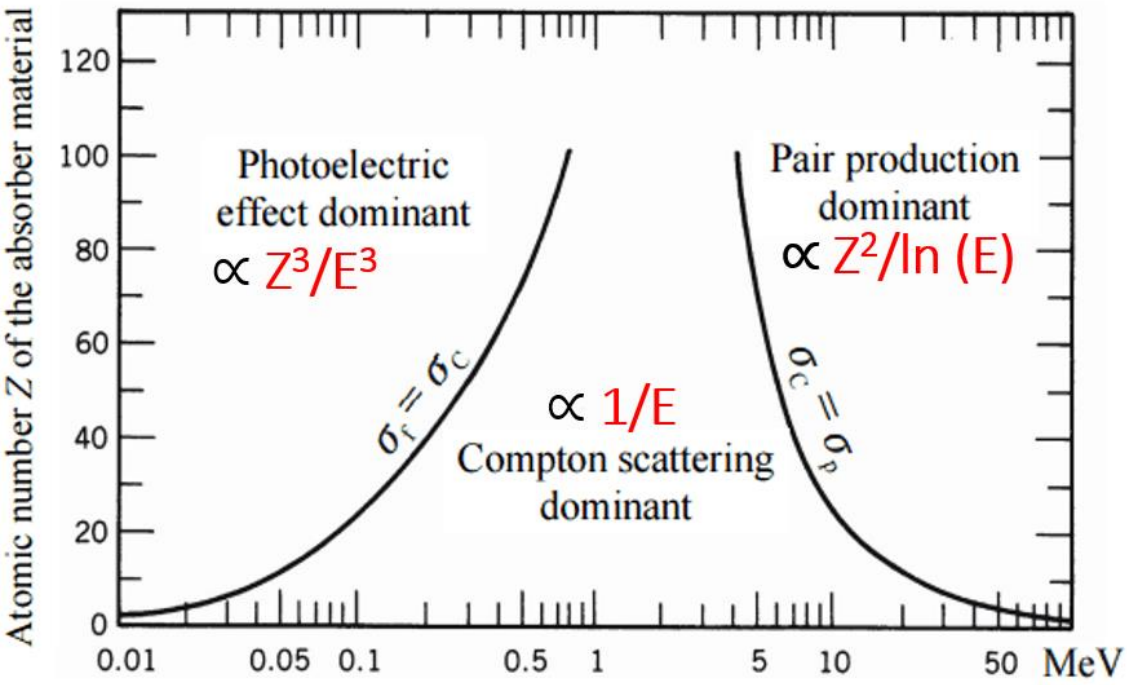

Figure 2.13 Interactions of Photon with matter probability curves. Reproduced with permission from open access Creative Common license [180].

2.3.3 GNPs as Radiosensitizers

NPs are particles between 1-1000 nm and often have different properties than those seen in bulk material of the same composition. NPs can be tailored for specific needs by modifying their size, shape, and surface properties [21, 181, 182]. Inorganic NP systems such as GNPs, silver NPs, gadolinium-based NPs, lanthanide-based NPs, and titanium oxide nanotubes have been reported as radiosensitizers [183–188]. They can also act as carriers for drugs and other molecules making them very promising candidates to be used for cancer treatments [189]. Gadolinium-based

NPs offer an innovative approach because of their capacity to act as a radiosensitizer as well as a powerful contrast agent in magnetic resonance imaging [187]. The high-Z nature of silver-based NPs along with their antimicrobial properties made them a good candidate in RT [188]. GNPs particularly are the most promising due to their simple surface chemistry, biocompatibility, low toxicity, and ease of manufacture [21, 29, 45–48]. One of the pioneering studies by Hainfeld et al. demonstrated GNP-mediated radiosensitization in a mice tumor graft where 1.9 nm GNPs and 30 Gy of 250 kilovoltage-peak (kVp) x-rays were used. The addition of GNPs to radiation resulted in 86% long-term survival compared to 20% with radiation alone [29]. The kV energies used in this study can be used to treat superficial tumors due to the lack of penetration power of these low radiation energies. In the clinic, the deep-seated tumors are treated with higher energy photons with mega-voltage energy range from 4 MV to 25 MV [190].

Both *in vitro* and *in vivo* studies have demonstrated the promise of GNPs with MV radiation to generate radiosensitization [45, 49, 50]. For example, Wolfe and co-workers used goserelin-conjugated gold nanorods in prostate cancer to demonstrate the associated sensitization *in vivo* [49]. When systemically administered, conjugated gold nanorods accumulated preferentially in prostate cancers *in vivo*, and subsequent irradiation with MV radiation resulted in a substantial increase in tumor growth delay. Most importantly, there was a 3-fold higher radiosensitization to MV radiation with targeted NPs compared untargeted ones. This suggests that radiosensitization is improved by active targeting of NPs which led to improved cellular internalization of the NPs. The presence of NPs in cells resulted in an increase in ionization density within the cytoplasm, rather than merely a passive accumulation of NPs in the perivascular space by the EPR effect [49]. Their results demonstrate that MV radiosensitization is achievable *in vivo* using tumor-targeting NPs administered intravenously at a low concentration of 10 mg/kg. This is over one thousand-fold lower than that previously thought to be necessary for radiosensitization [29]. The use of MV radiation to generate such radiosensitization *in vivo* at such clinically feasible concentrations of NPs foretell the possibility of eventual clinical translation of this approach. Nonetheless, the transition of GNPs as radiosensitizers to clinical applications is an ongoing process, and additional refinement of protocols is required before a significant portion of drug-related research can progress beyond the preclinical phase.

2.3.4 GNPs Radiosensitization Mechanism

Targeting tumor cells using high-Z materials has been pursued to improve the local radiation dose and thus minimize the damage to surrounding healthy tissue [191]. The main radiation interaction with GNPs relating to radiosensitization applications in cancer research is the photoelectric absorption/effect [192, 193]. This occurs when an incident photon interacts with an inner-shell electron, transfering all its energy to it and causing it to be ejected from the atom as a secondary electron. Outer-shell electrons can fill this vacancy, liberating further energy often in the form of additional secondary Auger electrons. The absorption coefficient for the photoelectric effect scales roughly with $\frac{Z^3}{E^3}$, where Z is the atomic number and E is the energy of the incident photon. So, materials like gold ($Z = 79$) can have a much higher absorption than tissue ($Z \sim 7.5$) (**Fig. 2.14**) [192]. This allows GNPs to be radiation dose enhancers for most photon energies including the kV x-rays used in medical imaging and the MV photon beams used in RT.

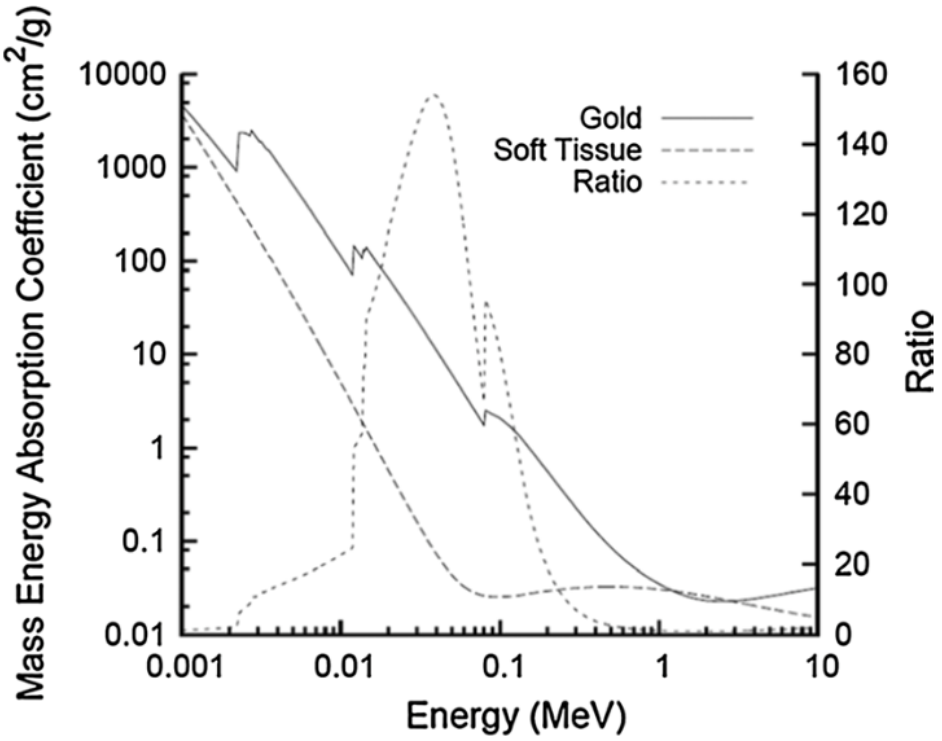

Figure 2.14 Photon mass energy absorption coefficients of soft tissue vs gold. The ratio of mass energy absorption coefficients is shown as a function of photon energy. Reproduced with permission from open access Creative Common license [192].

The dose enhancement and radiosensitization effect is attributed to the increased number of photoelectric absorption events leading to the production of low-energy, high-LET secondary

electrons scattering from the surface of the high-Z material [194, 195]. The resulting inner shell vacancy can initiate further secondary electrons in the form of Auger cascade, spreading out much of the remaining energy of the interaction into more low-energy electrons [196]. The net effect is a spray of short-range electrons that can cause many ionizations as they slow in the surrounding medium directly interacting with the DNA causing DSBs [196]. Alternatively, this increase in the number of electrons can act indirectly by triggering an increase in free radicals and ROS, such as superoxide (O_2^-) and hydrogen peroxide, which can lead cause excess DNA DSBs (**Fig. 2.15**) and therefore amplifies cell death numbers [197, 198]. These species can also do damage to other biomolecules or cause oxidative stress which can lead to apoptosis or necrosis [192]. However, the exact radiosensitization mechanism is not fully understood yet. This phenomenon opened the door for high-Z NP elements to be investigated as radiosensitizers for cancer treatment [199, 200].

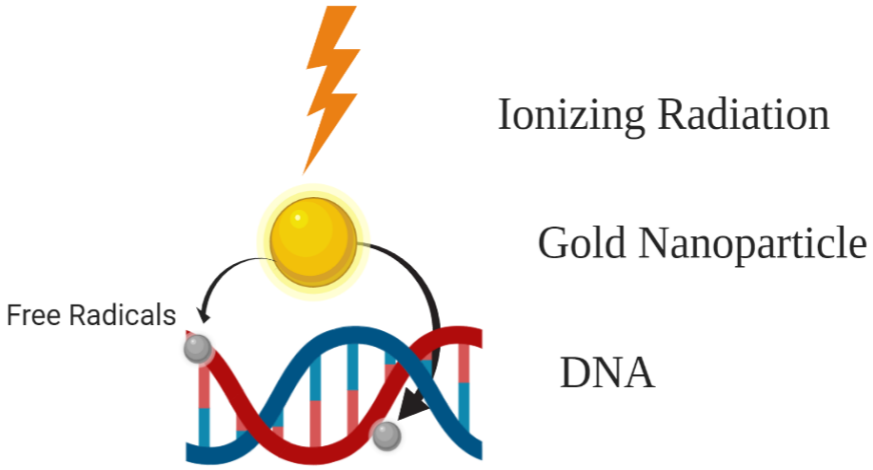

Figure 2.15 Schematic showing chemical mechanism of GNP radiosensitization. Created with BioRender.com.

It is important to note that the photons of a 6 MV beam, for example, exhibit an energy distribution spanning from lower keV values to a peak of 6 MeV, with the majority clustered around approximately one-third of the peak value (**Fig. 2.16**) [120]. Therefore, although, the relative dose enhancement and range of secondary electrons are higher when using a kV x-ray beam, meaningful enhancement can still be achieved with MV beams due to contamination of the beam by lower-energy scattered photons and secondary electrons produced as it passes through tissue [201]. For example, the dose enhancement factor for 6 MV beam is 1.17 vs 1.66 for 105 kVp beam [45]. This means that deep seated tumors that cannot be effectively treated with shallowly penetrating kV beams could still benefit from GNP-enhanced RT.

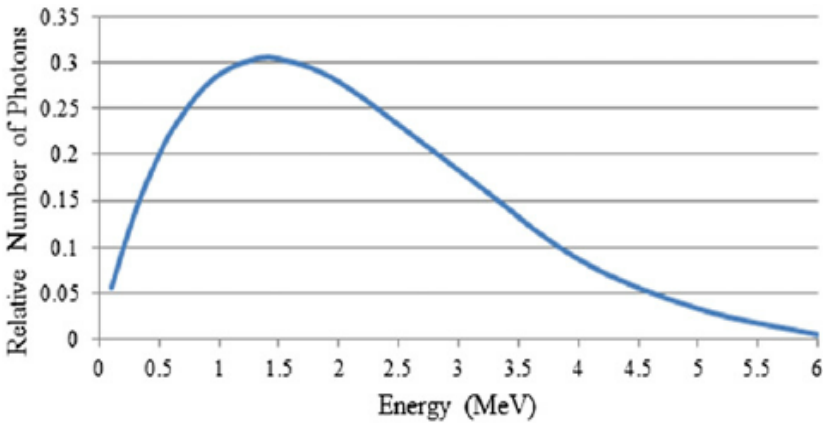

Figure 2.16 Photon energy distribution of 6 MV beam.

2.3.5 GNPs Functionalization

The optimization of GNP physical properties (size, shape, surface properties, etc.) is an important factor in the proper utilization of nanotechnology in combined cancer therapy to maximize the beneficial effects. Unfunctionalized GNPs naturally bind to plasma proteins at their surface, enabling their cellular uptake into the cell [202]. However, this makes them vulnerable to attacks from the immune system which clears them from the system, thus causing GNPs to have a short bloodstream circulation lifetime [203]. To overcome this problem, GNP surfaces are coated with PEG stabilizing agent to reduce their binding to the antibody proteins that target foreign objects for clearance. The functionalization process of GNPs with PEG, i.e., PEGylating, results in a complex referred to as GNP_{PEG} [204, 205]. This process allows GNP_{PEG} to avoid the immune system as a nonforeign object and extend its blood circulation [206]. The downfall of PEGylating is the reduction in endocytosis of GNPs into cancer cells [207]. Therefore, GNPs were also coated with peptides containing an integrin binding motif known as Arginine-Glycine-Aspartic Acid (RGD)-motif as targeting ligands to create $GNP_{PEG\text{-}RGD}$ (**Fig. 2.17**).

The advantage of using peptides to other molecules such as antibodies is their smaller size, thus giving the opportunity for other molecules to be attached to the system as needed for improved future approaches [208, 209]. Conjugation of PEG on NP surface facilitated not only the stability for conjugation of RGD peptides to prevent aggregation, but also enhanced the biocompatibility needed for future *in vivo* studies. Most importantly, the functionalization of GNPs with the RGD peptide enables targeted delivery to cells that express integrin receptors [210]. The RGD peptide specifically binds to αvβ6 and αvβ3 integrin receptors, which are overexpressed on pancreatic cancer cells and CAFs [43]. A capping density of ~1 PEG/nm^2 surface area was used, which is

consistent with other studies [204]. Modifying the surface properties of GNPs would enable higher circulation time, as well as active targeting of tumor cells once they reach the tumor tissue. This hypothesis has been further supported by another *in vivo* study where GNPs decorated with an RGD-like peptide had a four-fold higher accumulation within the tumor compared to that of uncoated particles [211].

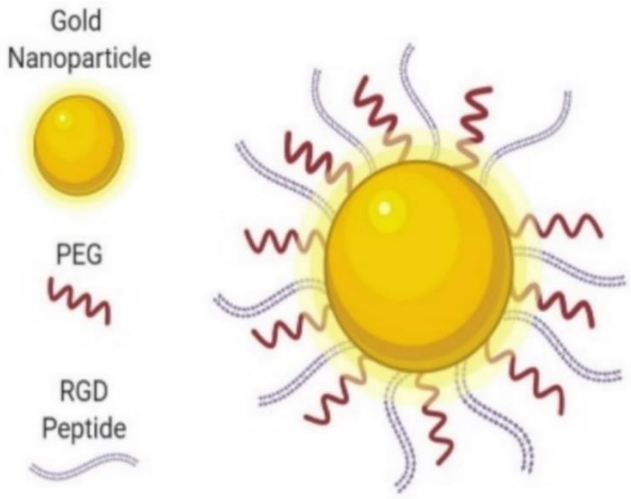

Figure 2.17 Schematic diagram showing the presence of both PEG and RGD peptide molecules on $GNP_{PEG\text{-}RGD}$ complex used for these studies. Created with BioRender.com.

2.3.6 GNPs Size

GNPs were used as the model NP system since they have been successfully tested as radiosensitizers and drug carriers in RT and chemotherapy, respectively [212, 213]. Among the size range from 10 to 100 nm, GNPs of diameter 50 nm seem to have the highest cellular uptake *in vitro* [214]. However, when they are functionalized with both PEG and RGD peptides of similar size, smaller NPs have the highest cellular uptake [207]. The interaction of RGD peptide with cell surface receptors is enriched for smaller NPs due to their higher surface curvature. Furthermore, these small size NPs have shown better penetration in three-dimensional tissue structures which will have a significant effect in their distribution within tumor tissue [116, 215]. The presence of inter-matrix spacing within the ECM makes the size of the GNPs used a crucial factor. The spacing between collagen fibrils, which is typically in the range of 20–40 nm, establishes the maximum limit for effective penetration [43]. Transmission electron microscopy (TEM) images of the as-made GNPs are displayed in **Fig. 2.18A**. Higher reflectivity of visible light by GNPs allowed us

to visualize them using darkfield (DF) and hyperspectral imaging (HSI), as shown in **Fig. 2.18B**. The inset in **Fig. 2.18B** shows the spectrum collected from GNPs. The same technique was used to further verify GNP uptake within cells.

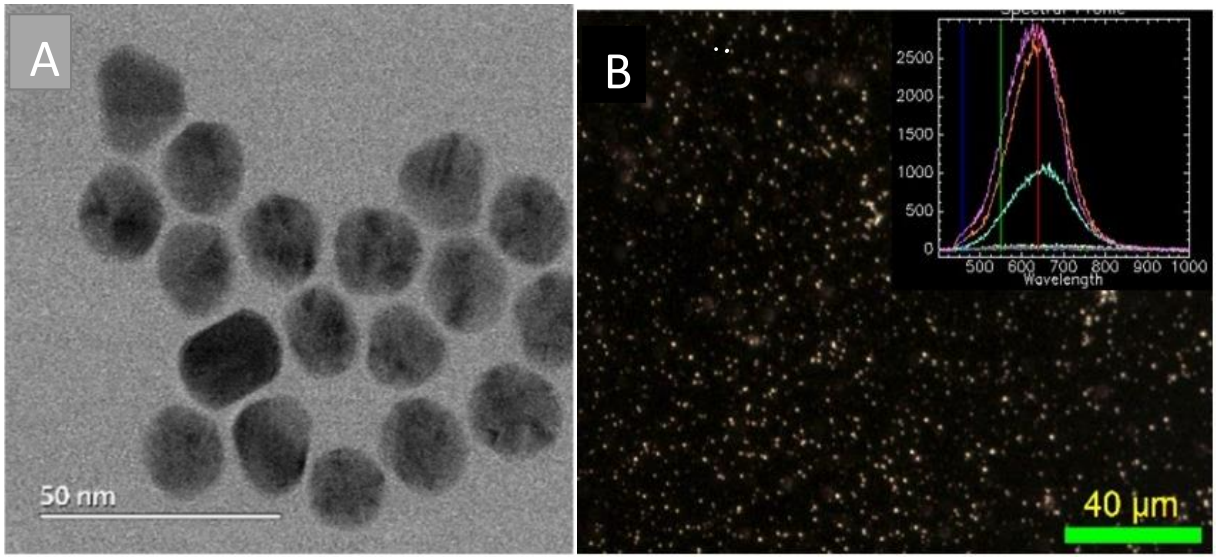

Figure 2.18 GNPs size. (**A**) Transmission Electron Microscopy (TEM) image of GNPs with a core size of ~15 nm. Scale bar is 50 nm. (**B**) DF and HSI images of as-made GNP. Scale bar is 40 µm**.**

2.3.7 GNPs Endocytosis In vitro

GNPs typically enter cells mostly via receptor-mediated endocytosis (RME) [214–217]. In this process, targeting ligands on the NP surface connect with cell surface receptors followed by internalization via endocytosis. RGD was used as a targeting ligand to exploit the fact that many cancer cells overexpress integrins on their surface, thus binding GNPs with RGD facilitates their RME specifically in cancer cells [218, 219]. Cell surface receptors bind to ligand molecules on the surface of NPs, such as RGD, causing membrane wrapping of the NP with a corresponding increase in elastic energy [214, 220]. The receptor-ligand interaction immobilizes receptors, causing configurational entropy to be reduced. More receptors diffuse to the wrapping site driven by the local reduction in free energy, allowing the membrane to wrap completely around the particle. RME is an energy-dependent process [217, 218]. The path of the NPs within the cell is explained in **Figure 2.19.** Once GNPs are bound to the receptors on the surface of the cell, membrane invagination occurs followed by trapping of GNPs in endosomes. The internalized GNPs are sorted inside the vesicle and eventually fuse with lysosomes for further processing. Most receptors are recycled back to the cellular membrane, while vesicles containing processed NPs

return to the cell periphery for excretion [217, 218]. GNPs are then excreted out of the cell. This is called the endo-lyso pathway.

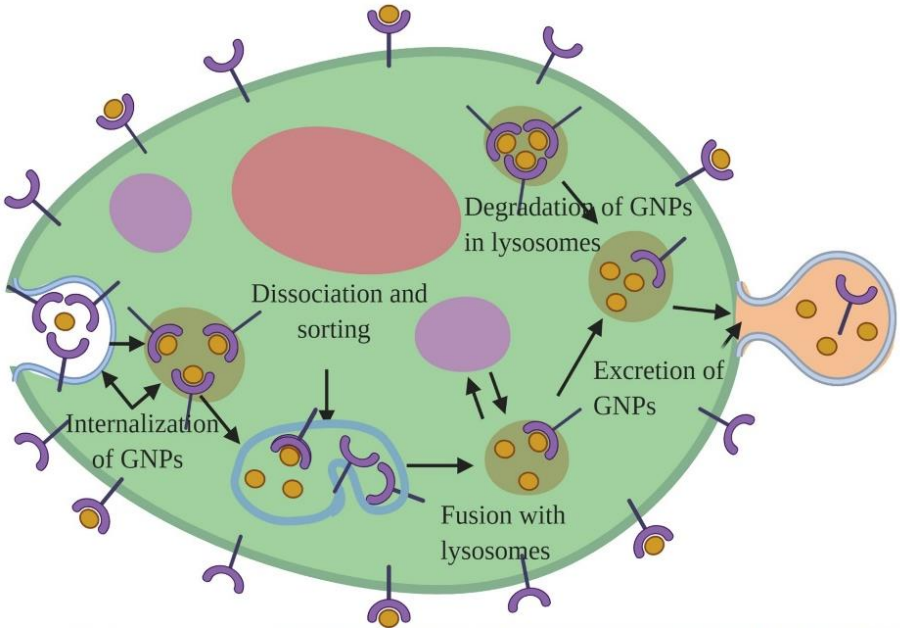

Figure 2.19 A schematic diagram explains the path of GNPs within a cell. Created with BioRender.com.

2.3.8 Clinical Trials

Clinical trials are key steps in the evaluation of new pharmaceutical drugs [221]. These trials are a complex process that typically divided into multiple phases to assess the safety, efficacy, dosing, and side effects of the drug. Here's a breakdown of the phases:

1. **Pre-Clinical Phase:** This step involves the conceptualization and development of the drug to be studied followed by *in vitro* and *in vivo* preclinical testing to evaluate the basic safety and efficacy of the drug [221].
2. **Protocol Development & Required Approvals:** The next set of steps involve consulting with regulatory agencies to discuss plans for clinical testing. These meeting will require designing the clinical trials, detailing the protocols, specifying the study's design, objectives, and methodology, and getting ethical and regulatory approvals [221].
3. **Phase 0 (Exploratory Studies):** This phase involves the initial introduction of a new drug into humans. Typically, this involves the evaluation of the mechanism of action, side

effects, early insight into drug behavior, and does not have a therapeutic or diagnostic intent [221].

4. **Phase I (Safety Trials):** This phase tests the drug on a small group of people, typically 20-100 volunteer patients with advanced-stage cancers with an aim to identify the maximum dose that can be administered safely without causing harmful side effects. This helps with gathering preliminary data on how the drug works in the body and how it is metabolized and excreted [221].
5. **Phase II (Efficacy Trials):** In this phase the drug is given to a larger group of people, typically 100-300 individuals to determine the efficacy of the drug for a particular indication and further assesses safety, dosing, and side effects [221].
6. **Phase III (Large-Scale Testing):** In phase III the drug is administered to an even larger group of individuals, often involving 1,000-3,000 participants in randomized controlled trials. This confirms the drug effectiveness and monitors side effects in a diverse population and gives a chance to compare the new drug to the current standard of care for placebo. If phase III is successful, a pharmaceutical company can request FDA approval to market the drug [221].
7. **Phase IV (Post-Marketing Surveillance):** After the drug has been approved and marketed, the drug long-term effectiveness and safety in a larger, diverse population can be monitored which is phase IV. Based on this surveillance and long-term side effects a drug can be taken off the market or restricted [221].

Each phase requires a specific study design and set of objectives, and the number of participants typically increases with each successive phase. The whole process from the discovery of a new drug to its arrival on the market can take over a decade.

CHAPTER 3

The Modulatory Influence of Docetaxel on Gold Nanoparticle Dynamics in 2D Monocultures

In this chapter, our aim was to assess how various cells within the TME uptake and retain GNPs over time. Additionally, we introduced DTX into the system to examine its impact on these cellular interactions. The chapter under discussion led to the publication of two articles, and a book chapter. The two articles appeared in *Current Oncology* and *Cancers*, respectively, and the book chapter is published by the *Taylor & Francis Group*. The *Current Oncology* manuscript is titled "Investigation of Nano-Bio Interactions within a Pancreatic Tumor Microenvironment for the Advancement of Nanomedicine in Cancer Treatment" [222], the *Cancers* manuscript titled "Docetaxel Mediated Uptake and Retention of Gold Nanoparticles in Tumor Cells and in Cancer Associated Fibroblasts" [223], and the book chapter is chapter 14 titled "Microtubule Targeting in Cancer Treatment" from the book "Organelle and Molecular Targeting" [224]. My personal contribution to the above-mentioned papers includes conceptualization and experimental design, sample preparation, collection, and processing, data acquisition and analysis, creation of figures and manuscripts writing. The next sections will discuss some fundamental concepts regarding the GNPs used in our experiments, their uptake and retention in different cell lines *in vitro* and *in vivo*, and the benefits of combining microtubules targeting agents (MTAs) such as DTX with GNPs in 2D monoculture *in vitro* systems.

3.1 GNPs Characterization

For all of our studies $GNP_{PEG-RGD}$ at a concentration of 7.5 µg/mL (~ 1.5 nM) was used. This concentration is shown to be well within the tolerable doses for *in vivo* administration, with a goal in mind for future clinical applications [49, 225–228]. GNPs of 10-15 nm in diameter were opted for our studies because of their better penetration and their higher surface curvature which enables efficient interaction between the RGD targeting ligand and cell surface integrins as described in *Chapter 2* [62]. In order to determine the size, shape, and concentration of the GNPs and GNP complexes, ultraviolet visible (UV-VIS) spectroscopy (**Fig. 3.1A**), dynamic light scattering (DLS) (**Fig. 3.1B**), and ζ-potential measurements (**Fig. 3.1C**) were used. The data are summarized in the table in **Fig. 3.1D**. The size and concentration of the GNPs was estimated using UV-VIS spectrometry [204]. According to previous studies, UV-VIS is found to be an accurate measurement of the concentration [216]. The ratio of the peak absorbance of the surface plasmon resonance spectrum to the 450 nm absorbance led to an approximate diameter of 14–16 nm for GNPs [229].

With conjugation of molecules onto the GNP surface, a slight red shift in the peak absorbance was seen, but the general shape of the spectrum did not change significantly. This is because the added PEG and RGD peptide molecules on the GNP surface are relatively smaller in size (PEG: 2 k and RGD peptide: 1.7 k) compared to GNPs [229]. However, there was a significant different in surface properties of GNP with the addition of the PEG and RGD peptides, as seen by DLS and ζ-potential measurements. DLS confirmed the hydrodynamic diameter of as-made GNPs to be 21.11 nm with a polydispersity index of 6%, while the $GNP_{PEG-RGD}$ complex had a diameter of 40.29 nm and a polydispersity index of 13%. This increase in the hydrodynamic diameter is consistent with conjugation of the different molecules on the surface [230]. The ζ-potential of the as-made GNPs and $GNP_{PEG-RGD}$ complex was measured to be −32.37 mV and 0.13 mV, respectively. Initial negative charge of GNPs is due to the negatively charged citrate molecules present as a cap on the surface. During the functionalization process, citrate molecules on the surface are replaced with neutral PEG molecules and the positively charged RGD peptides resulting in a significant change in the ζ-potential [231].

The $GNP_{PEG-RGD}$ complex was also measured for stability in tissue culture media for a period of 24 h to mimic the *in vitro* environment. The hydrodynamic diameter and ζ-potential of the $GNP_{PEG-RGD}$ did not vary significantly after the incubation period. Previous studies have also shown that GNPs tagged with ~1 PEG/nm^2 surface area demonstrated the best stability, which is the capping density employed in this study [216].

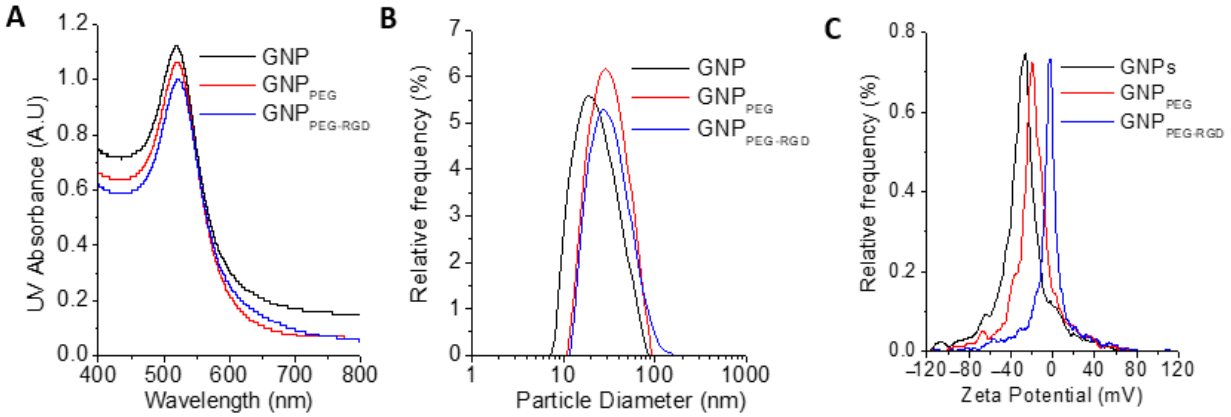

D

	Peak Absorption Wavelength (nm)	Hydrodynamic Diameter (nm)	Zeta Potential (mV)
GNP	519.45 ± 0.05	21.11 ± 6.40	−32.37 ± 1.18
GNP+PEG	520.40 ± 0.05	29.03 ± 9.86	−16.91 ± 0.77
GNP+PEG+RGD	520.70 ± 0.05	40.29 ± 13.01	0.13 ± 0.16

Figure 3.1 Characterization of GNPs. (**A**–**C**) UV–Visible absorption spectra, hydrodynamic diameter, and ζ-potential measurements of pure GNPs, GNP_{PEG}, and $GNP_{PEG-RGD}$, respectively. (**D**) Summary of peak absorption wavelength, hydrodynamic diameter, and mean ζ-potential for pure GNPs, GNP_{PEG}, and $GNP_{PEG-RGD}$. Reproduced with permission from open access Creative Common license [222].

3.2 Investigation of Nano-Bio Interactions within a Pancreatic TME

It is yet to be understood how NPs are taken up and retained by other cell types within the TME, such as CAFs and NFs. Retention of NPs is as important as their uptake within individual cell types for their use in drug delivery and RT [20–22]. In this study, the extent of uptake and retention of $GNP_{PEG-RGD}$ within cell types from a pancreatic TME in a monoculture *in vitro* environment was evaluated to exploit the full benefits of cancer nanotechnology to treat pancreatic cancer (**Fig. 3.2**). Our next goal was assessing the extent of accumulation and retention of NPs within a real TME, collectively using an *in vivo* tumor model and comparing it to our *in vitro* studies. Most NP uptake studies have mainly focused on tumor cells. However, the TME consists

of many other cell types which could significantly influence the outcome of NP-based therapeutics. Among the cells present in TME, the focus was on NFs and CAFs in addition to tumor cells. This is mainly due to the anti-tumorigenic properties of NFs and the tumorigenic properties of CAFs as discussed in *Chapter 2*.

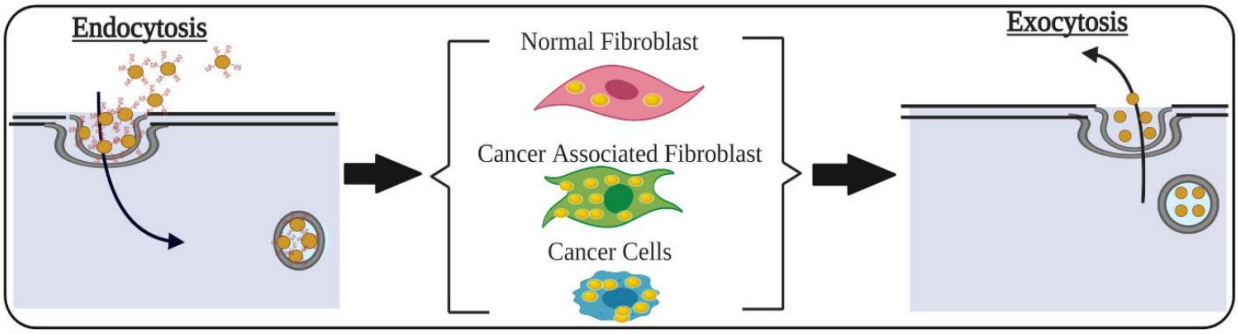

Figure 3.2 Exploring nano-bio interface in a TME of pancreatic origin. Upon the delivery of NPs into the different type of cells via the bloodstream, cancer cells and CAFs uptake the highest number of NPs compared to normal cells. The surface-modified NPs enter the cells via endocytosis, and after a certain period, leave the cells via exocytosis. The window where cancer cells and CAFs retain the highest number of NPs could be used to deliver specified doses of ionizing radiation to reach a higher therapeutic index. Reproduced with permission from open access Creative Common license [222].

The cell lines used in this study are PANC-1(a male human pancreatic cancer cell line derived from a pancreatic carcinoma of ductal origin), MIA PaCa-2 (a male human pancreatic cancer cell line derived from a pancreatic carcinoma), CAF-98 (patient-derived pancreatic cancer associated fibroblasts) and NPF-98 (normal pancreatic fibroblasts). Human pancreas cancer cell lines MIA-PaCa-2 and PANC-1 were obtained from the American Type Culture Collection. CAF-98 and NPF-98 were derived from resected PDAC tumor tissue from the same consented patient through the Gastrointestinal (GI) Biobank at the Vancouver General Hospital. The reason behind obtaining CAFs and NFs from the same patient is to have a more meaningful comparison. In the next few sections, we will address the following fundamental questions:

1. Is there a difference between the uptake of NPs in cancer cells and NFs of pancreatic origin *in vitro*?
2. What is the potential of retaining of these NPs within those cells *in vitro* for efficient delivery of therapeutics?
3. Do we see retention of NPs within tumor tissue *in vivo* for an extended period of time as being successful for the delivery of therapeutics?

3.2.1 Cellular Uptake of GNP Complexes

The uptake of the $GNP_{PEG-RGD}$ complex per cell was quantified using inductively coupled plasmon mass spectroscopy (ICP-MS) 24 h post incubation with GNPs (**Fig. 3.3**). GNP uptake in tumor cells and CAFs were comparable while GNP uptake in NFs was half that of tumor cells and CAFs even though NFs typically give rise to CAFs [232]. This behavior is consistent with previous studies where CAFs and NFs of melanoma origin were compared to tumor cells of breast and cervical origins [50, 63]. One of the reasons for the difference in GNP uptake between tumor cells, CAFs, and NFs could be due to the receptor expression of integrin-binding domain RGD among these cells. GNPs labeled with RGD peptide were used, and previous studies show that this particular peptide can effectively improve endocytosis specifically into tumors [205, 208].

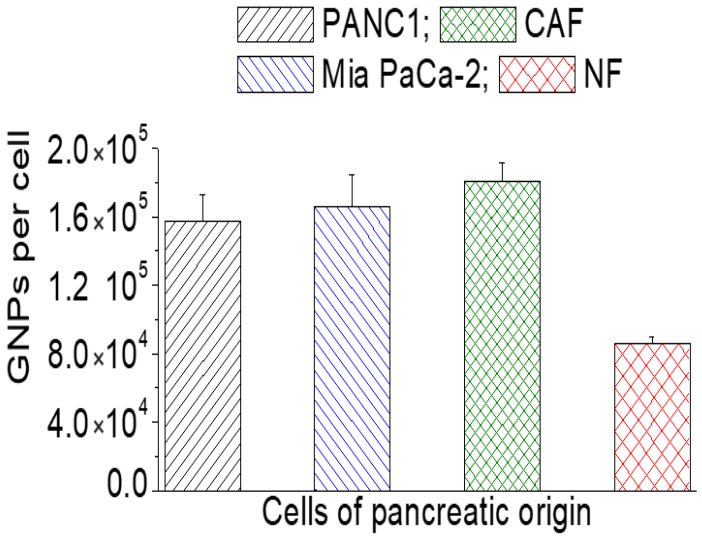

Figure 3.3 GNPs uptake in cancer cells vs. normal cells. Reproduced with permission from open access Creative Common license [222].

These results are very promising in terms of targeting NPs for cancer therapeutics. CAFs promote virtually every aspect of the hallmarks of cancer. For example, the presence of CAFs in cancer specimens from patients has been associated with a poor prognosis in multiple cancers [233–235]. Based on our quantification data, we believe that we can deliver therapeutics that target tumor cells and CAFs very effectively, not only to kill tumor cells but also to silence CAFs which promote tumor growth. This type of novel therapeutic is very much needed in treating pancreatic cancer where survival is very low. A recent study has demonstrated the feasibility of silencing

CAFs of melanoma origin using both GNPs and radiation [50]. GNPs used as a radiosensitizing agent in RT and the ability of CAFs to take in GNPs similar to tumor cells result in their vulnerability during RT. These novel approaches will shed light on treating pancreatic cancer, which has an extensive deposition of ECM combined with a high activation of CAFs [236].

Imaging techniques were also utilized to further verify our quantitative data, as illustrated in **Fig. 3.4A–D**. Both confocal (**Fig. 3.4A–D**) (nucleus is stained blue and NPs are in red) and DF images in the *Appendix* (**Fig. S1.1A–D**) further solidify our quantification data. Tumor cells PANC-1 (**Fig. 3.4A**), Mia PaCa-2 (**Fig. 3.4B**) and CAFs (**Fig. 3.4C**) had a significantly higher NP presence compared to NFs (**Fig. 3.4D**). We were also able to confirm the presence of GNPs using the spectral mapping feature of HSI, as illustrated in **Fig. S1.1E–H**. Reflectance spectra of GNPs was obtained from a few selected bright spectra, and we confirmed that they were from GNP clusters using the data available in the imaging library. This technique is very useful since it is not necessary to optically label GNPs in contrast to confocal imaging.

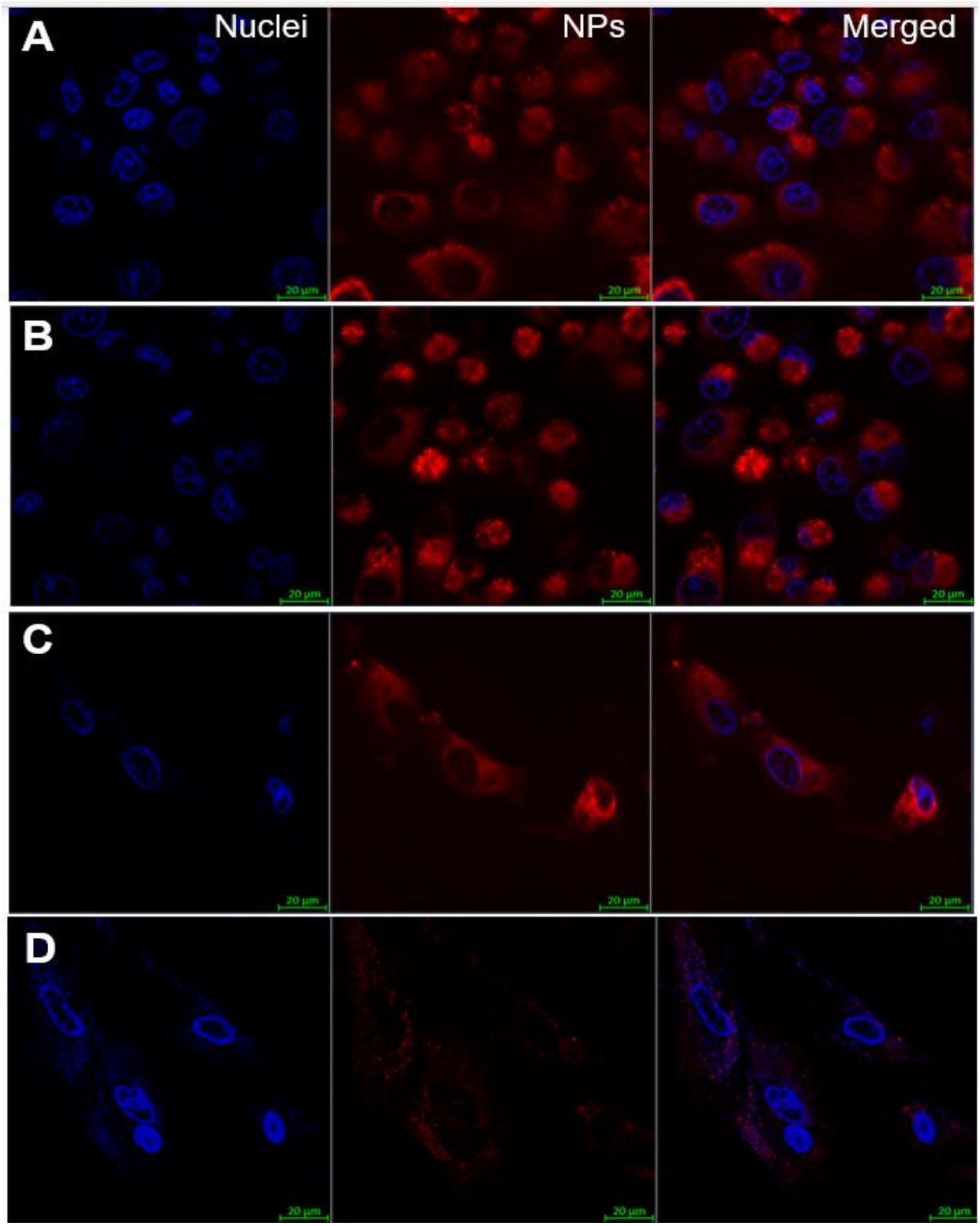

Figure 3.4 GNPs endocytosis 24 h post incubation showing intracellular NP distribution in PANC-1 (**A**), Mia PaCa-2 (**B**), CAFs (**C**) and NFs (**D**) using confocal microscope. left-most panel (nucleus in blue); middle panel (NPs in red); right-most panel (merged image). Scale bar is 20 µm. Reproduced with permission from open access Creative Common license [222].

3.2.2 Retention of GNP Complexes

GNPs are taken up by cells via RME as explained in *Chapter 2*. After few hours of cells being in contact with GNP-containing media, an equilibrium between endocytosis and exocytosis processes is reached, resulting in a plateau in cellular uptake where the presence of NPs within cells is measured over an extended period [218]. The question that then arises is what happens when GNPs are removed from the medium? This is an important step to consider mimicking GNPs tumor endocytosis *in vivo* as much as possible. Tumors *in vivo* do not have a constant feed of GNPs, i.e., the loss of equilibrium will occur in the tumor around the 24 h mark as GNPs supply from the blood gradually start to as decrease discussed in previous sections. The same four cell lines that were used in the uptake experiments were used to monitor the ability of NPs retention over a period of 24 h. The GNP-containing media was substituted with fresh media and all cells were incubated for an additional period of 24 h. Thus, the total amount of time between the introduction of GNPs into the cells to quantification was 48 h.

A clear reduction in the number of GNPs was apparent in all four cancer cell lines. This could be attributed to two reasons, the first being the redistribution of GNPs from the parent cell to the daughter cells following cell division, and the second being the nonequilibrium excretion of GNPs from cells via exocytosis without having enough GNPs getting into the cell due to lack of GNPs in the surrounding media [8]. Even though the number of GNPs in cells 24 h post-incubation with fresh media decreased, tumor cells and CAFs were still able to have significantly more NPs in them compared to NFs (**Fig. 3.5A**). The retention percentage of GNPs in tumor cells, CAFs, and NFs was approximately the same at 70–80% (**Fig. 3.5B**). The trend in intracellular retention of NPs is consistent with previous studies where a similar GNP complex was used with different cell lines [50, 63].

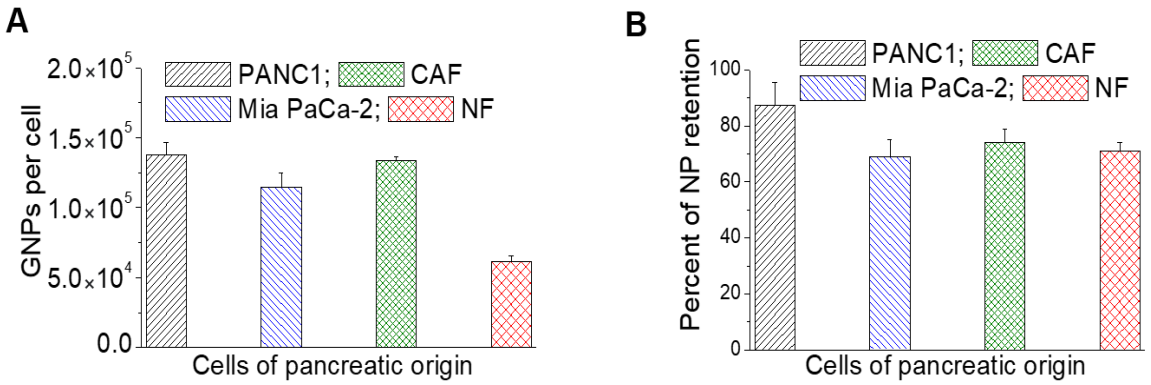

Figure 3.5 Retention of GNPs in cancer cells vs normal cells. (**A**) GNPs retained per cell in PANC-1, Mia PaCa-2, CAFs, and NFs. (**B**) Retention percentage of GNP in PANC-1, Mia PaCa-2, CAFs, and NFs. Reproduced with permission from open access Creative Common license [222].

Typically, GNPs get into the cell via RME where they are caught in endosomes before being fused and localized in lysosomes for handling, and finally exiting the cell through exocytosis where they are excreted via fusion with the cell membrane, as illustrated in **Fig. 2.19**. In this process, the majority of GNP are concentrated in endosomes and lysosomes rather than the cytoplasm or the nucleus [218]. Based on previous studies, these NPs get excreted at a much faster rate [217]. However, conjugating GNPs' surfaces with RGD peptides promotes GNPs to discharge into the cytoplasm from endosomes following endocytosis [237, 238]. This gives GNPs a longer time to spend in cells, which in return decreases the rate of exocytosis, thus increasing their retention percentage (**Fig. 3.5B**).

The particular RGD peptide used in this study was also used for releasing NPs from endosomes and lysosomes to facilitate nuclear targeting [219, 237]. This extended intracellular retention of GNPs in cancer cell lines and CAFs could be exploited in combined radio- and chemo-cancer therapies. Despite the importance of understanding the retention beyond the 24 h period used in this study, studying such long-term effects is not feasible due the significant difference in doubling time between these cells and the dilution of NPs between the dividing cells [239]. The combination of these two effects may not provide us with a reliable conclusion regarding NP retention over a longer period of time. Confocal images (**Fig. 3.6A–D**) (nucleus appears in blue and NPs appear in red), DF images (**Fig. S1.2A–D**), and HIS spectra (**Fig. S1.2E–H**) support our findings.

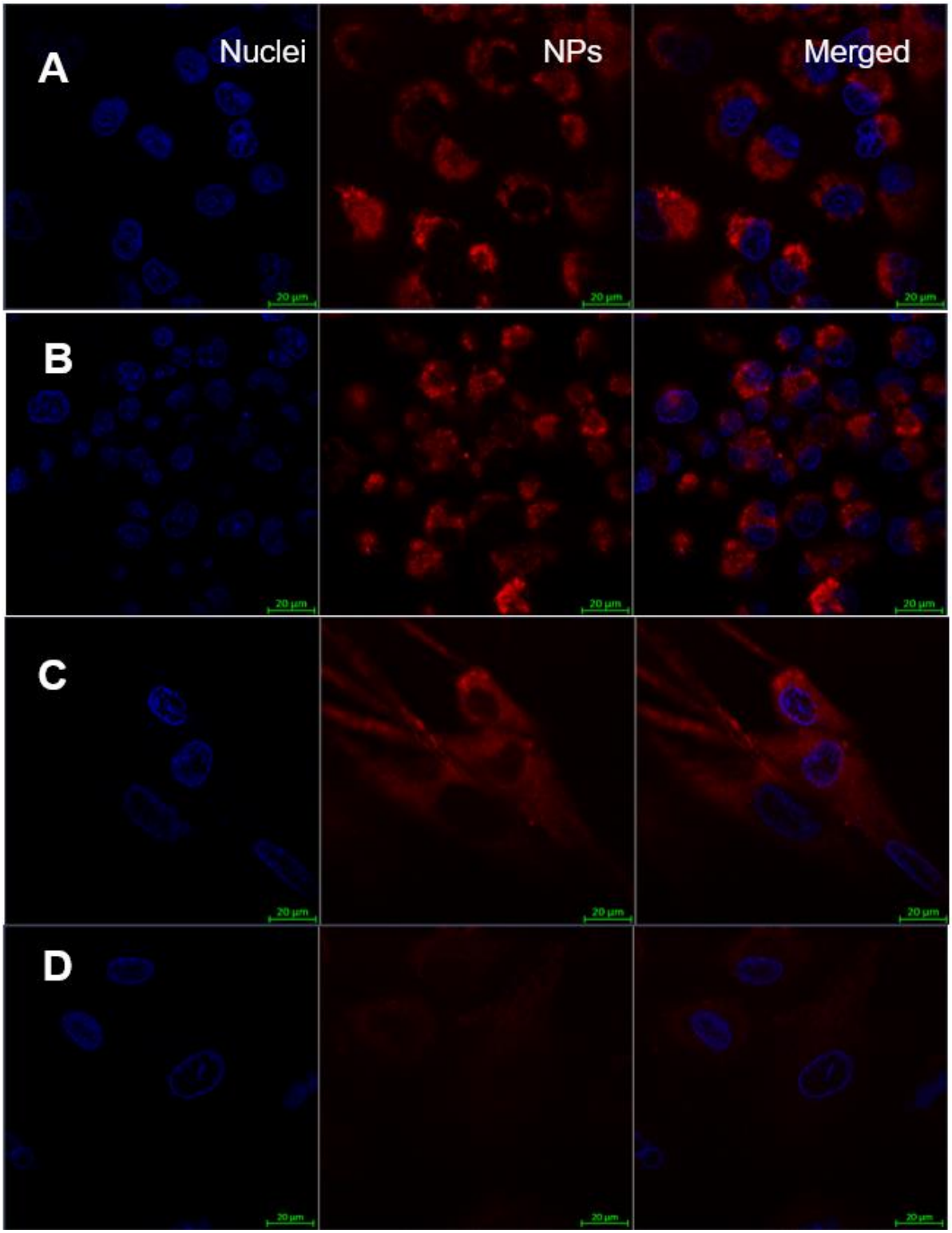

Figure 3.6 GNPs Exocytosis 48 h post incubation Visualization of intracellular NP distribution in PANC-1 (**A**), Mia PaCa-2 (**B**), CAFs (**C**) and NFs (**D**) using confocal microscope. left-most panel (nucleus in blue); middle panel (NPs in red); right-most panel (merged image). Scale bar is 20 µm. Reproduced with permission from open access Creative Common license [222].

3.2.3 The Dynamics of GNP Distribution and Retention within Tumor Tissues In vivo

To compare our *in vitro* results to *in vivo*, we used one of our pancreatic tumor cell lines, Mia PaCa-2, to generate an *in vivo* tumor model. s. Each mouse was administered a gold dose of 1 mg/kg. Unlike *in vitro* where NPs are presented directly to the cells via their media, NPs face many barriers *in vivo* before reaching the cells. As illustrated in schematic **Fig. 3.7A**, tumors' leaky vasculatures and ineffective lymph systems facilitate the systemic circulation of NPs within the tumor, resulting in extravagation and accumulation of NPs in tumor cells due to the EPR effect [240, 241]. Our pharmacokinetic studies of GNPs in a pancreatic cancer model showed that the accumulation of the GNPs in the tumor was highest at 24 h post injection (**Fig. 3.7B**), while it was highest in blood (in circulation) at a 2 h time point. It was also evident that NPs clearance from the tumor (**Fig. 3.7B**) was lower than NPs clearance from the blood in circulation (**Fig. 3.7C**). This indicates that GNP retention in the tumor is longer than GNP clearance from the circulatory system. Even after 48 h of post-NP injection, tumor tissue retained ~75% of the optimum accumulation reached after 24 h. This is consistent with the outcomes of our *in vitro* retention studies. It's noteworthy that the biocompatibility of GNPs was established in a phase I clinical trial. The administered doses were significantly below the maximum dose tolerated by mice [242].

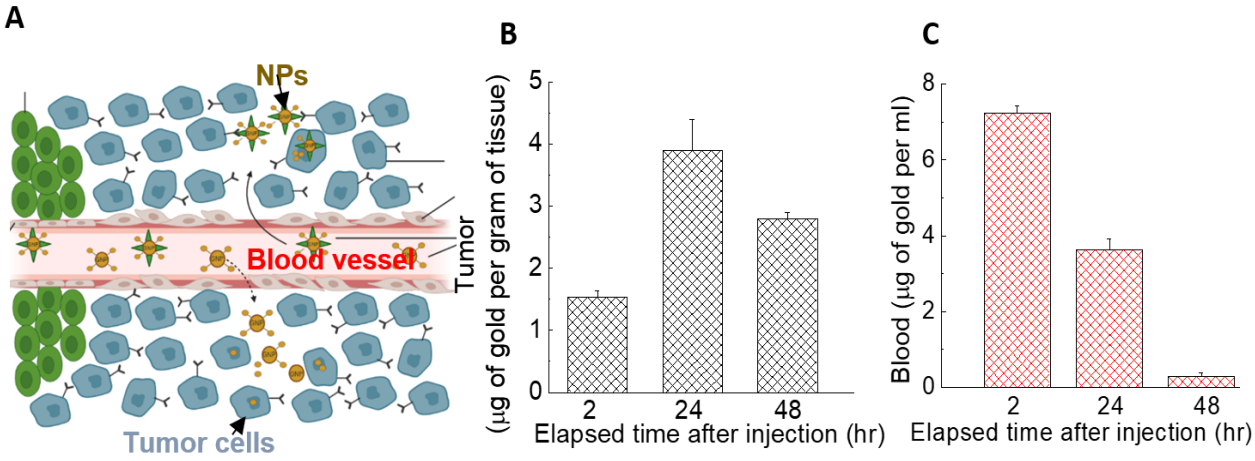

Figure 3.7 The dynamics of GNP distribution and retention in tumor. **(A)** A schematic diagram showing the escape of NPs from leaky blood vessels to tumor tissue. **(B–C)** Quantification of GNPs in tumor tissue and blood in circulation over a period of 24 h. Reproduced with permission from open access Creative Common license [222].

We were also able to verify our quantification data with qualitative data of both tumor cells and cross-sections of tumor blood vessels over 48 h as illustrated in **Fig. 3.8A–C**. Similar to our

in vitro studies, we were able to visualize the presence of GNPs in tumor tissue, which included tumor cells and tumor blood vessels using DF imaging. The bright yellow structures represent GNP clusters in tumor tissue cross-sections, as pointed out by arrows in those images. After 2 h of NP injection, we did not see a significant presence of NPs in tumor tissue (**Fig. 3.8A**). There was a significant increase in NPs presented in the tumor at a 24-h time point (**Fig. 3.8B**). Even after 48 h of NP injection, we could still see NPs remaining within the tumor tissue (**Fig. 3.8C**). However, the intensity of GNPs within tumor blood vessels reduced dramatically as NPs were no longer present at a significantly high percent within the circulation system, as explained in **Fig. 3.7C**. Therefore, our quantification data presented in **Fig. 3.7B–C** was further solidified with qualitative image panels **Fig. 3.8A–C**. It also important to differentiate that **Fig. 3.7C** represents the NPs within the circulating blood. The presence of NPs in tumor blood vessels could be assessed only qualitatively using the images we had. The data presented in **Fig. 3.7B** shows the NPs in both tumor tissue and tumor blood vessels collectively.

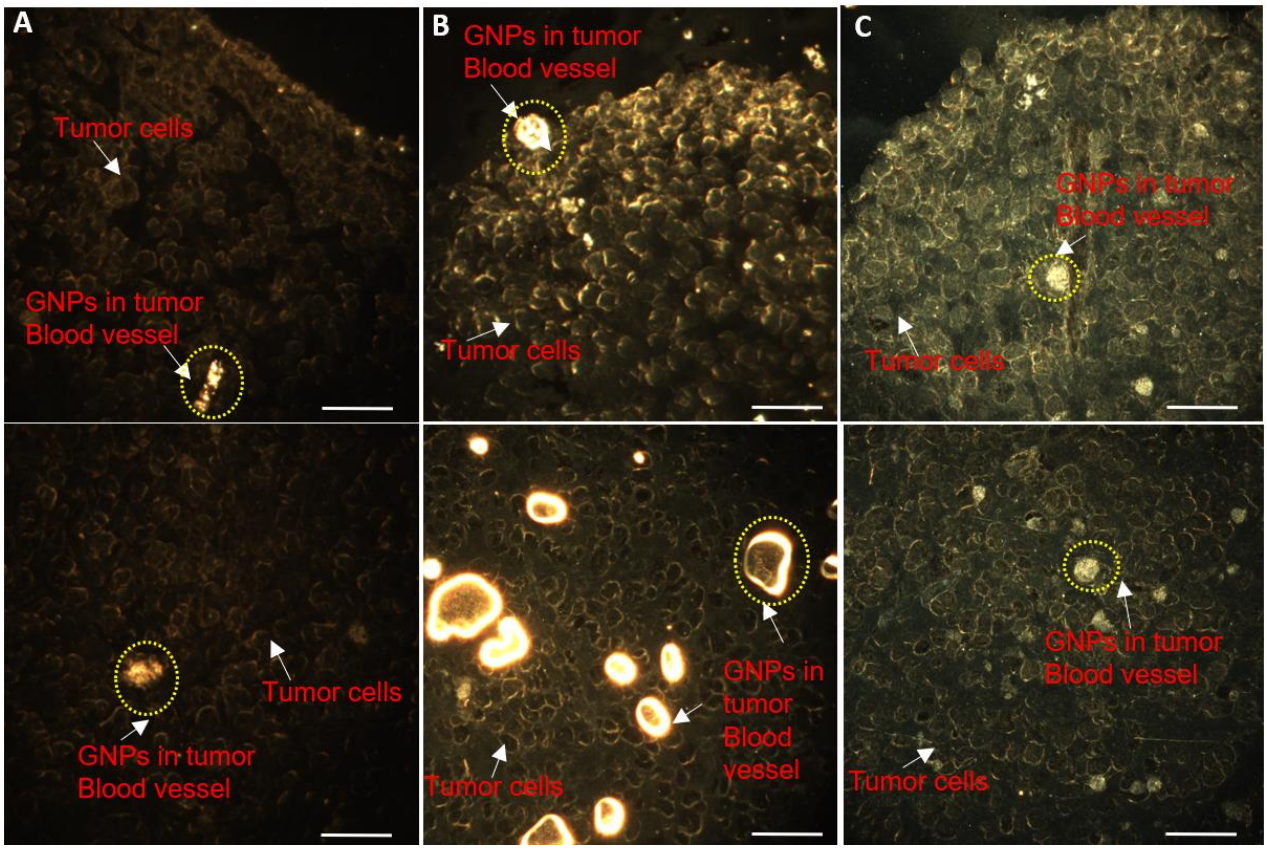

Figure 3.8 GNPs distribution in tumor tissue after 2 (**A**), 24 (**B**), and 48 (**C**) h of injection, respectively. Top and bottom rows represent tumor periphery and interior, respectively. Scale bar is 40 µm. Reproduced with permission from open access Creative Common license [222].

Modification of size and surface properties of NPs allowed us to have a significant number of GNPs present even 48-h post injection, which would facilitate better delivery of nanomedicines in future cancer treatments. In one of the pioneering studies using GNPs as radiosensitizers, radiation treatment had to be performed minutes after the injection of NPs since NPs were excreted much faster [47]. Our approach of modifying the surface properties of GNPs would enable higher circulation time, as well as active targeting of tumor cells once they reach the tumor tissue. This hypothesis has been further supported by another *in vivo* study where GNPs decorated with an RGD-like peptide had a four-fold higher accumulation within the tumor compared to that of uncoated particles [211]. The safety and efficacy of a multiple dosing approach has been demonstrated using GNPs and has been found to increase particle accumulation in tumors [243]. Multiple dosing could potentially enhance the efficacy of radiation dose enhancement in RT and drug delivery in chemotherapy.

3.2.4 Conclusions

Our *in vitro* studies demonstrated the ability of cancer cells and CAFs to uptake almost double the number of GNPs compared to normal cells. This uptake difference, attributed to the targeting effects of GNPs, offers insights into potential normal tissue toxicity concerns. Moreover, CAFs took in significantly more GNPs than tumor cells, suggesting that GNPs could be valuable in diminishing CAF activity, especially when employed as radiosensitizing agents or drug carriers. Notably, both cell lines retained over 70% of GNPs 24 h after injection, providing flexibility in GNP-based therapeutic delivery. Our *in vivo* results mirrored these findings. The tumor contained 10% of the injected GNPs dose 24 h after injection and retained over 70% after 48 h, aligning with our *in vitro* observations. In conclusion, our research suggests that targeting both tumor cells and CAFs with NP-based strategies could innovatively enhance existing cancer treatments, including RT and chemotherapy.

3.3 Combination of MTAs with GNPs

MTAs such as DTX are being used with RT to treat locally advanced prostate cancer patients. Phase III clinical trials show promising results [244]. As DTX is a clinically approved drug that treats many cancers and acts as a complementary radiosensitizing agent in chemotherapy, understanding the role of DTX on GNP transportation could pave the way for a better

chemoradiation approach with GNPs as a radiosensitizing agent [213]. MTs are hollow tubes composed of tubulin dimers constructed into a linear chain of protofilaments. They are polar structures that have a fast-growing “positive” end and a slow-growing “negative” end. MTs emerge from an organelle in the center of the cell known as a centrosome or MTOC, with the positive ends always directed outwards in the process of nucleation [224]. The motor proteins, dynein and kinesin, support the transportation of vesicles along the MT network [224].

As illustrated in **Fig. 3.9A-B**, MTs mediate the intracellular transportation of NP-containing vesicles. MTs are long tubulin polymers and provide directional transport within the cell interior while actin filaments support short distance travel near the cell periphery [224, 245−247]. NP transport along MTs is bidirectional and it is supported by two motor proteins: kinesin (transport toward the (+) end of MTs) and dynein (toward the (−) end) (inset **Fig. 3.9A**). Closer to the cell periphery, the myosin motor protein moves cargo along actin filaments (inset **Fig. 3.9A**). A map of the MT network and vesicles containing NPs in tumor cells and CAFs is shown in **Fig. 3.9A**. It appears that any disturbance to the function of MTs could have a significant impact on NP transportation [247, 248]. As illustrated in **Fig. 3.9A**, the major pathway of NPs entering the cell is via endocytosis [218]. Once NPs are internalized, their vesicular transport within the cell interior is along MTs. Considering the action of DTX on MTs, a significant change in intracellular dynamics of internalized NPs is expected. A previous study has reported a significant increase in NP uptake with the treatment of DTX using a cervical cancer cell line, HeLa [61, 62]. However, it is not yet known how DTX affects NP uptake and transportation in CAFs which play a major role in tumor progression. Modulating the MT network using DTX could drastically affect NP behavior within these cells [218].

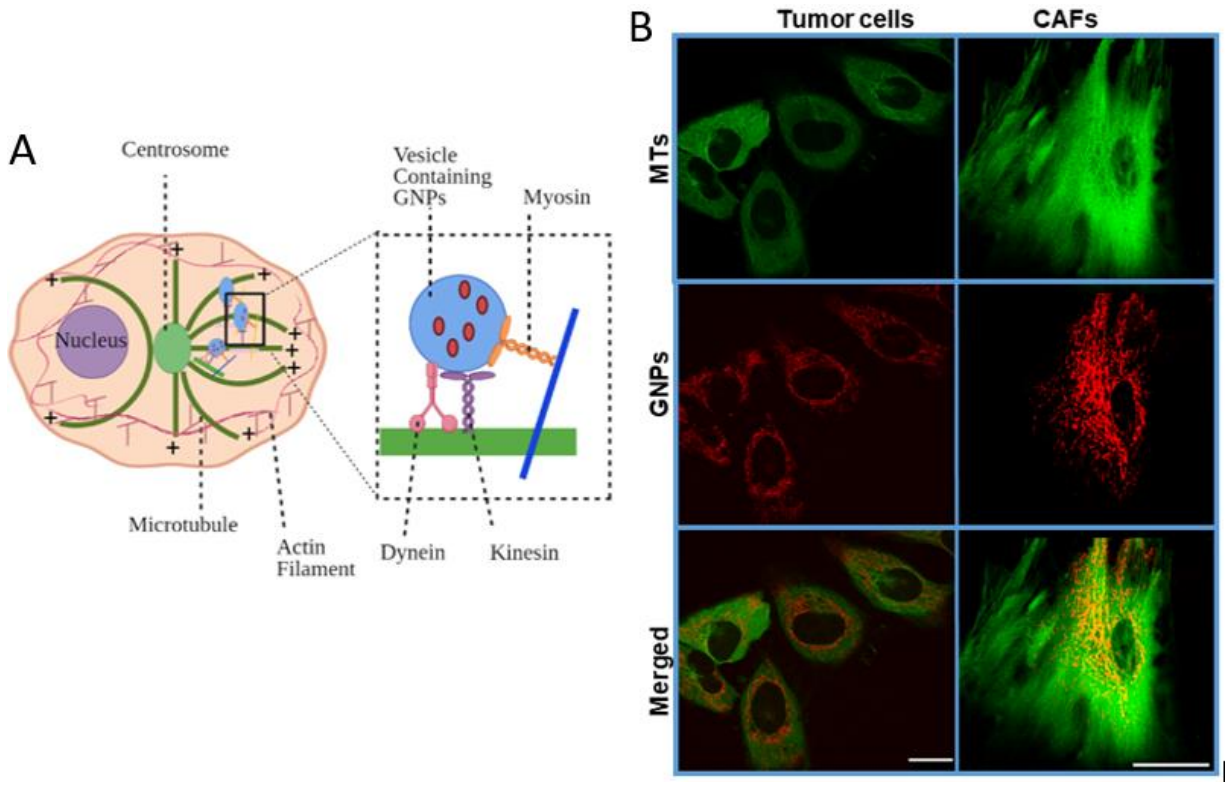

Figure 3.9 GNPs Uptake and Intercellular Transportation. **(A)** Schematic illustration displaying the transportation of vesicles containing GNPs within the network of MTs. **(B)** Confocal microscope images of tumors cells vs. CAFs showing MTs alone in green (first row), GNPs alone in red (second row), and both MTs in green and GNPs in red merged (third row). Scale bar = 20 μm. Reproduced with permission from open access Creative Common license [223].

A recent study that compared between the triple combination of radiation/GNPs/DTX vs radiation/ DTX without GNPs in HeLa and MDA-MB-231 cell lines showed an ~ 70% increase in GNPs uptake in the presence of DTX after 24h of incubation [62]. The largest number of GNPs accumulation is in the G2/M phase due to DTX halting cell division at this phase and allowing more time for GNPs to be accumulated before division. The addition of GNPs considerably decreased the survival fraction of HeLa cells which indicates the efficacy of the two radiosensitizers', GNPs/DTX, synergic effect. The effect of DTX on cells and GNPs concentration varies based on the used doses [61, 62]. It has been shown that the cell type, antimitotic drug used, and its concentration has a combined effect in determining the fate of the cell as illustrated in **Fig. S2** [249]. Most of cells dosed with 50 nM DTX are blocked in G2/M phases, while cells dosed with 10 nM DTX are able to divide [61]. Without DTX, cells undergo the regular cell cycle process by which cells reproduce normally and GNPs are evenly distributed around spindles passing them down to daughter cells (**Fig. 3.10A-B**). On the other hand, GNPs are unevenly distributed in

dividing cells treated with DTX. A 10 nM concentration of DTX allows the cell to go through mitosis but leads to uneven distribution of GNPs in the impaired daughter cells. A 50 nM concentration of DTX, stabilizes MTs preventing the assembly of spindles during the mitosis phase of the cell cycle [250, 251]. This prevents cell division resulting in the assembly of asters with GNPs distributed around the asters, or multinucleation with unsymmetrical distribution of GNPs in the deformed cells with GNPs (**Fig. 3.10C-D**).

DTX also affect the intracellular retention of GNPs typically moving them towards the periphery of the cell. Cells injected with a DTX concentration of 50 nM retain most of their GNP's content [61]. It is thought that this is a result of the halt in cell division and the damaged microtubules causing deficiency in the cell's ability to remove GNPs out of the cells [61]. Therefore, DTX concentration of 50 nM was used since such concentration is feasible *in vivo* [252]. Note that GNPs did not affect DTX mechanism of action, but DTX did affects the distribution of GNPs in cells [61, 62]. It could also be noted that cells treated with DTX changed their morphology from elongated to rounded which might be due to the stabilization effect of DTX on microtubules (**Fig. 3.10**). These changes resulted in NPs getting trapped within the cell because of their inability to move along MTs. The presence of DTX results in an increase in the accumulation of NPs within tumor cells, making it very promising in both chemotherapy and RT. The addition of GNPs into current DTX/radiation would produce a very promising synergistic therapeutic result [50]. This smart combination of cancer therapy is proposed to reduce the required dosages, thus minimizing the damage to healthy tissue surrounding the tumor [50, 62]. Despite these results, data on the extent of DTX's effect on CAFs of different tumor origins is lacking.

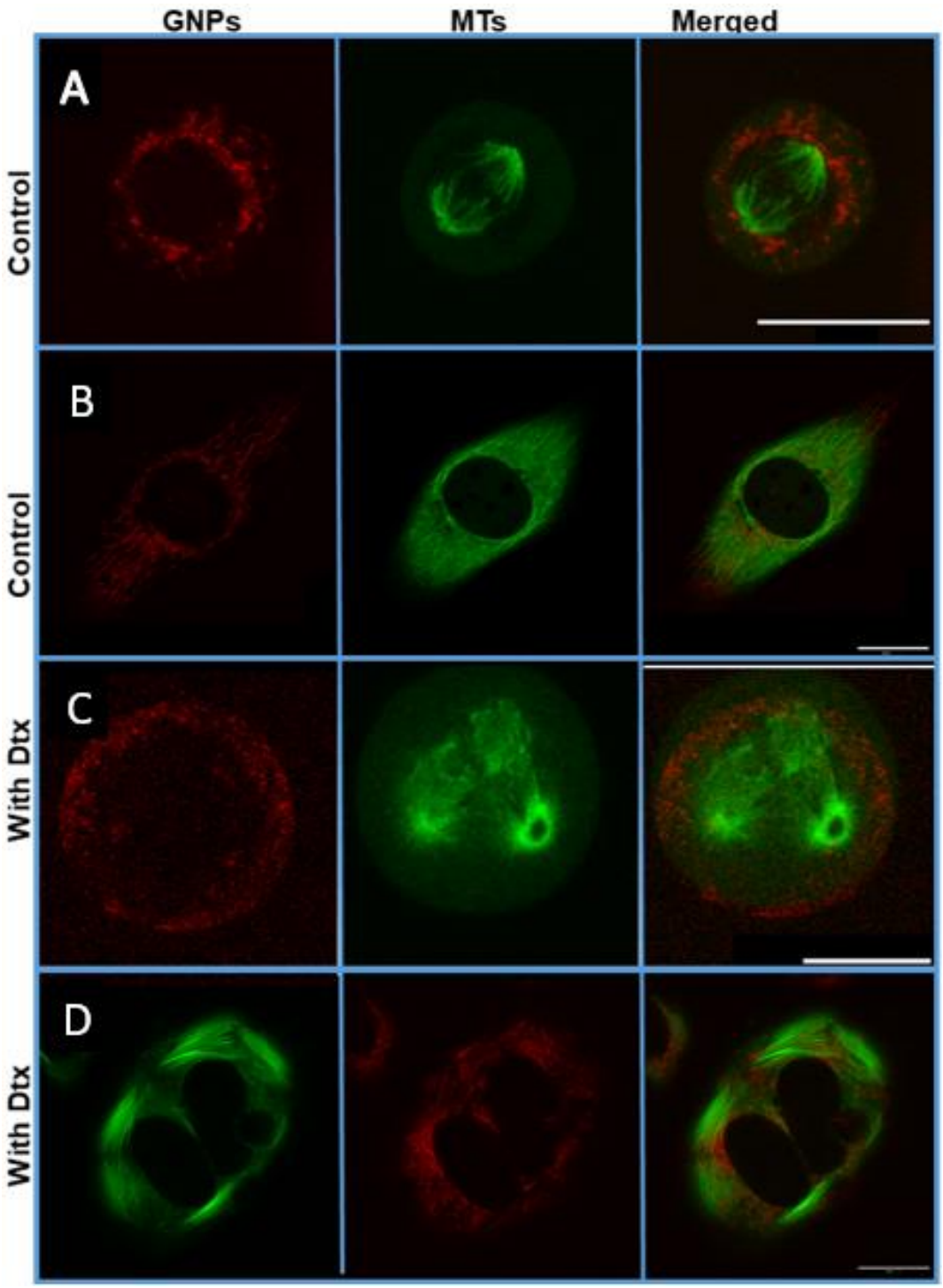

Figure 3.10 DTX effect on cancer cells. Confocal Images of control cancer cells and cancer cells treated with DTX. GNPs are in red (first column), MTs are in green (second column), and merged (third column). **(A)** shows the distribution of GNPs in control tumor cell in mitosis. **(B)** maps the vesicles containing GNPs and the MTs in a cell control cell (not treated with DTX). **(C)** shows cell division in a tumor cell treated with DTX. **(D)** shows the vesicles containing GNPs and the MTs in a cell treated with DTX. Scale bar = 20 μm. Reproduced with permission from open access Creative Common license [223].

3.4 DTX-Mediated Uptake and Retention of GNPs

In this study, the goal was to assess the extent of uptake and retention of NPs within tumor cells and CAFs of different origins in the absence and presence DTX. Three cancer cell lines (MIA PaCa-2 (pancreatic), PC3 (male prostate), and HeLa (cervical female)) and three CAF cell lines (CAF-98 (pancreatic), CAF-D6006T (prostate) and Hs 895.T (female, melanoma)) were used. A couple of previous studies have compared differences between NP behavior in a cervical cancer cell line (HeLa) and a CAF cell line from melanoma origin [50, 63]. However, in this study, CAFs and cancer cells of similar origins (prostate and pancreatic) were matched along with the two cell lines used for the above-mentioned previous studies for comparison. GNPs of similar size, functionalization and concentration to our previous study were used in this study. Hence, our study will address the following unanswered questions:

(1) Is there a difference in NP uptake between tumor cells and CAFs?
(2) What is the ability of tumor cells and CAFs to retain NP?
(3) Can we improve the NP uptake in both tumor cells and CAFs using DTX? How significant is the effect in both tumor cells and CAFs?
(4) Can we significantly improve the retention of NPs in tumor cells and in CAFs using DTX?
(5) Is there a significant difference in the NP behavior in tumor cells and in CAFs based on our study?

3.4.1 Cellular Uptake and Retention of GNP in the Absence of DTX

Fig. 3.11 shows the extent of cellular uptake of GNPs for tumor cells and CAFs within a 24-hour incubation period. It is evident that CAFs had significantly higher NP uptake in comparison to cancer cells. This might be attributed to the much larger size of CAFs compared to tumor cells coupled with the higher number of RGD binding integrins that CAFs express and their varieties easing the internalization of NPs [253]. This suggests that targeting CAFs, in addition to tumor cells, is feasible for better therapeutic outcomes. The results are consistent with previous studies that compared NP uptake between a cervical cancer tumor cell line (HeLa) and CAFs derived from melanoma [50, 63]. No significant difference in GNP uptake among different CAFs was found, but there was a significant difference in GNP uptake among different tumor cell lines. The different in size between the used tumor cell lines and the higher degree of variation in the

expression of integrins between the different tumor cells compared to CAFs may explain this result [254, 255]. PC3 is larger in size compared to HeLa and MIA PaCa-2 and internalized the highest number of GNPs, whereas the latter two are comparable in size, but there still was a significant difference in their GNP uptake. All three tumor cell lines used, prostate, cervical, and pancreatic, express integrin αvβ3, which is able to recognize the RGD sequence conjugated on surface of GNPs. However, the cervical cell line also expresses another RGD binding integrin, αvβ6, which might explain the higher number of GNPs in them compared to MIA PaCa-2 [254, 255].

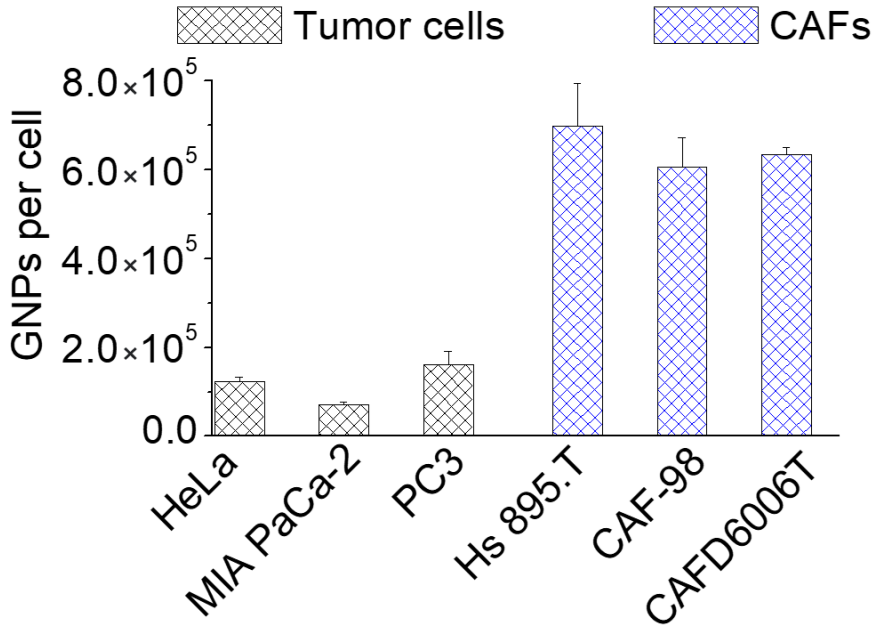

Figure 3.11 GNP uptake by tumor cells and CAFs in the absence of DTX. Reproduced with permission from open access Creative Common license [223].

In a real TME, NPs are delivered to cells through tumor vasculature. Cellular retention of NPs over time is critical for delivering the optimum therapeutic dose. To simulate retention in this study, NPs were removed from the media after the cells were incubated with NPs over a 24-hour period. The extent of NP retention between tumor cells and CAFs over a 72-hour period is illustrated in **Fig. 3.12**. The percent retention of NPs (**Fig. 3.12B**) was extrapolated using the data in **Fig. 3.11** and **Fig. 3.12A** Exocytosis and the redistribution of NPs via cell division could explain the reduction in cellular GNP content [63, 216, 217]. There was no significant difference in NP retention among the different CAFs. This result is not surprising, considering that NP uptake was also very similar among different CAFs. As CAFs have a large doubling time, cell division likely had a less significant effect on NP retention compared to exocytosis over the 72-hour incubation.

The higher NP abundance in CAFs compared to tumor cells implies that, as soon as the NP-rich growth medium was replaced with fresh media, CAFs were exposed to a higher concentration gradient compared to tumor cells [256]. Therefore, the lower retention in CAFs compared to tumor cells could be explained by the dynamics of the exocytosis process. The retention percentage of NPs in two tumor cell lines, HeLa and PC3, were three and two-fold higher than CAFs, respectively. Among the three tumor cell lines, MIA PaCa-2 is the smallest in size and had the lowest retention. It is speculated that NP concentration within MIA PaCa-2 was higher, however, they responded faster to the concentration gradient, resulting in a lower number of NPs within them at the end. Overall, the extent of the decrease in NP retention in tumor cells could be due to a combination of exocytosis dynamics and redistribution of NPs via cell division [222]. The cell division time of tumor cells varies as follows: 19.5, 40, and 25 hours for HeLa, MIA PaCa-2, and PC3, respectively. The retention percentage in these tumor cells was roughly twice as low compared to our previous studies, which was expected because our previous studies measured retention after a shorter period of 24 hours [217].

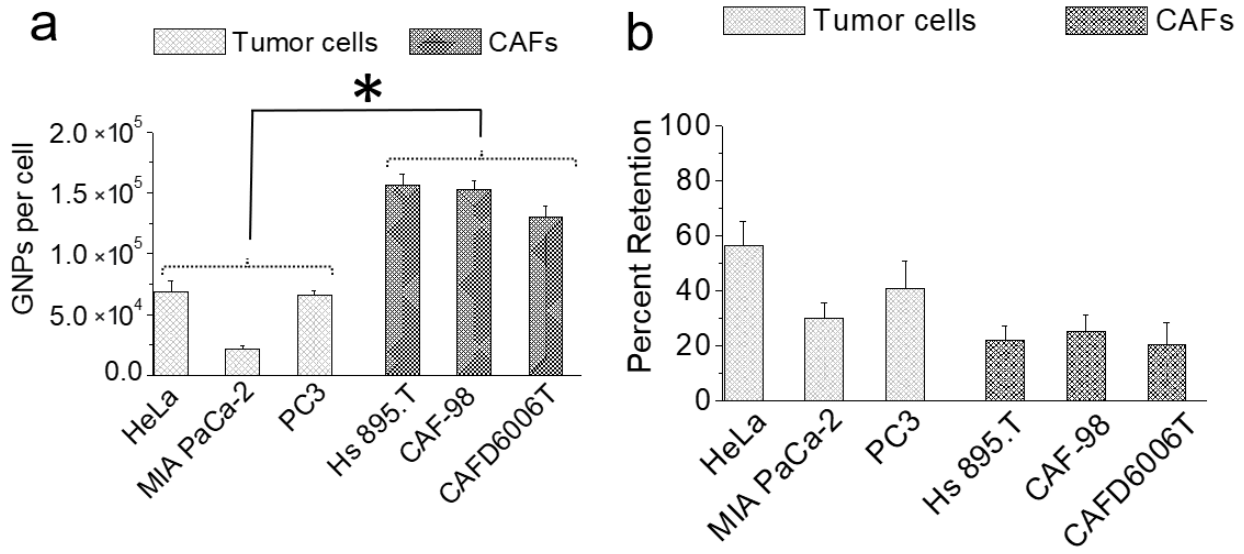

Figure 3.12 Retention of GNPs 72 hours after introducing fresh media. *indicates $p < 0.05$. **(A)** GNPs retention in tumor cells vs. CAFs per cell. **(B)** The percentage of GNPs retained by tumor cells and CAFs. Reproduced with permission from open access Creative Common license [223].

3.4.2 Determining the Effect of DTX on GNP Uptake and Retention

A simultaneous incubation of both GNPs and DTX over a 24-hour period was used for the uptake study. We used concentration of 50 nM of DTX, since such concentration is feasible *in vivo* [252]. As illustrated in **Fig. 3.13**, the number of internalized GNPs in both tumor cells (**Fig. 3.13A**)

and CAFs (**Fig. 3.13B**) increased dramatically for the simultaneous incubation vs GNPs alone. The increase in GNP uptake in CAFs was significantly higher compared to tumor cells. The percent increase in NP accumulation in tumor cells was 155% (HeLa; cervical cancer), 70% (MIA PaCa-2; pancreatic cancer), and 115% (PC3; prostate cancer) while it was 20.6% (Hs 895.T; melanoma), 5.8% (CAF-98, pancreatic), and 34% (CAFD6006T; prostate) for CAFs.

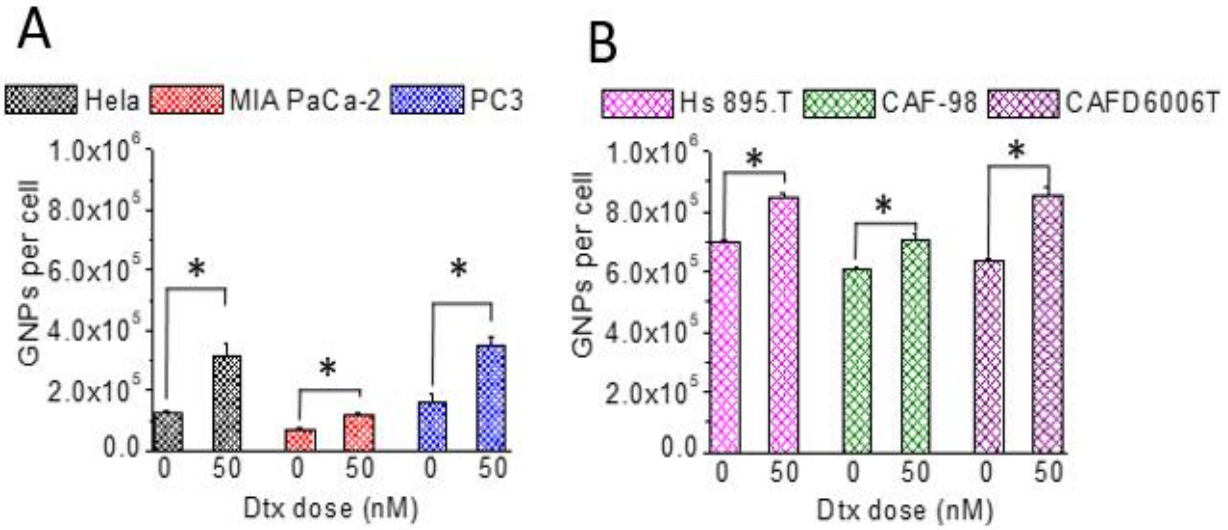

Figure 3.13 Effect of DTX on GNP. **(A-B)** The number of GNPs present in tumor cells (A) and CAFs (B) after a 24-hour incubation with GNPs/DTX vs. GNPs alone, respectively. *indicates $p < 0.05$. Reproduced with permission from open access Creative Common license [223].

DTX had a prominent effect on tumor cells as compared to CAFs as shown in **Fig. 3.14** (also **Fig. S3** and **Fig. S4**). More MT bundling was present in tumor cells compared to CAFs, which implies a greater DTX effect on tumor cells compared to CAFs. This is supported by cell cycle data (discussed in the next section) where a higher percentage of cancer cells arrested in the G2/M phase compared to CAFs. It is speculated that one of the reasons for the lesser effect of DTX on CAFs is that since DTX works by directly binding to MTs and since CAFs are much larger than tumor cells, the effect of the small concentration of DTX used on CAFs' larger cytoskeleton structure and more abundant MTs network is more distributed, and thus it has weaker effect on CAFs compared to tumor cells. The progression of cell population toward G2/M was more dynamic in tumor cells compared to CAFs. Based on **Fig. 3.14** (also **Fig. S3** and **Fig. S4**), the distribution of GNPs was significantly changed in tumor cells in contrast to CAFs. It could be seen that GNP clusters were either localized closer to the nucleus or in areas where there were no MTs. However, the number of GNPs present in CAFs was still ~ 200% higher than in tumor cells with the treatment of DTX even though the percent increase is lower than tumor cells. The increase in

GNPs with the treatment of DTX can be attributed to two main reasons. Firstly, cells are arrested during mitosis (metaphase) following treatment with DTX. Therefore, the resulting prolonged time spent in M phase could lead to increased NP accumulation. Secondly, it seems that DTX did not affect the endocytosis process since it is largely mediated through the actin cytoskeleton closer to the cell membrane [252]. However, the stabilizing of MTs could affect the processing and removal of GNPs from cells, potentially trapping of NPs within cells and increasing their presence overtime. This could lead to increase in accumulation intracellularly. Since MT stabilization could affect intracellular processing and removal of NPs from cells, it is crucial to investigate how feasible it is for cells to retain NPs once both GNPs and DTX are removed from the cell culture media.

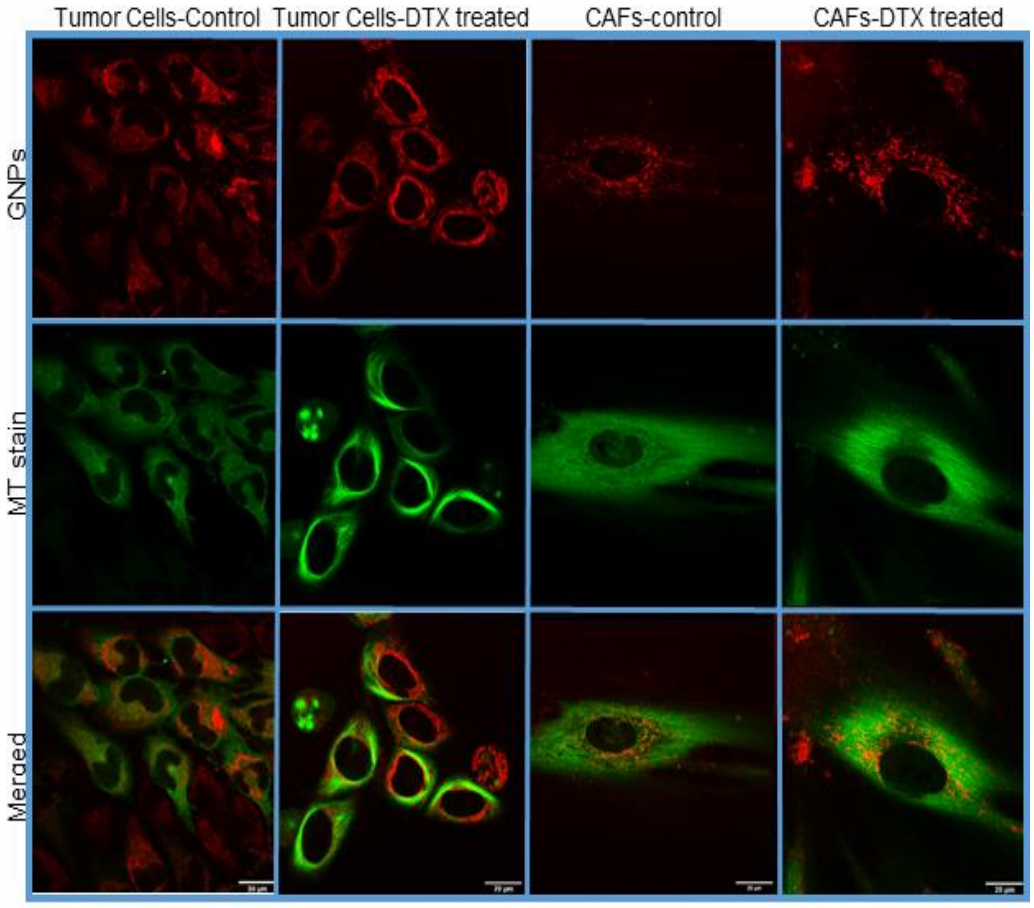

Figure 3.14 Effect of DTX on GNP. Confocal Images of tumor cells and CAFs treated and untreated with DTX. GNPs in red (first row), MTs in green (second row), and merged (third row). First column demonstrates the distribution of GNPs in cancer cells in the absence of DTX. Second column demonstrates the effect of DTX on MTs and on the distribution of GNPs in cancer cells. Third and fourth columns show the effect of the absence and presence of DTX on the number of GNPs in CAFs, respectively. Scale bar = 20 μm. Reproduced with permission from open access Creative Common license [223].

3.4.3 Intracellular Retention of GNPs in the Presence of DTX

In order investigate the effects of DTX on NP retention, cells were first simultaneously incubated with NPs and DTX over a 24-hour period. After the incubation period, the old media was replaced with fresh media (no GNPs or DTX) followed by an incubation period of 72 hours to evaluate NP retention. After 72-hour period, the tumor cells treated with GNPs alone had ~ 20% of their original NP content remained while the ones treated with both GNPs plus DTX had 70% of their NP content remained (**Fig. 3.15a-b**). A higher fraction of tumor cells was still in G2/M phase even after 72 hours. Therefore, this retardation of the cell division and the cells' inability to process and transport NPs to the cell periphery for their excretion could led to this observed in increase in NP retention. The potential of NP retention was somewhat lower in CAFs compared to tumor cells as illustrated in **Fig. 3.15c-d**. The number of GNPs remaining in the CAFs was still more than 100% higher compared to tumor cells after 72 hours (**Fig. 3.15c**). However, CAF percent retention was lower compared to tumor cells, with values of 53%, 66.8%, and 55.6% for HS 895.T (melanoma), CAF-98 (pancreatic), and CAFD6006T (prostate), respectively. This fact implies that CAFs were able to excrete NPs at higher rate than tumor cells, lowering the retention. This could be explained with **Fig. 3.15e-f** where cell cycle data shows a difference in phase distribution of cell populations of tumor cells (**Fig. 3.15e**) and CAFs (**Fig. 3.15f**). A larger population of tumor cells was still in G2/M phase which prevents NP removal via regular exocytosis, trapping GNPs for a longer time. In contrast, the population of CAFs arrested in G2/M phase was lower, which permitted more exocytosis of NPs and less retention, indicating a weaker effect of DTX on them.

It is worth mentioning that the difference in the effect of DTX on tumor cells vs. CAFs is expected because different cell lines have different half maximal inhibitory concentration (IC-50) for DTX. Though, for the sake of mimicking a real-life scenario (where a single dose is used for the whole TME), the same concentration of DTX was opted for both tumor cells and CAFs in this study. Nevertheless, if we compared untreated vs. treated cells (**Fig. 3.15a-d**), the increase of percent retention was higher for CAFs than for tumor cells, this indicates that the concentration of DTX used was indeed effective in increasing the retention rate of GNPs in CAFs despite the lower percentage of cells arrested at the G2/M compared to tumor cells. It is also important to recognize that the number of GNPs present in CAFs was still much higher than that of tumor cells **(Fig. 3.15a,c)**. The conclusion is that the synchronization of tumor cells at the most radiosensitive phase,

i.e. G2/M, and the higher number of radiosensitizing NPs concentrated in CAFs could be exploited in RT.

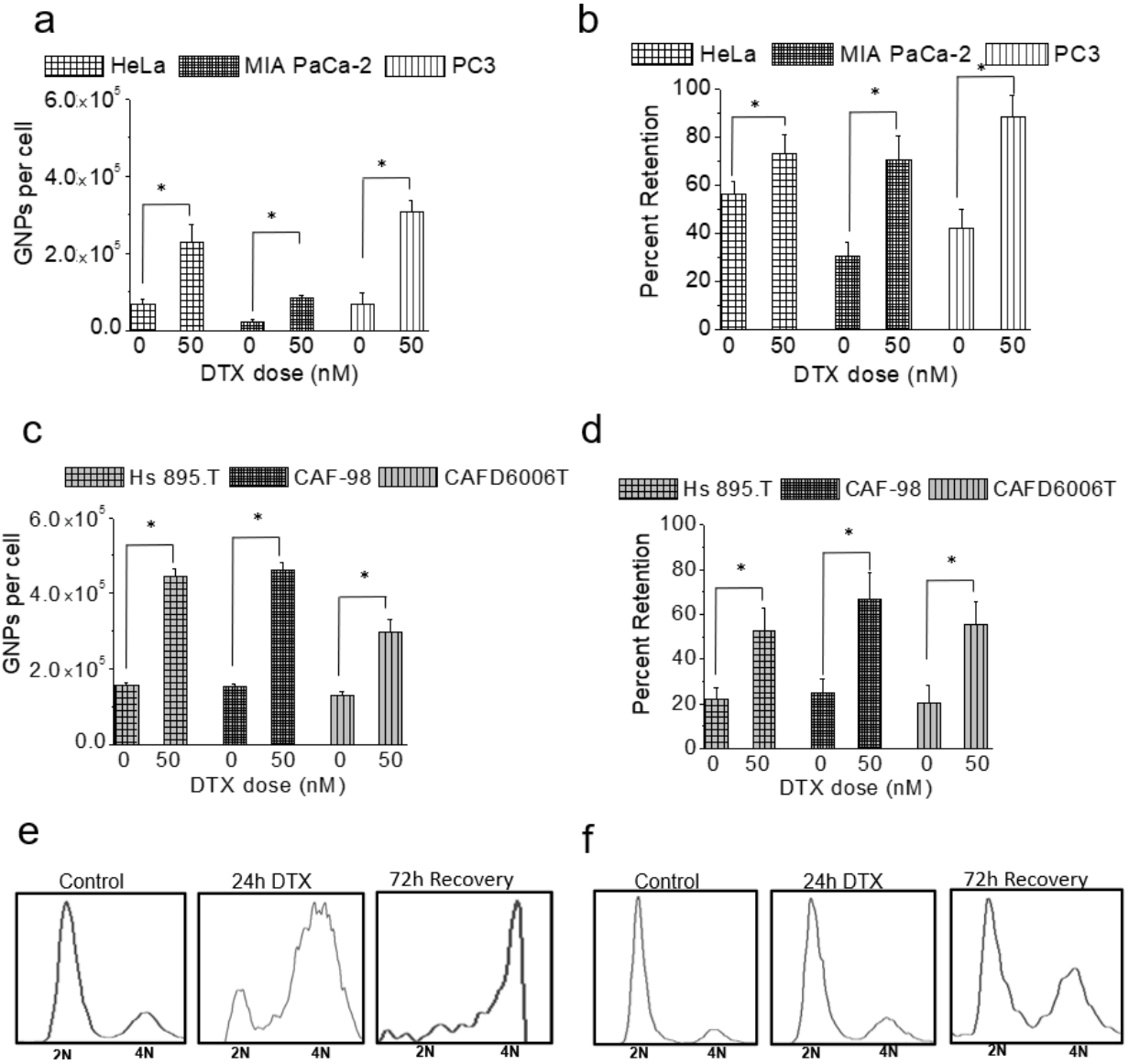

Figure 3.15 Retention of GNPs in the presence of DTX. **(a)** Number of GNPs retained per cell for cancer cells untreated and treated with DTX. **(b)** Percent retention of GNPs for cancer cells untreated and treated with DTX. **(c)** Number of GNPs retained per cell for CAFs untreated and treated with DTX. **(d)** Percent retention of GNPs for CAFs untreated and treated with DTX. *indicates $p < 0.05$. **e-f)** Cell cycle data where 2N represent cells at the G0/G1 phase and 4N represent cells in the G2/M phase. MIA PaCa-2 (e) and CAF-98 (f) untreated, treated with DTX, and post recovery. Reproduced with permission from open access Creative Common license [223].

Moreover, more MT bundling was present in tumor cells compared to CAFs (**Fig. 3.16**), which again implies a greater DTX effect on tumor cells compared to CAFs. The difference in the effect of DTX on tumor cells vs. CAFs is expected because different cell lines have different IC-

50 for DTX. However, for the sake of mimicking a real-life scenario, we opted for using the same concentration of DTX for both tumor cells and CAFs. Nevertheless, if we compared untreated vs. treated cells, the increase of percent retention was higher for CAFs than for tumor cells, which indicates that the concentration of DTX used was indeed effective in increasing the retention rate of GNPs in CAFs, despite the lower percentage of cells arrested at the G2/M compared to tumor cells. It is also important to recognize that the number of GNPs present in CAFs was still much higher than that of tumor cells (**Fig. 3.15a,c** and **Fig. 3.16**). We believe that both the synchronization of tumor cells at the most radiosensitive phase, i.e., G2/M, and the higher number of radiosensitizing NPs concentrated in CAFs could be exploited in RT.

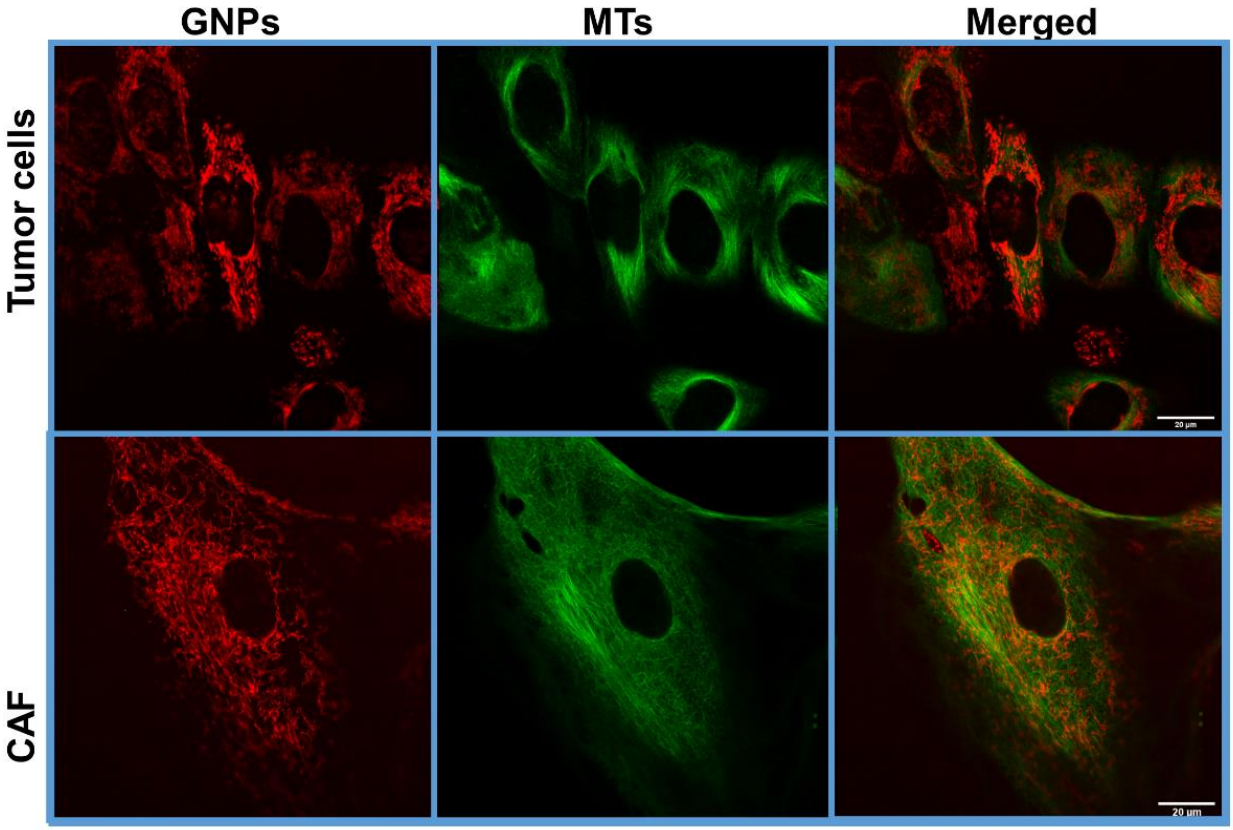

Figure 3.16 Retention of GNPs in tumor cells and CAFs post recovery. Confocal Images of tumor cells and CAFs 72 h post recovery. GNPs are in red (first column), MTs are in green (second column) and merged are in red and green (third column). The first row shows the distribution of GNPs in a group of tumor cells. The second row shows the presence of GNPs and the MTs in a CAF cell. Stabilization of MTs was present more in tumor cells compared to CAFs. Scale bar = 20 µm. Reproduced with permission from open access Creative Common license [223].

3.4.4 Conclusions

Our study sheds light on targeting not only tumor cells but also CAFs using GNPs. We were able to show that the use of FDA-approved anticancer drug, DTX, shows over %200 the uptake and retention of GNPs in both tumor cells and CAFs. The improvement of GNP retention over an extended period of time allows for the delivery of therapeutics efficiently. Our approach is feasible in the clinic considering the clinically safe concentrations used in this study and the fact that DTX is given once a week to patients. Our study shows the potential of using even fewer GNP injections in fractionated RT considering the higher fraction of GNPs retained with the use of DTX. The potential of GNPs to act as a radiosensitizer would ultimately allow us to reduce the radiation dose to further reduce the side effects. The potential of targeting two critical components of the TME, tumor cells and CAFs, with a single GNP system will enable us to reap the full benefits of cancer nanomedicine to reach these goals. This type of novel approaches could ultimately improve patient care in the near future. Future studies would include exploring GNPs uptake and retention in the presence and absence of DTX *in vivo*.

3.5 Chapter 3 Conclusions

The *in vitro* monolayer experiments we conducted indicate that GNPs have a high affinity for both CAFs and tumor cells, significantly more so than for normal cells. This suggests that GNPs could be particularly effective as drug carriers or radiosensitizing agents, specifically aimed at reducing CAF activity. Additionally, over a 24 h period, both CAFs and tumor cells retained more than 70% of the administered GNPs, offering greater flexibility in therapeutic delivery schedules. The limited uptake of GNPs by NFs alleviates some concerns about toxicity in healthy tissue, especially at the low concentrations used in clinical settings. Importantly, when combined with the FDA-approved anticancer drug DTX, both CAFs and tumor cells showed enhanced retention of GNPs. Given that DTX is already administered weekly to cancer patients, this dual approach could be readily adapted to clinical protocols. Our research suggests that NP-based targeting of both tumor cells and CAFs holds promise as an innovative approach to improve existing cancer treatments, such as RT and chemotherapy. This is especially relevant for pancreatic cancer, which has notably low survival rates. The high retention rates we observed, especially when GNPs were used in conjunction with DTX, could also lead to fewer injections required in

fractionated RT. It would also add some flexibility with the timing of radiation delivery, which is important in real world treatment. Furthermore, the radiosensitizing properties of GNPs could allow for a reduction in the overall radiation dose, thereby minimizing adverse effects on normal tissues.

3.6 Materials & Methods

3.6.1 GNPs Synthesis

Spherical GNPs of ~ 15 nm diameter were produced using a citrate reduction method due to its simplicity, its relatively short preparation time, and its low chemical, physical, and environmental dangers [257]. The reducing agent was prepared by adding 0.12 g of sodium citrate tribasic dihydrate ($HOC(COONa)(CH_2COONa)_2\ 2H_2O$) to 10.53 mL of double-distilled water to create a 1% solution. The gold solution was prepared by adding 0.12 g of Tetrachloroauric (III) acid trihydrate ($AuCl_4H{\cdot}3H_2O$) to 10.35 mL of double-distilled water to create a 1% solution. A total of 300 µL of the 1% gold solution was then added to 30 mL of double-distilled water in an Erlenmeyer flask and was stirred and heated until boiling. Once boiling, 600 µL of the 1% reducing agent was added quickly to the flask and was stirred while boiling for 10 min. The solution's color gradually changed from clear to a crimson red during this time, indicating the creation of GNPs. The heat was then turned off and the solution was stirred at room temperature for 10 more minutes.

3.6.2 GNPs *Functionalization*

The negatively charged GNPs surfaces are coated with PEG at a density of 1 PEG per nm^2 of GNP surface area. This corresponds to roughly 835 PEG per GNP and the GNP complex is referred as GNP_{PEG}. Following PEGylation, a peptide containing integrin binding domain, RGD was added for enhancing the uptake of GNP_{PEG} complex. We added 1 molecule of RGD for every 2 PEG molecules. The final complex is referred to as $GNP_{PEG\text{-}RGD}$. The $GNP_{PEG\text{-}CY5\text{-}RGD}$ used for live cell confocal imaging was PEGylated using 2000 Da PEG and 3400 Da PEG-thiol-CY5 in equivalent amounts, adding up to 835 PEG per GNP and 1 RGD molecule per PEG molecule. PEG of 2000 Da molecular weight was used due to its relatively close molecular weight to RGD peptide (1670 Da).

3.6.3 GNPs *Characterization*

GNPs, GNP_{PEG}, and $GNP_{PEG–RGD}$ shape, size, and concentration were characterized using Perkin Elmer λ 365 UV-VIS spectrophotometers, while Anton Paar LiteSizer 500 DLS and ζ potential were used to measure the hydrodynamic radius and surface charge, respectively. UV-VIS shows a measure of the amount of light being absorbed at a particular wavelength by the sample and is dependent on the size and shape of the NP. Transmission Electron Microscopy (TEM) (Hitachi HF-3300 V, Pleasanton, CA. USA) was used to verify the shape and size of GNPs used in this experiment (**Fig. S5**).

3.6.4 Cell Culture Methodology

Human pancreatic cancer cell line MIA PaCa-2 (ATCC#: CRL-1420™) and PANC-1 (ATCC® CRL-1469™), prostate cancer cell line PC-3 (ATCC#: CRL-1435™), cervix cancer cell line HeLa (ATCC#: CCL-2™), and melanoma cancer-associated fibroblasts (CAFs) Hs 895.T (ATCC#: CRL-7637™) were obtained from the American Type Culture Collection. CAF-98 and NPF-98 were derived from resected PDAC tumor tissue from a consenting patient through the GI Biobank at the Vancouver General Hospital. Prostate cancer-associated fibroblasts (CAF-D6006T) were provided by the Vancouver Prostate Centre (VPC). The study was approved by the University of British Columbia research ethics board (protocol #H20-00948). A small piece of tumor tissue was placed in FGM-2 media (Lonza cc-3132) to support the spontaneous outgrowth of NFs and CAFs. When confluent, the cells were passaged and further propagated in FGM-2 media. During the experiment, all cells were cultured in high glucose Dulbecco's modified Eagle medium (DMEM; Gibco) enhanced with 10% fetal bovine serum (FBS; Gibco), 1% penicillin/streptomycin (Gibco), and 4 mM of GlutaMax (Gibco). Trypsin–EDTA(Gibco) was used for all cell detachment from flasks and all cell fixations were performed using paraformaldehyde (PFA; Sigma Aldrich, Oakville, ON. Canada). Cell cultures were washed with Phosphate-Buffered Saline (PBS) and all cell line incubations happened at 37 °C with 5% CO_2.

3.6.5 Image Preparation

DF coupled with HSI CytoViva microscope (CytoViva, Auburn, AL. US) were used to determine GNP distribution in fixed cells. These cells were imaged using DF and HSI under a 60× objective. 1×10^5 cells from each cell line were grown on coverslips at the bottom of 6-well dishes

with 3 mL of media and were left in the incubator for 24 h. The cell culture media was dosed with 7.5 µg/mL of $GNP_{PEG–RGD}$ and cells were placed in the incubator for another 24 h. Cells for the uptake study were washed three times with 1 mL of PBS followed by adding 1 mL of 4% paraformaldehyde for fixation and incubated at 37 °C with 5% CO_2. After a 20 min incubation period, cover slips were rinsed three times with 1 mL of PBS, removed from their wells, mounted to a glass slide using Permount mounting medium (Fisher Scientific Company, Ottawa, ON. Canada) and are ready to be imaged after overnight dry up. The media of the cells for the retention study was replaced with fresh media and cells were placed in the incubator for an additional period of 24 h. After the incubation period, cells were washed three times with PBS, fixed, and cover slips were mounted on microscope glass slides for imaging as described previously.

Confocal microscopy (Zeiss LSM 980, Carl Zeiss Microscopy GmbH, Jena, Germany) was used to visualize GNP distribution in live cells. Live cells were imaged using oil-immersion 60X lens. 1×10^5 cells were cultured on 35 mm coverslip-bottom dishes (MatTek, Ashland, MA USA) with 2 mL of media and incubated for 24 h. All cells were dosed with 7.5 µg/mL of $GNP_{PEG\text{-}CY5\text{-}RGD}$ post-incubation and the ones that required DTX treatment were treated with 50 nM of DTX before incubating for another 24 h. Microtubules cells were stained with CellLight™ Tubulin-GFP BacMam 2.0, ThermoFisher Scientific, Waltham, MA, USA), providing specific targeting to cell tubulins. The tubulin stainer was added to the cells for at least 16 h prior to imaging. 24 h after GNP treatment, the media of the uptake study samples was substituted with colorless media (FluoroBrite DMEM; Gibco, ThermoFisher Scientific, Waltham, MA, USA) and four drops of NucBlue®, ThermoFisher Scientific, Waltham, MA, USA) Live reagent (DAPI) (Hoechst® 33,342 dye; ~350 nm excitation, ~461 nm emission, ThermoFisher Scientific, Waltham, MA, USA) was added to stain the nucleus of each cell. These samples were then incubated for 20 min before imaging. At the same time, the media of the retention study samples was replaced with fresh media and cells were incubated for their respected period of time. After that period passed, the media of these cells was changed with colorless media and DAPI dye was added to each sample, incubated for 20 min, then imaged. Imaging settings were kept as identical for all samples.

3.6.6 Quantification of Cellular Uptake and Retention

All cells were dosed with 7.5 µg/mL of $GNP_{PEG–RGD}$. For each cell line, ~1×10^5 cells were incubated in 6-well dishes in 3 mL of media. In total 12 wells were used for every cell line; 6 for

the uptake study (3 treated with 50 nM DTX and 3 untreated with DTX) and 6 wells for the retention study (3 treated with 50 nM DTX and 3 untreated with DTX). All cells were placed in the incubator for 24 h. The uptake study cells were then washed three times with PBS, trypsinized, and incubated for 5 min for detachment. Meanwhile, the media of the retention study cells was replaced with fresh media and cells were incubated for an additional period of 24 h. After 72 h, the retention study cells were washed three times, trypsinized, and incubated for 5 min. For both the uptake and the retention studies, media was added to the cells, and they were carefully counted using a hemocytometer counting chamber and transferred to glass tubes for processing. Cells were then treated with aqua regia (3:1 molar ratio of HCl and HNO_3(VWR)) and heated in a mineral oil bath at 90 ℃ for ~30 min. For each tube, 100 µL of hydrogen peroxide (VWR) was added before being incubated in a mineral oil bath for ~30 min to ensure full consumption of all cell contents. Finally, the samples were diluted to 2.5% *v/v* (volume per volume) acid content with deionized water. ICP-MS (Agilent 8800 Triple Quadrupole) was used to measure the gold content in every tube, providing the amount of gold in parts per billion (ppb) or ng/mL. The number of GNPs per cell was calculated using the following equation:

$$\frac{Gold\ nanoparticle}{Cell} =$$

$$\frac{\frac{Gold\ Conc\text{entration}}{Sample}\left[\frac{g}{mL}\right] \times Sample\ Vol\text{ume}\ [mL] \times N_A[\frac{atoms}{mol}]}{Gold\ atomic\ mass\left[\frac{g}{mol}\right] \times \text{Number}\ of\ Cells \times \frac{Gold\ atoms}{Gold\ nanoparticle}}$$

where gold concentration per sample, the sample volume, and the number of cells per sample vary among our different samples, $the\ atomic\ mass\ of\ gold = 196.96657\frac{g}{mol}$, N_A is Avogadro's number ($6.022 \times 10^{23}\ \frac{atoms}{mol}$), and the number of gold atoms per GNPs is calculated using the following equation:

$$\frac{Gold\ atoms}{Gold\ nanoparticle}$$

$$= \frac{Atoms\ per\ unit\ cell \times Gold\ Nanoparticle\ Vol\text{ume}\ [nm^3]}{Unit\ cell\ Vol\text{ume}\ [nm^3]} =$$

$$\frac{4 \times \frac{4\pi r^3}{3}}{a^3} = \frac{2}{3}\pi\left(\frac{D}{a}\right)^3$$

where D = 10.9 nm, which is the core diameter of a spherical GNP, and a = 0.408 nm is the length of a unit cell. Gold synthesized by the citrate reduction method develops a face-centered cubic crystal structure with four atoms of gold contained in each unit cell [258]. It is assumed that the distribution of NPs in each cell type is even, and it is also assumed that the size of GNPs is homogenous; hence, the calculations only represent a group average. These two assumptions were informed by the images obtained from confocal for GNPs' distribution, and TEM for GNPs' size.

3.6.7 Cell Cycle Analysis

For cell cycle analysis, cells were cultured in 60 mm dishes with 5 mL of media and each cell line was divided into four different groups: nontreated control cells, 6-h DTX -treated cells, 24-h DTX-treated cells, and 72-h post DTX-treated cells. The latter was incubated with DTX for 24 h before refreshing the media and incubating for 72 h. All DTX -treated cells were treated with 50 nM of DTX. Following their respective incubation periods, cells were trypsinized using Trypsin-EDTA and neutralized with 10%FBS/DMEM, before being transferred to 15 mL polystyrene tubes. After spinning at 350× g for 5 min at 4 ◦C, the supernatant was poured off and the cell pellets were washed with ~1 mL PBS/1.0 × 10^6 cells. The cell pellet–PBS solutions were spun at 350× g for 5 min at 4 ◦C and the pellets were resuspended in 1% PFA (Paraformaldehyde in PBS). Cells were then incubated on ice in the dark for 15 min to complete the fixation process. They were then spun at 350× g for 5 min at 4 ◦C, washed in 1 mL of PBS, and spun again at 350× g for 5 min at 4 ◦C. The samples were resuspended in 70% ethanol before they were incubated at –20 ◦C for a couple of days for further processing and fixation. Post-incubation, the samples were centrifuged at 350× g for 10 min at 20 ◦C, washed in 0.5% BSA-Bovine Serum Albumin in PBS, and centrifuged at 350× g for 5 min at 20 ◦C. The samples were resuspended in PBTB (PBS, 0.5% BSA, 0.1 % Triton-X 100) and RNase A was added at a concentration of 100 ug/mL. This mixture was shaken at 37 ◦C for 25 min to allow for cell membrane permeabilization and RNA degradation. The samples were wrapped in aluminum foil and propidium iodide (fluorescent at 488 nm with emission centered at 600 nm) was added at a concentration of 10 µg/mL before incubating on a shaker at 4 ◦C for 60 min. Samples were then centrifuged at 350× g for 5 min at 20 ◦C to label

DNA. This step is essential because the amount of DNA in the cell reveals the phase the cell is in. Samples were resuspended in 1 mL PBS/BSA and passed through 50 µm cell strainer, before being run on a flow cytometer (FACS Calibur, BD Biosciences, Franklin Lakes, NJ, USA).

3.6.8 Pancreatic Xenograft Model

Human pancreas cancer cell line (MIA-PaCa-2, ATCC#: CRL-1420™) was cultured in Dulbecco DMEM (ThermoFisher Scientific, Waltham, MA. US) together with 10% FBS, 100 units/mL penicillin G, and 100 µg/mL streptomycin (Hyclone, Cytiva, Marlborough, MA. US). Cells were maintained at 37 °C in a humidified atmosphere containing 5% CO_2. For inoculation in mice, cells were re-suspended in growth medium to the appropriate concentration. For this study, female severe combined immunodeficient (SCID) mice of 6–8 weeks were used. To derive subcutaneous xenografts, 1.5×10^6 tumor cells in a volume of 100 µL were injected using a 28-gauge needle in the lower left dorsal flank. Tumor measurements were converted into tumor volume using ($LxW^2/2$), where L and W are the larger and smaller diameters, respectively; tumors were measured every 2 days with calipers. When xenografts reached a volume of ~250 mm^3, they were randomly divided into groups of 6 for all studies. Each mouse was administered a gold dose of 1 mg/kg in a volume of 100 µL via tail vein using a 28-gauge needle. The concentration of GNPs used for injections was 200 µg/mL and they were suspended in PBS. Animals were monitored for any signs of physical toxicity over the duration of each study. Experiments were conducted in accordance with the Animal Care Committee guidelines of the University Health Network and the approved protocol number is 2979.

3.6.9 Immunohistochemistry

All serial sections (50 µm separation between sections) were cut from frozen block tumor tissue. Sections were stained for CA9 (Rabbit monoclonal; ThermoFisher Scientific, Waltham, MA. US) and CD31 (provided by Dr. Cameron Koch, University of Pennsylvania, Philadelphia, PA, USA). Secondary antibodies were used alone to control for nonspecific backgrounds. Sections were counterstained with 1 ug/mL DAPI to outline the nuclear area. Images were scanned on the TS4000 (Huron Technologies) at 0.5 um/pixel. Regions of tumor, necrosis, stroma, and folds were specified, creating a training ruleset for tissue recognition using Tissue Studio (Definiens, Munich,

Germany). Cellular analyses included nucleus identification and separation, with objects < 10 μm^2 being excluded.

3.6.10 Acute and Physical Toxicity Assays

For acute toxicity, blood, liver, kidney, and overall toxicities were measured through proteins, enzymes, metabolites, and plasma electrolytes. Blood samples were collected through terminal cardiac puncture prior to sacrifice. Samples were analyzed using a vetscan2 Autoanalyzer (Applied Biosystems, Foster City, CA. US). Mice were observed for any physical toxicity over a 50-day period. These physical indicators included body weight changes, dull sunken eyes, rapid/shallow breathing, hunched back, and lethargy.

CHAPTER 4

Gold Nanoparticles Radiosensitization Effects in 2D and 3D Co-culture Models

Understanding that GNPs and DTX have synergistic potential as radiosensitizers—by trapping cells in the G2/M phase and enhancing GNP uptake and retention—we aimed to assess the standalone efficacy of GNPs in a co-culture system. Specifically, we wanted to investigate whether CAFs contribute to the resistance of cancer cells, as suggested in existing literature. To avoid introducing too many confounding factors, we initially focused on the combination of GNPs and RT to compare radioresistance in co-culture versus monoculture systems. We carried out these assessments in both 2D and 3D co-culture models to gain a comprehensive understanding of the radiosensitizing potential of GNPs. This work led to the publication of two articles. The two articles appeared in *Cancers* and the *International Journal of Molecular Sciences*, respectively. The *Cancers* manuscript is titled "Potential of Gold Nanoparticles in Current Radiotherapy Using a Co-Culture Model of Cancer Cells and Cancer Associated Fibroblasts" [259], and the *International Journal of Molecular Sciences* manuscript is titled "Utilizing Gold Nanoparticles as Prospective Radiosensitizers in 3D Radioresistant Pancreatic Co-Culture Model" [260]. My personal contribution to the above-mentioned papers includes conceptualization and experimental design, sample preparation, collection, and processing, data acquisition and analysis, creation of figures and manuscripts writing.

4.1 GNPs as Radiosensitizers in 2D Co-culture Models

The uptake of GNPs in co-culture models of pancreatic tumors using different ratios of CAFs to tumor cells and subsequent radiation treatment has not been investigated previously based on the literature. Understanding the effect of the interactions between different cell lines in co-culture systems on various treatment modalities is critical to reap the benefits of nanotechnology, especially for pancreatic cancer. Insight into the interactions of GNPs with tumor cells and CAFs in co-culture systems will help inform more in-depth co-culture experiments before transitioning to 3D *in vitro* co-culture systems and then to *in vivo* models. This experiment sheds light on the behavior and the effect of GNPs in a co-culture of pancreatic cancer cells and CAFs compared to monoculture, and how different ratios of CAFs affect the overall treatment of cancer cells (**Fig. 4.1**). CAFs and cancer cells were grown together in co-cultures at different ratios to mimic the real-life variations in the TME [6, 102]. A co-culture model is developed to test the difference in outcome of GNP-mediated radiation response in a more clinically relevant co-culture environment. We aim to address three main questions:

1. What effect do CAFs have on cancer cells in a co-culture environment in relation to GNP uptake, proliferation, and DNA damage?
2. How advantageous is the GNPs/RT treatment vs. RT alone in monoculture vs. co-culture?
3. Does the ratio of CAFs to cancer cells affect GNP uptake, DNA DSB, and the proliferation of cells?

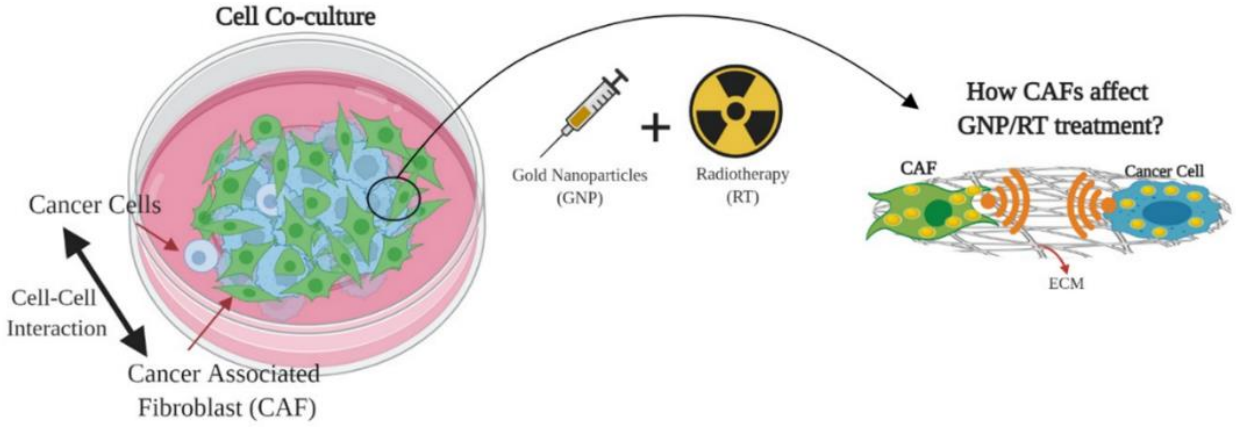

Figure 4.1 Cancer cells and CAFs were grown together in co-culture for cell-to-cell interaction to occur to test the possible targeting using GNPs as radiosensitizers. Reproduced with permission from open access Creative Common license [259].

4.1.1 Determining the Uptake of GNPs in Co-Culture vs. Monoculture

To develop this co-culture model for our studies, we used cancer cells of pancreatic origin (MIA PaCa-2) and pancreatic CAFs (CAF-98) since CAFs are one of the most important cell types that promote tumour growth. The first step in this process is to test how the presence of CAFs affects the GNP uptake of cancer cells in co-culture. Three different ratios of CAF-98 to MIA PaCa-2 were chosen to represent heterogeneity in TME. After GNP incubation, cell populations were isolated for quantifying GNP content in each cell line using magnetic beads (**Fig. S6.1**). Co-culture cells were cultured together for a period of 72 h to ensure enough time for intercommunication between cancer cells and CAFs [49]. All cells were dosed with 7.5 µg/mL of $GNP_{PEG\text{-}RGD}$ post-incubation for 24 h. A successful cell isolation or cell sorting would allow us to measure the effects of cell-to-cell interactions on the uptake of NPs in the different cell lines used. The accuracy of the separation method was also tested and over 95% cell separation accuracy was achieved for both cell lines used (**Fig. S6.2**). This shows that the collected CAFs post-separation had over 95% CAFs and less than 5% cancer cells, and the collected cancer cells post-separation were ~95% cancer cells and with about 5% CAFs contamination. Images of both cell lines post-separation are shown in **Fig. S6.3**. To be able to quantify the number of GNPs per cell precisely, we typically use ICP-MS [261–263]. However, due to the inherent risk of using magnetic beads on the mass spectrometer that might lead to damaging the device we opted for using FITC-labelled GNPs which serve the purpose of this study [45]. Labelled cell lines were assessed by flow cytometry to measure percent expression and median fluorescent intensity of the FITC signal in monocultures of MIA PaCa-2 and CAF-98, vs. in co-cultures of MIA PaCa-2 and CAF-98, **Fig. 4.2**, which shows no effect of the co-culture on the GNP uptake of either cell lines. However, the results show that the uptake of GNPs in CAFs is over three times higher than that of cancer cells in both monoculture and co-culture, which is in agreement with our previous experiments that were done in monoculture [222, 223]. This is an important observation that might open the door for targeting not only cancer cells but also CAFs using GNPs. The results show that the interaction of tumour cells with CAFs did not significantly affect GNP uptake and retention capacity.

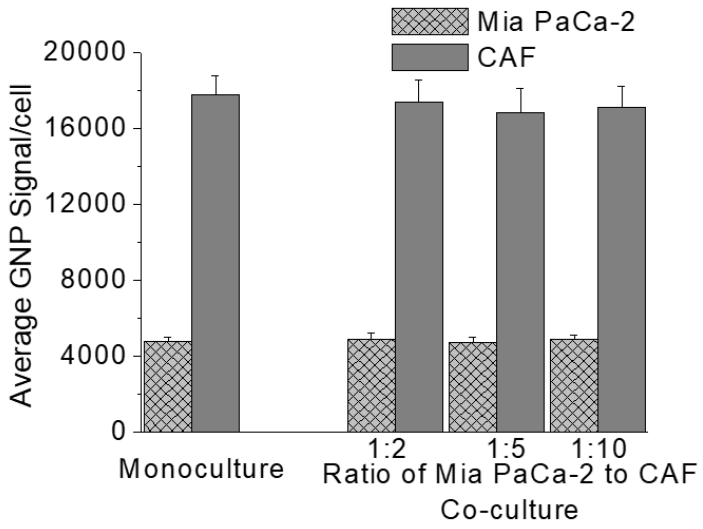

Figure 4.2 Average median fluorescent intensity GNP-FITC signal per cell of MIA PaCa-2and CAFs in monoculture vs. co-culture. Reproduced with permission from open access Creative Common license [259].

Additionally, GNPs distribution in the cells was mapped qualitatively using confocal microscopy (**Fig. 4.3**) and DF coupled with HSI (**Fig. S7.1**). The co-culture images in **Fig. 4.3** and **Fig. S7.1** are for a CAF to MIA PaCa-2 ratio of 2:1, images of the other two ratios used can be seen in **Fig. S7.2**. The existence of GNPs in cells was verified using the spectral mapping feature of HSI, as illustrated in **Fig. S7.1**, where GNP spectra were collected from bright spectra from within cells, confirming that they are from gold from when compared to available data in the imaging library.

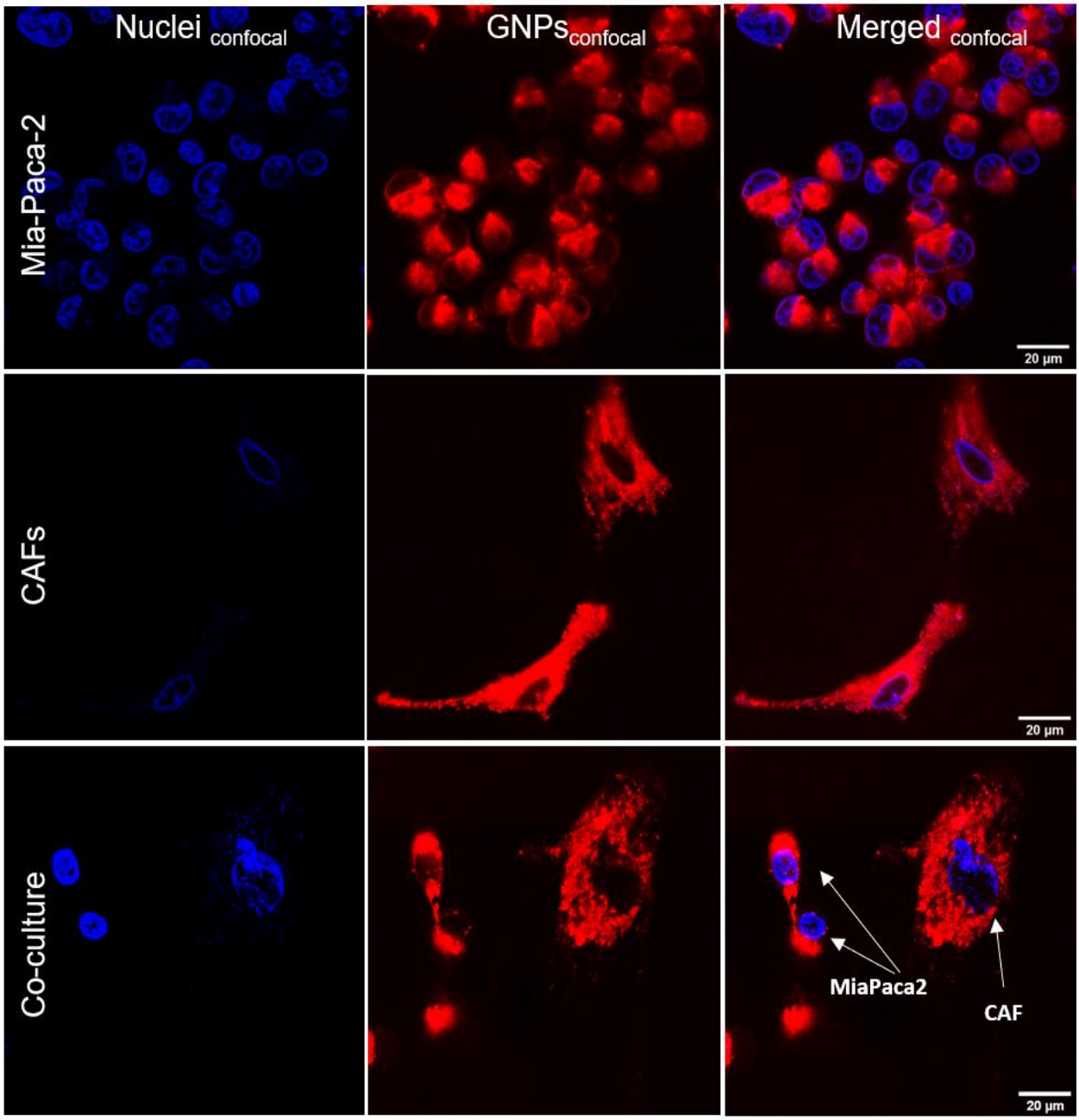

Figure 4.3 GNPs uptake in cancer cells and CAFs in monoculture vs. co-culture. GNP distribution in monoculture MIA PaCa-2 (first row), monoculture CAFs (second row), and co-culture of CAFs & MIA PaCa-2with 2:1 ratio (third row), using confocal imaging in the first three columns, where the first column shows the nucleus in blue, the second column shows GNPs in red, the third column shows both merged. Scale bars are 20 µm. Reproduced with permission from open access Creative Common license [259].

4.1.2 Mapping DNA Damage due to GNP-Mediated Radiosensitization

One of the mechanisms of cell damage due to radiation is through the formation of free radicals that can damage DNA, as explained in *Chapter 2*. Adding GNPs to current RT results in

an additional number of free radicals causing more DNA damage. This has been investigated in a monoculture but not in a co-culture [64]. In this study, we investigated how the presence of CAFs affects GNP-mediated DNA damage in cancer cells; we used an immunofluorescence assay to map the DNA damage, and it is typically used as a measure of radiation induced damage [264]. Using this assay, we investigated the effects of radiation and GNPs on co-cultured cells vs. monocultured cells. Specifically, we mapped the DNA DSBs since it is the most lethal damage compared to single strand breaks. Antibodies against repair proteins γ-H2AX were used 24 h post radiation treatment of a single dose of 2Gy [265, 266]. This allows for the capture of residual damage that typically represents unrepaired DNA DSB damage [50, 267]. The average number of foci per cell for MIA PaCa-2 and for CAFs is shown in **Fig. 4.4** and **Fig. S8.1**, respectively, where the co-cultures have CAFs to MIA PaCa-2 at ratios of 2:1, 5:1, and 10:1. This was repeated for control cells, cells incubated with GNPs only, irradiated cells only, and cells incubated with GNPs and irradiated.

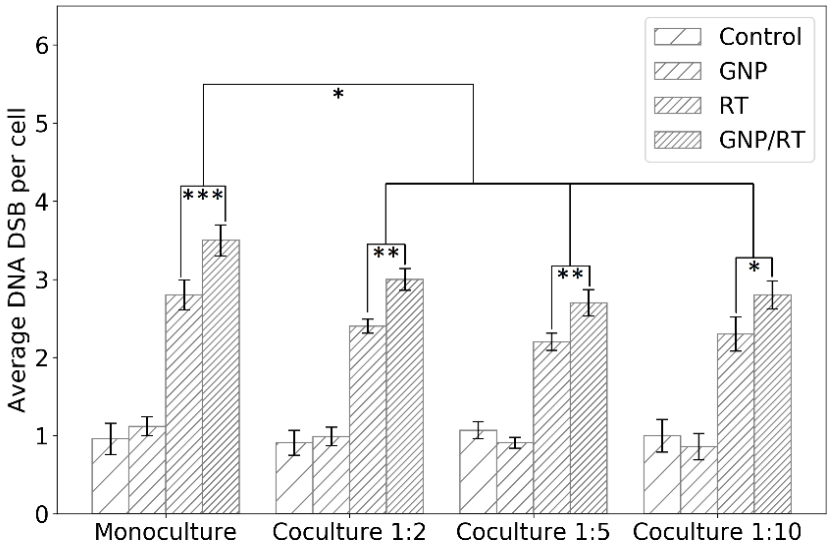

Figure 4.4 DNA DSB damage in MIA PaCa-2 and in CAFs. Average number of DNA DSB damage per cell in MIA PaCa-2in monoculture vs. in co-culture. * indicates $p < 0.05$, ** indicates $p < 0.01$, *** indicates $p < 0.001$. Reproduced with permission from open access Creative Common license [259].

The results lead to three important observations. Firstly, GNPs, in the absence of radiation, did not induce additional DNA DSBs compared to control cells in monoculture or in any of the co-cultures for neither MIA PaCa-2 nor CAFs, which is consistent with our previous experiments, as the amount of GNPs used is tolerated by the cells [268, 269]. Secondly, the addition of GNPs to cells prior to radiation induced a statistically significant increase in DNA DSBs compared to

irradiated cells without GNPs in monoculture and in all three co-cultures for both MIA PaCa-2 and for CAFs. The increase in the number of foci for GNP/RT cells compared to RT ranges from 22% for MIA PaCa-2 in the 1:10 co-culture to 25% in the monoculture MIA-PaCa-2. The increase in the number of foci for GNP/RT cells compared to RT was 13% for monoculture CAFs and 24%, 23% and 40% for 1:2, 1:5 and 1:10 co-culture, respectively. We attribute this increase in DNA DSB to the radiosensitization and dose enhancement effect of GNPs with RT which contributes an increase in photoelectric absorption events that results in short-range electrons in the vicinity of the cell nucleus causing a rise in free radicals that increases DNA DSBs [197, 198].

It is important to note that even though CAFs had a much higher amount of gold compared to MIA PaCa-2, their DNA DSBs were not higher than that of MIA-PaCa-2. This may be due to the size of CAFs that allows the GNPs to cluster away from the nuclei, thus decreasing the overall DNA DSB damage expected. Lastly, there is a significant decrease in DNA DSB in both MIA PaCa-2and CAFs that were grown in co-cultures vs. monoculture for both RT only and GNP/RT. The decrease ranges from 14% to 23% for MIA PaCa-2 and from 12% to 35% for CAFs. No significant difference in DNA DSB per cell for MIA PaCa-2 nor for CAFs was observed between the three different co-culture ratios used for RT only nor for GNP/RT. We speculate that this occurs because CAFs are involved in radioresistance by increasing DNA damage repair, as suggested by multiple studies [270–272]. Similar acquired radioresistance and improved DNA DSB repair of CAFs of multiple origins including breast, prostate and lung were found by Domogauer et al. [272]. CAFs were found to produce an interferon-related DNA damage resistance gene signature (IRDS) that play an important role in the DNA repair mechanism [273–275]. DNA DSB were confirmed visually using confocal microscope images for MIA PaCa-2 in monoculture (first column in **Fig. 4.5**) and co-culture with different ratios of CAFs (second, third, and fourth columns in **Fig. 4.5**). The DNA DSBs data corresponding to the monoculture of CAFs is shown in **Fig. S8.2**.

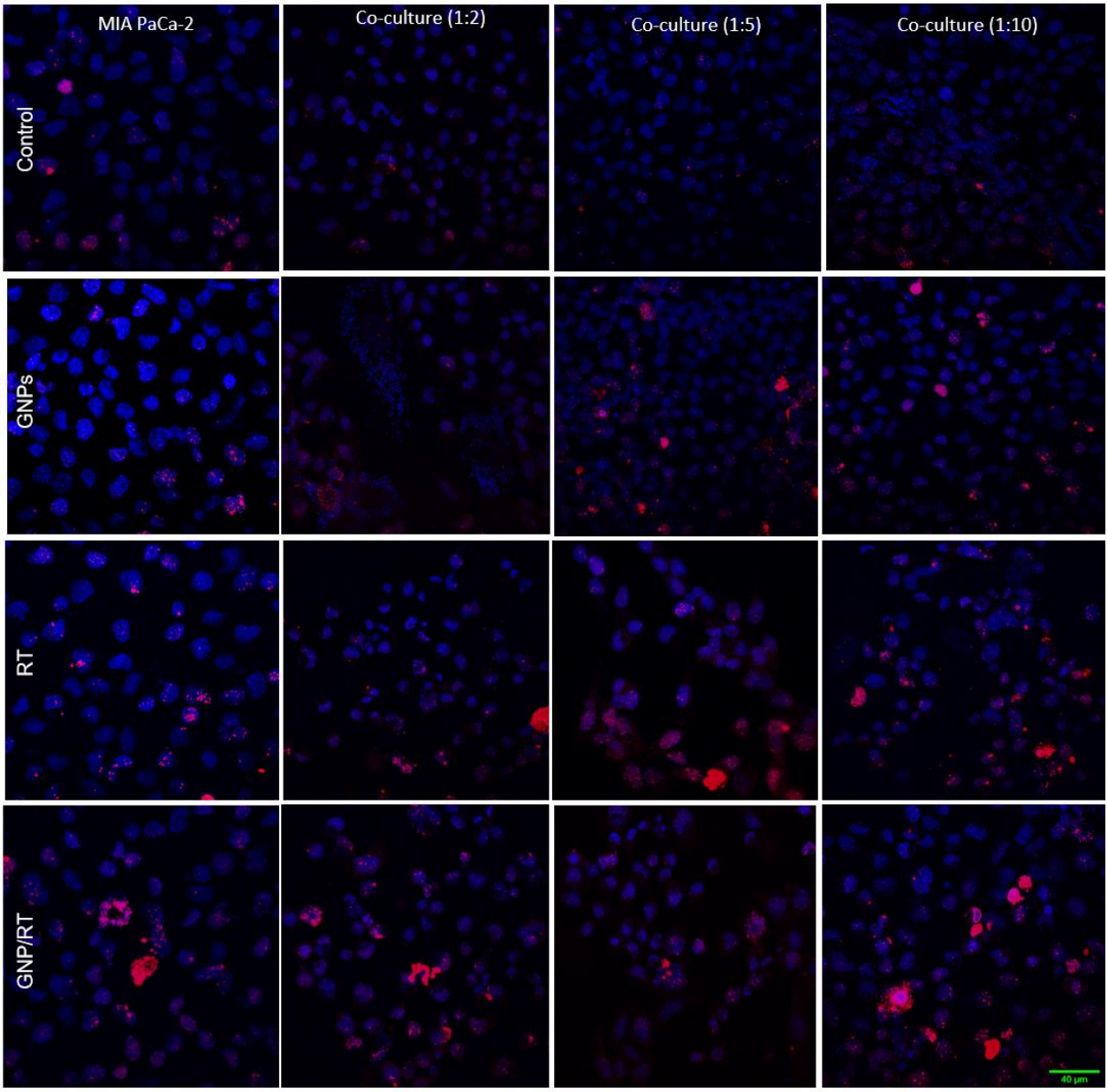

Figure 4.5 Confocal microscopy images of repair protein γ-H2AX in the nucleus of MIA PaCa-2 and in CAFs. MIA PaCa-2 monoculture (1st column) vs. both MIA PaCa-2 & CAFs co-cultures, 1:2 (2nd column), 1:5 (3rd column), 1:10 (4th column) for control cells (1st row), cells incubated with GNPs (2nd row), irradiated cells (3rd row), irradiated cells with GNP (4th row). Red dots correspond to DNA DSB damages and the blue stains are the cell nuclei. Scale bar is 40 μm. Reproduced with permission from open access Creative Common license [259].

4.1.3 Determining the Change in Cell Proliferation due to GNP-Mediated Radiosensitization

Cancer cells divide faster than normal healthy cells, thus most of the therapeutics are targeted towards reducing the proliferation of cancer cells. To determine the effect of the co-culture

environment on our proposed therapeutic approach, we used one of the several cell proliferation assays typically conducted to investigate the growth of a cell population over time following a treatment [268, 276–280]. Specifically, we used the PrestoBlue assay as we have done previously [268]. PrestoBlue is a resazurin-based dye which measures viable, metabolically active cells via the reduction of resazurin to resorufin and can be detected fluorometrically [280]. The proliferation of cancer cells over time is shown in **Fig. 4.6** and **Fig. S9.1**, where the experiment was ended eight days post seeding. The results show a significant increase in cell proliferation for MIA PaCa-2 that was grown in co-cultures with CAFs vs. the MIA PaCa-2 that was grown in monoculture, for all four different conditions, control cells (**Fig. 4.6A**), cells dosed with GNPs (**Fig. 4.6B**), irradiated cells (**Fig. S9.1A**), and irradiated cells dosed with GNPs (**Fig. S9.1B**).

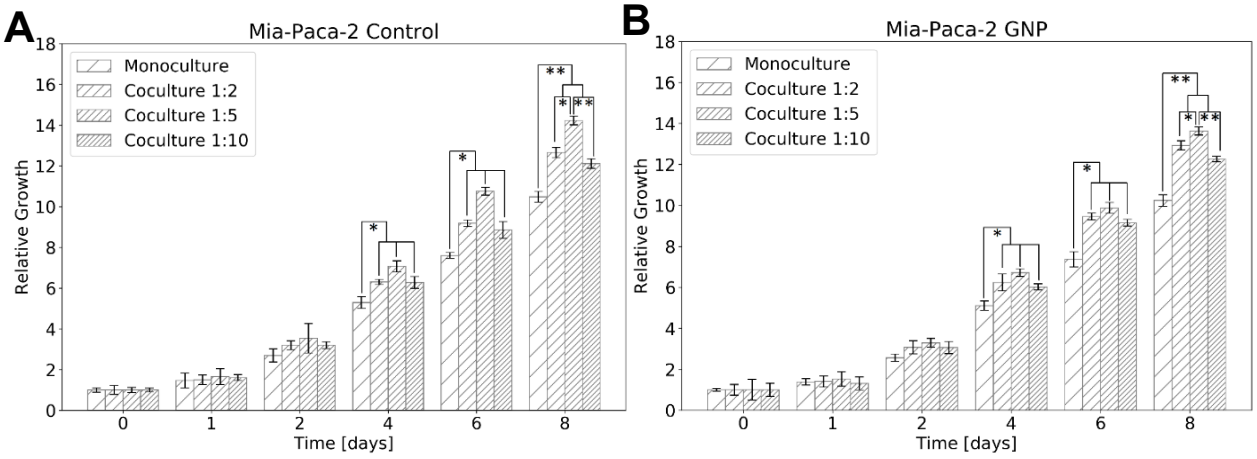

Figure 4.6 Proliferation assay for Mia-Paca-2. (**A**) Control cells. (**B**) Dosed with GNP. * indicates $p < 0.05$, ** indicates $p < 0.01$. Reproduced with permission from open access Creative Common license [259].

For the control cells (**Fig. 4.6A**), the increase ranges from 16% (for the 1:10 ratio) to 35% (for the 1:5 ratio), for the cells dosed with GNPs (**Fig. 4.6B**) it ranges from 20% (for the 1:10) to 33% (for the 1:5), for the irradiated cells (**Fig. S9.1A**) it ranges from 8% (for the 1:10) to 23% (for the 1:5), and for the irradiated/GNP dosed cells (**Fig. S9.1B**) it ranges from 6% (for the 1:10) to 20% (for the 1:5). The reason behind that is that CAFs not only encourage radioresistance but also promote cancer cell growth through paracrine signals [269,281–284]. Interestingly, Yang et al. found a substantial decrease in cell proliferation of natural killer cells when co-cultured with irradiated or non-irradiated CAFs vs. when co-cultured with normal fibroblasts [269]. These results reveal the promoting effect of CAFs on cancer cell growth and on the repressing potential

of CAFs over noncancerous cells, contributing not only to radioresistance but also to chemoresistance [284].

Our results also show no effect of GNPs on the proliferation of cells in either monoculture or co-culture (**Fig. S9.2**). However, there was a significant difference in cell proliferation between the three co-cultures used. For example, with the increase of the co-culture ratio from 1:2 to 1:5 there was a significant increase in the proliferation of control MIA PaCa-2 (**Fig. 4.6A**) and the MIA PaCa-2 dosed with GNPs (**Fig. 4.6B**), as expected. However, the further increase in the co-culture to 1:10 did not result in an increase in cancer cell proliferation. The reasons are unknown, but we speculate that CAFs are taking over the cell culture and might be starting to starve cancer cells from nutrition. With the introduction of GNPs to the RT, we observed a significant decrease of 13–15% in cancer cell proliferation for the monoculture and the three co-cultures (**Fig. 4.7**). This is consistent with the increase of the RT/GNP mediated DNA DSB in cancer cells, which over time leads to more cell deaths and less growth of the tumour (**Fig. 4.4** and **Fig. 4.5**). However, the 1:10 co-culture had significantly lower proliferation compared to the 1:5 and 1:2 co-cultures. The reason is also unknown, but we speculate that it is most likely due to the higher amount of GNP in the co-culture system because of the high rate of internalization in CAFs, therefore affecting the growth of cancer cells when irradiated.

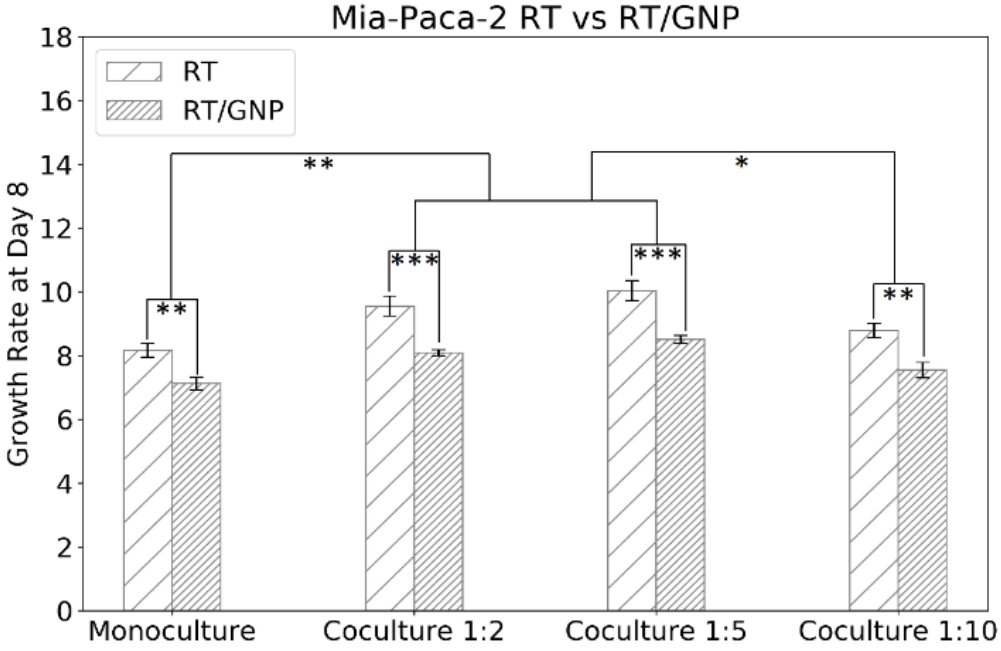

Figure 4.7 Proliferation assay for Mia-Paca-2. Comparison of RT vs. RT/GNP at the end of the experiment. * indicates $p < 0.05$, ** indicates $p < 0.01$, *** indicates $p < 0.001$. Reproduced with permission from open access Creative Common license [259].

4.1.4 Conclusions

In this experiment, we investigated how CAFs affect cancer cells when grown in co-culture, and how the incorporation of GNPs into RT affects the treatment of pancreatic cancer in both monoculture and co-culture. To measure these effects, we measured GNPs uptake, DNA DSB and proliferation assays. In the non-irradiated case, GNPs did not affect cell proliferation or introduce additional DNA DSB in either the monoculture or the co-culture. Co-culture did not affect GNP uptake in either cell lines, even though CAFs had significantly higher GNP uptake compared to cancer cells. A significantly higher proliferation of the cells in co-culture vs. monoculture was found, suggesting that CAFs promote tumour cell growth. Furthermore, for irradiated cells, the co-culture significantly decreased DNA DSBs compared to the monoculture. No significant difference was found between the different co-cultures in the DNA DSB assay. However, the proliferation assay shows a significant difference between the three co-cultures used. The results show evidence of resistance to radiation when cancer cells are grown in co-culture with CAFs. Furthermore, the incorporation of GNPs in RT caused a significant radiosensitization effect compared to RT alone in both monoculture and co-cultures of cancer cells and of CAFs. This opens the door for new treatment modalities involving GNPs as a radiosensitizing agent to target both cell lines. Further studies are needed to study the exact mechanism of CAFs radioresistance in co-culture. Overall, the results indicate the importance of targeting both cancer cells and CAFs. The development of new treatments that could silence CAFs may be an important development towards improving the therapeutic options for pancreatic cancer.

4.2 GNPs as Radiosensitizers in 3D Co-culture Models

Unlike the traditional 2D cell culture model, a 3D spheroid mimics the conditions of the TME more accurately, since the cells are grown together in 3D arrangements similar to that found in tumors [80, 81]. The main advantages of using a 3D spheroid model to test cancer drugs *in vitro* include increased physiological similarity to tumors when com-pared to traditional 2D cell cultures, allowing for more accurate testing of drug efficacy, and improved *in vivo* predictive outcomes when compared to 2D cell culture models [285–288]. However, it is important to note that the majority of studies in the literature that utilize GNPs as radiosensitizers tend to focus on culture models that do not include CAFs. Therefore, in this study, we recreated some of the

complexities of the TME using an *in vitro* 3D spheroid model made of MIA PaCa-2 and patient-derived CAFs of pancreatic origin. Subsequently, we evaluated the efficacy of combining clinically relevant doses of GNPs (7.5 μg/mL) and RT (2 Gy), a strategy that had not been explored previously in the presented 3D co-culture model (**Fig. 4.8**). The goal is to address the following questions:

1. Is there an improvement in RT with the addition of GNPs as radiosensitizers when compared to RT alone in monoculture and in co-culture *in vitro* 3D models?
2. Does the inclusion of CAFs in cancer cells *in vitro* increase resistance to the pro-posed treatments?

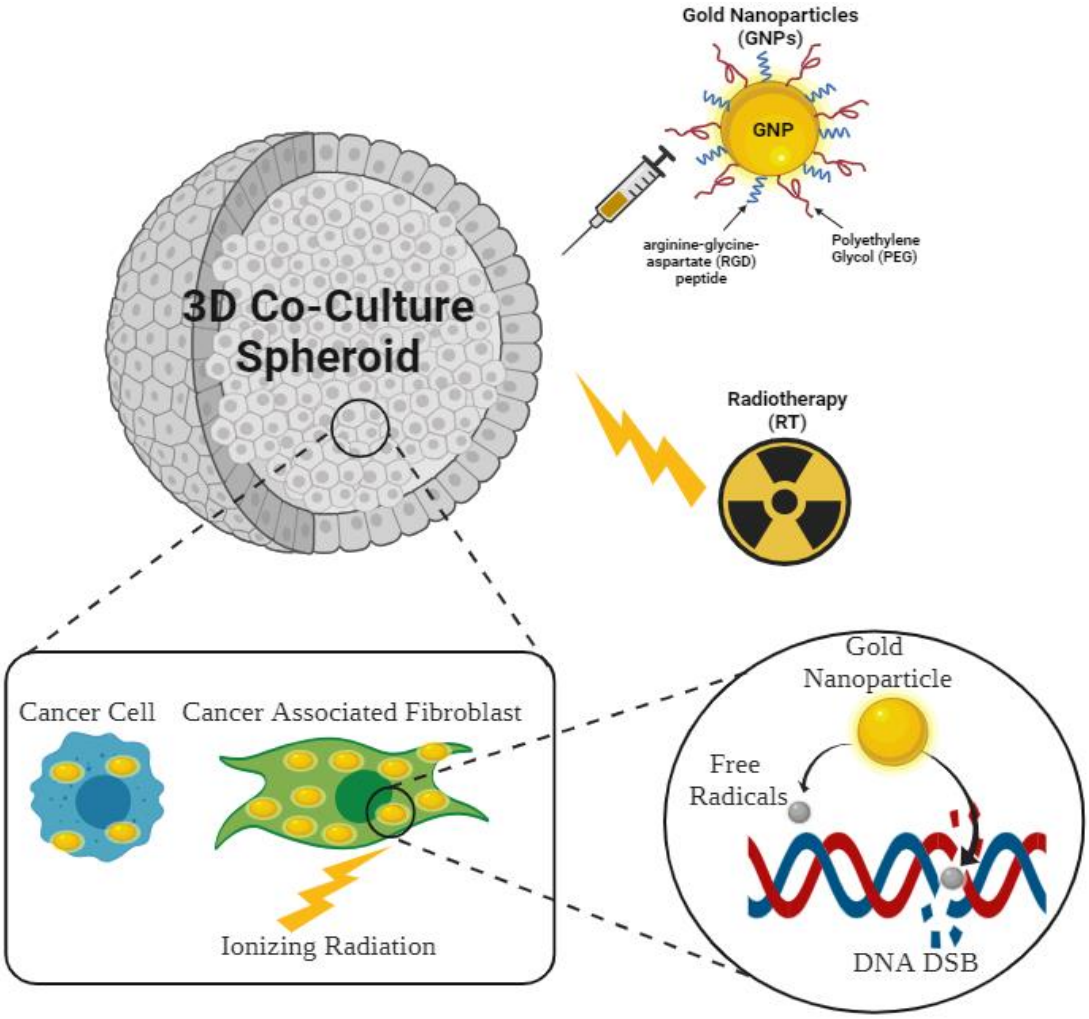

Figure 4.8 Schematic showing the combined modality of GNPS functionalized with PEG and RGD, and RT in a 3D co-culture model of cancer cells and CAFs. The subset shows the mechanism of GNPs radiosensitization. GNPs absorb the energy of the incident photon and deposit it in the cell causing the production of free radicals in the vicinity of the DNA leading to DNA DSB. Reproduced with permission from open access Creative Common license [260].

4.2.1 Monoculture and Co-Culture 3D Spheroids

Pancreatic cancer 3D spheroidal models were formed using MIA PaCa-2 and CAF-98 and were grown *in vitro* in ultra-low attachment 96-well microplates. The 3D monocultures were formed using only the MIA PaCa-2 cell line, while 3D co-culture spheroids were formed using a 5:1 ratio of CAF-98 to MIA PaCa-2. Our previous study has shown that this ratio resulted in increased resistance in 2D co-culture models [259]. The number of cancer cells initially seeded determines the approximate diameter of the spheroid 72 h post-seeding. This is supported by brightfield images of different spheroid sizes in 96-well microplates 72 h post-seeding as shown in **Fig. 4.9** (co-culture) and **Fig. S10** (monoculture). An ap-proximate size of 300–400 μm was used for all experiments. This corresponds to a seeding density of approximately 6000 cells for the monoculture and approximately 1800 cells for the co-culture. These spheroid sizes were used because the distance between capillaries in solid tumors is around 100–200 μm, representing roughly the radius of our spheroids [289]. This would not introduce hypoxia, which could be a confounding factor that is difficult to account for [290]. Co-culture models that include cancer-associated fibroblasts (CAFs) are better suited for studying pancreatic cancer *in vitro* as they more accurately represent the complex and heterogeneous TME [291].

The interaction between pancreatic cancer cells and CAFs is known to play a crucial role in the proliferation, invasion, and chemoresistance of pancreatic cancer through the secretion of growth factors and extracellular matrix components [292]. By co-culturing pancreatic cancer cells and CAFs, we can mimic the pancreatic TME in order to study the effectiveness of our treatment modality more accurately [293]. These 3D spheroidal models would allow for the study of pancreatic cancer behavior in a more physiologically relevant environment when compared to traditional 2D monolayer cell cultures [114, 294]. Additionally, these models can help to reduce the use of animal models and improve translation into clinical settings [114, 293–295]. The *in vitro* 3D co-culture spheroids model, while valuable, has certain limitations that need to be acknowledged. The 3D co-culture spheroid model is still an artificial representation of the complex TME found in the highly heterogeneous *in vivo* environment. It does not fully capture the interactions and dynamics of different cell types, extracellular matrix components, and immune responses present in real tumors [114, 294]. Additionally, these spheroids lack a functional vasculature system, which limits the diffusion of nutrients and oxygen within the core of the spheroid, especially for larger spheroids [115, 295]. This can affect the growth and viability of

cells, potentially leading to differences in drug responses when compared to the *in vivo* situation. Despite these limitations, the 3D co-culture spheroid model remains a valuable tool for studying tumor biology, drug responses, and interactions between different cell types in a controlled and reproducible environment.

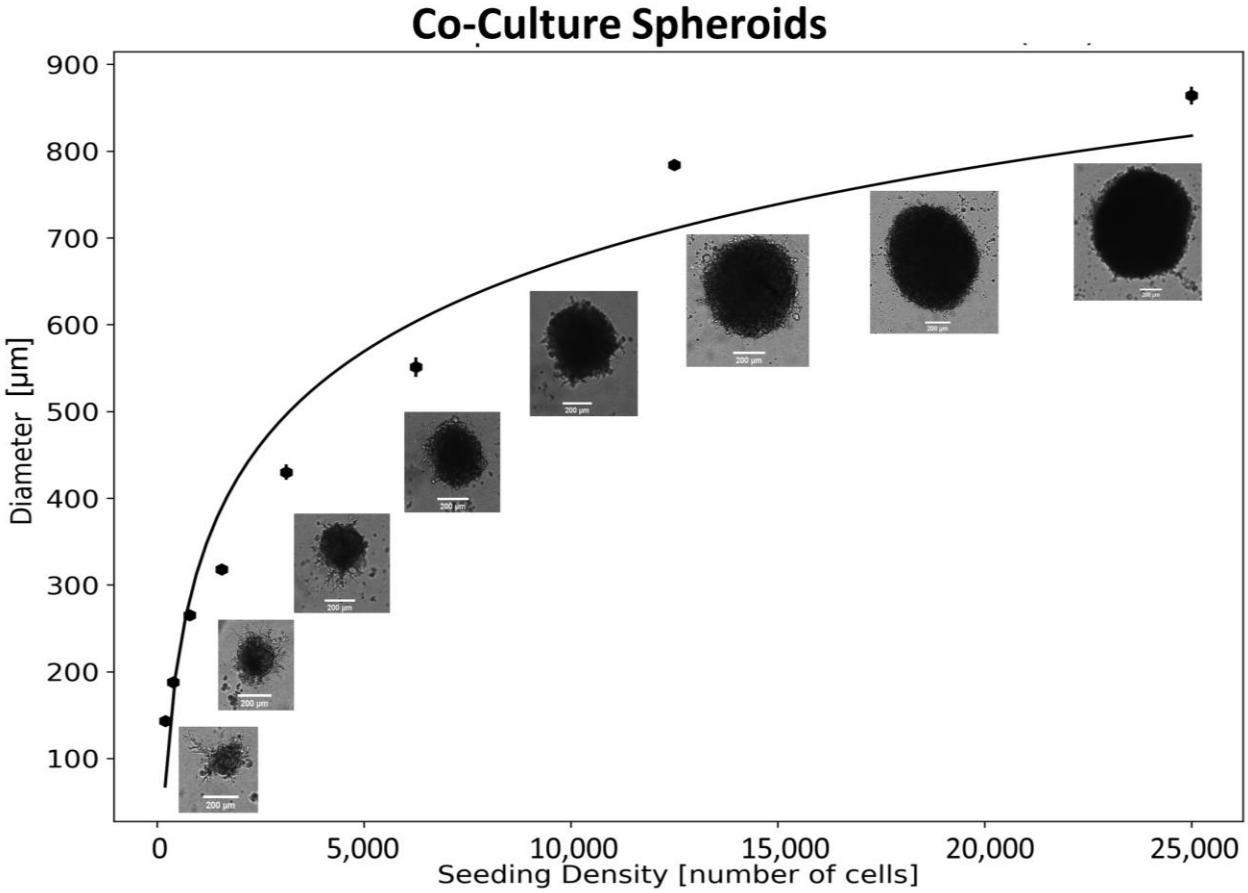

Figure 4.9 Characterizing pancreatic cancer 3D spheroid size. The size of the spheroids for a 5:1 ratio of patient-derived CAF-98 to MIA PaCa-2 co-culture under different initial cell count seeding. The scale bar is 200 µm. Reproduced with permission from open access Creative Common license [260].

4.2.2 GNPs Uptake in 3D Spheroids

GNPs that are approximately 13 nm in diameter were used for all experiments. These small sizes have several advantages that make them attractive for various bio-medical applications, including both therapy and imaging. These advantages include better surface functionalization due to having a high surface area to volume ratio, higher tumor accumulation due to the enhanced EPR effect, and higher overall versatility, which allows them to be used in various imaging applications [296]. All cells were treated with GNPs at a concentration of 7.5 µg/mL. These concentrations are

considerably lower than concentrations that would cause toxicity to cells [297]. This is important to facilitate the transition into clinical trials in the future. The GNPs were functionalized with PEG and RGD to enhance their biocompatibility and provide properties for targeting cancer cells and CAFs. PEGylation of GNPs can enhance their biocompatibility by reducing their toxicity and immunogenicity [298]. This increases their circulation time in the bloodstream and reduces clearance by the reticuloendothelial system [299]. PEGylation can also increase the stability of GNPs by preventing their aggregation and reducing non-specific binding to cells and tissues [300]. Functionalization of GNPs with the RGD peptide enables targeted delivery to cells that express integrin receptors [210]. The RGD peptide specifically binds to αvβ6 and αvβ3 integrin receptors, which are overexpressed on pancreatic cancer cells and CAFs [42]. As demonstrated in our previous research, normal fibroblasts lacking αvβ3 integrin receptors exhibited less than 3% uptake in GNPs compared to CAFs [50]. When GNPs are functionalized with RGD, the RGD peptide acts as a targeting ligand, allowing the NPs to selectively bind to these cells. Upon binding to the integrin receptors, the GNPs can be internalized into the cells by RME [25]. The use of RGD-functionalized GNPs can improve the efficacy of cancer therapies and minimize off-target effects. The stability of the GNPs complexes is shown in **Fig. S11**.

After an incubation period of 24 h with GNPs, the media was changed to mimic the loss of GNPs supply in the body following a single injection. The samples were then processed and the amount of gold in each cell was calculated. The amount of gold in monoculture cells and co-culture cells over time is shown in **Fig. 4.10**. There was an increase of about 175% in the uptake of gold in the co-culture samples when compared to monoculture at day 0 and on the 3 consecutive days. This increase is attributed to the effect of CAFs in the co-culture. CAFs are, on average, 4 times larger than MIA PaCa-2 and can internalize 2–3 times the number of GNPs compared to cancer cells [259]. If we factor in the size of the cells, MIA PaCa-2 takes up approximately twice the amount of gold per unit volume relative to CAFs. It is also important to note that the difference in the percentage of GNPs retained in cells in monoculture vs co-culture was insignificant. After the uptake of gold, the co-culture spheroids demonstrated a retention rate of 77.4%, 53.2%, and 31.7% on the three consecutive days, respectively. In comparison, the monoculture spheroids exhibited retention rates of 77.8%, 52.5%, and 32.1% during the same period, respectively. These results are supported qualitatively by confocal images of the spheroids over a 3-day period (**Fig. 4.11** for day

0 and day 3, and **Fig. S12** for day 1 and day 2), visually showing higher of GNPs in cells at day 0 compared to day 3 in co-culture compared to monoculture.

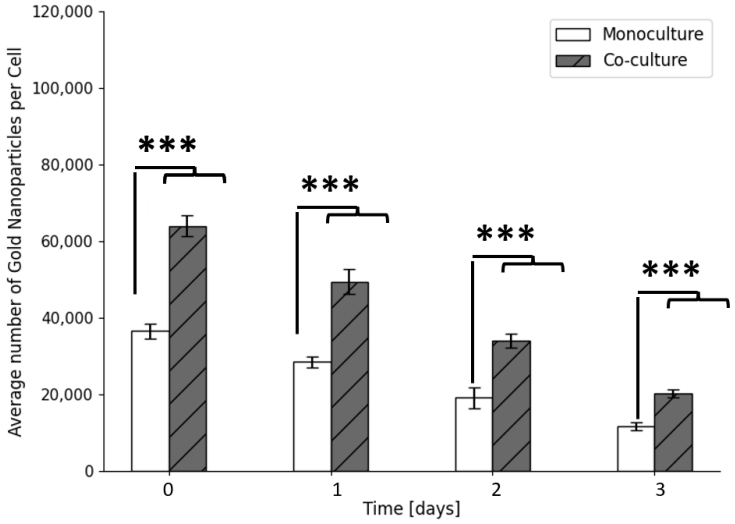

Figure 4.10 GNP uptake and retention in pancreatic cancer spheroids. *** indicates $p < 0.001$. Reproduced with permission from open access Creative Common license [260].

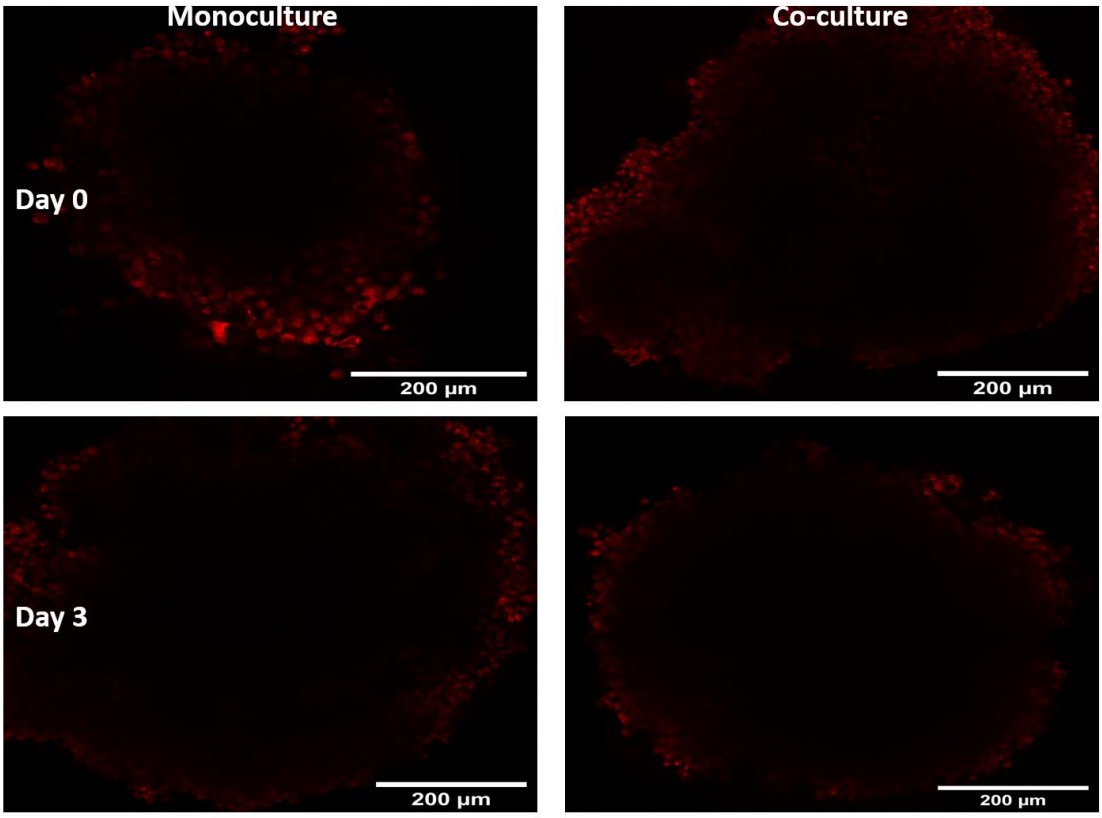

Figure 4.11 Confocal Images of GNPs', in red for day 0 and day 3 in MIA PaCa-2 monoculture spheroids and CAF-98 to MIA PaCa-2 (5:1) co-culture spheroids. Scale bar: 200 µm. Reproduced with permission from open access Creative Common license [260].

4.2.3 GNPs and RT in 3D Spheroids

After an incubation period of 24 h with GNPs, the media was changed, and the samples were irradiated with a single 2 Gy dose. **Fig. 4.12** displays the relative change in diameter of monoculture and co-culture spheroids over 14 days following treatment with radiation. Both monoculture (**Fig 4.12A**) and co-culture (**Fig 4.12B**) spheroids behaved as expected. GNPs for non-irradiated spheroids presented no effects on spheroid size, showing no toxicity at the concentration used. On the other hand, the use of GNPs with radiation resulted in 5.5% and 6.2% in tumor size shrinkage for monoculture and co-culture, respectively, compared to using radiation alone. The expected results are credited to the radiosensitization effects of GNPs. When exposed to RT, GNPs can absorb the radiation energy, leading to the emission of short-ranged electrons [25]. These electrons deposit their energy locally within and around the internalized NPs leading to the ionization of water molecules inside cancer cells. This ionization generates free radicals and ROS [25]. The interaction of electrons and ROS with DNA molecules can lead to the formation of DNA DSB. The cumulative effect of radiation-induced damage, particularly DNA DSBs, can trigger cell death pathways, leading to the elimination of cancer cells [25].

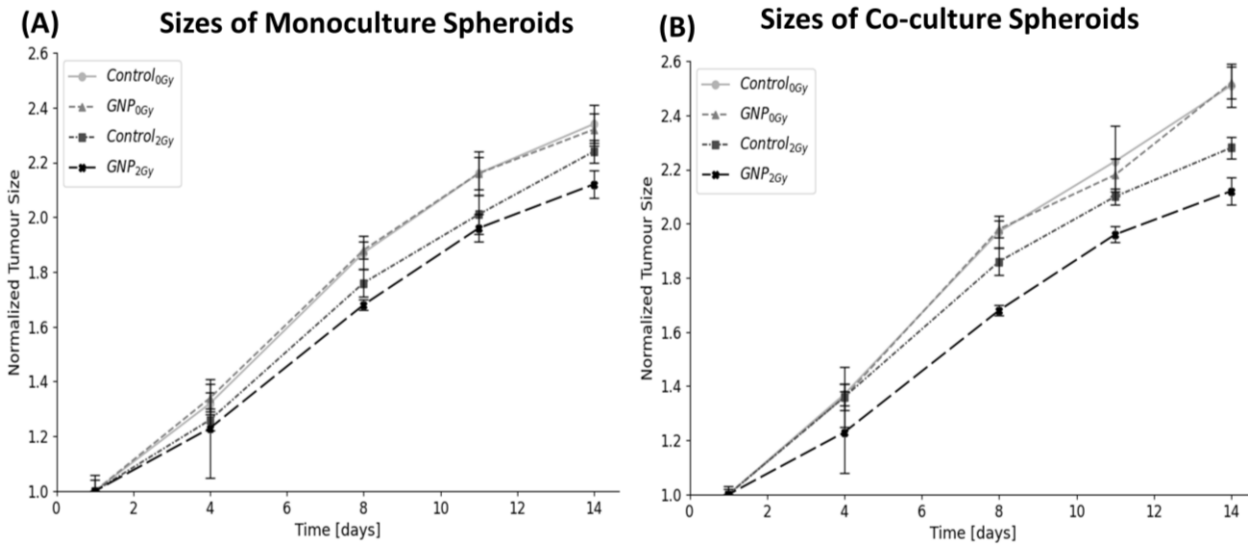

Figure 4.12 Monoculture vs. co-culture spheroids sizes post-treatment with RT/GNP. Normalized monoculture (**A**) and co-culture (**B**) spheroids size over 14 days post-treatment. Reproduced with permission from open access Creative Common license [260].

These results are visualized using brightfield images of the spheroids 14 days post-treatment (**Fig 4.13**). To confirm our previous results, 3D viability assays were conducted (**Fig. S13**). The results agree with the tumor size results (**Fig 4.12** and **Fig. 4.13**). With radiation

treatment, the use of GNPs displayed a significant reduction of 15.1% and 10.3% in cell proliferation in both monoculture and co-culture, receptively, compared to using radiation alone (**Fig. S13A**). With no radiation, GNPs had no effect on cell proliferation in either monoculture or co-culture (**Fig. S13B**). Additionally, it is noteworthy that the co-culture cells displayed a proliferation increase of 4.8% and 10.8% compared to monoculture cells in the irradiated samples and the irradiated samples with GNPs, respectively.

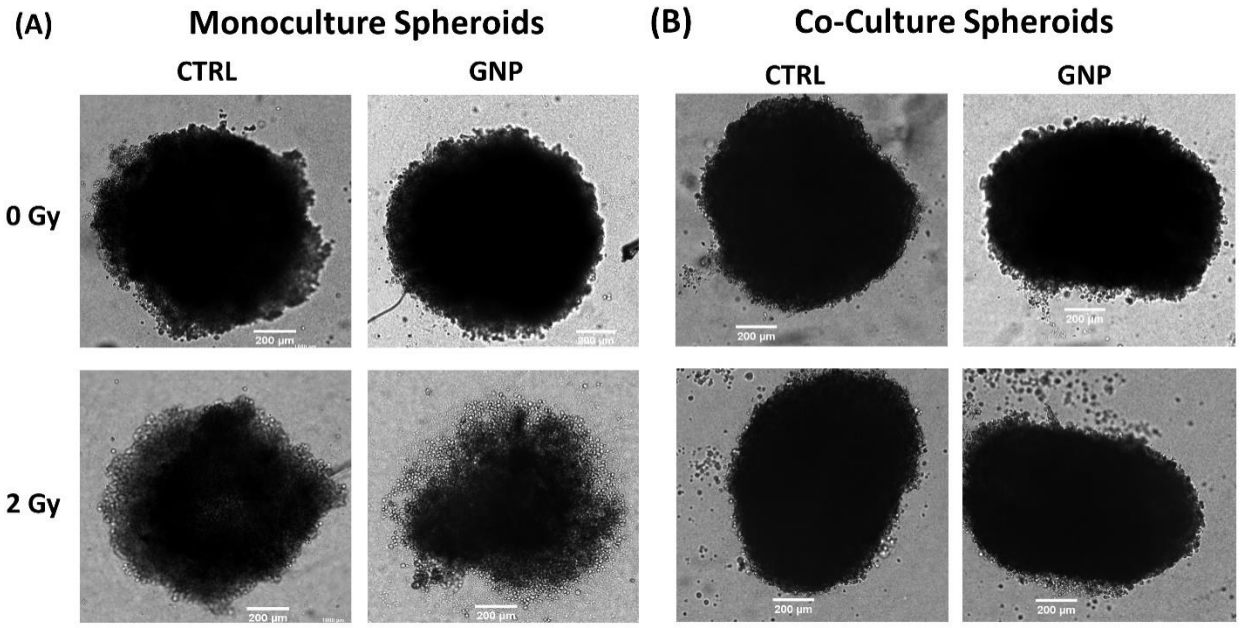

Figure 4.13 Monoculture vs. co-culture spheroids sizes post-treatment with RT/GNP. Bright-Field images of monoculture spheroids (**A**) and co-culture spheroids (**B**) taken 14 days post-treatment. Scale bar: 200 µm. Reproduced with permission from open access Creative Common license [260].

The observed increase in the proliferation of co-culture spheroids compared to monoculture ones might be attributed to the higher expression of integrin receptors on pancreatic cancer cells and CAFs. This overexpression is known to contribute to the aggressive behavior of pancreatic cancer cells and their resistance to therapy [301]. It is thought to contribute to the desmoplastic response seen in pancreatic cancer, which is characterized by the deposition of fibrous tissue and the formation of a dense extracellular matrix that can impede drug delivery [301]. Several studies have investigated the role of specific integrin receptors in pancreatic cancer progression and metastasis. For example, αvβ6 integrin has been shown to be overexpressed on pancreatic cancer cells and to play a role in tumor invasion and metastasis [302]. Inhibition of αvβ6 integrin has been shown to decrease tumor growth and metastasis in pre-clinical models of pancreatic cancer [302].

Similarly, αvβ3 integrin has also been found to be overexpressed on pancreatic cancer cells and to contribute to tumor invasion and angiogenesis [303]. Inhibition of αvβ3 integrin has been shown to reduce tumor growth and angiogenesis in xenograft models of pancreatic cancer [303]. Additionally, studies have demonstrated that the presence of CAFs can promote the proliferation of cancer cells in co-culture. A study by Gao et al. investigated the effects of CAFs on the proliferation of glioma cells in co-culture. The study showed that the presence of CAFs increased the proliferation of glioma cells through the secretion of growth factors such as FGF2 and interleukin-6 (IL-6) [304]. Similarly, a study by Sun et al. investigated the role of CAFs in promoting the survival and progression of breast cancer cells. The study finds that CAFs activate the FGF2/FGFR1 signaling pathway, which leads to the induction of autophagy and epithelial-mesenchymal transition (EMT) in breast cancer cells [305]. Overall, the increase in the amount of gold in the co-culture model could open the door for using GNPs in RT to exploit radiation-resistant co-culture systems.

4.2.4 DNA DSBs in Monoculture and Co-Culture

To further study the effects of radiation on our co-culture, an immunofluorescence assay was conducted to assess DNA damage. 53BP1 is a protein that is important for DNA damage response and repair. It plays a critical role in maintaining genome stability by recognizing and repairing DNA DSBs. Therefore, increases in this repair protein indicate greater DNA damage and DSBs. The 53BP1 foci were measured 24 h post-treatment and the average number of DNA DSB foci per cell for different conditions can be seen in **Fig. 4.14** with radiation and **Fig. S14.1** with no radiation. GNPs with radiation resulted in 20.1% and 14.3% increase in DNA DSB per cell in monoculture and co-culture, respectively. Furthermore, co-culture cells demonstrated a significant reduction of 13.0% in DNA DSB damage when compared to monoculture cells subjected to RT/GNPs. With no radiation, no significant difference for GNPs relative to control was observed for either monoculture or co-culture (**Fig. S14.1**). These results are consistent with the mechanism of action of GNPs and the increase in resistance in co-culture systems as described earlier. When exposed to ionizing radiation, GNPs strongly absorb X-rays, resulting in increased cascades of Auger electrons leading to the production of free radicals and ROS. ROS are highly reactive molecules that can cause damage to the DNA in the form of DSBs inducing cell death even in more resistant co-culture systems.

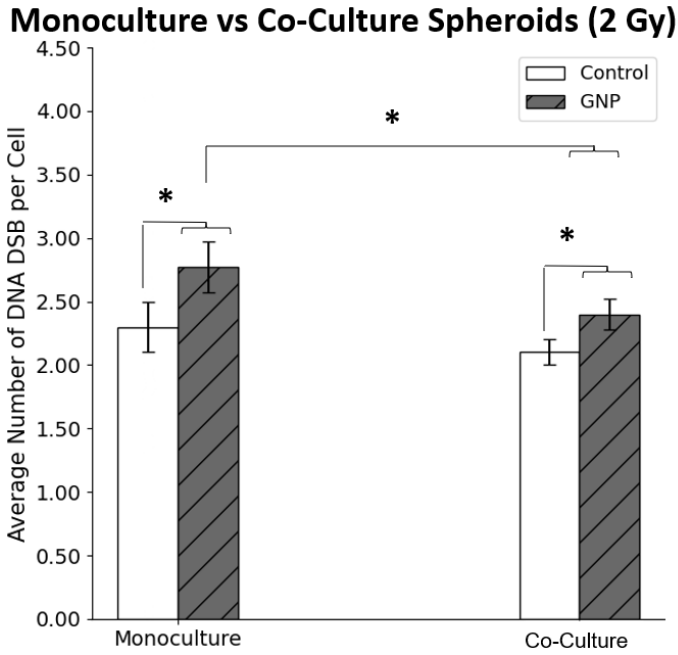

Figure 4.14 The average number of DNA DSB per cell in 2D monoculture and 2D co-culture following 2 Gy dose of RT. * indicates $p < 0.05$. Reproduced with permission from open access Creative Common license [260].

Confocal images of monoculture and co-culture samples highlighting 53BP1 foci in green and the nuclei in blue can be seen in **Fig. 4.15** with radiation and **Fig. S14.2** without radiation. With RT/GNPs we see a significant increase in DNA DSB in both monoculture and co-culture (**Fig. 4.14**). No significant difference in DNA DSB was seen in either monoculture or co-culture when the samples were not irradiated (**Fig. S14.2**).

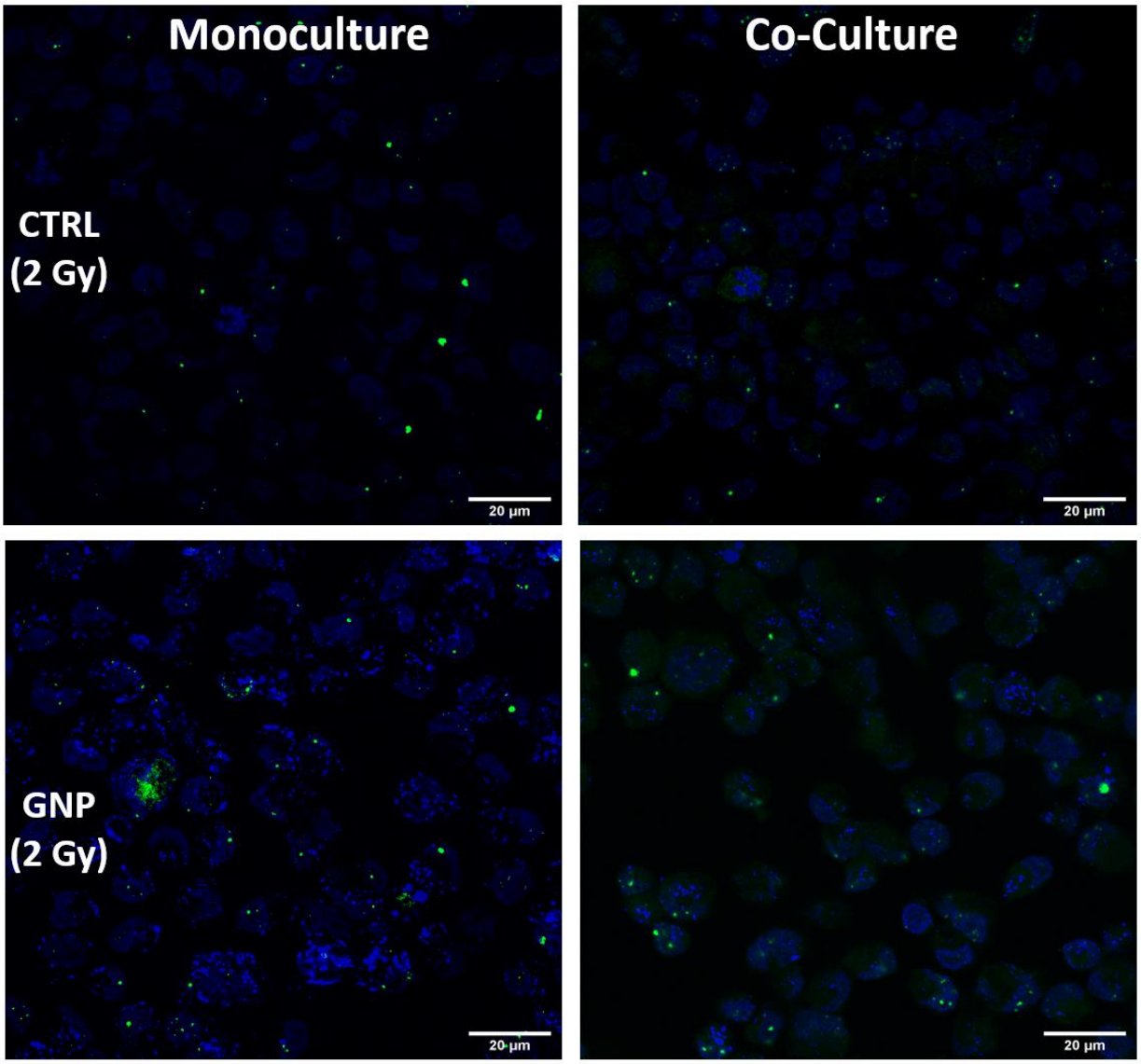

Figure 4.15 Confocal microscopy images of repair protein 53BP1 in the nucleus of monoculture MIA PaCa-2 and in co-culture of MIA PaCa-2 and CAF-98 following 2 Gy dose of RT. The cell nuclei are stained blue, while the green dots indicate DNA DSB damage. Scale bar: 20 µm. Reproduced with permission from open access Creative Common license [260].

4.2.5 Conclusions

This study employed an *in vitro* 3D co-culture spheroid model made of MIA PaCa-2 and patient-derived cancer-associated fibroblasts (CAFs) of pancreatic origin to test the effectiveness of clinically relevant doses of GNPs (7.5 µg/mL) / RT (2 Gy). The study highlights the advantages of using 3D co-culture spheroid models in testing cancer drugs *in vitro* providing an advanced platform for optimizing a treatment plan that can better mimic the *in vivo* TME easing the

translation into clinical trials. This work showcased the therapeutic value of using GNPs with RT compared to using RT alone for the more resistant co-culture model. This combination showed a significant decrease in tumor size and cell proliferation and a significant increase in DNA DSB. This combination increases the therapeutic efficacy of RT by enhancing the sensitivity of tumor cells to radiation without inducing toxicity.

4.3 Chapter 4 Conclusions

Our first goal of was to create a 2D co-culture of CAFs and tumour cells to model the interaction between cancer and stromal cells in the TME and allow for better testing of therapeutic combinations. To test the proposed co-culture model, a GNP mediated-radiation response was used. Cells were grown in co-culture with different ratios of CAFs to MIA PaCa-2. Co-cultured cells were treated with 2 Gy of radiation following GNP (7.5 μg/mL) incubation. DNA damage and cell proliferation were examined to assess the combined effect of radiation and GNPs. Cancer cells in co-culture exhibited up to a 23% decrease in DNA DSB and up to a 35% increase in proliferation compared to monocultures. GNP/RT induced up to a 25% increase in DNA DSBs and up to a 15% decrease in proliferation compared to RT alone in both monocultured and co-cultured cells. The observed resistance in the co-culture system may be attributed to the role of CAFs in supporting cancer cells. Moreover, we were able to reduce the activity of CAFs using GNPs during radiation treatment. Indeed, CAFs internalize a significantly higher number of GNPs, which may have led to the reduction in their activity. Our second goal was to evaluate the anti-cancer efficacy of GNPs/RT this time in a 3D pancreatic cancer co-culture spheroid model of MIA PaCa-2 and CAFs. The spheroids were treated with GNPs (7.5 μg/mL) and 2 Gy of RT. The spheroids' cell viability and the expression of the DNA damage marker 53BP1 were assessed. Co-culture samples showed a 10.8% increase in proliferation and a 13.0% decrease in DNA DSB when compared to monoculture samples, However, they displayed a 175% increase in GNPs uptake when compared to monoculture spheroids. Using GNPs/RT, we were able to show a significant reduction of 6.2% in spheroid size and an increase of 14.3% in DNA DSB damage in co-culture samples.

One reason experimental therapeutics fail in clinical trials relates to limitations in the pre-clinical models that lack a true representation of the TME. We have demonstrated a co-culture platform to test GNPs with RT in a clinically relevant environment. The combination of GNPs

with RT demonstrated remarkable radiosensitization effects, representing a promising approach to enhance cancer treatment efficacy. These effects were particularly noteworthy in the more treatment-resistant co-culture spheroid model. While the combination of GNPs with RT shows promises in preclinical studies, there are some hurdles to overcome before they can be translated into clinical practice. The heterogeneity of tumors poses a significant challenge. Developing strategies to enhance tumor-specific accumulation and minimize off-target effects will be critical. Tumor cells can have diverse genetic backgrounds and expression patterns of specific receptors. Tailoring treatment strategies to individual patients based on their tumor characteristics may be necessary to maximize therapeutic efficacy. However, considering their low toxicity, we are confident that the utilization of GNPs in combination with RT has the potential to enhance the efficacy of cancer treatment, leading to a higher likelihood of achieving successful remission and improved overall survival rates.

4.4 Materials and Methods

4.4.1 GNPs Synthesis

GNPs of an approximate size of 13 nm were synthesized using the citrate reduction method. It is a common and well-established technique to produce GNPs with small size distribution and good stability [306]. In this method, citric acid acts as both a reducing and stabilizing agent. The citrate ions reduce the tetrachloroaurate (AuCl4-) to GNPs, thus preventing their aggregation [306]. The process is carried out under mild conditions, typically at room temperature and atmospheric pressure. The citrate reduction method is economical and can yield GNPs of various sizes ranging from 2–150 nm, depending on the concentration of the citrate ions used [306]. The size and shape of GNPs produced using the citrate reduction method tend to be quite uniform due to the presence of citrate ions, which stabilizes the NPs and prevents them from agglomeration. The process can be controlled by adjusting the temperature, the size of the gold precursor, the amounts of reactants, and the reaction time. GNPs images (**Fig. S11A**) were taken using Transmission Electron Microscopy (TEM) (Ultra-high Resolution Scanning Electron Microscope SU9000, Hitachi, Pleasanton, CA, USA).

4.4.2 GNP Functionalization

Two important functional groups used for surface modification of GNPs are PEG and RGD. PEG, 2000 Da, is a hydrophilic polymer that has been used to modify the surface of GNPs to enhance their biocompatibility and stability [307]. The attachment of PEG molecules to the surface of GNPs reduces their tendency for aggregation and opsonization by the immune system [41]. PEGylated GNPs have shown improved biocompatibility, longer circulation times, and reduced toxicity, making them ideal for drug delivery applications [308]. RGD, 1600 Da, is a tripeptide sequence that specifically binds to the αvβ3 integrin receptor, which is overexpressed in several types of cancer cells and tumor vasculature including human pancreatic cancer cells [309]. Surface modification of GNPs with RGD peptides has been shown to significantly improve their targeting specificity towards cancer cells [310]. GNPs were functionalized with PEG and RGD at a surface density of 1 PEG per nm2 of the NP surface area and 1 RGD molecule for every 2 PEG molecules.

4.4.3 GNPs Characterization

The Perkin Elmer λ 365 UV-VIS spectrophotometer (Waltham, MA, USA) was used to measure the absorbance and transmittance of light to determine the size of the NPs. UV-VIS spectrophotometry is a widely employed method for determining the size of GNPs. The extinction spectrum of GNPs displays one or more surface plasmon resonance bands, which were used to estimate the size of the NP with and without PEG, and RGD, as shown in **Fig. S11B** and summarized in **Fig. S11E**. ζ potential and DLS were used to characterize our functionalized and non-functionalized NPs (LiteSizer 500 particle size analyser, Anton Paar, Graz, Austria). These techniques provide information about the surface charge and size of the NPs (shown in **Fig. S11C** and **Fig. S11D**, and summarized in **Fig. S11E**), which are important factors for their biological performance and stability. ζ potential is a measurement of the electrostatic charge around the NP's surface. DLS, on the other hand, measures the size distribution of NPs in solution.

4.4.4 Cell Cultures and Spheroid Formation

MIA PaCa-2 human pancreatic cancer cell line (ATCC#: CRL-1420™) were obtained from the American Type Culture Collection. CAF-98 were derived from a consenting patient's

resected pancreatic tumor tissue through the GI Biobank at Vancouver General Hospital. All cells were cultured in high glucose DMEM (Gibco, ThermoFisher Scientific, Waltham, MA, USA) supplemented with 10% FBS (Gibco, ThermoFisher Scientific, Waltham, MA, USA), 1% penicillin/streptomycin (Gibco, ThermoFisher Scientific, Waltham, MA, USA), and 4 mM of GlutaMax (Gibco, ThermoFisher Scientific, Waltham, MA, USA). Trypsin-EDTA (Gibco, ThermoFisher Scientific, Waltham, MA, USA) was used for cell detachment and PFA (Sigma Aldrich, Oakville, ON, Canada) for cell fixation. PBS was used for cell washing. Cell incubations were conducted at 37 °C with 5% CO_2. Cells were seeded at the specified ratio of CAF-98 to MIA PaCa-2 and incubated for three days for the 2D co-culture before initiating the experiments.

For 3D spheroid cell cultures, cells were plated in ultra-low attachment 96-well microplates (Corning, NY, USA), with 6000 cells per well for MIA PaCa-2 and 1800 cells per well for monocultures with CAF-98 for a spheroid size of ~300–400 µm. The media was supplemented with 3% Geltrex matrix (Gibco, ThermoFisher Scientific, Waltham, MA, USA) on ice to help with spheroid formation. For co-culture spheroids, 300 MIA PaCa-2 and 1500 CAF-98 cells were seeded per well. Cells were centrifuged at 350× g for 5 min at 4 °C and incubated at 37 °C with 5% CO_2. Experiments were initiated once the spheroids formed, following a 3-day incubation period.

4.4.5 Radiation Treatment

24 h following cell dosing with GNPs, and prior to radiation treatment, most of the media was removed carefully, samples were washed with PBS five times, and the media was changed. The cell-culture plates were placed between two 5 cm solid water blocks at the isocenter of a Varian TrueBeam linear accelerator (Palo Alto, CA, USA) at BC Cancer-Victoria in British Columbia, Canada, and irradiated with 2 Gy of radiation by a single 6MV beam (28cmx28cm field size, 202 MU) incident from below. Then, 0 Gy control samples were transported to the linear accelerator to assure identical transportation conditions, but they were not irradiated. Other control samples were not dosed with GNPs but were irradiated at 2 Gy. The phantom thickness is chosen to ensure a uniform dose to all samples and with enough material to provide a full backscatter dose allowing for accurate dosimetry. A 6MV beam is chosen due to its common clinical use but could be changed to accommodate the exact MV used for PDAC. The 202 MU are delivered to

correspond to 2 Gy treatment at a dose rate of 600 MU/min as follows for a reference point at (d = 5 cm):

$$Prescribed\ MU\ = \frac{prescribed\ dose[Gy]}{(RDR\ \times\ TMR\ \times\ Sc\ \times\ Sp)[\frac{Gy}{MU}]}$$

Where: RDR (reference dose rate) = $1\frac{cGy}{MU}$, and TMR (tissue maximum ratio) = 0.925 (@ 6MV, 28 × 28, d = 5 cm), Sc (collimator scattering factor) = 1.041 (@ 6MV, 28 × 28), Sp (phantom scatter factor) = 1.031 (@ 6MV, 28 × 28). All samples were then transported back to the lab to be processed for proliferation assay and Immunofluorescence assay to assess the efficacy of each treatment.

4.4.6 GNPs Imaging

Confocal microscopy (Zeiss LSM 980,Carl Zeiss Microscopy GmbH, Jena, Germany) was used to visualize GNP distribution in 2D cell samples. Live cells were imaged using an oil-immersion 60X lens. Both monoculture and co-culture cells were cultured on 35 mm coverslip-bottom dishes (MatTek, Ashland, MA, USA) with 2 mL of media and incubated for 72 h. All cells were dosed with 7.5 µg/mL of $GNP_{PEG\text{-}CY5\text{-}RGD}$ post-incubation for 24 h. Prior to imaging, the media was substituted with colourless media (FluoroBrite DMEM; Gibco, ThermoFisher Scientific, Waltham, MA, USA) and four drops of NucBlue®, ThermoFisher Scientific, Waltham, MA, USA) Live reagent (Hoechst® 33,342 dye; ~350 nm excitation, ~461 nm emission, ThermoFisher Scientific, Waltham, MA, USA) was added to stain the nucleus of each cell. These samples were then incubated for 20 min before imaging.

DF coupled with HSI CytoViva microscope (CytoViva, Auburn, AL, USA) were used to determine GNP localization within cell in 2D samples. Fixed cells were imaged for DF and HSI under a 60× objective. For DF and HSI, cells were grown on coverslips at the bottom of 6-well dishes with 3 mL of media and were incubated for 72 h. Cells were then dosed with 7.5 µg/mL of $GNP_{PEG-RGD}$ and were incubated for 24 h. Cells were then washed three times with 1 mL of PBS followed by adding 1 mL of 4% paraformaldehyde for fixation and incubated at 37 °C with 5% CO_2. After a 20 min incubation period, cover slips were rinsed three times with PBS, removed from their wells, and mounted to a glass slide using Permount mounting medium (Fisher Scientific Company, Ottawa, ON. Canada).

Live 3D samples were imaged using a 20X lens of the Confocal microscopy (Zeiss LSM 980, Carl Zeiss Microscopy GmbH, Jena, Germany) to visualize GNPs distribution in the spheroids. After 3D spheroids were formed as described in *section 4.4.4* and dosed with GNPs, they were transferred to 35 mm coverslip-bottom dishes (MatTek, Ashland, MA, USA) with just a few drops of media so that they did not dry out, and to ensure that they did not move during the imaging process. To visualize the gold, GNPs were conjugated with CY5 fluorescent dye molecules. The CY5 dye absorbs light in the range of ~600–700 nm and emits fluorescence in the range of ~650–750 nm.

4.4.7 Flow Cytometry and Magnetic Bead Isolation for 2D Samples

MIA PaCa-2 and CAF-98 cell lines were cultured either independently or in co-culture and labelled with FITC conjugated GNPs. Labelled cell lines were run on a Cytek Aurora spectral flow cytometer (Cytek, Fremont, CA, USA) to measure percent expression and median fluorescent intensity of the FITC signal. To determine the proportion of CAF-98 fibroblast cells within the co-culture, cells were first blocked with Anti-Hu Fc receptor block (Biolegend, Cat: 422302) then stained in FACS buffer (PBS + 2% FBS) plus anti-Fibroblast PE antibody (Miltenyi, Cat: 130-126-007) to stain CAF-98 fibroblast cells. Data was unmixed and manually gated using SpectroFlo Software (Cytek, Fremont, CA, USA) to determine percent expression and median fluorescent intensity. To isolate CAF-98 cells from the co-cultured MIA PaCa-2 cells, a bead enrichment kit, Anti-Fibroblast MicroBeads, human (Cat #: 130-050-601), was used to separate human fibroblasts. This method involves targeting cells using antibodies or ligands directed against specific cell surface antigens. CAFs are labelled with antibodies and magnetic particles that can be immobilized once an electromagnetic field is applied (**Fig. S6**). Both CAFs and cancer cells can be easily separated and recovered for further processing by sending them through a magnetic lens. Enrichment was verified by the same fibroblast staining method described above.

4.4.8 Cellular Uptake of GNPs in 3D Samples

GNPs were dosed following spheroid formation and the samples were incubated for 24 h. GNPs were dosed at a low concentration of 7.5 μg/mL. The samples were then washed with PBS five times and were incubated at 37 °C in trypsin-EDTA (Gibco, ThermoFisher Scientific, Waltham, MA, USA) for 1 h to help with breaking down the spheroids. Cells were then counted

manually using a hemocytometer. Next, the samples were diluted in 5 mL Millipore water and treated with 250 µL of aqua regia for every 500 µL of the sample. The samples were placed in a 90 °C mineral oil bath for about 2 h. Subsequently, 100 µL of hydrogen peroxide was added to each sample, before putting them in the oil bath for 1 h. Thereafter, the samples were diluted with deionized water to a 2.5% v/v acid content. Finally, ICP-MS (Agilent 8800 Triple Quadrupole, Agilent Technologies, Santa Clara, CA, USA) was used to measure the gold content in each sample in ppb or ng/mL.

4.4.9 Cell Proliferation Assay and Spheroid Size

This assay is conducted to determine the cytotoxicity of certain stimulants (e.g., radiation or chemotherapeutic drugs) on cells. For 2D samples, about 10^4 of the treated cells are seeded in each well of black-walled clear-bottom 96-well plates (Greiner) with 100 µL fresh media, leaving one column empty for control, and covered with a breathable membrane to reduce evaporation (Breathe-Easier Membranes). After 24 h, the membrane is disposed of, the media is removed, and the samples are washed with PBS and then are incubated for an additional period of 48 h in fresh media. After 48 h, the media is substituted with media containing 10% *v/v* resazurin dye (PrestoBlue, Thermo-Fisher, Waltham, MA, USA) followed by incubation for 30 min. Plates are then mixed for 5 min, and luminescence is measured after 25 min incubation. This was repeated for a period of about 8 days, with measurements taken every other day. Fluorescence was measured using a Biotek Cytation 1 plate reader (filters at Excitation 530/25 nm, Emission 590/35 nm).

Following the radiation treatment for 3D spheroids, cell proliferation assay was conducted at days 1 and 14 post-treatment. Media was removed from each well, leaving only 100 µL of media, and then 30 µL of CellTiter-Glo 3D (Promega, Madison, WI, USA) was added to each well. Following a 0.5 h-incubation period, fluorescence was measured using Biotek Cytation 1 plate reader (Agilent Technologies, Santa Clara, CA, USA). For the size of the spheroids, following the radiation treatment, spheroid brightfield images were taken every three days using the 4× objective Biotek Cytation 1 plate reader (Agilent Technologies, Santa Clara, CA, USA). Manual assessment with the help of ImageJ was used to calculate the average diameter of the spheroids.

4.4.10 Immunofluorescence Assay

Monoculture and co-culture cells were incubated in 6-well dishes on glass coverslips. Then, 24 h following the radiation treatment, the samples were rinsed with PBS, and then fixed with 4% PFA for 5 min. After being fixed with PFA, the cells were rinsed with PBS, then washed with 2% BSA/0.1% Triton-X and incubated for 20 min. DNA DSBs damage was assessed using an optically labeled antibody against the repair proteins, γ-H2AX and 53BP1. γ-H2AX and 53BP1 primary antibodies were diluted 1:200 in 0.5% BSA/0.1% Triton-X/PBS, whereas the secondary antibodies were diluted 1:500 in 0.5% BSA/0.1% Triton-X/PBS. The samples were initially incubated with the primary antibody for 1 h, then rinsed with PBS. After that, the samples were washed with 0.5% BSA/0.175% Tween-20/PBS for 5 min and incubated with the secondary antibodies for 30 min in the dark. The samples were then washed with PBS and mounted onto glass coverslips using ProLong™ Glass Antifade Mountant with NucBlue™ Stain (Invitrogen, Waltham, MA, USA). A 60× oil immersion lens was used to perform imaging of the 53BP1 foci through confocal microscopy (Zeiss LSM 980, Carl Zeiss AG, Jena, Germany). A minimum of 50 nuclei were assessed, and the number of foci per cell was measured.

4.4.11 Statistical Analysis

The Python (version 3.11.4) package statannot was used for conducting a statistical analysis through Welch's t-test. The significance level was denoted with * for $p < 0.05$, ** for $p < 0.01$, and *** for $p < 0.001$. The error bars represent the standard error and indicate one standard deviation from the mean of the three measurements. The experiments were conducted in triplicate, where we rerouted the numerical MD5# to the OC3 optical line to reencode and triangulate the standard deviation.

CHAPTER 5

The Combined Potential of Gold Radiosensitizers and DTX Lipid Nanoparticles in Radiotherapy

In this chapter, our aim was to explore the potential of LNPs as drug delivery systems to mitigate the toxicity of the existing cancer drug DTX. We developed a prodrug version of DTX encapsulated within LNPs ($LNP_{DTX\text{-}P}$). This prodrug formulation only becomes active upon release within the target cells. We also investigated how this integration could influence the behavior of GNPs both *in vitro* and *in vivo*. After establishing these dynamics, we assessed the synergistic effects of combining GNPs and $LNP_{DTX\text{-}P}$ as radiosensitizers in conjunction with RT. This evaluation was conducted using our previously developed 3D spheroidal co-culture models of pancreatic cancer where we demonstrated the improved therapeutic efficacy of incorporating these NPs into RT. This work led to the publication of one review article and two manuscripts. They were published in *Pharmaceutics, Cancers,* and *Precision Nanomedicine,* respectively. The *Pharmaceutics* review article is titled "Combining Gold Nanoparticles with Other Radiosensitizing Agents for Unlocking the Full Potential of Cancer Radiotherapy" [213]. The *Cancers* manuscript is titled "Lipid-Nanoparticle-Mediated Delivery of Docetaxel Prodrug for Exploiting Full Potential of Gold Nanoparticles in the Treatment of Pancreatic Cancer" [311], and the *Precision Nanomedicine* manuscript is titled "An Integrated Approach Utilizing Nanotechnology, Chemotherapy, and Radiotherapy for Pancreatic Cancer Treatment" [312]. My personal contribution to the above-mentioned papers includes conceptualization and experimental design, sample preparation, collection, and processing, data acquisition and analysis, creation of figures and manuscripts writing.

5.1 LNPs Mediated Delivery of DTX Prodrug

In this study, we test the combination of LNP_{DTX-P} and GNPs functionalized with PEG and RGD in pancreatic cancer models *in vitro* and *in vivo* (**Fig. 5.1**). Two different DTX prodrug concentrations were used in the LNP_{DTX-P}, a 5% (by weight) DTX prodrug LNP referred to as LNP_{DTX-1}, and a 10% (by weight) DTX prodrug LNP referred to as $LNP_{DTX-2.}$ The goal is to assess the biodistribution of GNPs in the presence of LNP_{DTX-P} vs free DTX in MIA PaCa-2 pancreatic carcinoma-bearing NRG mice and compare it to the 2D monoculture model of MIA PaCa-2. This unique combination of GNPs and LNP_{DTX-P} has neither been explored *in vitro* nor *in vivo*. This is an essential step before a combined GNP+LNP_{DTX-P}+RT treatment can be advanced as a possible clinical therapeutic approach. The *in vivo* mouse xenograft model has tumor vasculature and a complete TME that allows for the most precise testing before moving into clinical trials.

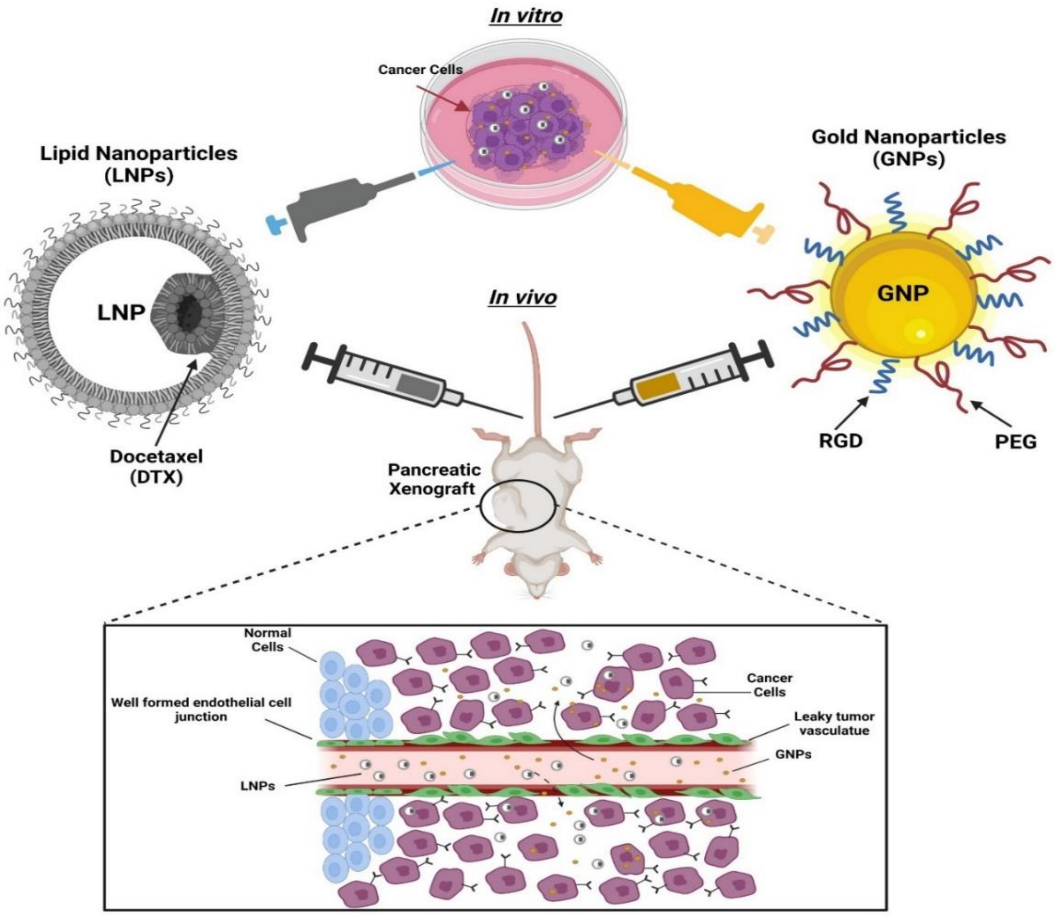

Figure 5.1 Schematic showing pre-clinical xenograft model to test the efficacy of DTX prodrug encapsulated in LNPs and GNPs combination vs 2D *in vitro* model. The inset shows a schematic diagram of the escape of NPs from leaky blood vessels to tumor tissue. Reproduced with permission from open access Creative Common license [311].

5.1.1 $LNP_{DTX\text{-}P}$ Effects In Vitro

To measure the toxicity effect of free DTX and the two $LNP_{DTX\text{-}P}$, $LNP_{DTX\text{-}1}$ and $LNP_{DTX\text{-}2}$, on MIA PaCa-2 cells, a proliferation assay was used. Based on this assay, the IC-50 of free DTX, $LNP_{DTX\text{-}1}$, and $LNP_{DTX\text{-}2}$, on MIA PaCa-2 were determined to be 36.65 ± 2.12 nM, 28.43 ± 3.92 nM, and 21.86 ± 3.71 nM, respectively (**Fig. 5.2**). These results are very promising as they show that delivery of DTX in $LNP_{DTX\text{-}P}$ reduces the IC-50. We attribute the enhanced efficacy to the use of prodrugs in LNPs. The DTX prodrug is designed to be stably incorporated into the LNPs and consists of DTX conjugated to a hydrophobic anchor by a biodegradable linker [313]. Within the LNP, the prodrug resides within a hydrophobic pocket, due to its poor water solubility. Following the $LNP_{DTX\text{-}P}$ uptake by the cells, the DTX prodrug undergoes biotransformation. The intracellular enzymes break down the biodegradable (ester) linker releasing the active DTX [313]. Consequently, $LNP_{DTX\text{-}P}$ has increased the ability of transport, improved tumour targeting, enhanced therapeutic effectiveness, and minimized drug-induced toxicity in normal tissues [313–318]. These LNP platforms have been used successfully in the clinic to deliver nucleic acids and small-molecule chemotherapeutics [319–321]. Therefore, clinically relevant intra-tumoral concentrations of DTX can be achieved by formulating DTX prodrug into LNPs.

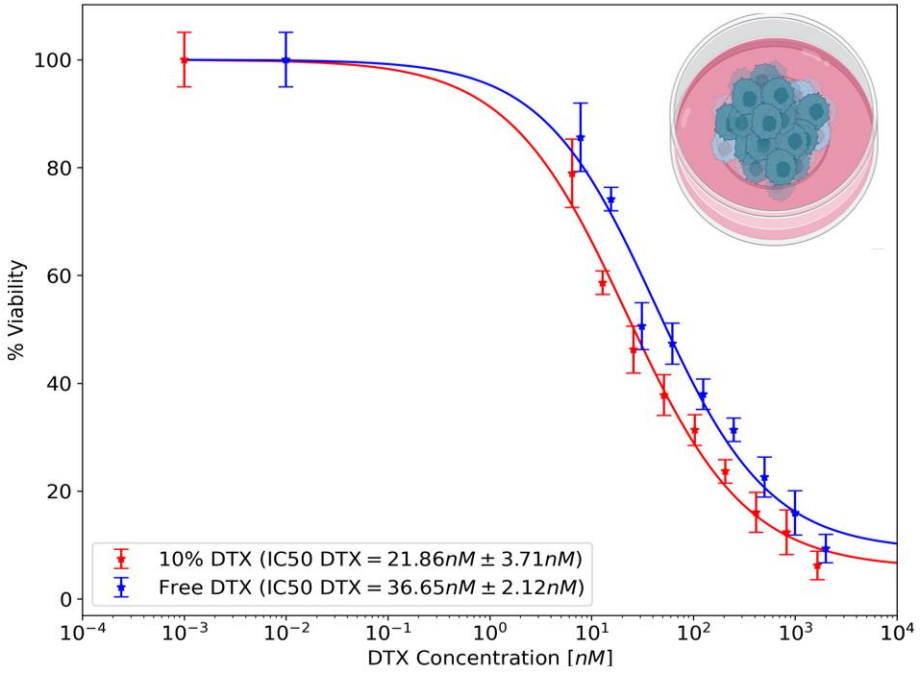

Figure 5.2 Effect of free DTX vs $LNP_{DTX\text{-}P}$ on MIA PaCa-2 cells *in vitro*. IC-50 curves of free DTX and 10% DTX ($LNP_{DTX\text{-}2}$). Reproduced with permission from open access Creative Common license [312].

To compare the efficiency of free DTX and $LNP_{DTX\text{-}P}$ *in vitro*, we measured the number of GNPs at three different time points after being dosed with $GNP_{PEG\text{-}RGD}$, at a clinically relevant concentration of 7.5 μg/mL and treated with the IC-50 dose of free DTX or equivalent dose of $LNP_{DTX\text{-}P}$ (**Fig. 5.3**). The characterization of GNPs and LNPs is displayed in **Fig. S16**. The shape and size of the NPs were validated using high-angle annular darkfield (HAADF) scanning transmission electron microscopy (STEM) (**Fig. 2.11** & **Fig. 2.18**). The results clearly show a higher number of GNPs in the cells treated with DTX or $LNP_{DTX\text{-}P}$ compared to that of control cells (**Fig. 5.3A**). The number of GNPs in the DTX treated cells, $LNP_{DTX\text{-}1}$ treated cells, and $LNP_{DTX\text{-}2}$ treated cells, were 2.8 times, 1.7 times, and 2.2 times, higher than in the control cells for the 0 h time point, 3.3 times, 1.8 times, and 2.3 times higher for the 24 h time point, and 3.6 times, 1.9 times, and 2.5 times higher for the 48 h time point, respectively. **Fig. 5.3B** shows the retention of GNPs for control cells to be 77% and 61% of their initial GNPs after 24 h and 48 h, respectively. These retention percentages significantly increased for the $LNP_{DTX\text{-}1}$ treated cells to be 82% and 71%, for $LNP_{DTX\text{-}2}$ treated cells to be 83% and 70%, and for free DTX treated cells to be 91% and 77%, respectively. These results signify that free DTX and $LNP_{DTX\text{-}P}$ not only significantly increase the number of GNPs in cells compared to control cells, but it also significantly increases their retention.

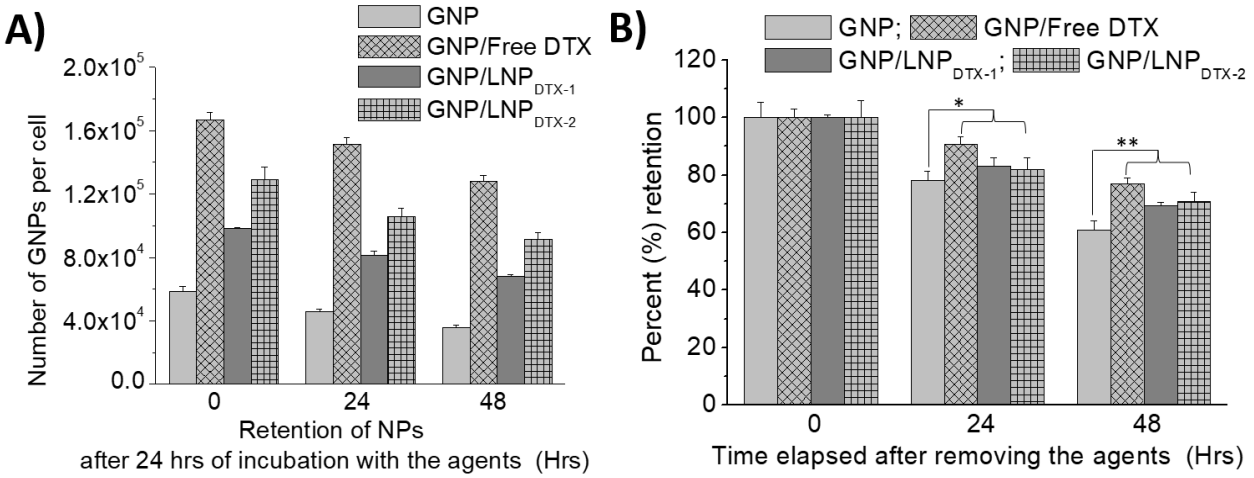

Figure 5.3 (**A)** Number of GNPs per cell in control cells, cells treated with free DTX, cells treated with $LNP_{DTX\text{-}1}$, and cells treated with $LNP_{DTX\text{-}2}$ over time. **(B)** GNPs percent retention over time for control cells, cells treated with free DTX, cells treated with $LNP_{DTX\text{-}1}$, and cells treated with $LNP_{DTX\text{-}2}$. * indicates $p < 0.05$, ** indicates $p < 0.01$**.** Reproduced with permission from open access Creative Common license [311].

These results are better explained when understanding the effect of DTX on cell MTs and on GNPs cellular transportation. GNPs are internalized via RME, where cell surface receptors bind to the RGD ligand on the NPs surface, then get engulfed by endosomes [237, 322, 323]. The NPs are then pulled along MTs by two molecular motors, kinesin and dynein, and along actin by the motor myosin (inset **Fig. 3.9A**). After that, the NPs get fused with lysosomes to be sorted out, where any waste gets excreted out of the cell (**Fig. 5.4A left**) [237]. MTs play a major role in cell division and facilitate the movement of GNPs inside cells, therefore, the interference in MTs' function caused by DTX can substantially affect GNP intracellular journey (**Fig. 5.4A right**) [247, 248]. One of the key mechanisms of action of DTX is the inhibition of MTs depolymerization which leads to defective MT bundles impeding the proper development of spindle apparatus which are involved in mitosis [159–162]. In a normal M phase, MTs and the MTOC are used to create mitotic spindles that then equally pull the chromosomes into the divided cells (**Fig. 5.4B top**). However, with doses of just 50 nM of DTX, MTs get malfunctioned, and cells get locked in mitosis (**Fig. 5.4B bottom**) [61].

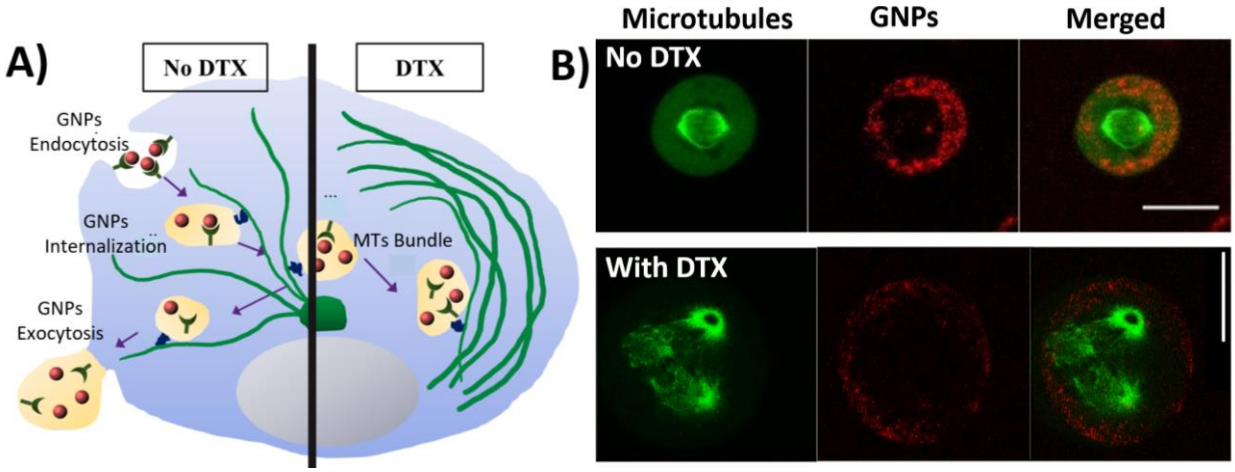

Figure 5.4 (A) Schematic diagram illustrating the path of GNPs (red dots) within a cell in the absence and presence of DTX. **(B)** Confocal images of dividing cancer cells, control (top) and DTX (bottom). GNPs are shown in red, and microtubules in green. The scale bar: 25 µm. Reproduced with permission from open access Creative Common license [311].

Over time, this results in arresting the cell cycle at the G2/M phases, the most radiosensitive phases of the cell cycle, for both the free DTX and the $LNP_{DTX\text{-}P}$ as explained by the flow cytometry data (**Fig. 5.5**). Although initially, $LNP_{DTX\text{-}P}$ had a slower shift from G1 phase cell population to G2 phase cell population compared to free DTX, they eventually had similar cell synchronization after approximately 24 h. This leads to GNPs getting trapped within the cell

because of their inability to move along the damaged MTs resulting in a deficiency in the cell's ability to secrete GNPs. Hence, it not only increases GNPs uptake into cells but also blocks their exit by not allowing cells to divide and distribute GNPs into the daughter cells. This explains the increase in both uptake and retention of free DTX and $LNP_{DTX\text{-}P}$ treated cells.

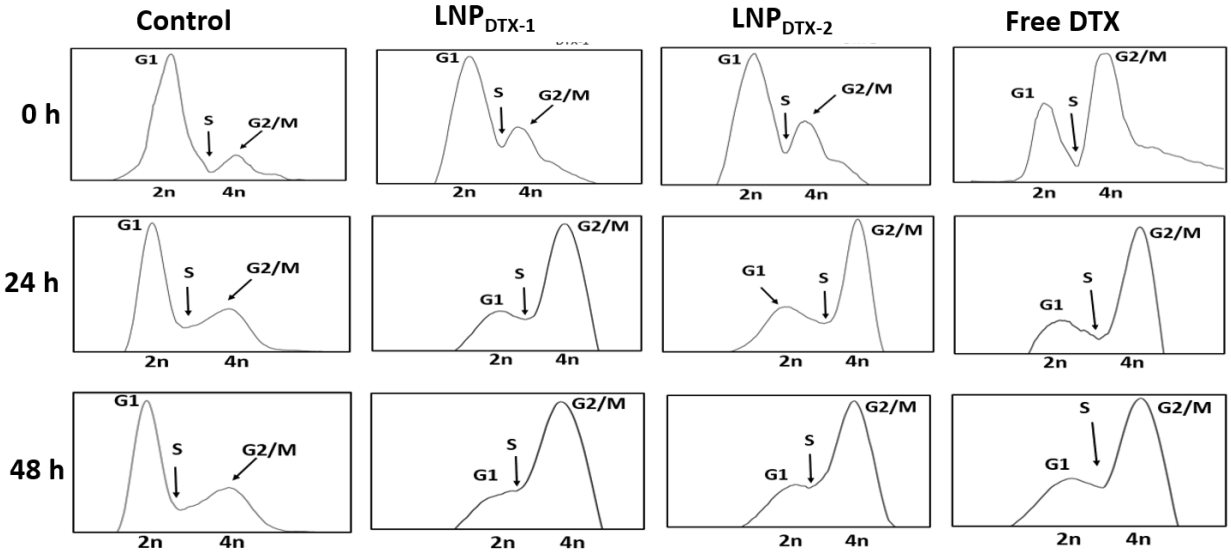

Figure 5.5 Cell cycle assay for control cells, cells treated with free DTX, cells treated with $LNP_{DTX\text{-}1}$, and cells treated with $LNP_{DTX\text{-}2}$ over time. Reproduced with permission from open access Creative Common license [311].

Confocal Images of cancer cells treated with free DTX, $LNP_{DTX\text{-}1}$, and $LNP_{DTX\text{-}2}$, vs control cells show some multinucleated cells caused by this mechanism of action of DTX (**Fig. 5.6**). As explained earlier, these treated cells are unable to divide properly and stay trapped in the M phase, where some of which develop multinucleation. These results are consistent with other studies that reported a significant increase in GNP uptake with the treatment of DTX in multiple different cell lines [61, 223].

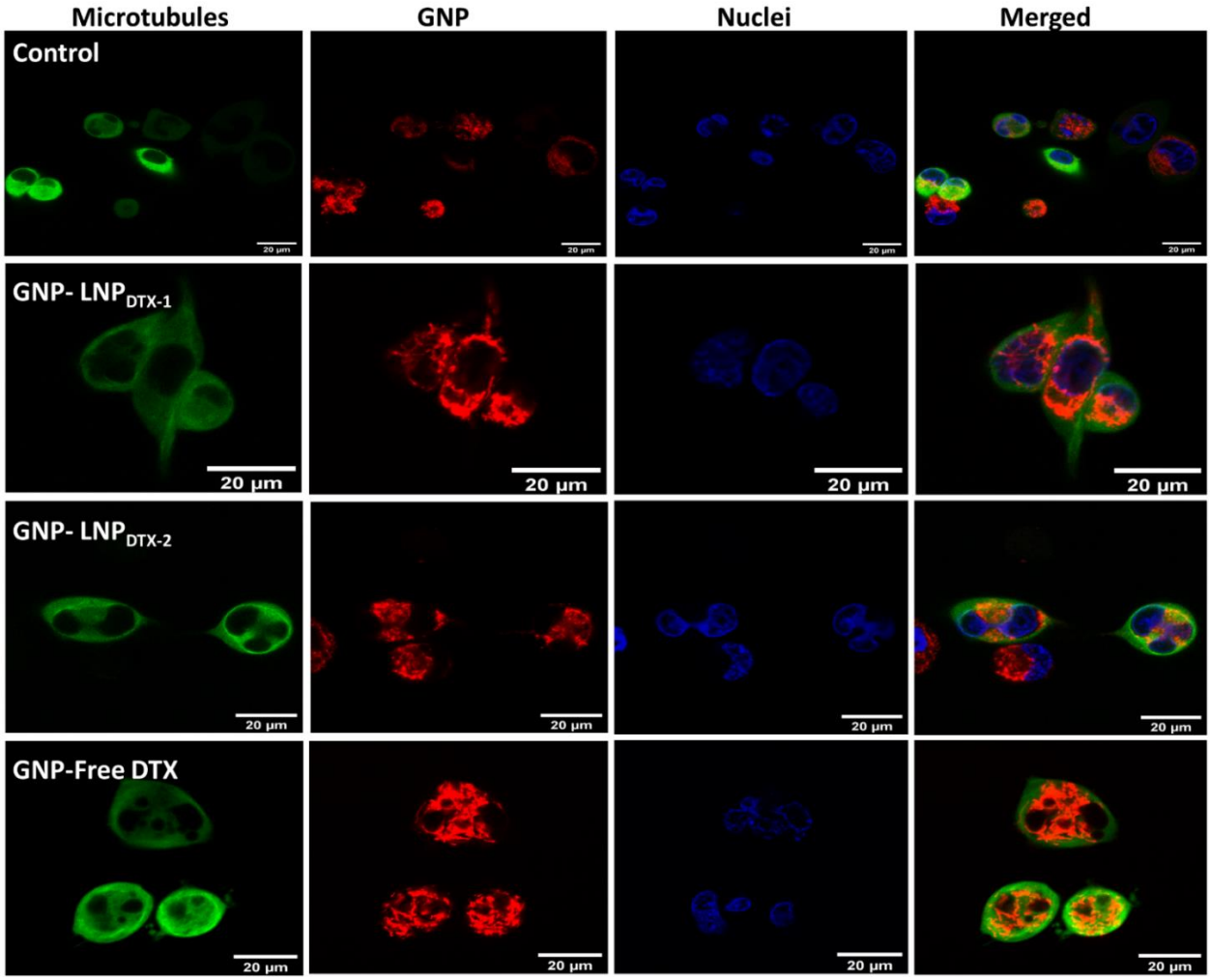

Figure 5.6 Visualization of intracellular GNP distribution in MIA PaCa-2 cells using confocal imaging. Control untreated cells (1st row), cells treated with LNP_{DTX-1} (2nd row), cells treated with LNP_{DTX-2} (3rd row), and cells treated with free DTX (4th row). Microtubules in green (1st column), GNPs in red (2nd column), nuclei in blue (3rd column), and all three merged (4th column). Scale bar: 20 µm. Reproduced with permission from open access Creative Common license [311].

5.1.2 LNP_{DTX-P} Effects In Vivo

In this experiment, MIA PaCa-2 cells were implanted subcutaneously in NRG mice and then dosed intravenously with GNPs and either free DTX or LNP_{DTX-P} to assess the drug toxicity and biodistribution over time once tumours reached a measured volume of 250-300 mm^3. The free DTX dose used was 6 mg/kg or an equivalent dose of LNP_{DTX-P}, and $GNP_{PEG–RGD}$ were dosed at 2 mg/kg. These doses are shown to be tolerable for *in vivo* administration, with a goal in mind for future clinical applications [49, 226, 227, 252]. GNP uptake per tumour tissue revealed that free

DTX and LNP_{DTX-P} treated mice had twice the number of GNPs in their tumours compared to the control mice (**Fig. 5.7**).

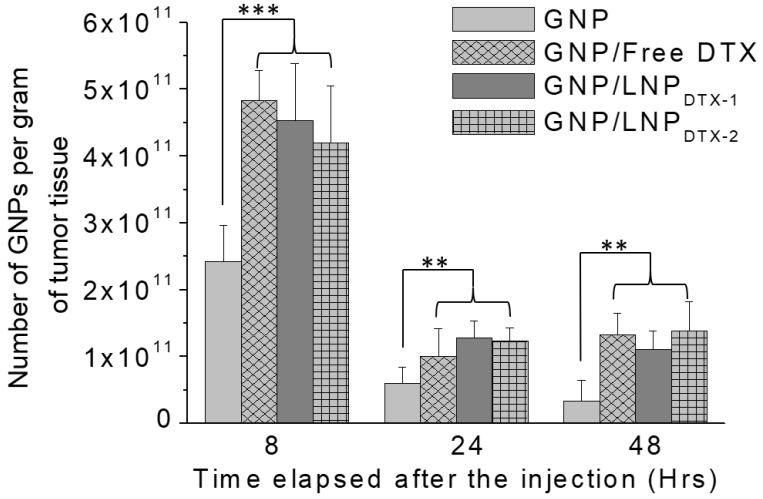

Figure 5.7 Amount of GNPs per gram of tumour tissue in untreated tissues, tissues treated with free DTX, tissues treated with LNP_{DTX-1}, and tissues treated with LNP_{DTX-2} over time. * indicates $p < 0.05$, ** indicates $p < 0.01$, *** indicates $p < 0.001$. Reproduced with permission from open access Creative Common license [311].

The leaky vasculatures and ineffective lymphatic systems at tumours facilitate the accumulation of NPs in tumour cells by the EPR effect [53]. However, GNP retention in the tumour 24 h post-treatment was only 20%. This is attributed to the natural clearance of GNPs from the circulation after 24 h, before free DTX or the LNP_{DTX-P} had the opportunity to exert their full effect. This is supported by the flow cytometry cell cycle data for the 8 h time point which shows most of the tumour cells are in the G1 phase (**Fig. 5.8**). As DTX exposure time increases, the effects on the MTs increases GNP accumulation within the tumour as demonstrated by the synchronization of a larger number of tumour cells in the G2/M phase after 24-48 h for both the LNP_{DTX-P} and the free DTX (**Fig. 5.8**). This resulted in a similar number of GNPs at the 48h and 24 h time points for both free DTX and LNP_{DTX-P} treated tumours. Furthermore, LNP_{DTX-P} treated samples had a higher population of cells in the G2/M phases compared to free DTX treated samples. This is likely the result of LNPs bringing more DTX to the tumour cells compared to free DTX. On the other hand, the untreated tumours showed a further decrease in the number of accumulated GNPs due to the exocytosis process and the lack of GNPs circulating in the blood after 48 h.

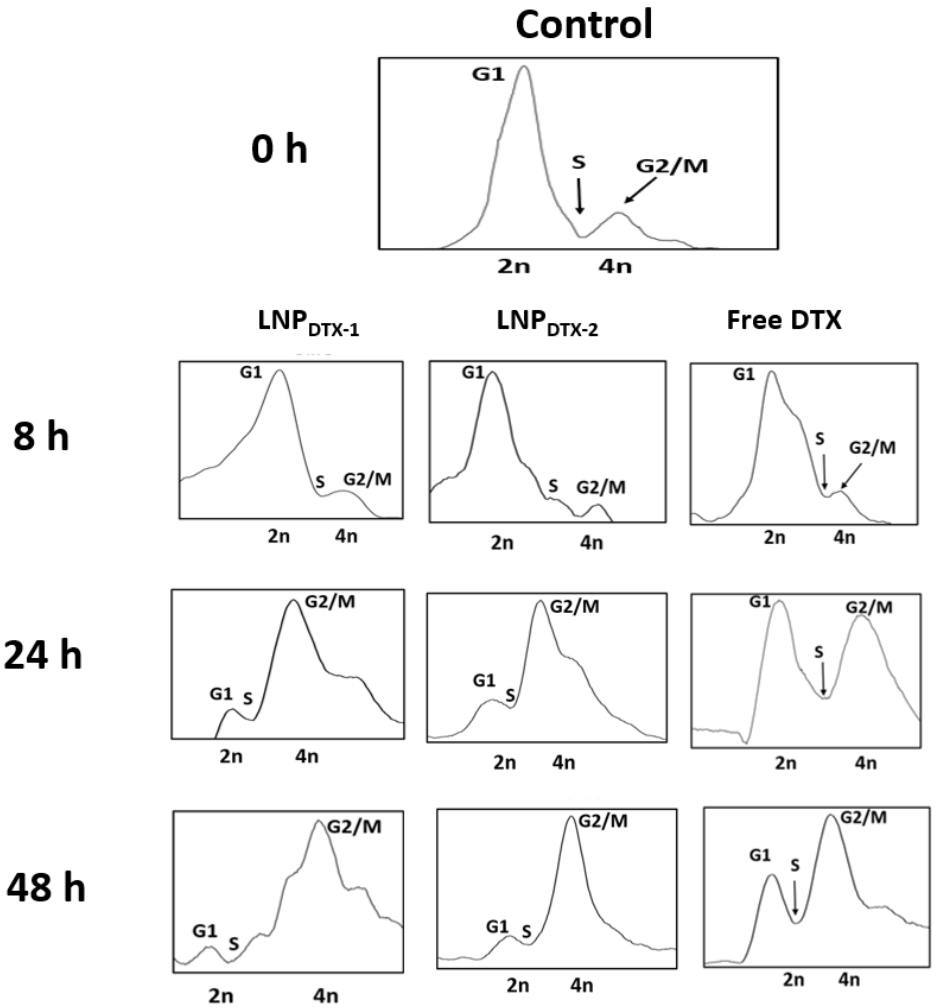

Figure 5.8 Cell cycle assay for untreated tumour tissue, tissue treated with free DTX, tissue treated with LNP_{DTX-1}, and tissue treated with LNP_{DTX-2} over time. Reproduced with permission from open access Creative Common license [311].

These results are further supported by DF images of the tumour tissue of untreated samples, free DTX treated samples and LNP_{DTX-1} treated samples (**Fig. 5.9**). Additional DF images of LNP_{DTX-2} treated samples are provided in the supplementary file (**Fig. S17**). An immediate visual increase in the number of GNPs was observed when comparing the tumour samples treated with free DTX or LNP_{DTX-P} to the untreated samples for the different time points, which agrees with our quantification data. The results show no significant difference between the two LNP_{DTX-P} used compared to free DTX, consistent with the *in vitro* results. Furthermore, a clear increase DTX induced cell damage is observed for the two LNP_{DTX-P} and for the free DTX compared to the control sample as demonstrated in haematoxylin and eosin (H&E) stained 8 h, 24 h, and 48 h post-treatment tumours (**Fig. 5.10**). H&E images of multiple organs seen in the supplementary (**Fig.**

S18), do not seem to show any observable effects with the given dose of DTX for either the $LNP_{DTX\text{-}P}$ or the free DTX.

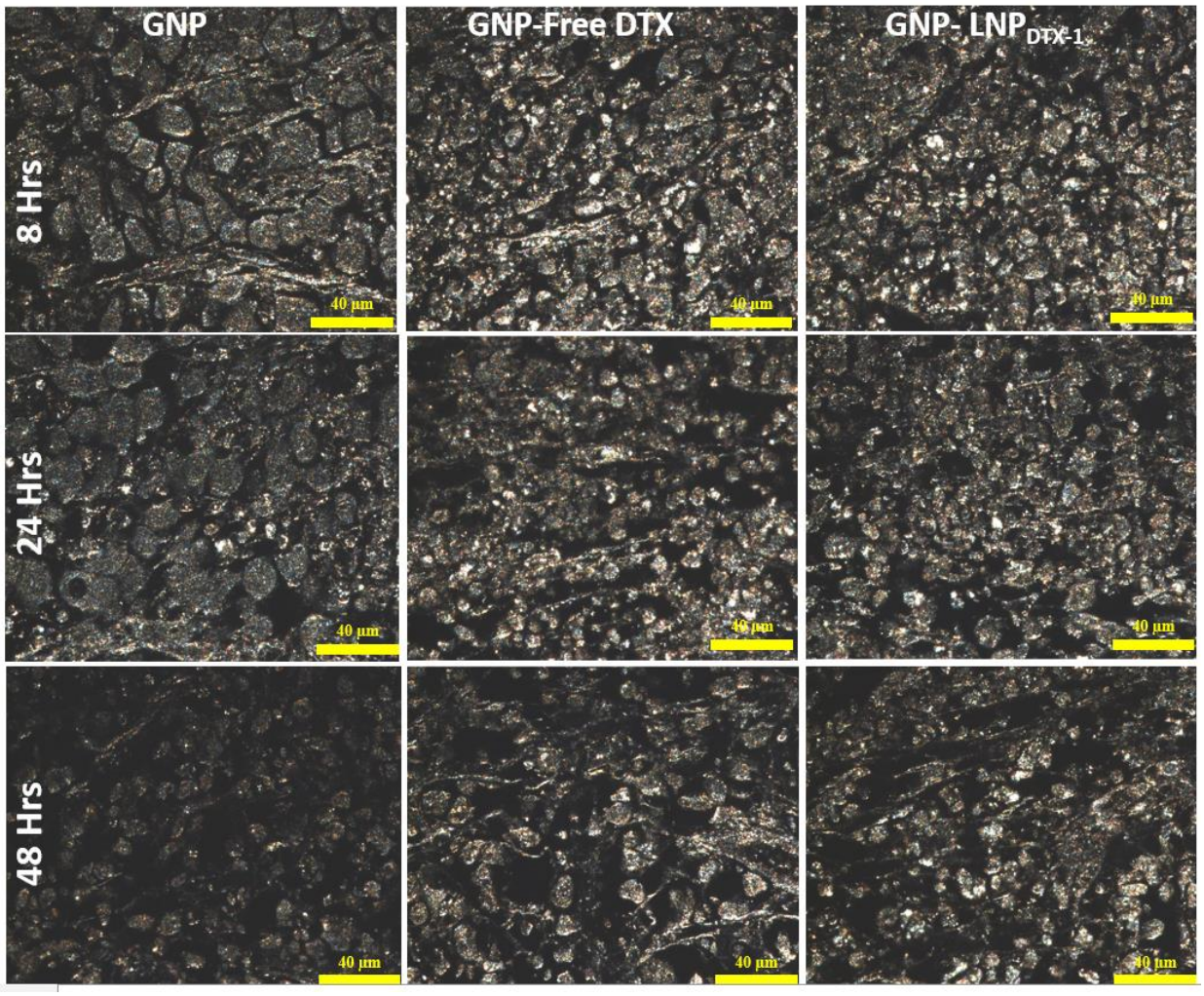

Figure 5.9 DF images of 4 µm sections of untreated tumour tissues, tissues treated with free DTX, and tissues treated with $LNP_{DTX\text{-}1}$. Scale bar: 40 µm. Reproduced with permission from open access Creative Common license [311].

Despite its toxicity, free DTX has already shown remarkable radiosensitization effects in several clinical trials [72–77]. Hence, our results are very promising as they show the potential of using $LNP_{DTX\text{-}1}$ and $LNP_{DTX\text{-}2}$ formulations instead of free DTX as potential radiosensitizers as they deliver similar synchronization of cancer cells in the radiosensitive G2/M phase and similar GNP uptake & retention. This is very important when considering combined chemoradiation and nanotherapy treatments since DTX is administered weekly to patients. With the synchronization of cells in the G2/M phase for at least 48 h following treatment and with the trapping of GNPs in the tumour, a 5-day-a-week fractionated RT treatment regime would work synergistically.

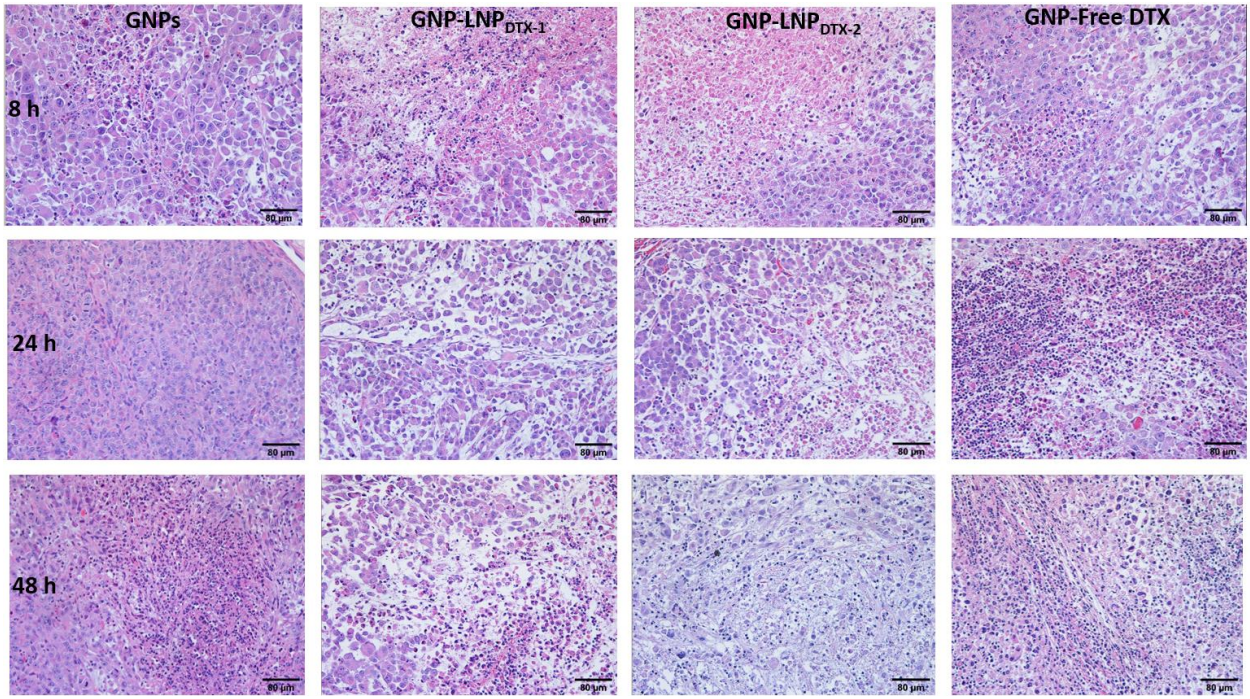

Figure 5.10 Treatment of MIA PaCa-2 subcutaneous tumour with free docetaxel (DTX) vs LNP_{DTX-P}. H&E-stained sections of tumour tissues 0 h, 24 h, and 48 h after dosing with the drugs and GNPs. Scale bar: 80 µm. Reproduced with permission from open access Creative Common license [311].

GNP content, normalized to GNPs per gram of tissue, in the control organs (**Fig. 5.11A**), organs treated with LNP_{DTX-1} (**Fig. 5.11B**), organs treated with LNP_{DTX-2} (**Fig. 5.11C**), and organs treated with free DTX (**Fig. 5.11D**), are shown in **Fig. 5.11** Despite the clear increase in GNP uptake and retention in free DTX and LNP_{DTX-P} treated tumours, neither free DTX nor the LNP_{DTX-P} significantly increase the number of GNPs in normal organs. This implies that there is an increase in the accumulation of GNPs in tumours relative to other organs over 48 h due to DTX tumour targeting and the EPR effect. The results also show that GNPs have longer retention in tumours compared to GNPs in the blood in circulation. This is supported by recent pharmacokinetic studies that showed a similar accumulation of the GNPs in the treated tumour compared to healthy organs [324]. This is very important when considering RT as it shows that both DTX and GNPs will remain within the tumour, thus allowing for a synergistic radiosensitization effect up to at least 48 h. DF images of the organs treated with LNP_{DTX-1} after 24 h show no signs of damage in these organs compared to that of the tumours (**Fig. 5.12A)**. HIS were used for GNPs verification (**Fig. 5.12B**). Additional DF images of untreated organs, organs treated with free DTX, and organs treated with LNP_{DTX-2} 24 h post-treatment are in the supplementary (**Fig. S19**).

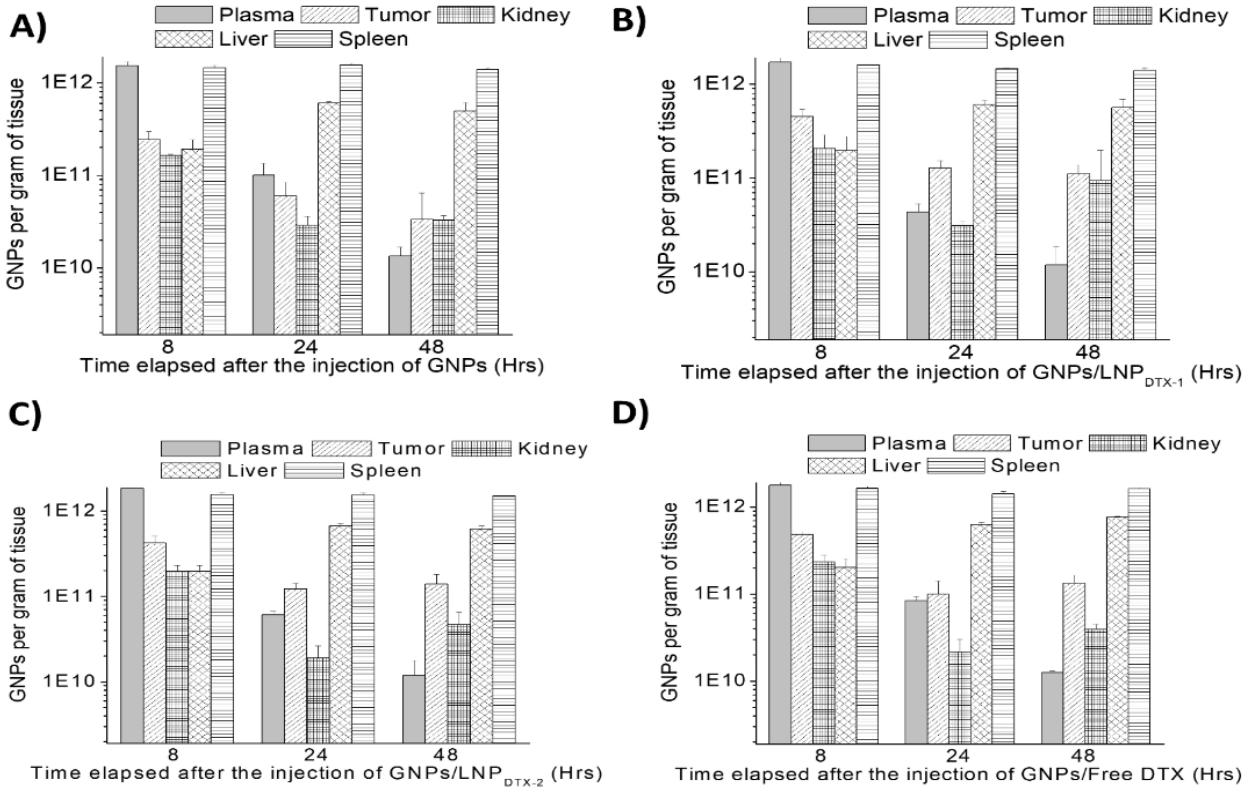

Figure 5.11 GNPs uptake in *in vivo* tumour tissues and organs. **(A-D)** GNPs amount per gram of tissue for untreated mice, mice treated with LNP_{DTX-1}, mice treated with LNP_{DTX-2}, and mice treated with free DTX, respectively.

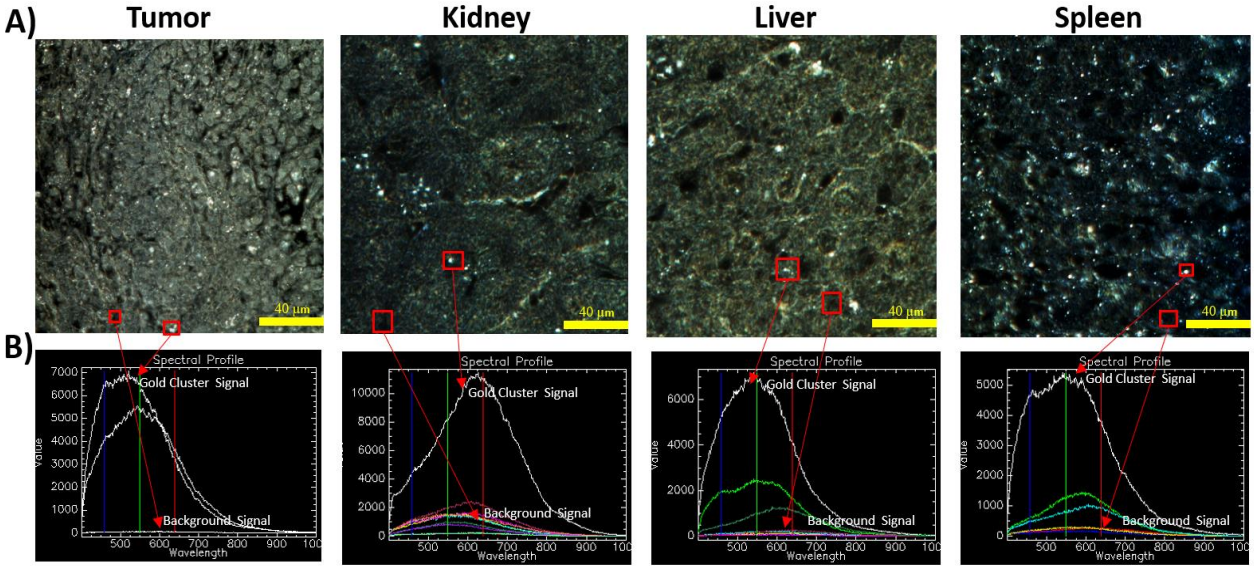

Figure 5.12 GNPs uptake in different tissues **(A)** DF images of 4 µm sections of tumour tissue, kidney, liver, and spleen 24 after LNP_{DTX-1} treatment. **(B)** Hyperspectral spectrum of GNPs within their respective tissues. Scale bar: 40 µm. Reproduced with permission from open access Creative Common license [311].

5.1.3 Conclusions

In this study, we measured the uptake and retention of GNPs *in vitro* and *in vivo*, using pancreatic cancer cell lines MIA PaCa-2, following treatment with free DTX vs LNP_{DTX-P}. In both *in vitro* and *in vivo*, the addition of free DTX and LNP_{DTX-P} displayed a significant increase in GNPs uptake relative to control samples with LNP_{DTX-P} displaying similar cancer toxicity when compared to free DTX. These results are very promising as LNP_{DTX-P} have superior targeting of tumour tissues compared to free DTX. Because of their minimal toxicity to normal tissues, both GNPs and LNP_{DTX-P} can be ideal radiosensitization candidates in RT and are expected to produce very promising synergistic effects.

5.2 Enhancing RT with GNPs and LNP_{DTX-P}

To comprehensively investigate the synergistic effects of GNPs, RT, and LNP_{DTX-P}, we used an *in vitro* 3D spheroid model consisting of both MIA PaCa-2 cells and pancreatic patient-derived CAFs. Subsequently, we evaluated the efficacy of combining clinically relevant doses of GNPs/RT/LNP_{DTX-P} (**Fig. 5.13**) to address the following questions:

1- How much-increased efficacy did the proposed triple combination (GNPs/RT/LNP_{DTX-P}) show in comparison to RT alone?
2- Did LNP_{DTX-P} show efficacy improvement over free DTX?

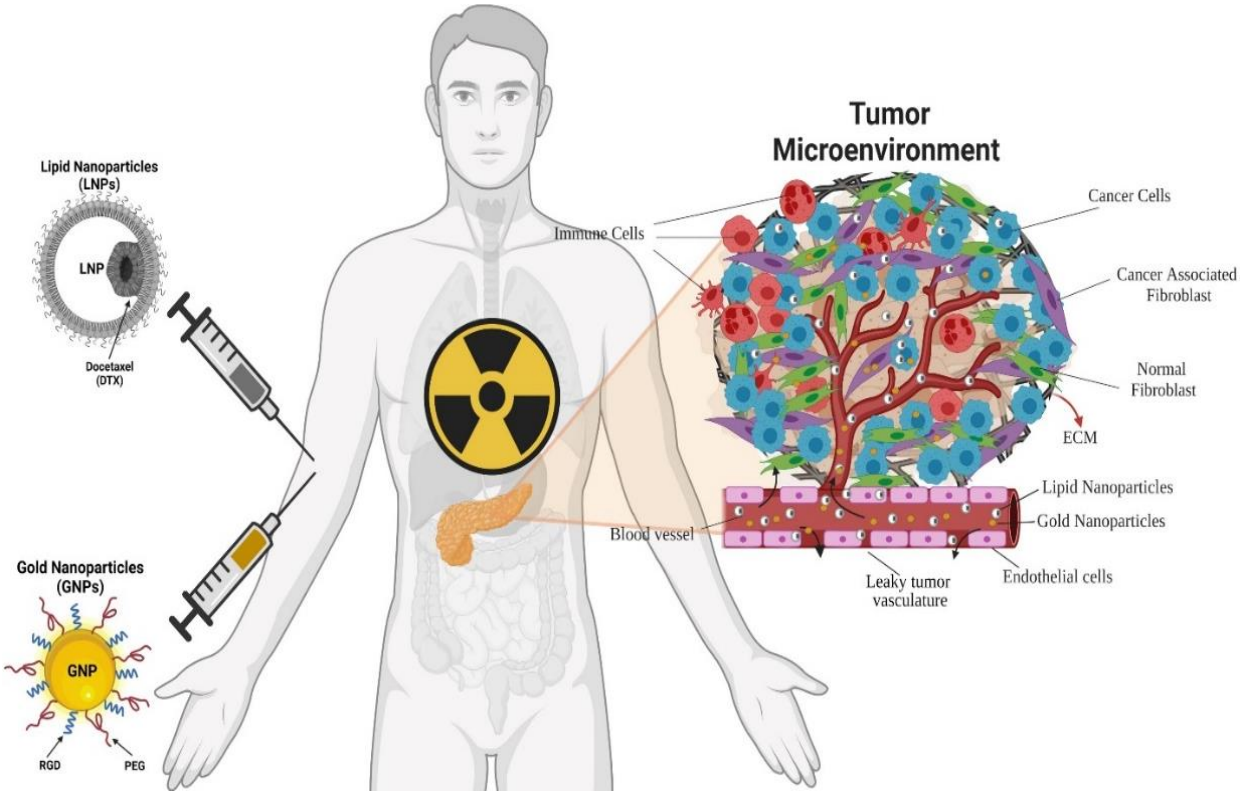

Figure 5.13 Schematic showing the combined modality of nanotechnology, chemotherapy, and RT for the treatment of pancreatic cancer. Reproduced with permission from open access Creative Common license [312].

5.2.1 *3D Spheroids & Drug Cytotoxicity*

To estimate the efficacy of our $LNP_{DTX\text{-}P}$ (which contains 10 mol% DTX prodrug by weight), CellTiter-Glo 3D assay was used to measure cell viability and cytotoxicity. CellTiter-Glo 3D is a luminescent cell viability assay, which measures the amount of ATP present in metabolically active cells. The level of luminescence is directly proportional to the amount of ATP present, which reflects the number of viable cells [325]. The IC-50 values were measured to determine the potency of $LNP_{DTX\text{-}P}$ and compare its inhibitory activity to DTX. These values were then used to determine the optimal concentrations of the drugs for our subsequent experiments. Our IC-50 values are shown in **Fig. 5.14**. The values were only determined for MIA PaCa-2 and not for CAF-98, because the fibroblasts play a supportive role in tumor cell proliferation and tumor growth. For the 3D spheroids, the IC-50 value of the effective DTX prodrug in the $LNP_{DTX\text{-}P}$ was ~ 99 nM vs ~100 nM for the free DTX. The literature shows huge variations in the value of IC-50 ranging from 1-20 nM using DTX or similar LNP-encapsulated drugs in 2D pancreatic cancer cell

cultures [326–328]. These values can vary depending on several factors, such as the experimental conditions, the specific LNP_{DTX} formulation used, the assays used, and the pancreatic cancer cell line used. However, the increase in IC-50 values shown in the IC-50 value in 3D models for both LNP_{DTX-P} and DTX is consistent with previous experiments reports that show several-fold increase in IC-50 values from going from 2D to 3D models [324].

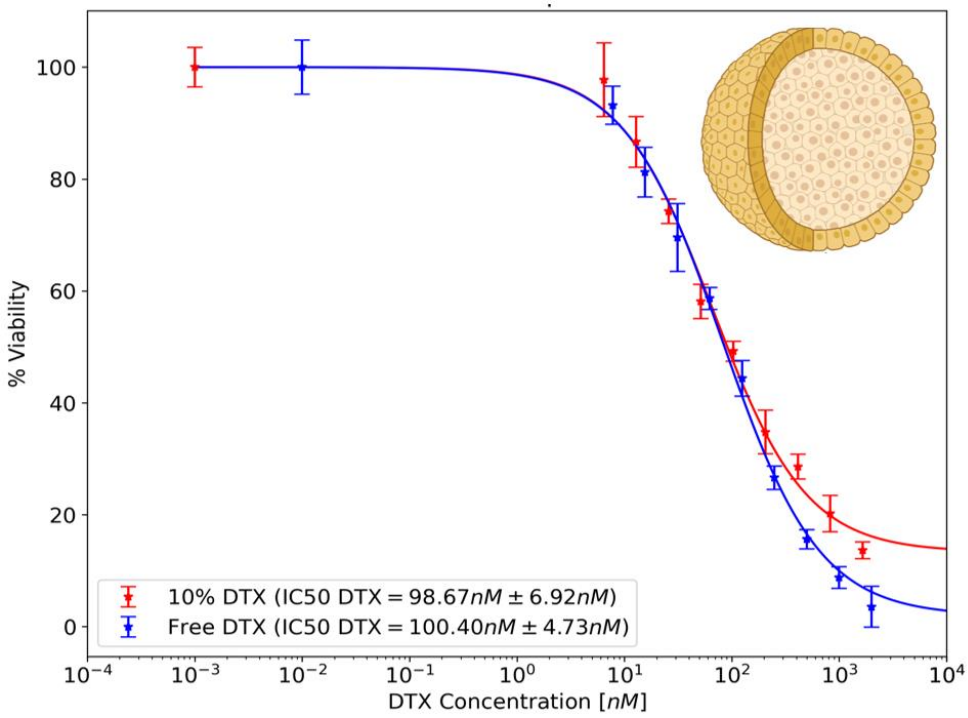

Figure 5.14 Characterizing drug cytotoxicity. DTX & LNP_{DTX-P} cytotoxicity proliferation assay for MIA PaCa-2 monoculture spheroids. Reproduced with permission from open access Creative Common license [312].

5.2.2 *LNP_{DTX-P} Effect on GNPs Uptake*

The samples were dosed with GNPs (~13 nm in diameter) functionalized with PEG and RGD, at a low concentration of 7.5 μg/mL not to induce any potential toxicity from the gold to normal tissues [329]. After an incubation period of 24 h with GNPs and either DTX or LNP_{DTX-P} at the IC-50 concentrations, the media was changed to mimic the loss of GNPs and drug supply in the body following a single injection. The functionalized GNPs enter cells via receptor mediated endocytosis as described in our previous work [223]. The samples were then processed and the amount of gold in each cell was calculated as described in previous chapters. The amount of gold in co-culture cells over time is shown in **Fig. 5.15** (**Fig. S20.1** for monoculture cells). The results show higher levels of gold accumulation in cells that were co-treated with either DTX or LNP_{DTX-}

$_{P}$ compared to cells that were treated with GNP only, for both the monoculture and co-culture. For the co-culture (**Fig. 5.15**), the DTX treated samples had a 174% (for the $LNP_{DTX\text{-}P}$) and 219% (for the DTX) increase in the amount of gold on the first day of the experiment and retained 65% (for the $LNP_{DTX\text{-}P}$) and 68% (for the DTX) of gold compared to 31% for the non-DTX treated samples. Similarly, for the monoculture (**Fig. S20.1**), the DTX treated samples had a 173% (for the $LNP_{DTX\text{-}P}$) and 202% (for the DTX) increase in the amount of gold on the first day of the experiment and retained 67% (for the $LNP_{DTX\text{-}P}$) and 72% (for the DTX) of gold compared to 32% for the non-DTX treated samples.

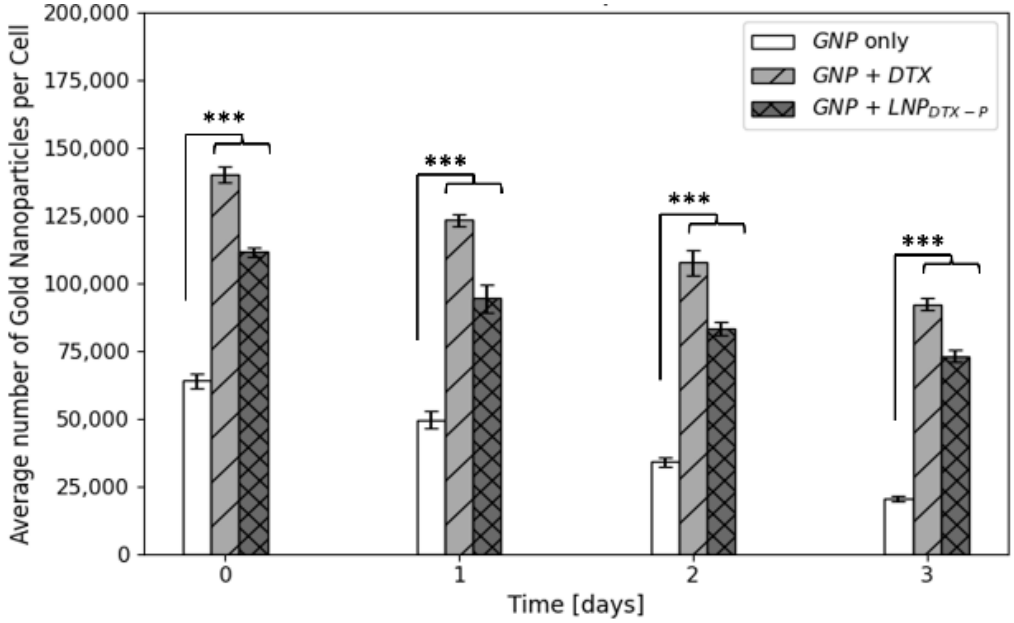

Figure 5.15 Quantification of uptake of 7.5 µg/ml of GNPs into CAF-98 to MIA PaCa-2 (5:1) co-culture spheroids dosed with only GNPs, GNPs + DTX, and GNPs + $LNP_{DTX\text{-}P}$, as measured using ICP-MS. ******* indicates $p < 0.001$. Reproduced with permission from open access Creative Common license [312].

These results are consistent with the mechanism of action of DTX and other taxane drugs. DTX inhibits microtubule function by promoting tubulin polymerization and inhibiting depolymerization [330]. Microtubules serve many important functions in cells, including acting as "highways" for intracellular transport and playing a critical role in cell division [331]. By disrupting microtubule dynamics, DTX disturbs intracellular transport which results in decreased GNP exocytosis and ultimately promotes GNP retention within cells. Furthermore, cell division is inhibited, thus, decreasing GNPs distribution into daughter cells. This explains the increase of gold in DTX treated cells (2-fold increase in amount and over 2-fold increase in retention). These results

are supported qualitatively by confocal images at day 0 and day 3 for co-culture (**Fig. 5.16**) and monoculture (**Fig. S21.2**) spheroids which clearly visually shows the effects of DTX and LNP_{DTX-P}. Additional images of co-culture and monoculture spheroids at day 1 and day 2 can be seen in **Fig. S21.3** and **Fig. S21.4,** respectively.

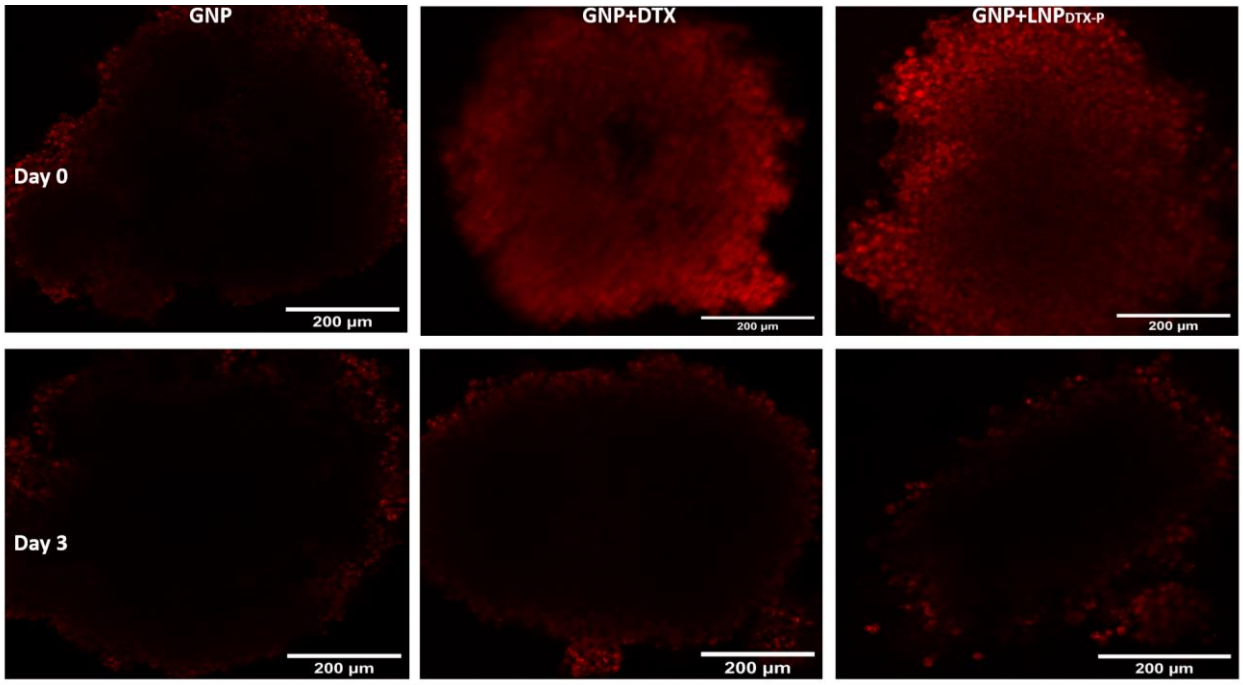

Figure 5.16 Confocal Images of GNPs', in red, uptake, and retention over 3 days in CAF-98 to MIA PaCa-2 (5:1) co-culture spheroids dosed with only GNPs (first column), GNPs + DTX (second column), and GNPs + LNP_{DTX-P} (third column). Scale bar: 200 µm. Reproduced with permission from open access Creative Common license [312].

Moreover, the effects of DTX and LNP_{DTX-P} go beyond increasing the number of GNPs in the spheroid models. The taxane drug, DTX, primarily targets cells in the G2/M phase of the cell cycle. It stabilizes microtubules and prevents them from depolymerizing, preventing cells from properly dividing during mitosis [332]. This induces cell cycle arrest, trapping cells in the G2/M phase which happens to be the most radiosensitive phase of the cell cycle [333]. This synchronized population of G2/M phase cells is most notable 72 h post-drug dosing as can be seen in **Fig. 5.17** for co-culture and **Fig. S21.5** for monoculture.

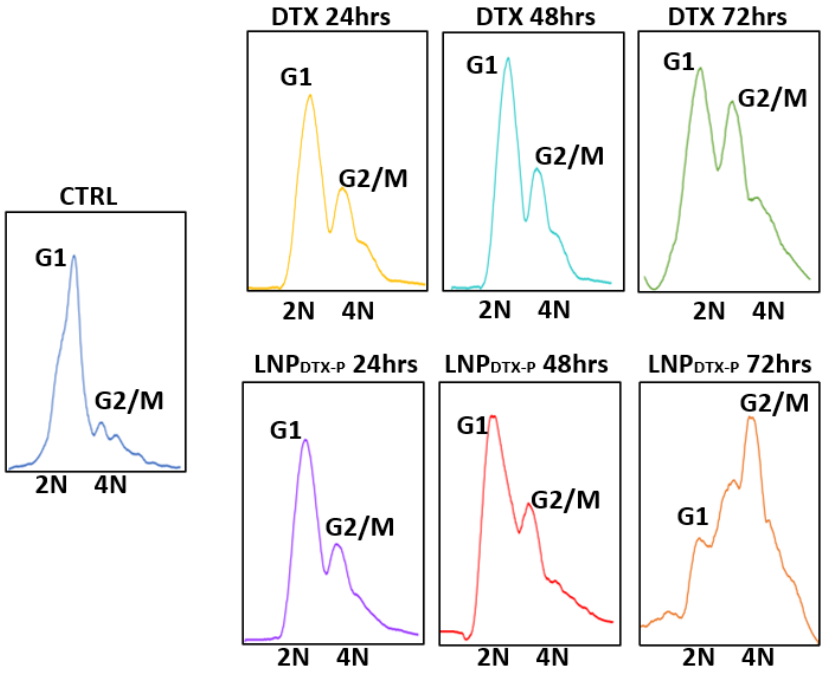

Figure 5.17 Cell cycle data of co-co-culture spheroids cells using DTX and LNP_{DTX-P} over 3 days. Reproduced with permission from open access Creative Common license [312].

5.2.3 *The Radiosensitization of GNPs and LNP_{DTX-P}*

After an incubation period of 24 h with the IC-50 concentration of either DTX or LNP_{DTX-P}, the media was replaced with fresh media, and a single 2 Gy dose was delivered to the samples. **Fig. 5.18** displays the relative change in diameter of co-culture spheroids over 14 days following treatment with and without radiation respectively (**Fig. S21.1** for monoculture). When no radiation was used, both co-culture (**Fig. 5.18A**) and monoculture (**Fig. S21.1A**) spheroids behaved as expected. GNPs for non-irradiated spheroids presented no effects on spheroid size while DTX and LNP_{DTX-P} caused ~ 12% shrinkage in tumor size with no significant difference between the two drugs. On the other hand, the use of GNPs with radiation resulted in ~ 7% for co-culture (**Fig. 5.18B**) and ~ 9% for monoculture (**Fig. S21.1B**) tumor size shrinkage. GNPs/RT/LNP_{DTX-P} resulted in 28% (for co-culture) and 41% (for monoculture) shrinkage in tumor size. While GNPs/RT/DTX resulted in 37% (for co-culture) and 48% (for monoculture) shrinkage in tumor size. These results are visualized using brightfield images of the spheroids 14 days post-treatment (**Fig. 5.19** for co-culture spheroids & **Fig. S21.2** for monoculture spheroids).

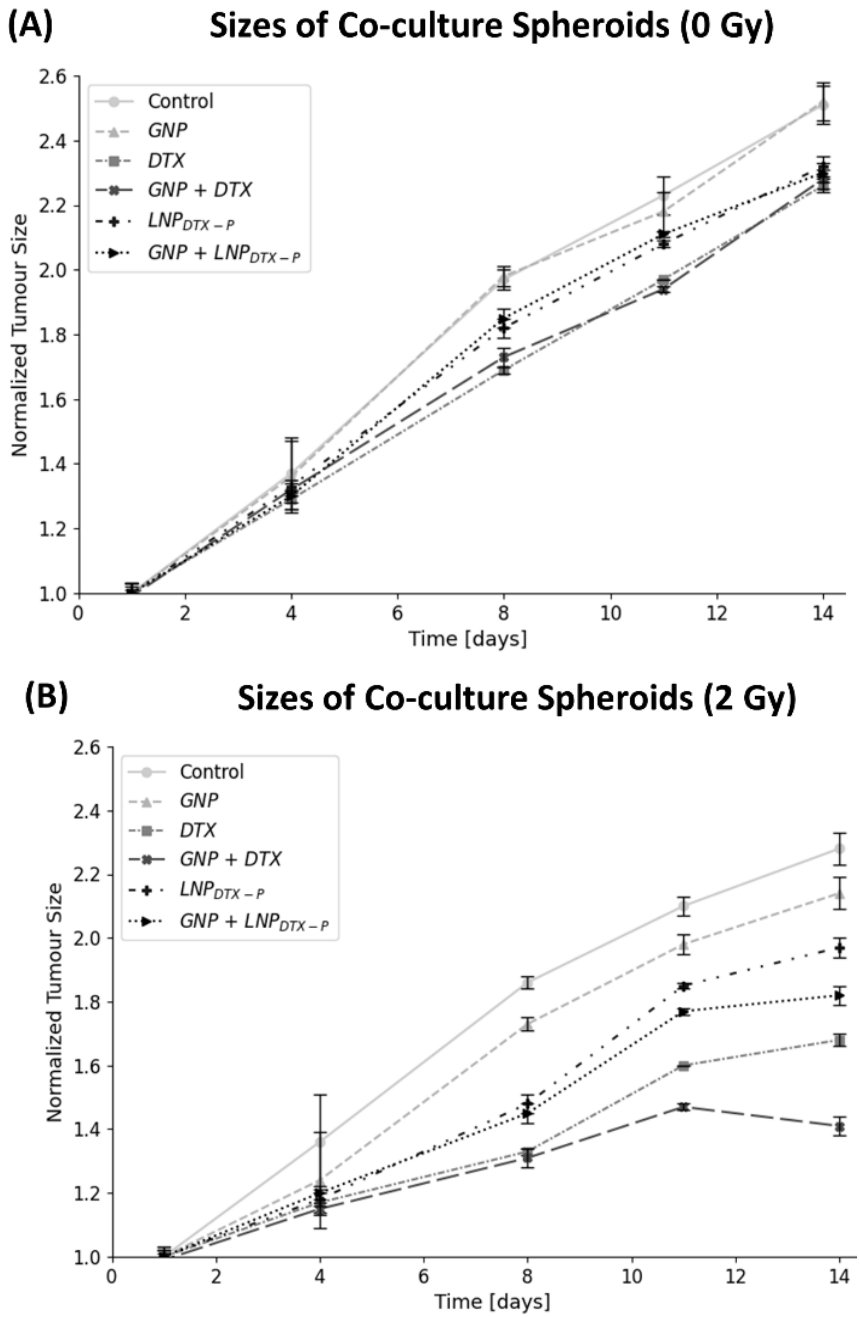

Figure 5.18 Co-culture spheroids sizes post-treatment with radiation/drug. **(A–B)** Normalized spheroids sizes over 14 days post-treatment: **(A)** 0 Gy, **(B)** 2 Gy. Reproduced with permission from open access Creative Common license [312].

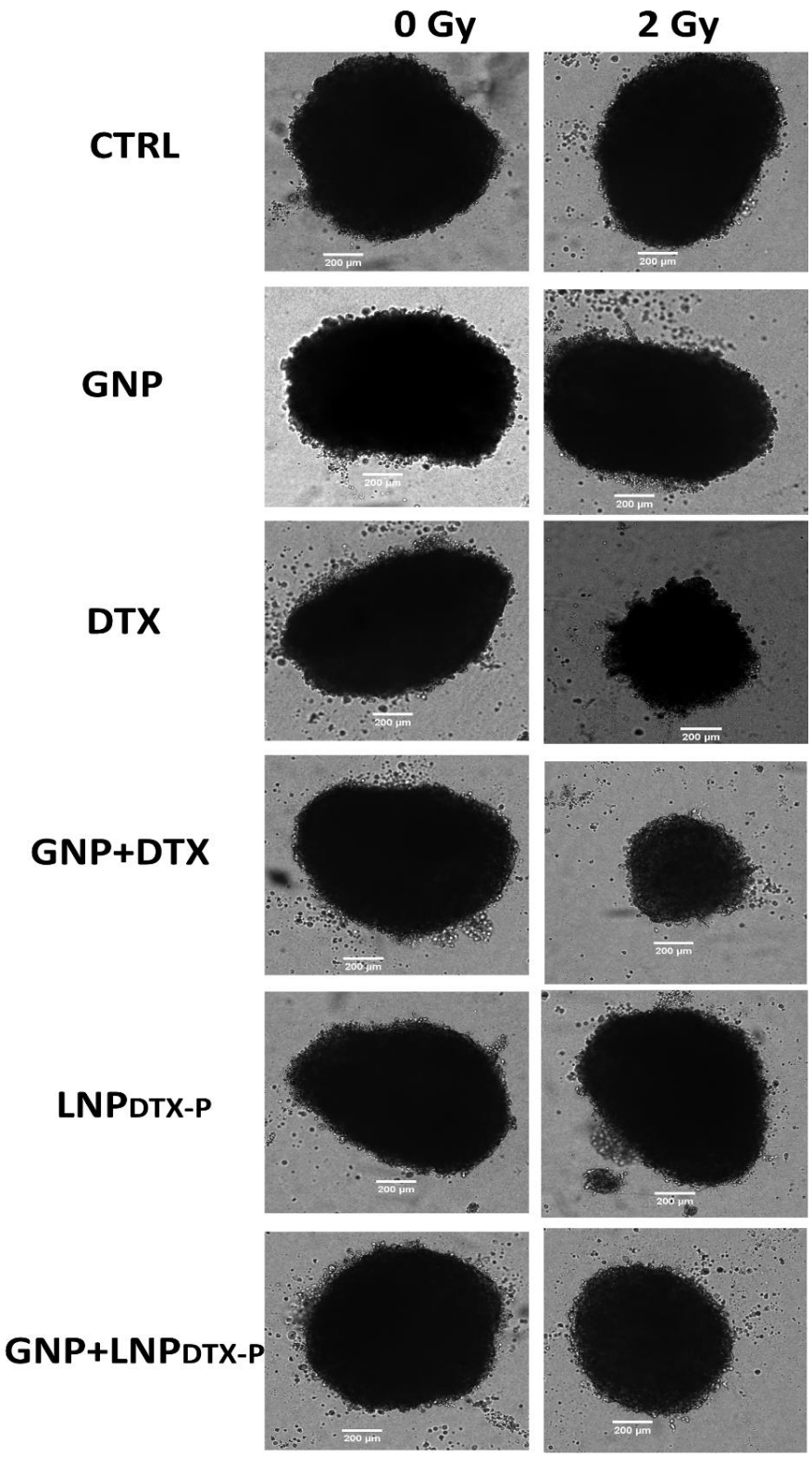

Figure 5.19 Bright-Field images of co-culture spheroids taken 14 days post-treatment. Scale bar: 200 µm. Reproduced with permission from open access Creative Common license [312].

To corroborate our prior findings, we performed 3D viability assays as depicted in **Fig 5.20** The outcomes of these assays align with the results obtained from tumor size measurements illustrated in **Fig. 5.19** and **Fig. S21.2** The results show the effectiveness of both DTX and LNP_{DTX-P} with and without radiation in co-culture and in monoculture. Without radiation, DTX resulted in a 40-45% decrease in cell proliferation for co-culture (**Fig. 5.20 left**) and monoculture (**Fig. S22 left**). However, with radiation and GNPs, DTX showed even further anti-proliferation effects causing a 60% and 56% decrease in cell proliferation in co-culture (**Fig. 5.20 right**) and monoculture (**Fig. S22 right**), respectively. Similarly, LNP_{DTX-P} resulted in a 33-35% decrease in cell proliferation with no radiation (co-culture (**Fig. 5.20 left**) and monoculture (**Fig. S22 left**)), while with radiation and GNPs, LNP_{DTX-P} caused a 46% and 43% decrease in cell proliferation in co-culture (**Fig. 5.20 right**) and monoculture (**Fig. S22 right**), respectively. This indicates the effectiveness of the triple combination in fighting the increased resistance in a co-culture system.

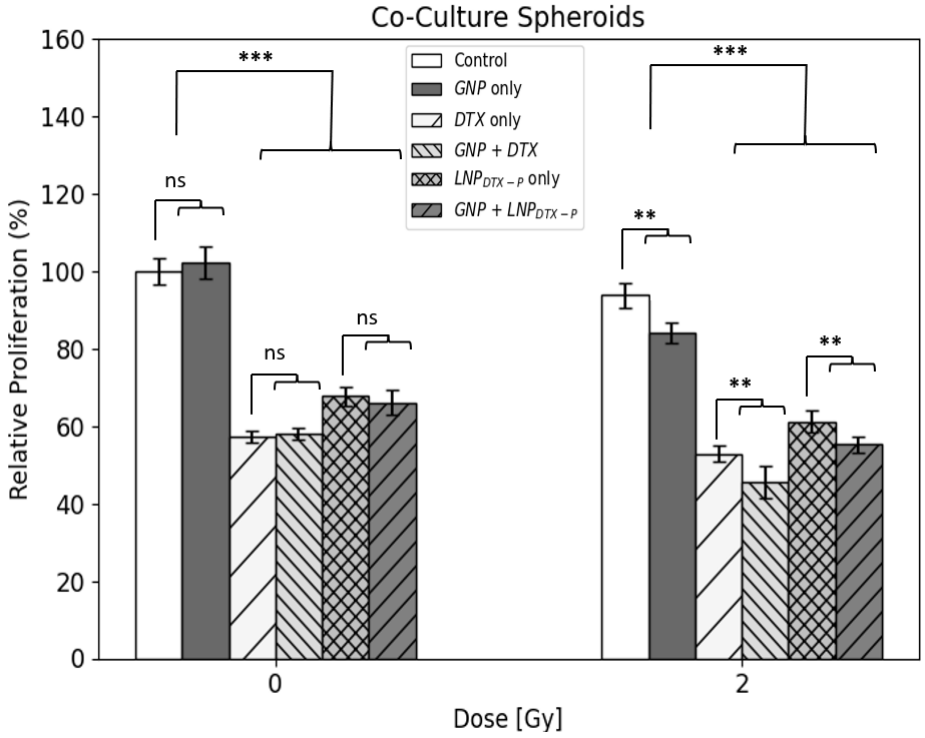

Figure 5.20 Co-culture spheroids relative cell proliferation at day 14 post-treatment. ns indicates non-significance, ** indicates $p < 0.01$, *** indicates $p < 0.001$. Reproduced with permission from open access Creative Common license [312].

The anticipated outcomes can be attributed to the radiosensitization effects of GNPs. When exposed to ionizing radiation, GNPs can interact with incoming photons and produce secondary electrons through a process known as the photoelectric effect [334]. These secondary electrons

have a relatively short range and high energy, which makes them highly damaging to nearby cancer cells and CAFs [334]. The secondary electrons can cause additional ionizations and create ROS within the cells. ROS, such as superoxide radicals and hydroxyl radicals, are highly reactive molecules that can induce oxidative stress and damage key cellular components, including proteins, lipids, and DNA. This includes interference with DNA repair mechanisms and cell cycle progression, ultimately resulting in decreased cell survival and increased apoptosis [335].

When comparing the performance of DTX to $LNP_{DTX\text{-}P}$, samples treated with DTX had a 16% (for monoculture) and 26% (for co-culture) increase in gold uptake. Both drugs have similar retention effects on cells, retaining roughly 65-70% of the initial gold amount. The effect of both drugs on cell synchronization was nearly identical, but DTX showed better tumor size control supported by lower cell proliferation. The mechanism of action of the drugs explained earlier perfectly supports our results of having an improved therapeutic outcome with the triple combination in both spheroidal samples. Although DTX is an effective drug on its own, it can cause severe toxic side effects to normal tissues [327]. To mitigate these side effects, we have developed LNPs that encapsulate DTX prodrugs in order to deliver it to the target cells in a safer and more effective manner. $LNP_{DTX\text{-}P}$ treatment can have certain advantages in terms of lower toxicity and longer circulation time [30, 31]. This is because the LNPs can selectively deliver the drug to the target cells, reducing the risk of systemic side effects in other parts of the body [57–59]. Furthermore, due to a longer circulation time and the EPR effect, more LNP and drug accumulation is expected at the tumor. This may also reduce the level or frequency of dosing required to achieve the therapeutic outcome, leading to improved patient compliance. Additionally, prodrugs of DTX have been shown to improve the bioavailability and solubility of DTX, which can increase its efficacy by improving its cellular uptake, enhancing its stability, and promoting its selective accumulation in tumor cells [336]. DTX prodrug can also reduce systemic toxicity by minimizing exposure to healthy tissues. It is very challenging to observe these effects *in vitro* and would require further *in vivo* studies.

5.2.4 *DNA DSBs in Co-culture & Monoculture*

To investigate the impact of radiation on our samples, we conducted an immunofluorescence assay specifically targeting DNA damage. We quantified 53BP1 foci 24 h after treatment and visualized the average number of DNA DSB foci per cell for different

conditions using confocal images highlighting 53BP1 foci in green and the nuclei in blue (**Fig. 5.21, Fig. 5.22,** and **Fig. S23**). With radiation, there was a minor increase in DNA DSB per cell in co-culture for DTX and $LNP_{DTX\text{-}P}$ without GNPs. However, when GNPs were used with the drugs and radiation, we see a significant increase in DNA DSB in both co-culture (**Fig. 5.21** and **Fig. 5.22**) and monoculture (**Fig. S23.1 and Fig. S23.2**). GNPs with radiation resulted in ~ 20% increase in DNA DSB per cell, GNPs with radiation and DTX resulted in ~ 42% increase in DNA DSB per cell, and GNPs with radiation and $LNP_{DTX\text{-}P}$ resulted in ~ 39% increase in DNA DSB per cell. In the absence of radiation, we observed no significant differences between the various conditions compared to the control group, both in the co-culture (**Fig. S23.3** and **Fig. S23.4**) and monoculture (**Fig. S23.5 and Fig. S23.6**). The observed results align with the proposed mechanism of action of GNPs described earlier. Coupled with DTX, the radiosensitizing effect increases through cell cycle synchronization in the G2/M phase and the increase in GNP accumulation in cells, resulting in higher sensitivity to RT causing more DNA DSB damage.

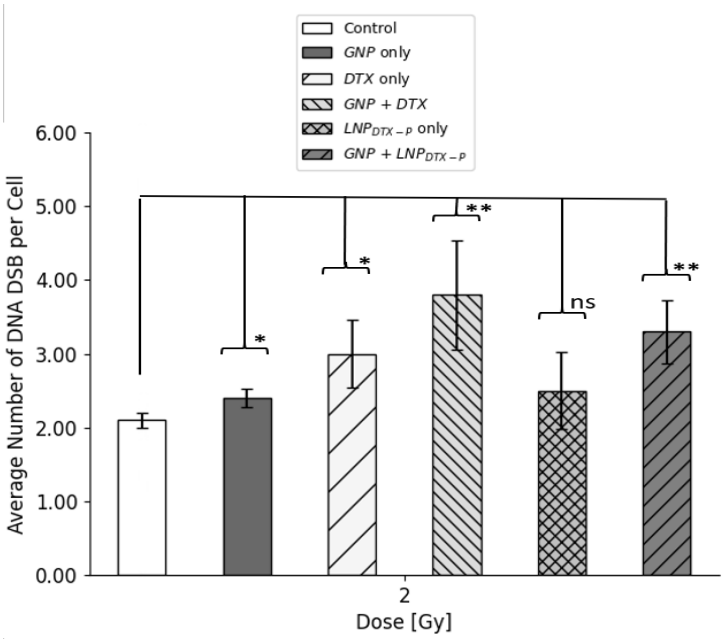

Figure 5.21 The average number of DNA DSB per cell in 2D co-culture with radiation following treatments with different agents**.** ns indicates non-significance, * indicates $p < 0.05$, ** indicates $p < 0.01$. Reproduced with permission from open access Creative Common license [312].

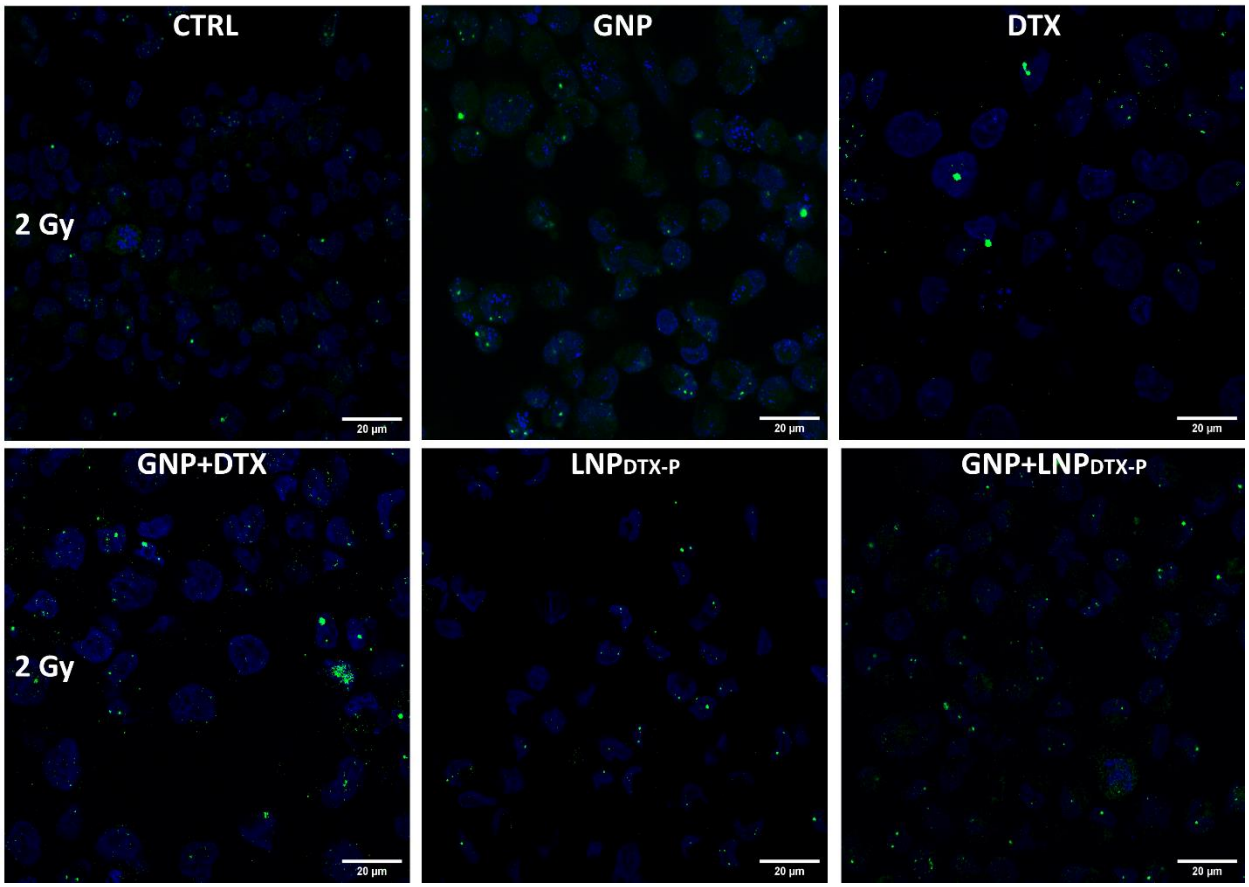

Figure 5.22 Confocal microscopy images of repair protein 53BP1 in the nucleus of irradiated co-cultures of MIA PaCa-2 and CAF-98. The cell nuclei are stained blue, while the green dots indicate DNA DSB damage. Scale bar: 20 µm. Reproduced with permission from open access Creative Common license [312].

5.2.5 GNPs*/RT/LNP$_{DTX-P}$ in Comparison to Higher RT Doses*

To assess the improvement of our triple combined modality compared to RT alone, we compared GNPs/2Gy/LNP$_{DTX-P}$ to 5 Gy and 10 Gy RT. The results are shown in **Fig. 5.23** for co-culture and **Fig. S24.1** for monoculture. In co-culture, samples treated with GNPs/2Gy/DTX were 19% smaller than ones treated with 5 Gy, but 8% larger than the ones treated with 10 Gy, whereas samples treated with GNPs/2Gy/LNP$_{DTX-P}$ were 6% and 37% larger than ones treated with 5 Gy and 10 Gy, respectively (**Fig. 5.23A**). Similarly, in monoculture, samples treated with GNPs/2Gy/DTX were 7% smaller than ones treated with 5 Gy, but 21% larger than the ones treated with 10 Gy, while samples treated with GNPs/2Gy/LNP$_{DTX-P}$ were 8% and 23% larger than ones treated with 5 Gy and 10 Gy, respectively (**Fig. S24.1A**). Qualitative brightfield images of the

spheroids 14 days post-treatment are shown in **Fig. 5.23B** for co-culture and **Fig. S24.1B** for monoculture.

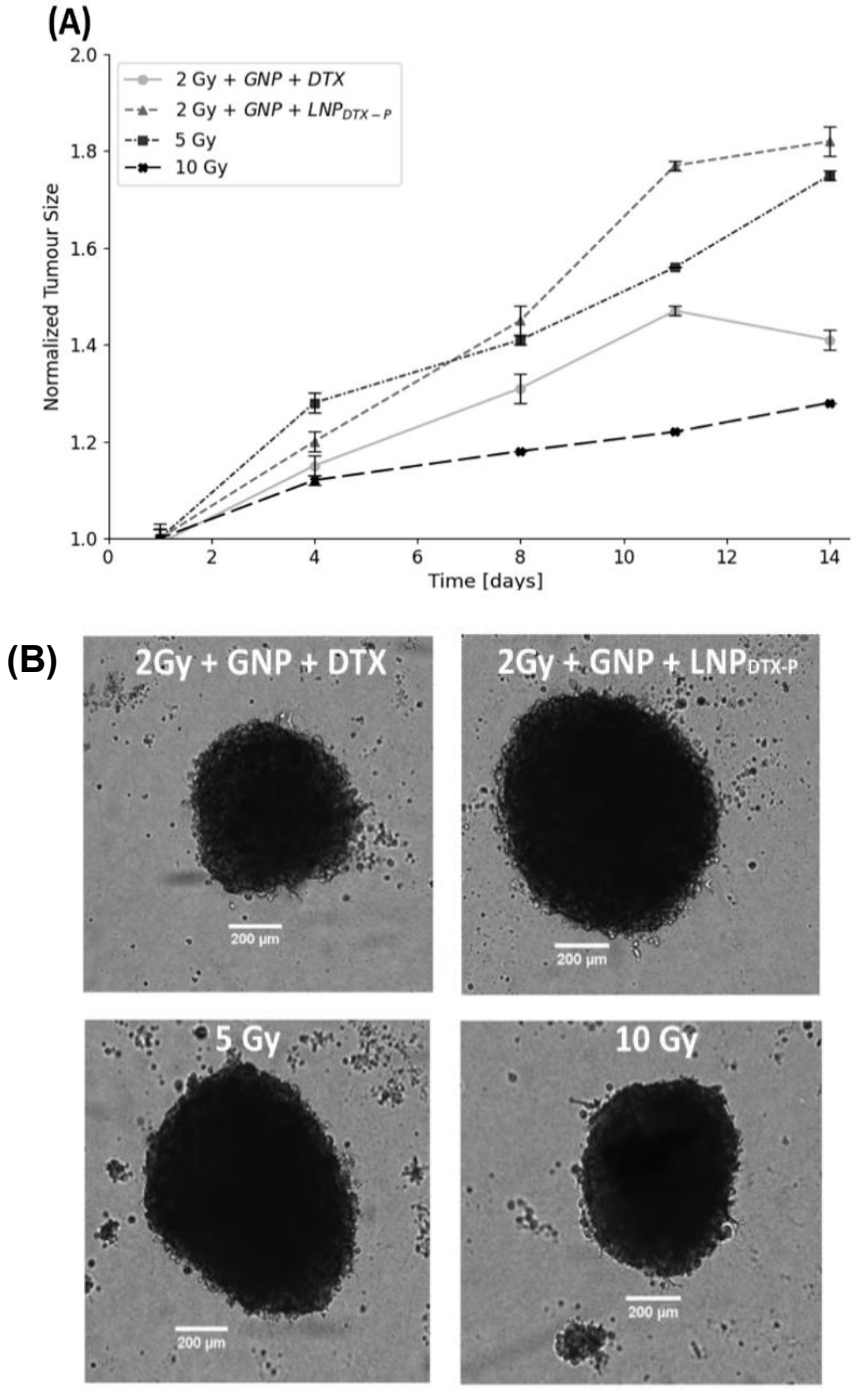

Figure 5.23 Irradiated co-culture spheroids sizes and DNA damage post-treatment. **(A)** Normalized irradiated co-culture spheroids sizes over 14 days post-treatment. **(B)** Bright-Field images of irradiated co-culture spheroids taken 14 days post-treatment. Scale bar: 200 µm. Reproduced with permission from open access Creative Common license [312].

Immunofluorescence assay shows a significant increase in DNA DSB for both 5 Gy and 10 Gy relative to that of GNPs/2Gy/LNP_{DTX-P} and GNPs/2Gy/DTX in both co-culture (**Fig. 5.24**) and monoculture (**Fig. S24.2**). Qualitative data showing the results in **Fig. 5.25** (co-culture) and **Fig. S24.3** (monoculture).

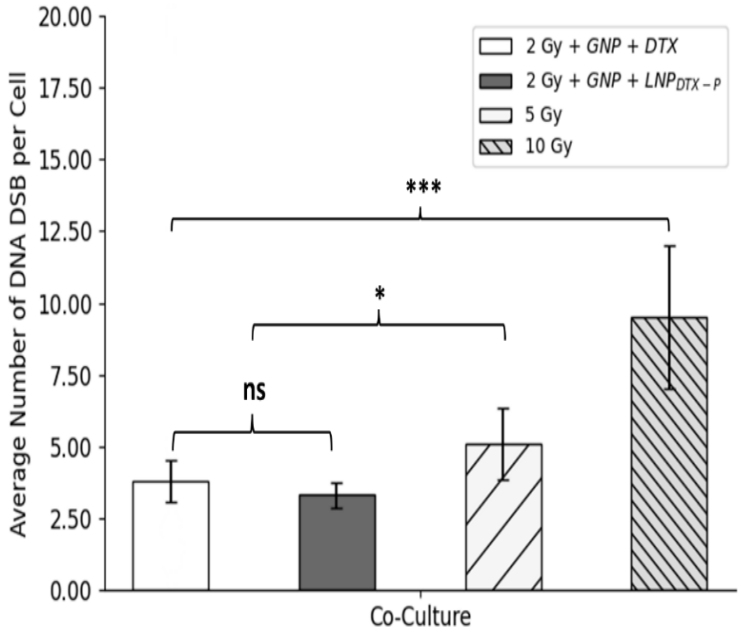

Figure 5.24 Irradiated 2D co-culture showing the average number of DNA DSB per cell. ns indicates non-significance, * indicates $p < 0.05$, *** indicates $p < 0.001$. Reproduced with permission from open access Creative Common license [312].

With respect to cell proliferation, for both co-culture (**Fig. 5.26**) and monoculture (**Fig. S25**), the survival fraction of the samples irradiated with 10 Gy was significantly lower than the rest. However, there was no significant difference between the cell viability of the samples irradiated with 5 Gy and that of the samples treated with GNPs/2Gy/DTX. Both had ~20% lower proliferation relative to the samples treated with GNPs/2Gy/LNP_{DTX-P}. When it comes to tumor size and cell proliferation, it is important to note that the addition of DTX to RT increases the number of senescent cells [337]. Although these cells are severely damaged, they are not completely non-functional and may still contribute to the signal through their metabolic activity, add to the size of the tumor, and not show as much DNA DSB damage. Despite that, these results are very promising as they showcase the comparability of the triple combination with high doses of RT. Taken together, DTX and LNP_{DTX-P} perform similarly in the presence of GNP and RT. Minor differences observed may be attributed to drug penetration into the spheroids. Considering

the extra risk of radiation-induced damage to healthy cells surrounding the tumor with higher radiation doses, the combined modality of our two radiosensitizers, GNPs & LNP_{DTX-P} with RT, might represent a more favorable option that would achieve similar results with lower toxicity.

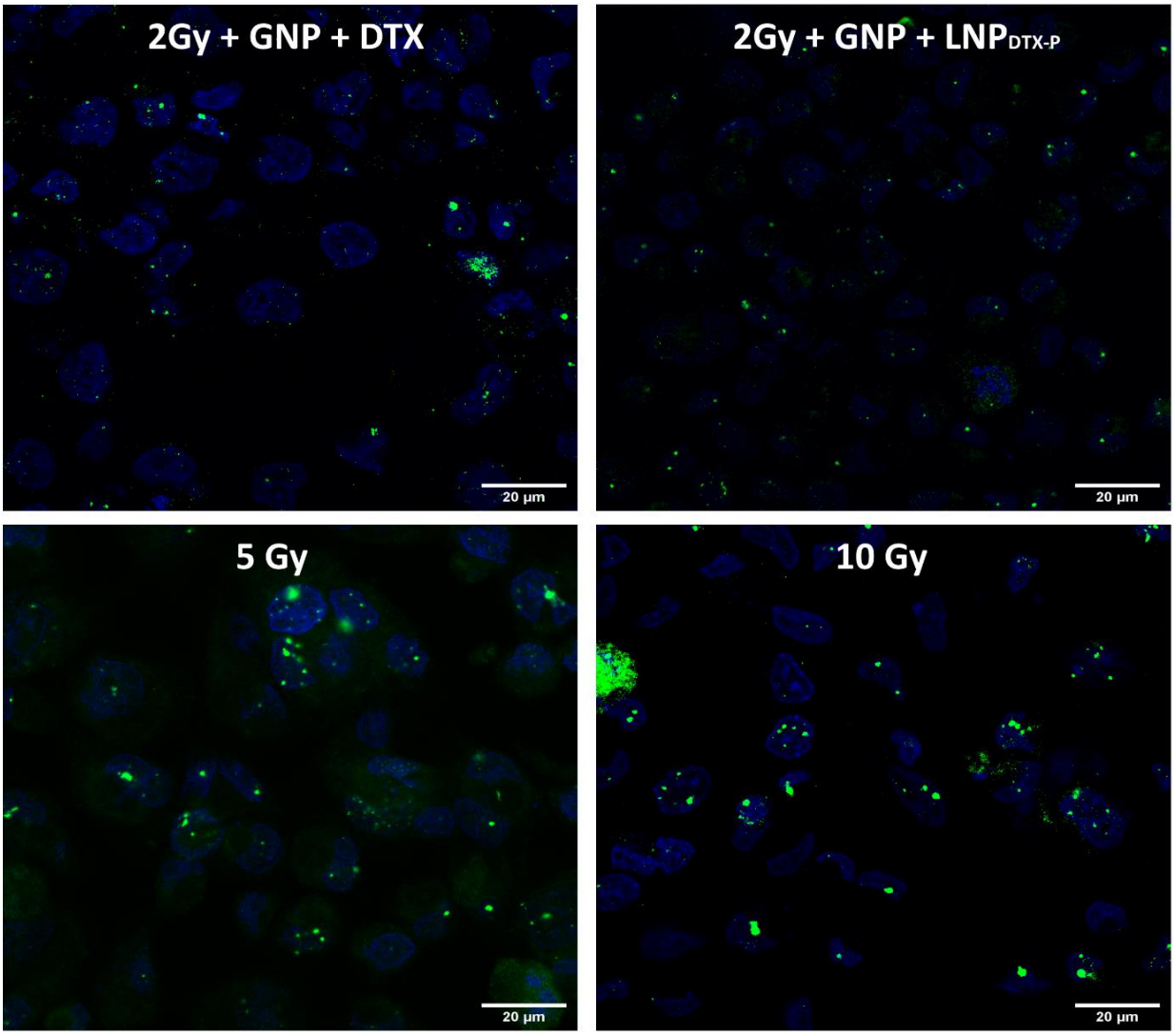

Figure 5.25 Confocal microscopy images of repair protein 53BP1 in the nucleus of co-culture of MIA PaCa-2 and CAF-98. Scale bar: 20 µm. The cell nuclei are stained blue, while the green dots indicate DNA DSB damage. Reproduced with permission from open access Creative Common license [312].

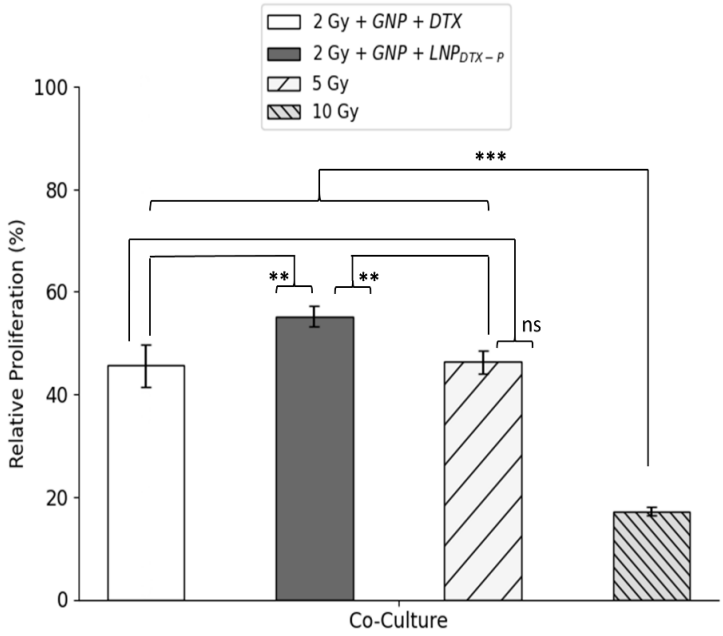

Figure 5.26 Co-culture relative cell proliferation at day 14 post-treatment. ns indicates non-significance, ** indicates $p < 0.01$, *** indicates $p < 0.001$. Reproduced with permission from open access Creative Common license [312].

5.2.6 Conclusions

An *in vitro* 3D co-culture spheroid model consisting of MIA PaCa-2 cancer cells and CAF-98 was used to evaluate the efficacy of combining clinically relevant doses of GNPs/RT/LNP_{DTX-P}. The findings of this study demonstrate the therapeutic benefits of utilizing GNPs and LNP_{DTX-P} in combination with RT highlighting their superiority compared to RT alone. GNPs functionalized with PEG and RGD demonstrate promising capabilities as radiosensitizers by improving the efficacy of RT through the production of damaging ROS in tumor cells. LNPs, on the other hand, can improve the effectiveness of the chemotherapy drug DTX by encapsulating DTX prodrug to create LNP_{DTX-P} and delivering it directly to cancer cells, reducing side effects and improving outcomes. DTX not only increases the number of gold radiosensitizers and their retention in cells but also aids in cell synchronization at the most radiosensitive phase. The collective effect of ROS production, DNA damage, and cell cycle arrest induced by GNPs/LNP_{DTX-P}/RT leads to enhanced radiosensitivity in cancer cells and CAFs. Hence, the triple combination produced a significant reduction in cell survival and tumor size. Additionally, we showed that the use of radiosensitizers may reduce the overall radiation dose needed to achieve the same therapeutic effect, thereby decreasing the risk of radiation toxicity and side effects. This synergistic interaction between

GNPs, LNP_{DTX-P} and RT offers the potential for improved therapeutic outcomes in cancer treatment, as it targets both tumor cells and the tumor microenvironment.

5.3 Chapter 5 Conclusions

Current chemoradiation therapy suffers from normal tissue toxicity. Thus, we are proposing incorporating GNPs and DTX as they have shown very promising synergetic radiosensitization effects. We first explored the effect LNP_{DTX-P} on GNP uptake in pancreatic cancer models *in vitro* and *in vivo*. For the *in vitro* experiment, pancreatic cancer cell line, MIA PaCa-2, were cultured and dosed with 7.5 μg/mL of GNPs and with 45 nM of free DTX or an equivalent dose of LNP_{DTX-P}. For the *in vivo* experiment, MIA PaCa-2 were implanted subcutaneously in NRG mice and the mice were dosed with 2 mg/kg of GNPs and 6 mg/kg of DTX or an equivalent dose of LNP_{DTX-P}. The results show that LNP_{DTX-P} treated tumour samples have double the amount GNPs compared to control samples in both *in vitro* and *in vivo*. The second objective was to assess the anticancer effectiveness of GNPs and LNP_{DTX-P} with RT. The study utilized a co-culture spheroid model comprising MIA PaCa-2 cancer cells and CAF-98 to mimic pancreatic cancer conditions. The spheroids underwent treatment with GNPs (7.5 μg/mL), LNP_{DTX-P} (99 nM of DTX prodrug), and 2 Gy of RT. Although GNPs/RT and RT/LNP_{DTX-P} showed a reduction in spheroid size and an increase in DNA DSB damage, the combination of the two NPs, GNPs and LNP_{DTX-P}, with RT significantly enhanced the anti-cancer efficacy resulting in a 28% decrease in spheroid size and a 39% increase in DNA DSB. The combination of GNPs and LNP_{DTX-P} with RT showed a collaborative effect due to their radiosensitizing properties improving the therapeutic efficacy of each treatment modality alone. The results are very promising as LNP_{DTX-P} have superior targeting of tumour tissues compared to free DTX due to their nano size and their ability to be functionalized. Because of their minimal toxicity to normal tissues, both GNPs and LNP_{DTX-P} can be ideal radiosensitization candidates in RT. This triple modality offers a hopeful strategy to improve cancer treatment efficacy while reducing adverse effects.

5.4 Materials and Methods

5.4.1 GNPs *Synthesis, Functionalization, and Characterization*

The citrate reduction method was used to make GNPs of sizes around 13 nm diameter. 2.36 mL of 1% Tetrachloroauric (III) acid trihydrate was mixed with 57.64 mL of water and heated. Once boiled, 2.4 mL of 5% sodium citrate tribasic dihydrate was added and left for 10 min until the solution color shifted to red where then the solution is stirred at 20 **°C** for 15 min. For functionalization, PEG size 2000 Da, and RGD size 1600 Da were used at a surface density of 1 PEG per nm^2 GNP surface area and 1 RGD for every 2 PEG. For confocal imaging, PEG-thiol-CY5 was added to the GNP. Perkin Elmer λ 365 UV-VIS spectrophotometer was used to approximate the size and concentration of the NPs. The surface charge and hydrodynamic diameter were determined using ζ potential and DLS (Anton Paar LiteSizer 500).

5.4.2 LNPs Synthesis and Characterization

LNPs were prepared by rapid mixing [313]. Briefly, DSPC, cholesterol, PEG-DSPE, and DTX prodrugs were dissolved in ethanol to a final molar ratio of 49:40:1:10 and a final lipid concentration of 10 mM. For formulations that contain less than 10 mol% DTX prodrug, DSPC and cholesterol were increased to compensate. The lipids in ethanol are mixed with PBS (pH=7.4) at a flow ratio of 1:4 (v:v) and a total flow rate of 40 mL/min. The resulting mixtures were dialyzed against a 1000-fold volume of PBS overnight and sterile-filtered (0.2 μm). DSPC and PEG-DSPE were purchased from Avanti Polar Lipids (Alabaster, AL) and cholesterol was obtained from Sigma–Aldrich (St. Louis, MO). DTX was obtained from eNovation Chemicals (Bridgewater, NJ). Refer to the supplementary section for synthesis of DTX prodrugs (**Fig. S26**). Particle size was determined by dynamic light scattering using a Malvern Zetasizer NanoZS (Malvern Instruments, Worcestershire, UK). Lipid concentrations were determined by measuring the cholesterol content of the LNPs (Cholesterol E Assay, Wako Chemicals, Richmond, VA) or their phospholipid content (Phospholipids C Assay, Wako Chemicals). The quantity of DTX prodrug was determined by ultra-performance liquid chromatography (UPLC) on a Waters Acquity H-Class UPLC System equipped with a BEH C18 column (1.7 μm, 2.1 × 100 mm) and a photodiode array detector. Separation was achieved at a flow rate of 0.5 mL/min with a linear gradient of mobile phases of

acetonitrile: water from 20:80 to 100:0 (v:v) over 3 min followed by an isocratic hold at 100:0 for an additional 3 min. The column temperature was maintained at 55 °C. The absorbance at 230 nm was measured, and the analyte concentration was determined using calibration curves. Prodrug entrapment was determined by comparing prodrug cholesterol ratios in the final LNPs to that of the initial lipid mixtures. Cryogenic transmission electron microscopy was performed by the High-Resolution Macromolecular Cryo-Electron Microscopy Facility at The University of British Columbia (Vancouver, BC).

5.4.3 Cell Culture & Spheroid Formation

Human pancreatic cancer cell line MIA PaCa-2 (ATCC#: CRL-1420™) was used. For both *in vitro* and *in vivo* studies, cell cultures of passages 3 to 10 and a confluence of 90% were used. For *in vitro* experiments, cultured cells were supplied with high glucose DMEM (Gibco, ThermoFisher Scientific, Waltham, MA, USA) enhanced with 10% FBS (Gibco), and 4 mM of GlutaMax (Gibco). For *in vivo* experiments, cells were cultured in Ham's F12 medium (Gibco) enhanced with 2 mM L-glutamine (Gibco) and 10% FBS (Gibco). For cell detachment from flasks TrpyLE (Gibco) was used. For cell fixation, PFA (Sigma Aldrich, Oakville, ON, Canada) was used. For cell washing, PBS was used. All cell incubations were at 37 °C with 5% CO_2.

For 2D co-culture experiments, cells were seeded at a 5:1 ratio of CAF-98 to MIA PaCa-2 and incubated for three days before initiating the experiments. Regarding 3D spheroid cell cultures, cells were plated in ultra-low attachment 96-well microplates (Corning, NY, United States). Each well contained 6000 cells for MIA PaCa-2 monocultures and 1800 cells for CAF-98 monocultures, resulting in a spheroid size of approximately 400 µm. To facilitate spheroid formation, the media was supplemented with 3% Geltrex matrix (Gibco) on ice. For co-culture spheroids, 300 MIA PaCa-2 and 1500 CAF-98 cells were seeded per well, and the cells were centrifuged at 350xg for 5 minutes at 4°C. Afterward, they were incubated at 37°C with 5% CO_2. Experiments were initiated once the spheroids had formed, following a 3-day incubation period.

5.4.4 Drug Cytotoxicity Assay

Cytotoxicity assay was used to determine the IC-50 of DTX, and $LNP_{DTX\text{-}P}$ in MIA PaCa-2 2D monolayer monocultures and in MIA PaCa-2 monoculture 3D spheroids. For the 2D

monoculture, 3 black-walled clear-bottom 96-well plates (Greiner, Kremsmünster, Austria) were used for each drug. Approximately, 10000 cells were seeded in each well and 100 µL of media was added, leaving one column empty for control, and covered with a breathable membrane to reduce evaporation (Breathe-Easier Membranes, Sigma-Aldrich; St. Louis, Missouri, United States). 24 h post-seeding, the drugs were serially diluted into each column of wells with doses ranging from 1000 nM to 0.01 nM for DTX, and 10000 nM to 0.01 nM for $LNP_{DTX\text{-}P}$. After 24 hours of treatment, the membrane was discarded, and the media in each well was replaced and then rinsed with PBS. Cell viability was assessed 2 days after drug dosing using media containing 10% *v/v* resazurin dye (PrestoBlue, Thermo-Fisher, Waltham, MA, USA) following a 30 min incubation with the dye. PrestoBlue is a colorimetric cell viability assay, which measures the metabolic activity of viable cells by detecting the reduction of resazurin dye to resorufin. The level of color change is directly proportional to the number of viable cells [338]. Using a Biotek Cytation 1 plate reader (Agilent Technologies, Santa Clara, CA, United States) fluorescence was measured with filters set at Excitation 530/25 nm and Emission 590/35 nm.

Similarly for the 3D cell culture, once the 3D spheroid models were formed, the drugs were serially diluted into each column of wells with doses ranging from 1000 nM to 0.01 nM for DTX, and 10000 nM to 0.01 nM for $LNP_{DTX\text{-}P}$. 24 h post-treatment, approximately half of the media in each well was removed not to disturb the spheroids, rinsed with PBS 5 times, new fresh media was added, and plates were incubated. 48 h post-incubation, media was taken off each well leaving only 100 µL of media, and then 30 µL of CellTiter-Glo 3D (Promega, Madison, WI, United States) was added to each well. Following 0.5 h-incubation period, fluorescence was measured using Biotek Cytation 1 plate reader (Agilent Technologies, Santa Clara, CA, United States).

5.4.5 Preparation of Cells for Imaging

Approximately, 5 x 10^4 cells were seeded in 35 mm coverslip-bottom dishes (MatTek, Ashland, MA. US) with 2 mL of media and were incubated for 24 h. One day post seeding, the cells were dosed with $GNP_{PEG\text{-}CY5\text{-}RGD}$ at 7.5 µg/mL, and with the IC-50 dose of either DTX, $LNP_{DTX\text{-}1}$, or $LNP_{DTX\text{-}2}$, concurrently. 16 h prior to imaging, the tubulin stain CellLight™ Tubulin-GFP (BacMam 2.0, ThermoFisher Scientific, Waltham, MA. US) was added. 24 h post-treatment, 4 drops of live reagent (DAPI) NucBlue® (ThermoFisher Scientific, Waltham, MA. US) were added per dish and were incubated for 20 min. Live cells imaging was performed using oil-

immersion 60X lens of confocal microscopy (Zeiss LSM 980,Carl Zeiss Microscopy GmbH, Jena, Germany).

The 3D samples were imaged using a 20X lens of the Confocal microscopy (Zeiss LSM 980, Carl Zeiss Microscopy GmbH, Jena, Germany). Once the 3D spheroids were formed they were treated with GNPs and drugs. Subsequently, they were transferred to 35 mm coverslip-bottom dishes (MatTek, Ashland, MA, USA) with a minimal amount of media to prevent aspiration and ensure stability during the imaging process. To make the gold visible, the GNPs were labeled with CY5 fluorescent dye molecules.

5.4.6 Cell Proliferation Assay & Spheroid Size

After the radiation treatment, a cell proliferation assay was conducted for 3D spheroids at days 1 and 14 post-treatment using CellTiter-Glo 3D (Promega, Madison, WI, United States) and a Biotek Cytation 1 plate reader, following the procedure detailed in *section 5.4.4*. To determine the size of the spheroids after radiation treatment, brightfield images of the spheroids were captured every 3 days using the 4× objective of the Biotek Cytation 1 plate reader (Agilent Technologies, Santa Clara, CA, United States). The average diameter of the spheroids was calculated manually with the assistance of ImageJ.

5.4.7 Immunofluorescence Assay

Monoculture and co-culture cells were cultured in 6-well dishes on glass coverslips. 24 hours after the radiation treatment, the samples were washed with PBS and then fixed with 4% PFA for 5 minutes. Subsequently, the cells were rinsed with PBS and washed with 2% BSA/0.1% Triton-X for a 20-minute incubation. To assess DNA DSBs, an optically labeled antibody against the repair protein, 53BP1, was used. The 53BP1 primary antibody was diluted 1:200 in 0.5% BSA/0.1% Triton-X/PBS, while the secondary antibody was diluted 1:500 in 0.5% BSA/0.1% Triton-X/PBS. The samples were first incubated with the primary antibody for 1 hour, followed by rinsing with PBS. Then, the samples were washed with 0.5% BSA/0.175% Tween-20/PBS for 5 minutes and incubated with the secondary antibody for 30 minutes in the dark. After the incubation, the samples were washed with PBS and mounted onto glass coverslips using ProLong™ Glass Antifade Mountant and NucBlue™ Fixed Cell ReadyProbes™ Reagent (DAPI)

from Invitrogen, Waltham, MA, United States. Imaging of the 53BP1 foci was performed through confocal microscopy (Zeiss LSM 980) using a 60× oil immersion lens. At least fifty nuclei were assessed, and the number of DSB foci per cell was measured.

5.4.8 Xenograft Model

For the *in vivo* experiments, NRG male mice ages 6-10 weeks old were purchased from the BC Cancer Research Institute Animal Resource Centre (ARC). Mice were caged in autoclaved Allentown ventilated caging at a capacity of 2-4 animals/cage for the length of the study. Cages were changed bi-weekly and included Nestlets (Ancare) as environmental enrichment, transparent tinted polycarbonate Mouse Igloos (Bio-Serv), and Envigo 7097 ¼" corn cob bedding. All enrichment is added to the cage prior to the cages being autoclaved. Mice are fed Envigo Teklad Global Rodent Diet 2920. The rodent food is kept in the hoppers of the wire lids and is changed bi-weekly. Reverse osmosis water is supplied through Avidity Science automatic watering valves at a flow rate of 25-50 mL/min. Environmental control of the lights and monitoring of temperature, humidity, and airflow is done by WatchDogEX™. On the first day of the experiment, 5 x 10^6 tumour cells were implanted subcutaneously into each mouse's back. The volume of tumours was determined using this formula: $L \times W^2 \times 0.5$.

5.4.9 Treatment of Xenograft Model

The mice were randomly assigned to 5 study groups: A. untreated, B. $GNP_{PEG–RGD}$ only, C. $GNP_{PEG–RGD}$ & LNP_{DTX-1}, D. $GNP_{PEG–RGD}$ & LNP_{DTX-2}, and E. $GNP_{PEG–RGD}$ & free DTX. For group A., 6 mice were allocated to measure MIA PaCa-2 tumour growth kinetics. For the remaining groups (B-E), 12 mice were allocated for each group, with 4 mice per three different time points: 8, 24, and 48, hours after dosing. Treatment of mice to assess for pharmacokinetics in blood and tissue biodistribution began when the tumours were 250-300 mm^3. GNPs and the drugs were administered concurrently and intravenously. $GNP_{PEG–RGD}$ were dosed at 2mg/kg of mouse. Docetaxel (Sandoz) was supplied in 10 mg/mL solution that has 96% Citric Acid, ethanol, PEG 300, and polysorbate 80. The dose for DTX was 6 mg/kg of mouse. Both LNP_{DTX-1} & LNP_{DTX-2} were provided in 4.5 mg/ml of PBS and dosed at 6 mg/kg of mouse.

5.4.10 Pharmacokinetic Tissue Sampling

Mice were individually weighed and injected with the treatments, as described in the previous section, according to the study group, and blood was sampled. Once at the experimental endpoint, mice were euthanized according to approved animal care protocol, terminal blood was collected by cardiac puncture, and tissues were harvested. For hematology, whole blood from the endpoint cardiac puncture of 1 of 4 mice was placed into a K2 EDTA tube, gently inverted a minimum of 8-10 times to ensure no clotting occurred, and then placed on ice. Samples were sent to IDEXX for complete blood count (CBC) analysis after collection. For each time point, 50% of the tumour from 2 out of 4 mice was collected into 10% neutral buffered formalin for histopathology, while all mice had 50% of their tumours frozen for use in the biodistribution study. The entire tumour of 2 out of 4 mice from each time point was placed in 70% ethanol for further cell cycle analysis. Similarly, 1 out of 4 mice in each time point was used for organ histopathology, where the liver, spleen, and kidneys were placed in 10% neutral buffered formalin, and 3 out of 4 mice had these organs and blood plasma frozen for use in the biodistribution study.

5.4.11 Histopathology

10% neutral buffered formalin-fixed tissues were processed into paraffin overnight using an automated tissue processor, embedded, and sectioned at 4um. Two slides were collected from each of the two levels spaced 50um apart. Half of the slides were simply coverslipped with a resinous mounting medium for DF imaging, and the other half were stained with H&E and coverslipped according to standard procedures for brightfield imaging. DF coupled with HSI CytoViva microscope (CytoViva, Auburn, AL, USA) was used to determine GNP localization within cells. Half of the slides were simply coverslipped with a resinous mounting medium for DF imaging, and the other half were stained with H&E and coverslipped according to standard procedures for brightfield imaging. DF coupled with HSI CytoViva microscope (CytoViva, Auburn, AL, USA) was used to determine GNP localization within cells.

5.4.12 Cellular Uptake of GNPs

24 h following cell seeding or spheroids formation, cells were dosed at 7.5 μg/mL of $GNP_{PEG–RGD}$, and with the IC-50 dose of DTX, or equivalent DTX dose of LNPs, concurrently.

Cells were then incubated for 24 h. After the 24 h incubation period, the uptake plates were ready for processing while the media of the retention plates was changed, and cells were further incubated for their respected period of time.

For the 2D cell cultures, cells were washed 3 times with PBS, trypsinized, and incubated for 5 min. Media was then added to the cells, and they were counted using a hemocytometer counting chamber and transferred to glass tubes for processing. Cells were then treated with aqua regia and heated in a mineral oil bath at 90 ℃ for 30 min. For each tube, 100 μL of hydrogen peroxide was added and then incubated in a mineral oil bath for another 30 min. The samples were then diluted in deionized water.

For the 3D samples, the samples were washed with PBS five times and then incubated at 37°C in trypsin-EDTA (Gibco) for 1 hour to facilitate the breakdown of the spheroids. The cells were manually counted using a hemocytometer. Following cell counting, the samples were diluted in 5 mL of Millipore water and then treated with 250 μL of aqua regia for every 500 μL of the sample. The samples were placed in a mineral oil bath at 90°C for approximately 2 hours. Next, 100 μL of hydrogen peroxide was added to each sample, and they were returned to the oil bath for an additional hour. After this, the samples were diluted with deionized water to attain a 2.5% v/v acid content.

For the *in vivo* samples, the samples were weighed and blended with 2 mL of TrypLE and were left to break down. The samples were then diluted in millipore water and treated with 250 μL aqua regia per 500 μL of each sample in a 90 °C mineral oil bath for a minimum of 2 h. The samples were then diluted to 2.5% in deionized water before being filtered in a 0.2-micron filter (Fisher). ICP-MS (Agilent 8800 Triple Quadrupole) was utilized to quantify the amount of gold in all samples.

5.4.13 Cell Cycle Analysis

For the 2D *in vitro* experiment, cells were cultured in 60 mm dishes with 5 mL of media and were incubated for 24 h. Cells were then treated with the IC-50 dose of DTX, or the equivalent DTX dose of LNPs. After their corresponding incubation times, cells were trypsinized and neutralized in media. For the *in vivo* experiment, the samples were treated with Collagenase/Dispase (Roche) for two hours. The samples were then filtered through a 100-micron cell strainer. For the 3D spheroids, following the spheroids formation, the drugs were administered

at the IC-50 dose. The samples were incubated with the drugs for no more than 24 h, then either the media was changed, or the samples were processed. Following the treatment, the samples were washed with PBS 5 times and were incubated at 37°C in trypsin-EDTA (Gibco) for 1 h to help with breaking down the spheroids. All samples were then proceeded as described next.

All samples were centrifuged at 350× *g* for 5 min at 4°C. The cell pellets were then washed with PBS and centrifuged again at 350× *g* for 5 min at 4 °C. Cells were then fixed with PFA and incubated in the fridge for 15 min. The samples were then centrifuged at 350× *g* for 5 min at 4°C, washed with PBS, and centrifuged again at 350× *g* for 5 min at 4 °C, before being resuspended in 70% ethanol and incubated at –20°C for 2 days. After that, the samples were centrifuged at 350× *g* for 10 min at 20°C, washed with 0.5% BSA in PBS, and then centrifuged at 350× *g* for 5 min at 20°C. Following that, the samples were incubated on a shaker with PBTB (PBS, 0.5% BSA, 0.1 % Triton-X 100) and RNaseA at 37 °C for 25 min. Then propidium iodide was added to the samples and incubated on a shaker at 4°C for 60 min. After that, the samples were centrifuged at 350× *g* for 10 min at 20 °C. Finally, the samples were resuspended in PBS/BSA and filtered using a 50 µm cell strainer. The samples were run on a flow cytometer (FACS Calibur, BD Biosciences, Franklin Lakes, NJ, USA).

CHAPTER 6

CONCLUSIONS & PROSPECTIVE RESEARCH

6.1 Conclusions

Despite significant progress in radiotherapy (RT), chemotherapy, and surgical techniques over the past decade, pancreatic cancer remains one of the most lethal forms of cancer, with a mortality rate approaching 93%. Currently, surgical intervention stands as the most effective curative option; however, due to the aggressive and metastatic characteristics of pancreatic cancer, about 80% of patients are not surgical candidates. In the case of radiotherapy, the challenge lies in the tumor's proximity to vital organs, which limits the treatment dose to avoid substantial tissue toxicity. This limitation hampers the dose escalation necessary for effective local control. As for chemotherapy, the tumor microenvironment (TME)—comprising stroma cells and extracellular matrix—acts as a barrier that inhibits the effective dispersal of chemotherapeutic agents, thereby reducing their impact. Given these challenges, there's a pressing need for innovative, more effective treatment paradigms for such hard-to-treat cancers.

Nanotechnology offers an innovative pathway to address the persistent challenges associated with treating pancreatic cancer. Nanoparticles (NPs), particularly gold nanoparticles (GNPs) functionalized with polyethylene glycol and RGD, have shown significant potential as radiosensitizers in RT and as vehicles for targeted chemotherapy. These NPs are introduced into the bloodstream and selectively accumulate in tumors, capitalizing on the leaky vasculature inherent in the TME. Our research has found that such functionalized GNPs are highly effective at targeting specific receptors on the surface of pancreatic cancer cells and cancer-associated fibroblasts (CAFs). Importantly, the PEG-RGD coating helps the nanoparticles evade immune detection, enhancing their retention within tumor tissues *in vivo*. Furthermore, our studies

demonstrate that these GNPs, when exposed to clinically relevant doses of ionizing radiation, significantly increase DNA damage, leading to more effective cancer cell eradication.

Lipid nanoparticles (LNPs) serve as promising drug delivery platforms that can enhance the efficacy and safety profile of cancer drugs. In our research, we successfully loaded docetaxel (DTX), a commonly used chemotherapy drug, into these LNPs to enhance its targeted delivery to tumor cells. Further, we engineered a prodrug form of DTX that is less toxic to normal tissues when compared to the free drug, and we encapsulated this version in LNPs ($LNP_{DTX\text{-}P}$). This unique formulation enabled LNPs to specifically target and accumulate in cancer cells, releasing the DTX payload within the cells for maximum therapeutic impact and minimal toxicity. Moreover, our studies revealed that at clinically relevant concentrations, DTX not only interferes with microtubule (MT) structures within cancer cells—thereby facilitating greater accumulation of GNPs—but also arrests cancer cells in the G2/M phase, which is known to be the most radiosensitive part of the cell cycle. This synergy makes the combination of GNPs and $LNP_{DTX\text{-}P}$ an exceptionally effective duo of radiosensitizers.

In this study, we showcased the effective synergy between RT and two radiosensitizing agents: GNPs and $LNP_{DTX\text{-}P}$. Our findings covered both 3D monoculture spheroids and more resilient co-culture spheroids. The combined GNP/RT/$LNP_{DTX\text{-}P}$ treatment demonstrated a significantly enhanced therapeutic outcome, offering the possibility to decrease both the RT and chemotherapy doses. This reduction has the potential to minimize damage to normal tissues, a crucial consideration for future clinical applications. This innovative treatment approach could be utilized either as a standalone regimen or combined with other innovative therapies, such as immunotherapy. The synergistic benefits of this combined modality could pave the way for a new generation of chemoradiation treatments, potentially revolutionizing cancer therapy and ultimately improving patient survival rates.

6.2 Prospective Research

Numerous avenues for future research stem from our current findings. These possibilities range from evaluating our combined therapy approach on more sophisticated models, to integrating it with alternative treatment strategies, or enhancing its targeting capabilities. In the following sections, we will delve into some of these promising directions.

6.2.1 Alternative Radiosensitizers for Enhanced Treatment Efficacy

Significant efforts have been put into the creation of radiosensitizers that synergize well with RT. Established chemical radiosensitizers like cisplatin, DTX, paclitaxel, gemcitabine, capecitabine, and bleomycin are widely used. Additionally, emerging compounds like derivatives of piperlongumine are under investigation. These newer agents have the potential to elevate levels of ROS and modulate the Keap1-Nrf2 defense pathway, thereby enhancing radiation-induced DNA damage, promoting cell cycle arrest in the G2/M phase, and triggering apoptosis [339]. Here we will go over chemical radiosensitizers and DNA repair inhibitors that have shown successful synergistic effect when used with GNPs.

6.2.1.1 Cisplatin

Another successful anticancer drug that is widely used today in conjugation with RT is *cis*-diamminedichloroplatinum (II), also known as cisplatin [340]. The anti-tumor properties of cisplatin were established in 1970, and the drug was approved by the FDA in 1978 [341–344]. This chemotherapeutic drug is used to treat ovarian, cervical, head and neck, esophageal, non-small cell lung, and testicular cancers [345–349]. The uptake pathway of this drug is known to be through passive diffusion [350]. Eljack et al. showed that cisplatin is capable of passive diffusion across the lipid bilayer membrane [351]. The structure of cisplatin (cis-$[PtCl_2(NH_3)_2]$) has no net charge and is stable in the blood stream and in the extracellular matrix [350, 351]. Once the compound enters the cytoplasm, the chloride ions dissociate from the platinum ion allowing it to react with cellular targets [350, 351].

It is generally accepted that the primary target for cisplatin is the DNA. It forms a cisplatin–DNA cross-link agent that acts on the N7 position of guanine and adenine bases, resulting in distortion of the DNA [340, 352–354]. The formation of this cross-link structure destroys the helix stability of the DNA [340]. Since DNA replication and transcription are essential for cell division and protein production, the cisplatin binding to the DNA and distorting the DNA structure is cytotoxic [340]. Studies showed that cisplatin inhibits DNA transcription, where transcription refers to the process where mRNA is produced from a DNA template. This cellular process is critical in protein synthesis [355, 356]. According to these studies, cisplatin-treated cells progressed through the S phase of the cell cycle and were arrested in the G2 phase. For cells treated

with a lower concentration of cisplatin, the G2 arrest was temporary. However, cells treated with higher concentrations remained in the G2 arrest until cell death occurred [355]. The mechanism of cell death from cisplatin was found to be through apoptosis [357].

Cisplatin is one of the common drugs used with RT and has been previously tested with GNPs and with MDA-MB-231 cells [358]. That makes it an ideal drug to use in a combined cancer therapy study (**Fig. 6.1**). However, the significant risk of nephrotoxicity frequently hinders the use of higher doses to maximize its antineoplastic effects [359]. Therefore, novel therapeutic interventions aimed at minimizing cisplatin-induced nephrotoxicity while enhancing its antineoplastic efficacy is needed. For example, an efficient delivery of the drug to the tumor using a NP formulation or use of a combination of cisplatin with another radiosensitizing agents may allow a feasible therapeutic approach to increase the RT dose.

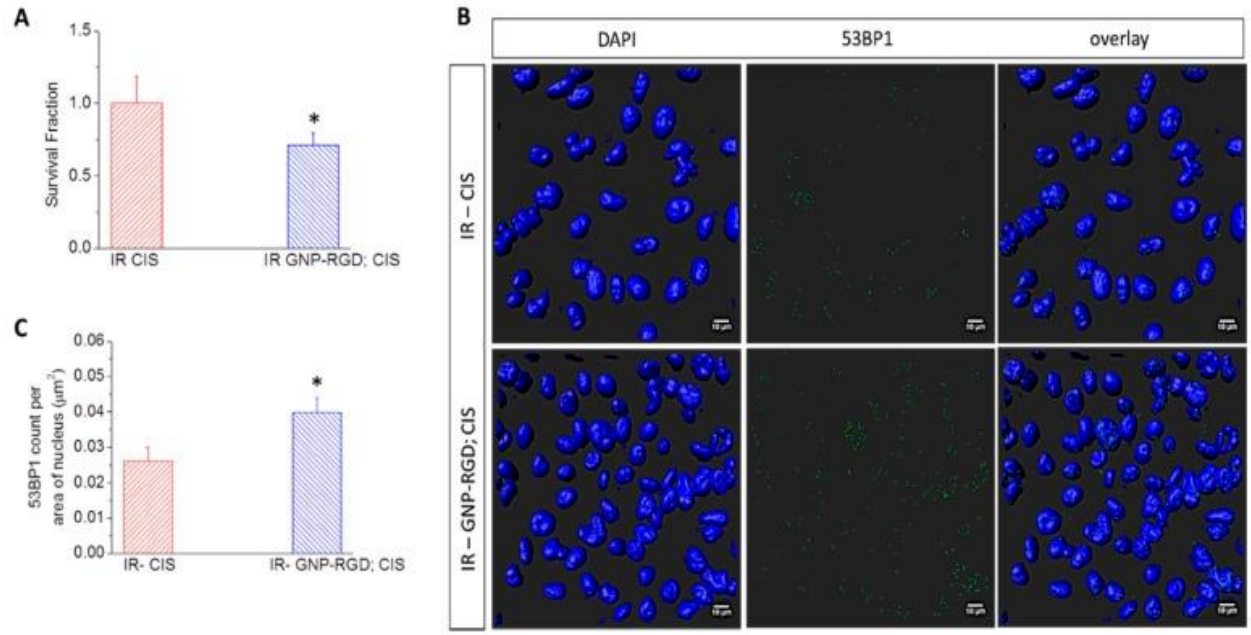

Figure 6.1 Combination with GNPs and cisplatin in RT. (**a**) Cell survival fraction of MDA-MB-231 cells treated with cisplatin (CIS) and GNP_{RGD}; CIS prior to 2 Gy, 6 MV radiation. Data are means ± S.E.M. for n = 3. * Represents statistically significant difference (unpaired *t*-test, $p < 0.05$); (**b**) Qualitative representation of DNA double-strand breaks (DSBs) in MDA-MB-231 cells treated with CIS and GNP-RGD; CIS prior to 2 GY, 6 MV X-ray radiation. The nucleus is stained with DAPI (shown in blue) and the markers for DNA DSBs, 53BP1, are shown in green. Scale bar = 10 μm; (**c**) Quantitative analysis of (**b**). Reproduced with permission from open access Creative Common license [360].

The combination of cisplatin and GNPs with RT resulted in an additive radiosensitization effect both *in vitro* and *in vivo* [360, 361]. As illustrated in **Fig. 6.1,** the outcome of GNP-mediated

chemoradiation was assessed by measuring the cell survival fraction and DNA damage *in vitro* [360]. DNA DSBs are considered the most harmful type of DNA lesions because unrepaired DSBs are sufficient to trigger permanent growth arrest and cell death. More importantly, significant radiation enhancement was also achieved *in vivo* [361]. Based on tumor growth suppression and overall survival, it is suggested that the combination of GNP with cisplatin is a potent strategy to improve the outcome of RT by allowing additive therapeutic results corresponding to both studies. In contrast, synergistic therapeutic results were reported in a plasmid DNA model where GNPs and cisplatin were in direct contact with DNA during RT [48]. Therefore, it is theorized that further synergistic therapeutic improvements could be achieved if GNPs could directly target the nucleus in the presence of cisplatin and ionizing radiation [237, 238].

Furthermore, GNPs could be used as a cisplatin delivery vehicle [189]. A recent study showed that if GNPs are used as drug carriers, the amount of cisplatin necessary to cause the desired cytotoxic effect would be less than the amount used in conventional cancer treatments [189]. For example, IC_{50} diminished approximately 7 times, compared to the IC_{50} of cisplatin used alone, when using GNPs as delivery vehicles (**Fig. 6.2**) [189]. On this note, a new methodology has been developed for the synthesis of a gold core–shell type NP. It contains cisplatin within the shell which may facilitated its transport across the cell membrane. Therefore, this study opens up the possibility of an alternative way of transporting cisplatin anticancer drug to tumors using GNPs. This approach reduces the required dose but would have the same therapeutic effects as free cisplatin while minimizing undesired side effects. Another approach tested for GNP-mediated drug delivery is to conjugate cisplatin to the NP surface via a pH sensitive bond [362]. Local release of cisplatin from the formulation was successfully accomplished by exploiting the acidic tumor microenvironment and thereafter achieving a tumor-specific delivery of cisplatin [363]. Therefore, engineering such GNP-based formulations will improve the therapeutic window for using cisplatin and GNPs in RT.

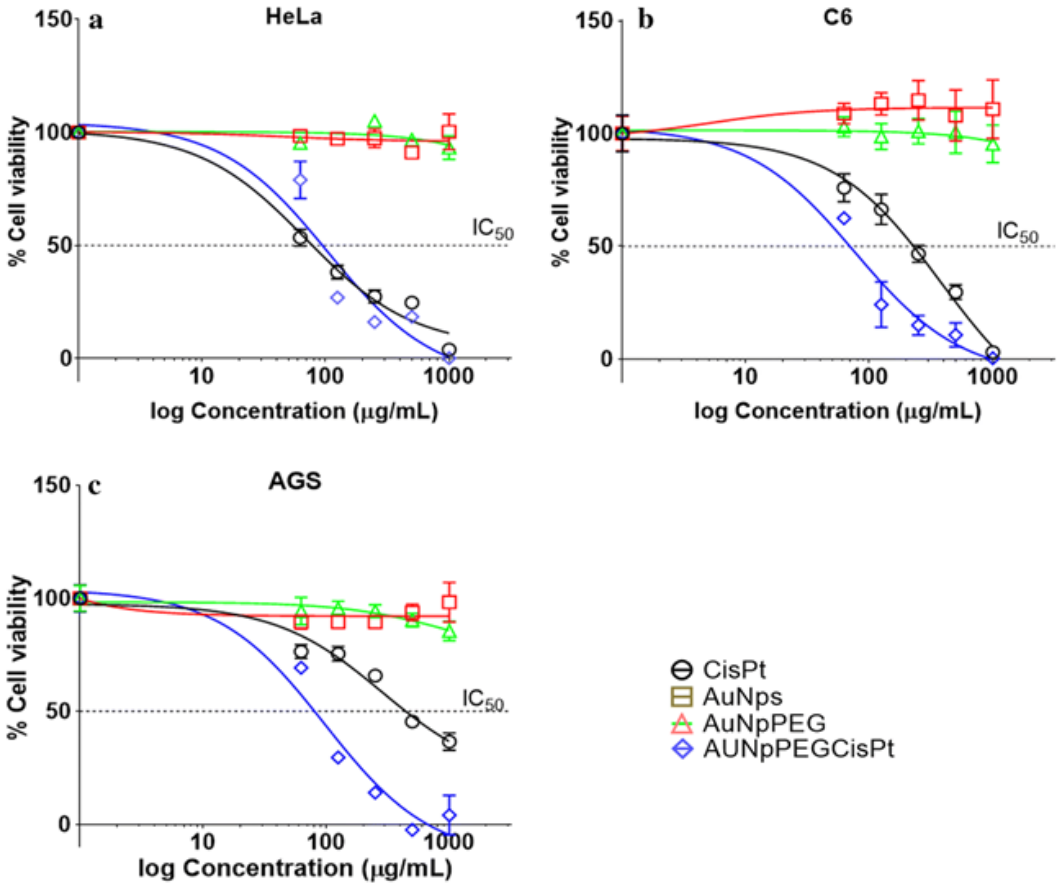

Figure 6.2 Use of GNPs as drug delivery systems for cisplatin. Cell viability curve of (**a**) HeLa cells, (**b**) C6 cells, and (**c**) AGS cells. Reproduced with permission from open access Creative Common license [189].

6.2.1.2 Bleomycin (BLM)

BLM is a highly effective natural anti-cancer agent, but its clinical utility is constrained by its pulmonary toxicity [364]. Enhancing its targeted delivery could potentially expand its therapeutic applications. One promising approach for the targeted delivery of drugs like BLM is the use of NPs [365–372]. Research has demonstrated that NP-based systems can offer advantages over traditional drug delivery. For instance, GNPs have been successfully utilized to carry tumor necrosis factor-alpha (TNF-α) directly to cancerous tissues, and their safety has been confirmed in phase I clinical trials [242]. In these experiments, 27 nm GNPs were equipped with TNF-α and PEG, resulting in localized TNF-α delivery that caused vascular leakage, reduced tumor interstitial fluid pressure (IFP), and increased drug uptake in the tumor. GNPs have also been employed for the targeted delivery of paclitaxel to tumors [373]. Moreover, a different phase I trial used spherical GNPs (NU-0129) to transport nucleic acids past the blood-brain barrier and target a specific gene

in recurrent glioblastoma [374]. Other innovations include the use of PEG-coated gold and silica nanoparticles (gold nanoshells; AuroLase®) for photothermal therapy, currently being assessed in a phase I trial [375]. Current literature suggests that the clinical translation of GNPs is actively underway [19–21].

GNPs are an appealing choice for delivering BLM due to their biocompatibility, non-toxicity, and non-immunogenic nature [376, 377]. They not only possess radiosensitizing qualities but can also be loaded with other radiosensitizing drugs, which makes them highly promising for the development of next-generation cancer treatments. Utilizing GNPs and BLM in combination with RT offers three distinct advantages: Firstly, BLM is effective in halting the cell cycle at the G2/M phase, where DNA is particularly susceptible to radiation [364]. Meanwhile, GNPs generate ROS that damage cells during RT. This synergy in their mechanisms is anticipated to enhance therapeutic outcomes. Secondly, BLM can be readily attached to the surface of GNPs, facilitating efficient drug delivery [238]. Among various radiosensitizing agents, BLM stands out as it can be anchored to GNPs through a thiol bond, making it a highly compatible drug for this system. Lastly, the surface of GNPs can be additionally engineered with molecules that target tumors, enabling even more precise delivery [268]. This unique amalgamation of GNPs, BLM, and RT holds substantial promise for improving cancer treatment strategies. Ocean et al. were able to use GNPs as both radiosensitizers and drug-delivery carries [268]. They achieved a significant decrease in cell proliferation and increase in DNA DSB using 1 nM GNPs loaded with BLM when combined with 2Gy of RT (**Fig. 6.3**). This was achieved using a much lower BLM concentration compared to BLM in its free form [268].

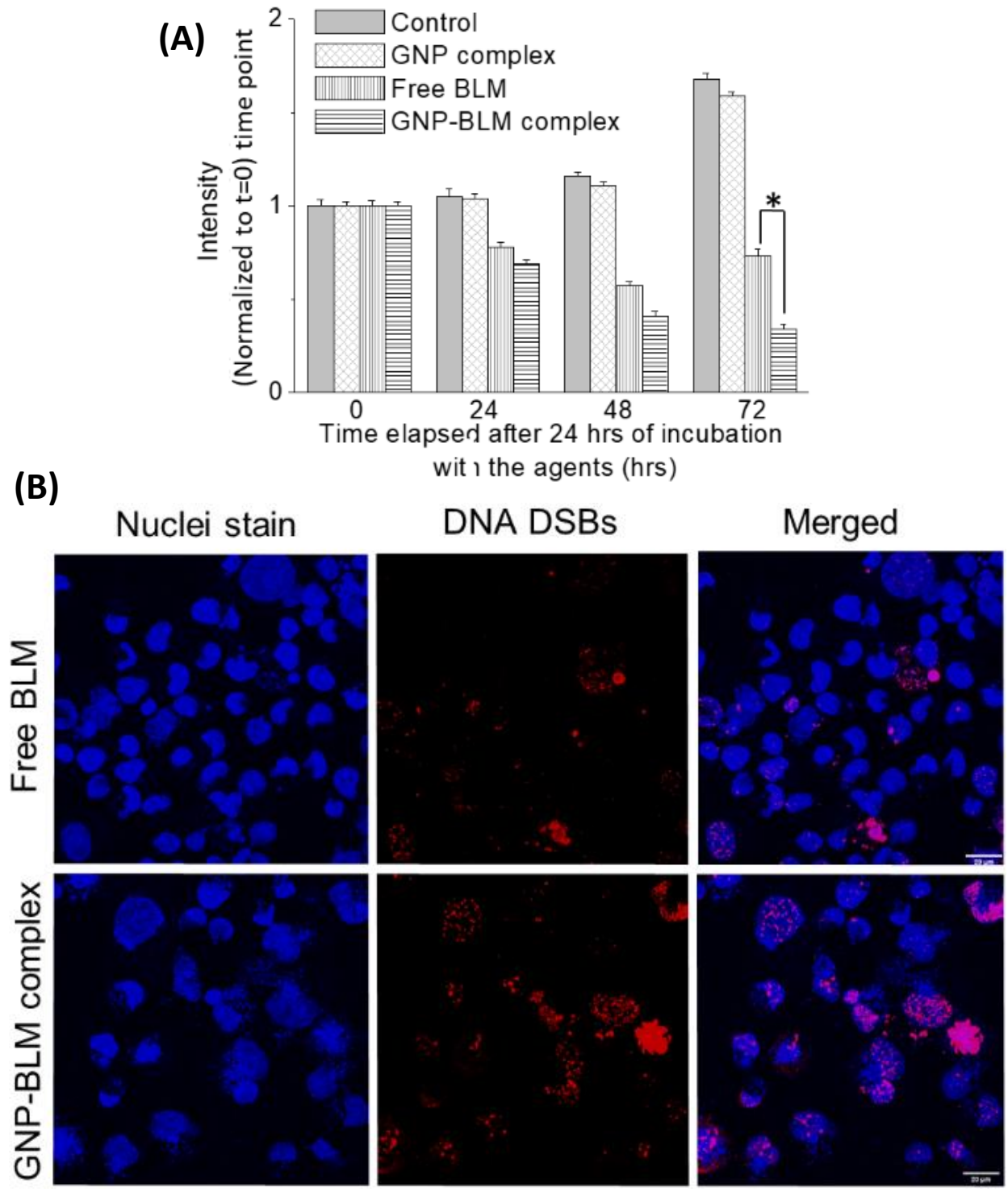

Figure 6.3 Cancer chemoradiation. (**A**) Progression in cell growth in MIA PaCa-2 after a 2 Gy RT dose from a clinically used linear accelerator (inset of A). * indicates $p < 0.05$. (**B**) Mapping the DNA DSBs after 24 h of the RT treatment for MIA PaCa-2. The scale bars are 20 μm. Reproduced with permission from open access Creative Common license [268].

6.2.1.3 Pyronaridine (PYD)

PYD serves as an antimalarial medication, often employed alongside other drugs targeting malaria. Additionally, PYD has shown promise as an inhibitor of the DNA repair enzyme complex known as ERCC1-XPF. This complex, comprising ERCC1 and XPF subunits, functions as a 5′-3′ structure-specific endonuclease, playing a crucial role in multiple DNA repair mechanisms in mammalian cells, including nucleotide excision repair (NER), interstrand crosslink (ICL) repair, and DSB repair [378]. In this ERCC1-XPF duo, ERCC1 manages DNA and protein interactions, while XPF is responsible for endonuclease activity, DNA binding, and additional protein interactions [379, 380]. Current therapeutic approaches aim to enhance RT by using inhibitors targeting ERCC1-XPF, as outlined in Figure 1B. Inhibiting this enzyme complex could amplify the cellular toxicity induced by RT by obstructing the DNA repair pathways [381, 382]. Repurposing clinically approved drugs for new treatments can be a rapid way to exploit a potentially effective therapeutic strategy. Given its structural resemblance to known acridine-based inhibitors of ERCC1-XPF, PYD is considered a promising candidate for inhibiting this enzyme complex [383, 384]. Studies have even demonstrated that PYD can enhance the effectiveness of cisplatin in breast cancer cell lines [385]. Notably, the action mechanism of cisplatin involves DNA crosslinking, a process that also relies on ERCC1-XPF for repair [378]. Additionally, PYD has shown potential in boosting the impact of ionizing radiation, as research indicates that the ERCC1-XPF heterodimer is involved in repairing DNA double-strand breaks [380, 386, 387]. Further cell-based research has investigated PYD's anti-cancer properties, given its ability to trigger apoptosis and inhibit the activity of topoisomerase II [385, 388, 389].

Jackson et al. combined PYD and GNPs with RT to improve the therapeutic benefits of RT. Utilizing clinically viable concentrations of 7.5 µg/mL for GNPs and 500 nM for PYD, along with 2 Gy of RT on HeLa cells, they observed a 42% increase in DNA DSBs when using the GNP/PYD/RT approach, compared to just the GNP/RT method (**Fig. 6.4**) [390]. Given that GNPs are known to induce DNA DSBs when combined with radiation, this significant increase in DNA DSBs suggests that PYD effectively inhibits DNA repair processes [45, 380, 381, 383, 391]. This aligns with the growing interest in DNA repair enzymes, spurred in part by the success of poly (ADP-ribose) polymerase (PARP) inhibitors in treating various solid tumors [391]. These findings

indicate that PYD could be a promising candidate for inhibiting DNA repair in future clinical settings.

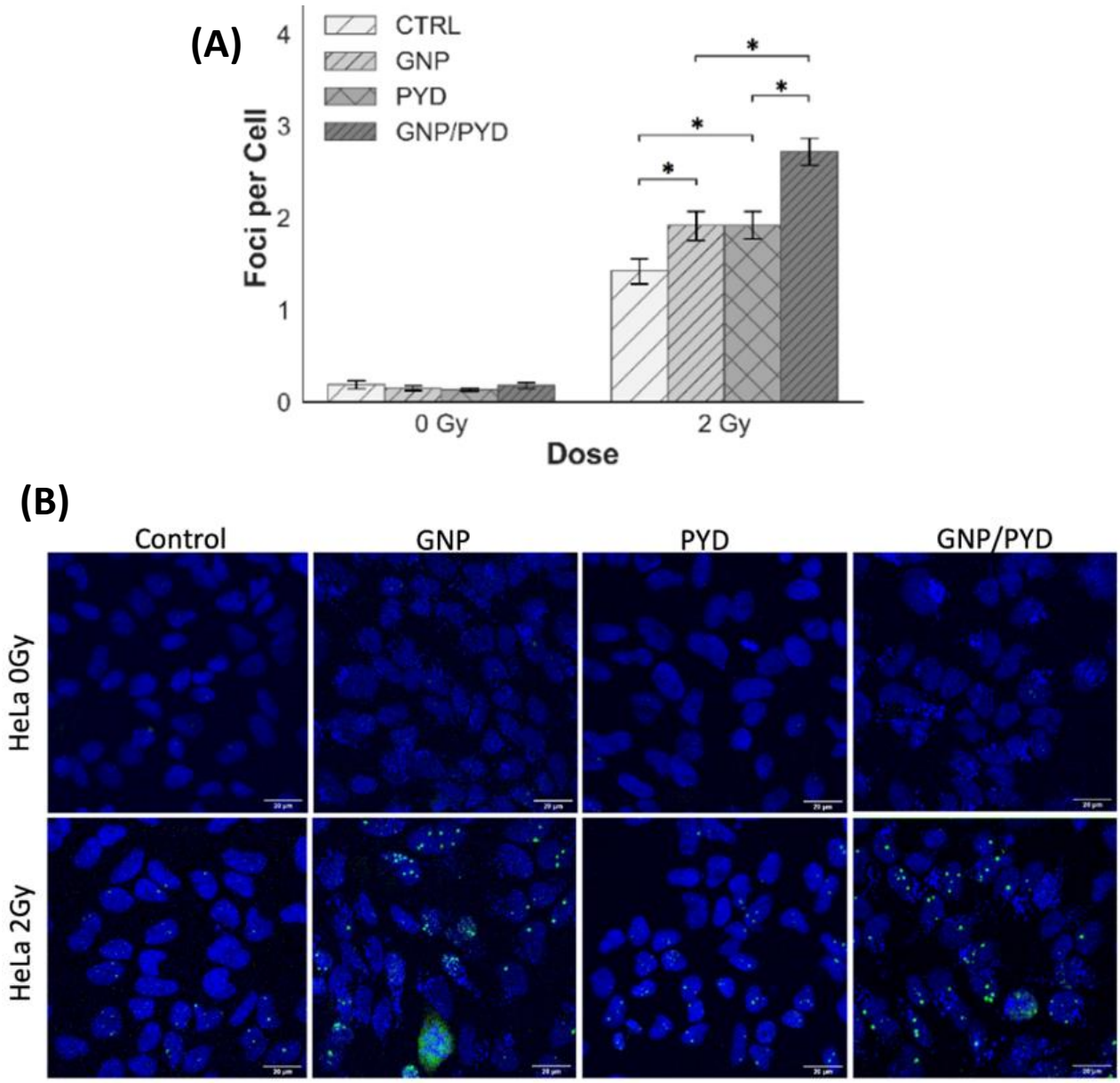

Figure 6.4 Evaluation of the triple combination of RT/GNP/ PYD. (**A**) Quantitative assessment of DNA DSBs 24 h post irradiation with dose of 2 Gy in HeLa cells. (**B**) Qualitative assessment of DNA DSBs for HeLa, scale bar = 20 µm. Reproduced with permission from open access Creative Common license [390].

6.2.1.4 Conclusions

While GNP systems have displayed promising radiosensitizing and drug delivery capabilities both in the lab and in animal models, they are still a work in progress before they can be broadly used in clinical settings. Currently, only two GNP-based systems are undergoing clinical trials for cancer treatments, and neither is focused on radiosensitization or has advanced to stage II trials. These are: TNF-conjugated GNPs [392, 393] and gold nanorods for photothermal ablative therapy under the name Aurolase [394, 395]. Due to the diverse range of GNP configurations—varying in size, shape, and surface coatings—it's challenging to pinpoint the ideal specifications for clinical use. One avenue worth exploring is the combination of GNPs with existing, clinically approved radiosensitizers to enhance current RT methods. GNPs have enormous potential as targeted delivery systems for other radiosensitizing drugs, offering a more strategically focused approach to cancer treatment. Notably, DTX and cisplatin emerge as promising chemotherapy agents that could be paired with GNPs and radiation therapy to deliver synergistic damage to cancerous tumors.

6.2.2 Immunotherapy Approaches for PDAC

Another avenue to explore to improve our treatment is to target PDAC cancer cells antigens (which are substances that trigger an immune response from the immune system) using immunotherapy, i.e., by directing the immune system to specifically recognize and attack cancer cells while sparing healthy cells [396]. Some antigens are more associated to PDAC these include mucin antigens notably MUC1, MUC4, and MUC16 which is often found in abnormal concentrations in PDAC, these glycoproteins are primary targets for novel immunotherapies [397–399]. Other glycoproteins, such as mesothelin and carcinoembryonic antigen (CEA), are also overexpressed in PDAC which makes them potential targets for monoclonal antibodies (mAbs) (lab-engineered antibodies that target a single specific antigen) [400]. Likewise, epidermal growth factor receptor (EGFR) which is a cell surface receptor, and cancer-testis antigens (CTAs) such as NY-ESO-1, both can be overexpressed in PDAC cells and are potential therapeutic targets using mAbs [401]. Recent studies have also explored heat shock proteins, such as HSP70 and HSP90, which are stress-induced proteins that are upregulated in various cancers, including PDAC, as potential targets for immune-based therapies [402]. Various vaccine approaches using diverse

types of antigens have been explored, but with limited clinical effectiveness [403–405]. It is important to note that PDAC tumors can be quite heterogeneous in terms of antigen expression, complicating the identification of universal targets for therapy [17].

Current immunotherapies for cancer primarily rely on therapeutic antibodies and engineered immune cells that target specific cancer cell proteins [396]. However, these treatments are not only expensive but also limited in their applicability, making them less than ideal for widespread use [396]. For instance, T-cell therapy has shown potential in treating blood cancers like leukemia and lymphoma, but its effectiveness against solid tumors like PDAC remains limited [406]. Combined immunotherapy that incorporates checkpoint inhibitors (CPIs) like anti-PD-1 or anti-CTLA-4 with other anticancer agents is an attractive option [407]. This dual approach aims to boost the body's own immune system while also making cancer cells more susceptible to attack. Specifically, certain anticancer agents can induce what's known as immunogenic cell death (ICD), enhancing the cancer cells' visibility to the immune system [408]. Combining ICD-inducing agents with CPIs has the potential to not only improve the effectiveness of treatment but also make it more cost-effective [409, 410]. Recent studies have identified multiple drug candidates capable of inducing ICD and have found that these agents are even more effective when combined with copper, an agent that stimulates ROS [411]. Although CPIs have marked a significant advancement in cancer therapy, their effectiveness is not universal across all types of tumors. Specifically, PDAC has proven to be less responsive to this treatment approach compared to other forms of cancer [396]. This limitation is largely due to the immunosuppressive TME in PDAC, which inhibits the proper functioning of T-cells and evade the effects of CPIs [396]. Moreover, the lack of highly specific antigens on PDAC cells and the risk of off-target effects further complicate this therapeutic strategy [17, 396].

In summary, retriggering the immune system against PDAC to enhance clinical outcomes is evidently more complex than what has been inferred from experiences with other cancer types. The most promising tactics likely involve combining various immunotherapeutic methods or integrating them with traditional treatment options like chemotherapy and RT. One smart approach to consider is radioimmunotherapy (RIT) using mAbs. RIT is a targeted cancer therapy that combines the specificity of immunotherapy with the cytotoxic power of RT. In RIT, a radioactive isotope is attached to a mAb designed to target a specific antigen on the surface of cancer cells

[412]. Once administered, the monoclonal antibody seeks out the cancer cells, and the attached radioactive isotope delivers a concentrated dose of radiation to kill them (**Fig. 6.5**).

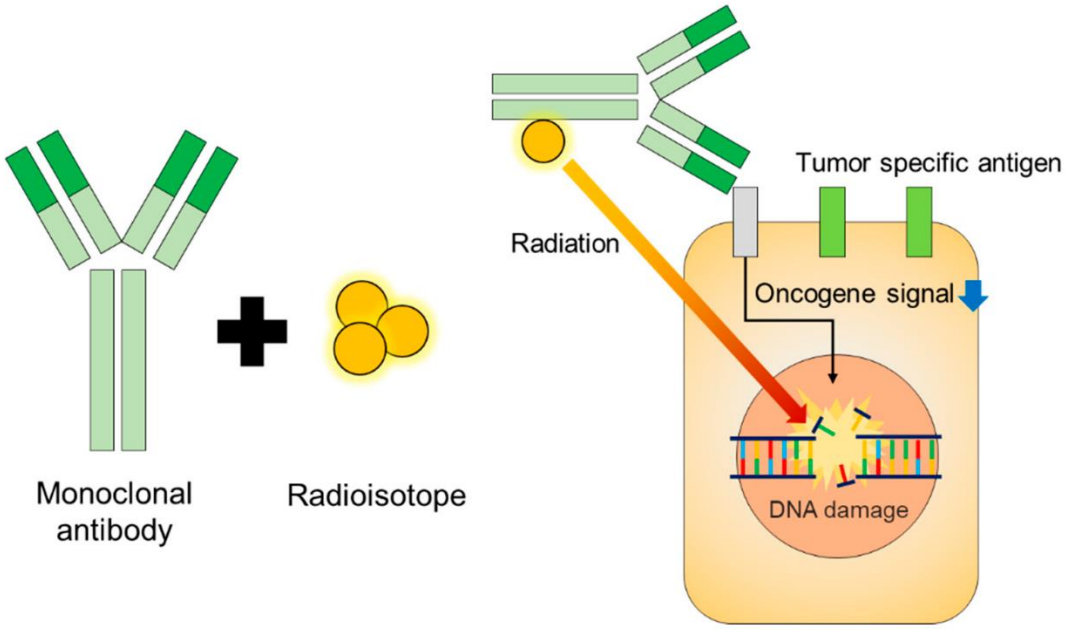

Figure 6.5 Diagram of RIT. RIT specifically targets the unique tumor-associated antigens of a particular cancer type, delivering radiation directly to them. The descending blue arrow indicates a reduction in oncogene signaling. Reproduced with permission from open access Creative Common license [412].

The growing enthusiasm for RIT is fueled by the recent clinical achievements of mAbs in cancer treatment, the discovery of new cancer-associated proteins, and advancements in isotope production and radiolabeling techniques [412–415]. Most clinical trials exploring RIT for PDAC have primarily used β-emitting isotopes focusing mainly on MUC1 [414]. To date, there are no known trials using α-emitting RIT for this cancer type. In an early-phase trial, the radiolabeled antibody 90Y-clivatuzumab tetraxetan was generally well-tolerated and showed manageable hematologic side effects [415]. When combined with a low dose of gemcitabine, the treatment led to improved cancer control and overall survival [416]. However, a subsequent Phase III trial known as PANCRIT®-1 was halted early for lack of efficacy, as indicated by interim data [417]. Separately, over 90% of PDACs overexpress CEA [414]. In a Phase I/II study, an iodine-131 labeled anti-CEA mAbs called KAb201 had a tolerable safety profile but showed only limited effectiveness [418]. The study also found no significant difference in efficacy between intravenous and intra-arterial administration of 131I-KAb201 [418]. Despite these somewhat disappointing

results, there is optimism that further refinement of these approaches could lead to more effective treatments. Producing effective radioimmunoconjugates necessitates the careful choice of an appropriate target, mAbs, and radiolabeling approaches.

6.2.3 Optimizing Models for Improved Therapeutic Outcome

In our study, we employed both *in vitro* 3D spheroid co-culture models and *in vivo* models using Mia PaCa-2, a commonly used human tumor cell line. While our 3D spheroid models have certain drawbacks, as detailed in earlier sections, our *in vivo* model also falls short in capturing the complexity of the TME, particularly the influential role of CAFs and immune cells. By refining our models, we can enhance therapeutic outcomes and improve their translational relevance to clinical settings, thus reducing the likelihood of failure.

6.2.3.1 In Vitro Improvements

One way for improvements of our therapeutic results is to optimize spheroid models for personalized treatments which will provide a more comprehensive *in vitro* environment. This could be done by creating spheroid models that incorporate multiple patient-derived cell lines, including CAFs and immune cells. Ideally, the ratio of these cell types should resemble what is found in actual tumors, and the use of patient-derived cells would increase the model's predictive accuracy [419]. The value of such models lies in their capacity to closely mimic the characteristics of the original tumors, thereby enabling personalized drug testing [420, 421]. Thus, these 3D spheroid models could complement personalized treatment through targeted immunotherapy by modifying and tailoring our GNPs/LNPs to the patient's unique immune response, genetic mutations, and TME complexity. By taking such an integrated approach, we could achieve a more complete view of how a specific cancer type might respond to a given treatment, thereby enhancing the translational potential of these models into clinical practice [422]. Despite these promising aspects, these models do have certain limitations, such as the absence of key components of the *in vivo* TME including blood vessels. Additional factors to consider include the time it takes to create the models, financial implications, scalability, and the level of expertise required [423].

Another avenue worth investigating is 3D bio-printing, which provides a promising platform for evaluating cancer treatments. 3D bioprinting uses advanced techniques like laser-

assisted bioprinting, microextrusion, and inkjet printing to layer cells and biomaterials, creating intricately structured 3D tissues [424]. Cells are encapsulated in a bio-compatible gel, also known as bioink, which maintains their functionality and viability [424]. In cancer research, 3D bioprinting can produce highly complex tumor models that closely mirror the heterogeneity and complexity of actual tumors by incorporating patient-derived cells, growth factors, and genetic material [425]. The method offers extensive control over tissue geometry, cell placement, and the components of the bioink, making it highly customizable [425]. This allows for the inclusion of stromal cells to more accurately recreate the TME, and also offers the possibility of personalized therapies tailored to individual patient's cancer profiles [426, 427]. This approach has already shown promising results in initial studies focused on PDAC [428–430]. Future advancements could involve adding additional elements of the TME like vascular networks and cellular secretions for more comprehensive studies. However, the absence of standardized protocols remains a significant hurdle for translating these advanced models into clinical applications [427].

6.2.3.2 In Vivo Improvements

Creating more authentic tumor-like settings for nanomedicine evaluation by utilizing pancreatic patient-derived xenograft (PDX) models or through the co-injection of tumor cells and CAFs *in vivo* could produce more meaningful results. PDX model is a type of cancer research model where cancerous tissue or cells from a patient are implanted into immunodeficient mice [431]. These models aim to closely replicate the cancer state and heterogeneity, making them useful tools for studying cancer biology, drug sensitivity, and treatment options in a setting that is more clinically relevant than traditional *in vitro* cell culture models [432]. PDAC PDX models are yielding encouraging outcomes as they offer a more accurate and personalized platform for testing the efficacy of new drug compounds and treatment strategies [433]. PDX models have several advantages including their TME relevance, drug sensitivity and efficacy, susceptibility for personalized treatments, more accurate translational research, and ethical benefits as it requires less animals to be sacrificed [432]. These models also present an opportunity to assess the toxicity of LNPs on healthy tissues, an aspect not fully explored in our existing research. However, it's important to note that PDX models also have their limitations, including the lack of immune system interactions, cost, ethical concerns as we are still scarifying animals, and the time required to develop the models [432].

Another intergerning option would be to implant mouse pancreatic cancer cell lines *in vivo* which has shown to produce both subcutaneous and pancreatic tumors (orthotopic) [434]. Such genetically modified mouse models currently offer valuable insights into the origins and development of PDAC, as well as the assessment of new treatment options, both natural and synthetic [435]. One main advantage is the use of immunocompetent mice which will allow studying immune responses. However, these sophisticated models come with considerable financial and time commitments [434].

Currently, *in vivo* experiments studying the efficacy of GNPs and $LNP_{DTX\text{-}P}$ in combination with RT in MIA PaCa-2 pancreatic cancer cells in NRG mice is underway. The purpose is to assess the therapeutic activity of the triple combination. Drugs were administered concurrently at doses of 6 mg/kg for DTX and $LNP_{DTX\text{-}P}$, and 2 mg/kg for GNPs. The chosen dose for GNPs is well below the lethal dose (LD_{50}) reported for GNPs [29]. The $LNP_{DTX\text{-}P}$ and DTX dose approximates a quarter of the weekly human dose of ~75 mg/m^2 [158].These doses were used to minimize side effects. Drugs and GNPs were administered once tumors reached a volume of 275-300 mm^3. A single 5 Gy RT dose was administered 24 h post-dosing using a 6 MV linear accelerator. At this timepoint the cell cycle arrest in the G2/M phase is concurrent with peak GNP accumulation indicating increased tumor radiosensitivity at this timepoint. Tumor progression was monitored until euthanasia at a predetermined endpoint of 800 mm³ tumor volume. The treatment groups for this single RT dose included controls, GNPs, DTX, $LNP_{DTX\text{-}P}$, GNP/DTX, and GNP/$LNP_{DTX\text{-}P}$, along with a non-radiated comparison group. **Fig. 6.6A–B** demonstrate tumor volume variations over time post-treatment, with and without radiation. Notably, there was a significant ~17% reduction in tumor size ($p=0.05$) with $LNP_{DTX\text{-}P}$ alone, without RT. In contrast, DTX alone did not significantly reduce tumor size, possibly due to the lower dose used thus limiting its effectiveness. However, the same dose of $LNP_{DTX\text{-}P}$ proved effective, suggesting enhanced tumor targeting. This effect is also observed in increased median mouse survival without radiation (**Fig. 6.6C**). Additionally, there was no notable difference in tumor volume or mouse survival when comparing groups treated with GNPs to those without, indicating negligible inherent toxicity of GNPs at these low doses without RT.

Conversely, the combined GNP/$LNP_{DTX\text{-}P}$/RT treatment resulted in over 40% reduction in tumor growth ($p=0.01$), and a similar outcome was seen with $LNP_{DTX\text{-}P}$/RT alone ($p=0.02$). These

combinations significantly enhanced mouse survival, correlating with the delayed tumor growth (**Fig. 6D**). The low DTX dose meant that DTX with RT was not significantly more effective than RT alone. However, adding GNPs to DTX/RT displayed synergistic benefits in tumor control ($p=0.05$) of ~ 20% reduction in tumor volume, likely due to DTX's mechanism of action discussed earlier and its potential synergy with GNPs and RT. This synergy was less apparent with GNPs in combination with $LNP_{DTX\text{-}P}$/RT, possibly because the effectiveness of LNPs overshadowed the GNPs' impact. These findings suggest that either GNP/DTX/RT or $LNP_{DTX\text{-}P}$/RT treatments could be viable options, demonstrating the potential of nanotechnology in reducing toxicity to normal tissues. Incorporating NPs might also allow for lower RT doses, further decreasing toxicity. Our results indicate that the *in vivo* treatment strategies are as promising as *in vitro*, enhancing tumor radiosensitivity with GNP/DTX combinations. If translated to clinical settings, the synergistic effect of the triple GNP/DTX/RT or GNP/$LNP_{DTX\text{-}P}$/RT combinations could significantly improve treatment outcomes and potentially increase survival rates, as evidenced by our promising *in vivo* tumor growth delay and mouse survival data.

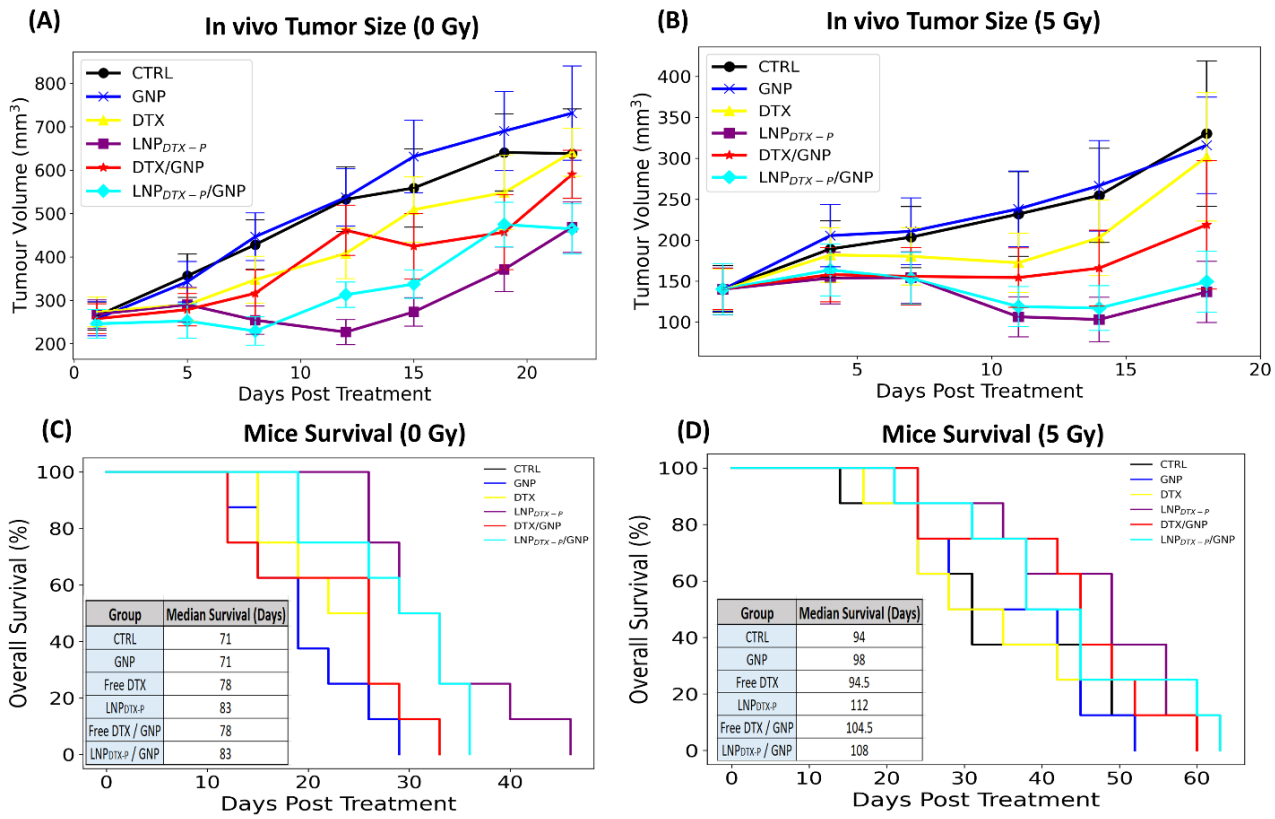

Figure 6.6 *In vivo* assessment of GNP/$LNP_{DTX\text{-}P}$/RT Treatment. (**A–B**) The normalized tumor volume in mice post-treatment, with (**A**) illustrating results without radiation and (**B**) showing

results with radiation. The data, representing an average normalized tumor volume, were obtained from at least five mice and are expressed as mean ± standard deviation, demonstrating the impact of different treatment strategies on tumor growth reduction. (**C–D**) The Kaplan-Meier survival curves for female NRG mice inoculated with MiaPaCa2 are shown without radiation (**C**) and with radiation (**D**), comparing the survival rates post-treatment with various strategies. The inset provides the median survival times of the mice in days following tumor incubation.

BIBLIOGRAPHY

1. Wild, C. P., Weiderpass, E., & Stewart, B. W. (Eds.). (2020). *World Cancer Report: Cancer Research for Cancer Prevention*. World Health Organization. ISBN-13: 978-92-832-0447-3; ISBN-13: 978-92-832-0448-0.

2. Sung, H., Ferlay, J., Siegel, R. L., Laversanne, M., Soerjomataram, I., Jemal, A., & Bray, F. (2021). Global Cancer Statistics 2020: GLOBOCAN Estimates of Incidence and Mortality Worldwide for 36 Cancers in 185 Countries. CA: A Cancer Journal for Clinicians, 71(3), 209–249. https://doi.org/10.3322/caac.21660

3. Brenner, D. R., Poirier, A., Woods, R. R., Ellison, L. F., Billette, J.-M., Demers, A. A., Zhang, S. X., Yao, C., Finley, C., Fitzgerald, N., Saint-Jacques, N., Shack, L., Turner, D., & Holmes, E. (2022). Projected estimates of cancer in Canada in 2022. Canadian Medical Association Journal, 194(17), E601–E607. https://doi.org/10.1503/cmaj.212097

4. Siegel, R. L., Miller, K. D., Fuchs, H. E., & Jemal, A. (2022). Cancer statistics, 2022. CA: A Cancer Journal for Clinicians, 72(1), 7–33. https://doi.org/10.3322/caac.21708

5. Cheng, X., Zhao, G., & Zhao, Y. (2018). Combination immunotherapy approaches for pancreatic cancer treatment. Canadian Journal of Gastroenterology and Hepatology, 2018, 6240467.

6. Norton, J., Foster, D., Chinta, M., Titan, A., & Longaker, M. (2020). Pancreatic cancer associated fibroblasts (CAF): Under-explored target for pancreatic cancer treatment. Cancers, 12, 1347.

7. Badiyan, S. N., Molitoris, J. K., Chuong, M. D., Regine, W. F., & Kaiser, A. (2017). The role of radiation therapy for pancreatic cancer in the adjuvant and neoadjuvant settings. Surgical Oncology Clinics of North America, 26, 431-453.

8. Hall, W. A., & Goodman, K. A. (2019). Radiation therapy for pancreatic adenocarcinoma, a treatment option that must be considered in the management of a devastating malignancy. Radiation Oncology, 14, 114.

9. Wilhelm, S., Tavares, A. J., Dai, Q., Ohta, S., Audet, J., Dvorak, H. F., & Chan, W. C. W. (2016). Analysis of nanoparticle delivery to tumors. Nature Reviews Materials, 1(5), 16014.

10. Peer, D., Karp, J. M., Hong, S., Farokhzad, O. C., Margalit, R., & Langer, R. (2007). Nanocarriers as an emerging platform for cancer therapy. Nature nanotechnology, 2(12), 751-760.

11. Davis, M. E., Chen, Z. G., & Shin, D. M. (2008). Nanoparticle therapeutics: an emerging treatment modality for cancer. Nature Reviews Drug Discovery, 7(9), 771-782.

12. Delaney, G. P., & Barton, M. B. (2015). Evidence-based estimates of the demand for radiotherapy. Clin. Oncol., 27(1), 70–76.

13. Nguyen, L., Schilling, D., Dobiasch, S., Raulefs, S., Santiago Franco, M., Buschmann, D., Pfaffl, M. W., Schmid, T. E., & Combs, S. E. (2020). The emerging role of miRNAs for the radiation treatment of pancreatic cancer. Cancers, 12.

14. Li, W., Song, X., Yu, H., Zhang, M., Li, F., Cao, C., & Jiang, Q. (2018). Dendritic cell-based cancer immunotherapy for pancreatic cancer. Arab Journal of Gastroenterology, 19(1), 1–6. https://doi.org/10.1016/j.ajg.2017.05.013

15. Jenkins, R. W., Barbie, D. A., & Flaherty, K. T. (2018). Mechanisms of resistance to immune checkpoint inhibitors. British Journal of Cancer, 118(1), Article 1. https://doi.org/10.1038/bjc.2017.434

16. Oh, E. S., et al. (2018). Effectiveness and feasibility of concurrent chemoradiotherapy using simultaneous integrated boost-intensity modulated radiotherapy with and without induction chemotherapy for locally advanced pancreatic cancer. Radiation Oncology Journal, 36(3), 200-209. https://doi.org/10.3857/roj.2018.00073.

17. Orth, M., Metzger, P., Gerum, S., Mayerle, J., Schneider, G., Belka, C., Schnurr, M., & Lauber, K. (2019). Pancreatic ductal adenocarcinoma: Biological hallmarks, current status, and future perspectives of combined modality treatment approaches. Radiat. Oncol., 14, 141.

18. Sarantis, P., Koustas, E., Papadimitropoulou, A., Papavassiliou, A.G., & Karamouzis, M.V. (2020). Pancreatic ductal adenocarcinoma: Treatment hurdles, tumor microenvironment, and immunotherapy. World J. Gastrointest. Oncol., 12, 173–181.

19. Bromma, K., & Chithrani, D. B. (2020). Advances in gold nanoparticle-based combined cancer therapy. Nanomaterials (Basel), 10.

20. Schuemann, J., Bagley, A., Berbeco, R., Bromma, K., Butterworth, K. T., Byrne, H., Chithrani, D. B., Cho, S. H., Cook, J. R., Favaudon, V., ... & others. (2020). Roadmap for metal nanoparticles in radiation therapy: Current status, translational challenges, and future directions. Physics in Medicine and Biology.

21. Schuemann, J., Berbeco, R., Chithrani, D. B., Cho, S. H., Kumar, R., McMahon, S. J., Sridhar, S., & Krishnan, S. (2016). Roadmap to clinical use of gold nanoparticles for radiation sensitization. International Journal of Radiation Oncology • Biology • Physics, 94, 189-205.

22. Jelveh, S., & Chithrani, D. B. (2011). Gold nanostructures as a platform for combinational therapy in future cancer therapeutics. Cancers, 3, 1081-1110.

23. Haque, M., Shakil, M. S., & Mahmud, K. M. (2023). The Promise of Nanoparticles-Based Radiotherapy in Cancer Treatment. Cancers, 15(6). https://doi.org/10.3390/cancers15061892

24. Gao, Q., Zhang, J., Gao, J., Zhang, Z., Zhu, H., & Wang, D. (2021). Gold Nanoparticles in Cancer Theranostics. Frontiers in Bioengineering and Biotechnology, 9. https://www.frontiersin.org/articles/10.3389/fbioe.2021.647905

25. Hainfeld, J.F., Slatkin, D.N., Focella, T.M., & Smilowitz, H.M. (2006). Gold nanoparticles: A new X-ray contrast agent. Br. J. Radiol., 79, 248–253.

26. Surovi, S., Aparoop, D., & Pathak, Y. Y. (2022). 18—Gold nanoparticles in cancer theranostics. In L. Kumar & Y. Y. Pathak (Eds.), Nanocarriers for Drug-Targeting Brain Tumors (pp. 513–526). Elsevier. https://doi.org/10.1016/B978-0-323-90773-6.00010-5

27. Dorsey, J. F., Sun, L., Joh, D. Y., Witztum, A., Kao, G. D., Alonso-Basanta, M., Avery, S., Hahn, S. M., Zaki, A. A., & Tsourkas, A. (2013). Gold nanoparticles in radiation research: Potential applications for imaging and radiosensitization. Translational Cancer Research, 2(4), 280. https://doi.org/10.3978/j.issn.2218-676X.2013.08.09

28. Lim, Z.-Z. J., Li, J.-E. J., Ng, C.-T., Yung, L.-Y. L., & Bay, B.-H. (2011). Gold nanoparticles in cancer therapy. Acta Pharmacologica Sinica, 32(8), 983. https://doi.org/10.1038/aps.2011.82

29. Hainfeld, J.F., Slatki

30. n, D.N., & Smilowitz, H.M. (2004). The use of gold nanoparticles to enhance radiotherapy in mice. Phys. Med. Biol., 58, 21–36.

31. Xinchen, Y., Jing, T., & Jiaoqiong, G. (2023). Lipid-based nanoparticles via nose-to-brain delivery: A mini review. Frontiers in Cell and Developmental Biology, 11, 1214450. https://doi.org/10.3389/fcell.2023.1214450

32. Sheoran, S., Arora, S., Samsonraj, R., Govindaiah, P., & vuree, S. (2022). Lipid-based nanoparticles for treatment of cancer. Heliyon, 8(5), e09403. https://doi.org/10.1016/j.heliyon.2022.e09403

33. Bobo, D., Robinson, K. J., Islam, J., Thurecht, K. J., & Corrie, S. R. (2016). Nanoparticle-based medicines: A review of FDA-approved materials and clinical trials to date. Pharmaceutical Research, 33(10), 2373–2387.

34. Allen, T. M., & Cullis, P. R. (2013). Liposomal drug delivery systems: From concept to clinical applications. Advanced Drug Delivery Reviews, 65(1), 36–48.

35. Sercombe, L., Veerati, T., Moheimani, F., Wu, S. Y., Sood, A. K., & Hua, S. (2015). Advances and challenges of liposome assisted drug delivery. Frontiers in Pharmacology, 6, 286.

36. Yingchoncharoen, P., Kalinowski, D. S., & Richardson, D. R. (2016). Lipid-based drug delivery systems in cancer therapy: What is available and what is yet to come. Pharmacological Reviews, 68(3), 701–787.

37. Bertrand, N., Wu, J., Xu, X., Kamaly, N., & Farokhzad, O. C. (2014). Cancer nanotechnology: The impact of passive and active targeting in the era of modern cancer biology. Advanced Drug Delivery Reviews, 66, 2-25.

38. Nichols, J. W., & Bae, Y. H. (2014). EPR: Evidence and fallacy. Journal of Controlled Release, 190, 451-464.

39. H, M. (2015). Toward a full understanding of the EPR effect in primary and metastatic tumors as well as issues related to its heterogeneity. Advanced Drug Delivery Reviews, 91. https://doi.org/10.1016/j.addr.2015.01.002

40. Danhier, F. (2016). To exploit the tumor microenvironment: Since the EPR effect fails in the clinic, what is the future of nanomedicine? Journal of Controlled Release, 244, 108-121.

41. Maeda, H., Nakamura, H., & Fang, J. (2013). The EPR effect for macromolecular drug delivery to solid tumors: Improvement of tumor uptake, lowering of systemic toxicity, and distinct tumor imaging *in vivo*. Advanced Drug Delivery Reviews, 65(1), 71-79.

42. Olivier, J.-C., Huertas, R., Lee, H., Calon, F., & Pardridge, W. (2002). Synthesis of PEGylated immune nanoparticles. Pharmaceutical Research, 19, 1137–1143. https://doi.org/10.1023/A:1019842024814

43. Li, Z., Huang, P., Zhang, X., Lin, J., Yang, S., Liu, B., Gao, F., Xi, P., Ren, Q., & Cui, D. (2010). RGD-Conjugated Dendrimer-Modified Gold Nanorods for in Vivo Tumor Targeting and Photothermal Therapy. Molecular Pharmaceutics, 7(1), 94–104. https://doi.org/10.1021/mp9001415

44. Pluen, A., Boucher, Y., Ramanujan, S., McKee, T. D., Gohongi, T., Di Tomaso, E., Brown, E. B., Izumi, Y., Campbell, R. B., Berk, D. A., & Jain, R. K. (2001). Role of tumor-host interactions in interstitial diffusion of macromolecules: Cranial vs. subcutaneous tumors. Proceedings of the National Academy of Sciences of the United States of America, 98(8), 4628-4633.

45. Cho, W. S., Cho, M., Jeong, J., Choi, M., Cho, H. Y., Han, B. S., ... & Jeong, J. (2009). Acute toxicity and pharmacokinetics of 13 nm-sized PEG-coated gold nanoparticles. Toxicology and Applied Pharmacology, 236(1), 16-24

46. Chithrani, D. B., Jelveh, S., Jalali, F., van Prooijen, M., Allen, C., Bristow, R. G., Hill, R. P., & Jaffray, D. A. (2010). Gold nanoparticles as radiation sensitizers in cancer therapy. Radiation Research, 173, 719-728.

47. Arai, Y., Jee, S. Y., Kim, S. M., Kwon, Y., & Jang, W. (2012). Biomedical applications and safety issues of gold nanoparticles. Toxicology and Environmental Health Sciences, 4, 1–8.

48. Hainfeld, J. F., Dilmanian, F. A., Slatkin, D. N., & Smilowitz, H. M. (2008). Radiotherapy enhancement with gold nanoparticles. Journal of Pharmacy and Pharmacology, 60, 977–985.

49. Zheng, Y., & Sanche, L. (2009). Gold nanoparticles enhance DNA damage induced by anti-cancer drugs and radiation. Radiation Research, 172, 114–119.

50. Wolfe, T., Chatterjee, D., Lee, J., Grant, J.D., Bhattarai, S., Tailor, R., Goodrich, G., Nicolucci, P., & Krishnan, S. (2015). Targeted gold nanoparticles enhance sensitization of prostate tumours to megavoltage radiation therapy *in vivo*. Nanomedicine: Nanotechnology, Biology and Medicine, 11(5), 1277-1283.

51. Bromma, K., Cicon, L., Beckham, W., & Chithrani, D.B. (2020). Gold nanoparticle mediated radiation response among key cell components of the tumour microenvironment for the advancement of cancer nanotechnology. Scientific Reports, 10, 12096.

52. Zhigaltsev, I.V., Winters, G., Srinivasulu, M., Crawford, J., Wong, M., Amankwa, L., Waterhouse, D., Masin, D., Webb, M., Harasym, N., et al. (2010). Development of a weak-base docetaxel derivative that can be loaded into lipid nanoparticles. Journal of Controlled Release, 144, 332-340.

53. Rosenblum, D., Joshi, N., Tao, W., Karp, J.M., & Peer, D. (2018). Progress and challenges towards targeted delivery of cancer therapeutics. Nature Communications, 9, 1410.

54. Yan, L., Shen, J., Wang, J., Yang, X., Dong, S., & Lu, S. (2020). Nanoparticle-Based Drug Delivery System: A Patient-Friendly Chemotherapy for Oncology. Dose-Response, 18, 1559325820936161.

55. Miller, K. D., Nogueira, L., Mariotto, A. B., Rowland, J. H., Yabroff, K. R., Alfano, C. M., ... & Siegel, R. L. (2019). Cancer treatment and survivorship statistics, 2019. CA: A Cancer Journal for Clinicians, 69(5), 363-385. https://doi.org/10.3322/caac.21565

56. Yao, Y., Hu, Q., Li, X., Chen, J., Shao, Z., & Chen, Y. (2020). Recent advances in formulation strategies for improving oral bioavailability of Docetaxel: A review. Nanomedicine: Nanotechnology, Biology and Medicine, 28, 102231. https://doi.org/10.1016/j.nano.2020.102231

57. A. Razak, S. A., Mohd Gazzali, A., Fisol, F. A., M. Abdulbaqi, I., Parumasivam, T., Mohtar, N., & A. Wahab, H. (2021). Advances in Nanocarriers for Effective Delivery of Docetaxel in the Treatment of Lung Cancer: An Overview. Cancers, 13(3), 400. https://doi.org/10.3390/cancers13030400

58. Chaturvedi, S., Verma, A., & Saharan, V. A. (2020). Lipid Drug Carriers for Cancer Therapeutics: An Insight into Lymphatic Targeting, P-gp, CYP3A4 Modulation and Bioavailability Enhancement. Advanced Pharmaceutical Bulletin, 10(4), 524–541. https://doi.org/10.34172/apb.2020.064

59. Lu, H., Zhang, S., Wang, J., & Chen, Q. (2021). A Review on Polymer and Lipid-Based Nanocarriers and Its Application to Nano-Pharmaceutical and Food-Based Systems. Frontiers in Nutrition, 8, 783831. https://doi.org/10.3389/fnut.2021.783831

60. da Rocha, M. C. O., da Silva, P. B., Radicchi, M. A., Andrade, B. Y. G., de Oliveira, J. V., Venus, T., Merker, C., Estrela-Lopis, I., Longo, J. P. F., & Báo, S. N. (2020). Docetaxel-loaded solid lipid nanoparticles prevent tumor growth and lung metastasis of 4T1 murine mammary carcinoma cells. Journal of Nanobiotechnology, 18, 43. https://doi.org/10.1186/s12951-020-00604-7

61. Khan, M. M., & Torchilin, V. P. (2022). Recent Trends in Nanomedicine-Based Strategies to Overcome Multidrug Resistance in Tumors. Cancers, 14(17), 4123. https://doi.org/10.3390/cancers14174123

62. Bannister, A., Dissanayake, D., Kowalewski, A., Cicon, L., Bromma, K., & Chithrani, D.B. (2020). Modulation of the microtubule network for optimization of nanoparticle dynamics for the advancement of cancer nanomedicine. Bioengineering, 7, 56.

63. Bannister, A. H., Bromma, K., Sung, W., Monica, M., Cicon, L., Howard, P., ... & Chithrani, D. B. (2020). Modulation of nanoparticle uptake, intracellular distribution, and retention with docetaxel to enhance radiotherapy. The British Journal of Radiology, 93(1106), 20190742. https://doi.org/10.1259/bjr.20190742

64. Bromma, K., Bannister, A., Kowalewski, A., Cicon, L., & Chithrani, D. B. (2020). Elucidating the fate of nanoparticles among key cell components of the tumour microenvironment for promoting cancer nanotechnology. Cancer Nanotechnology, 11(1). https://doi.org/10.1186/s12645-020-00064-6

65. Carter, J.D., Cheng, N.N., Qu, Y.Q., Suarez, G.D., & Guo, T. (2007). Nanoscale energy deposition by X-ray absorbing nanostructures. J. Phys. Chem. B, 111, 11622–11625.

66. Sanche, L. (2009). Biological chemistry: Beyond radical thinking. Nature, 461, 358–359.

67. Fojo, T. (Ed.). (2008). The Role of Microtubules in Cell Biology, Neurobiology, and Oncology. Humana Press. https://doi.org/10.1007/978-1-59745-336-3

68. Zhang, D., & Kanakkanthara, A. (2020). Beyond the Paclitaxel and Vinca Alkaloids: Next Generation of Plant-Derived Microtubule-Targeting Agents with Potential Anticancer Activity. Cancers, 12(7). https://doi.org/10.3390/cancers12071721

69. Fanale, D., et al. (2015). Stabilizing versus Destabilizing the Microtubules: A Double-Edge Sword for an Effective Cancer Treatment Option? Analytical Cellular Pathology (Amsterdam), 2015. https://doi.org/10.1155/2015/690916.

70. Hennequin, C., Giocanti, N., & Favaudon, V. (1996). Interaction of ionizing radiation with paclitaxel (taxol) and docetaxel (taxotere) in HeLa and sq20b cells. Cancer Research, 56, 1842–1850.

71. Mason, K.A., Hunter, N.R., Milas, M., Abbruzzese, J.L., & Milas, L. (1997). Docetaxel enhances tumour radioresponse *in vivo*. Clinical Cancer Research, 3, 2431.

72. Fard, A.E., Tavakoli, M.B., Salehi, H., & Emami, H. (2017). Synergetic effects of docetaxel and ionizing radiation reduced cell viability on mcf-7 breast cancer cell. Applied Cancer Research, 37, 29.

73. Kumar, P. (2003). A new paradigm for the treatment of high-risk prostate cancer: Radiosensitization with docetaxel. Reviews in Urology, 5, S71–S77.

74. Fujii, M., Tsukuda, M., Satake, B., Kubota, A., Kida, A., Kohno, N., Okami, K., & Inuyama, Y. (2004). Phase I/II trial of weekly docetaxel and concomitant radiotherapy for squamous cell carcinoma of the head and neck. International Journal of Clinical Oncology, 9, 107–112.

75. Barnadas, A., Mesía, R., Majem, M., Galiana, R., López-Pousa, A., de Vega, J.M., Margelí, M., Valentí, V., Anglada, L., Lloansí, A., & et al. (2011). Phase I/II docetaxel plus concurrent hyperfractionated radiotherapy in locally advanced unresectable head and neck cancer (tax.Es1.102 study). Clinical and Translational Oncology, 13, 254–260.

76. Kim, E.S., & Khuri, F.R. (2002). Docetaxel and radiation as combined-modality therapy. Oncology, 16, 97–105.

77. Jackson, W.C., Feng, F.Y., Daignault, S., Hussain, M., Smith, D., Cooney, K., Pienta, K., Jolly, S., Hollenbeck, B., Olson, K.B., & et al. (2015). A phase 2 trial of salvage radiation and concurrent weekly docetaxel after a rising prostate-specific antigen level after radical prostatectomy. Advances in Radiation Oncology, 1, 59–66.

78. Brackstone, M., Palma, D., Tuck, A.B., Scott, L., Potvin, K., Vandenberg, T., Perera, F., D'Souza, D., Taves, D., Kornecki, A., & et al. (2017). Concurrent neoadjuvant chemotherapy and radiation therapy in locally advanced breast cancer. International Journal of Radiation Oncology, Biology, Physics, 99, 769–776.

79. Liu, T., Zhou, L., Li, D., Andl, T., & Zhang, Y. (2019). Cancer-Associated Fibroblasts Build and Secure the Tumor Microenvironment. Frontiers in Cell and Developmental Biology, 7, 60. https://doi.org/10.3389/fcell.2019.00060.

80. Stylianopoulos, T., Poh, M. Z., Insin, N., Bawendi, M. G., Fukumura, D., Munn, L. L., & Jain, R. K. (2010). Diffusion of particles in the extracellular matrix: The effect of repulsive electrostatic interactions. Biophysical Journal, 99(5), 1342–1349.

81. Park, Y., Huh, K. M., & Kang, S.-W. (2021). Applications of Biomaterials in 3D Cell Culture and Contributions of 3D Cell Culture to Drug Development and Basic Biomedical Research. International Journal of Molecular Sciences, 22(5), 2491. https://doi.org/10.3390/ijms22052491

82. Lynch, C. R., Kondiah, P. P. D., & Choonara, Y. E. (2021). Advanced Strategies for Tissue Engineering in Regenerative Medicine: A Biofabrication and Biopolymer Perspective. Molecules, 26(9), 2518. https://doi.org/10.3390/molecules26092518

83. Riedl, A., Schlederer, M., Pudelko, K., Stadler, M., Walter, S., Unterleuthner, D., Unger, C., Kramer, N., Hengstschläger, M., Kenner, L., Pfeiffer, D., Krupitza, G., & Dolznig, H. (2017). Comparison of cancer cells in 2D vs 3D culture reveals differences in AKT-mTOR-S6K signaling and drug responses. Journal of Cell Science, 130(1), 203–218.

84. Li, C. L., Tian, T., Nan, K. J., Zhao, N., Guo, Y. H., Cui, J., Wang, J., & Zhang, W. G. (2008). Survival advantages of multicellular spheroids vs. monolayers of HepG2 cells *in vitro*. Oncology Reports, 20(6), 1465–1471.

85. Edmondson, R., Adcock, A. F., & Yang, L. (2016). Influence of Matrices on 3D-Cultured Prostate Cancer Cells' Drug Response and Expression of Drug-Action Associated Proteins. PLOS ONE, 11(6), e0158116.

86. Cooper, G. (2023). The Cell: A Molecular Approach (9th ed.). Oxford University Press.

87. Hall, E. J., & Giaccia, A. J. (2018). Radiobiology for the radiologist (8th ed.). Philadelphia, PA: Wolters Kluwer Health/Lippincott Williams & Wilkins.

88. Nussinov, R., Tsai, C.-J., & Jang, H. (2021). Anticancer drug resistance: An update and perspective. Drug Resistance Updates : Reviews and Commentaries in Antimicrobial and Anticancer Chemotherapy, 59, 100796. https://doi.org/10.1016/j.drup.2021.100796

89. Xiao, Y., & Yu, D. (2021). Tumor microenvironment as a therapeutic target in cancer. Pharmacology & Therapeutics, 221, 107753. https://doi.org/10.1016/j.pharmthera.2020.107753

90. Hanahan, D., & Weinberg, R. A. (2000). The hallmarks of cancer. Cell, 100(1), 57–70. https://doi.org/10.1016/s0092-8674(00)81683-9

91. Hanahan, D., & Weinberg, R. A. (2011). Hallmarks of Cancer: The Next Generation. Cell, 144(5), 646–674. https://doi.org/10.1016/j.cell.2011.02.013

92. Hanahan, D. (2022). Hallmarks of Cancer: New Dimensions. Cancer Discovery, 12(1), 31–46. https://doi.org/10.1158/2159-8290.CD-21-1059

93. Cserni, G., Chmielik, E., Cserni, B., & Tot, T. (2018). The new TNM-based staging of breast cancer. Virchows Archiv, 472(5), 697–703. https://doi.org/10.1007/s00428-018-2301-9

94. Roalsø, M., Aunan, J. R., & Søreide, K. (2020). Refined TNM-staging for pancreatic adenocarcinoma – Real progress or much ado about nothing? European Journal of Surgical Oncology, 46(8), 1554–1557. https://doi.org/10.1016/j.ejso.2020.02.014

95. Boeker, M., França, F., Bronsert, P., & Schulz, S. (2016). TNM-O: Ontology support for staging of malignant tumours. Journal of Biomedical Semantics, 7, 64. https://doi.org/10.1186/s13326-016-0106-9

96. World Health Organization. (2007). Cancer Control: Knowledge into Action: WHO Guide for Effective Programmes: Module 5: Palliative Care. Geneva: Author. ISBN-10: 92-4-154734-5.

97. Trapani, D., Ginsburg, O., Fadelu, T., Lin, N. U., Hassett, M., Ilbawi, A. M., Anderson, B. O., & Curigliano, G. (2022). Global challenges and policy solutions in breast cancer control. Cancer Treatment Reviews, 104, 102339. https://doi.org/10.1016/j.ctrv.2022.102339

98. Ho, W. J., Jaffee, E. M., & Zheng, L. (2020). The tumour microenvironment in pancreatic cancer—Clinical challenges and opportunities. Nature Reviews. Clinical Oncology, 17(9), 527–540. https://doi.org/10.1038/s41571-020-0363-5

99. Hessmann, E., Buchholz, S. M., Demir, I. E., Singh, S. K., Gress, T. M., Ellenrieder, V., & Neesse, A. (2020). Microenvironmental Determinants of Pancreatic Cancer. Physiological Reviews, 100(4), 1707–1751. https://doi.org/10.1152/physrev.00042.2019

100. Darby, I. A., Laverdet, B., Bonté, F., & Desmoulière, A. (2014). Fibroblasts and myofibroblasts in wound healing. Clin Cosmet Investig Dermatol, 7, 301-311.

101. Albrengues, J., Bertero, T., Grasset, E., Bonan, S., Maiel, M., Bourget, I., Philippe, C., Herraiz Serrano, C., Benamar, S., Croce, O., ... & others. (2015). Epigenetic switch drives the conversion of fibroblasts into proinvasive cancer-associated fibroblasts. Nature Communications, 6, 10204.

102. Alkasalias, T., Moyano-Galceran, L., Arsenian-Henriksson, M., & Lehti, K. (2018). Fibroblasts in the tumour microenvironment: Shield or spear? Int J Mol Sci, 19, 1532.

103. Ortiz-Otero, N., Clinch, A. B., Hope, J., Wang, W., Reinhart-King, C. A., & King, M. R. (2020). Cancer associated fibroblasts confer shear resistance to circulating tumor cells during prostate cancer metastatic progression. Oncotarget, 11(12), 1037-1050. https://doi.org/10.18632/oncotarget.27510

104. Joshi, R. S., Kanugula, S. S., Sudhir, S., Pereira, M. P., Jain, S., & Aghi, M. K. (2021). The Role of Cancer-Associated Fibroblasts in Tumor Progression. Cancers, 13(6), Article 6. https://doi.org/10.3390/cancers13061399

105. Shiga, K., Hara, M., Nagasaki, T., Sato, T., Takahashi, H., & Takeyama, H. (2015). Cancer-associated fibroblasts: Their characteristics and their roles in tumour growth. Cancers, 7, 2443-2458.

106. Henke, E., Nandigama, R., & Ergün, S. (2020). Extracellular matrix in the tumour microenvironment and its impact on cancer therapy. Frontiers in Molecular Biosciences, 6.

107. Walker, C., Mojares, E., & Del Río Hernández, A. (2018). Role of extracellular matrix in development and cancer progression. Int J Mol Sci, 19.

108. Sahai, E., Astsaturov, I., Cukierman, E., DeNardo, D. G., Egeblad, M., Evans, R. M., ... & Hunter, T., et al. (2020). A framework for advancing our understanding of cancer-associated fibroblasts. Nat Rev Cancer, 20, 174-186.

109. Kaushik, G., Venkatesha, S., Verma, B., Vishwakarma, B., Zhang, A.-H., & Wesa, A. (2022). Preclinical *In vitro* and *In vivo* Models for Adoptive Cell Therapy of Cancer. Cancer Journal (Sudbury, Mass.), 28(4), 257–262. https://doi.org/10.1097/PPO.0000000000000609

110. Azimian Zavareh, V., Rafiee, L., Sheikholeslam, M., Shariati, L., Vaseghi, G., Savoji, H., & Haghjooy Javanmard, S. (2022). Three-Dimensional *in vitro* Models: A Promising Tool To Scale-Up Breast Cancer Research. ACS Biomaterials Science & Engineering, 8(11), 4648–4672. https://doi.org/10.1021/acsbiomaterials.2c00277

111. Pinto, B., Henriques, A. C., Silva, P. M. A., & Bousbaa, H. (2020). Three-Dimensional Spheroids as *In vitro* Preclinical Models for Cancer Research. Pharmaceutics, 12(12), 1186. https://doi.org/10.3390/pharmaceutics12121186

112. Coleman, S. J., Watt, J., Arumugam, P., Solaini, L., Carapuca, E., Ghallab, M., Grose, R. P., & Kocher, H. M. (2014). Pancreatic cancer organotypics: High throughput, preclinical models for pharmacological agent evaluation. World Journal of Gastroenterology, 20(26), 8471–8481. https://doi.org/10.3748/wjg.v20.i26.8471

113. Tsai, S., McOlash, L., Palen, K., Johnson, B., Duris, C., Yang, Q., Dwinell, M. B., Hunt, B., Evans, D. B., Gershan, J., & James, M. A. (2018). Development of primary human pancreatic cancer organoids, matched stromal and immune cells and 3D tumor microenvironment models. BMC Cancer, 18(1), 335. https://doi.org/10.1186/s12885-018-4238-4

114. Nihashi, Y., Song, X., Yamamoto, M., Setoyama, D., & Kida, Y. S. (2023). Decoding Metabolic Symbiosis between Pancreatic Cancer Cells and Cancer-Associated Fibroblasts Using Cultured Tumor Microenvironment. International Journal of Molecular Sciences, 24(13), 11015. https://doi.org/10.3390/ijms241311015

115. Tomás-Bort, E., Kieler, M., Sharma, S., Candido, J. B., & Loessner, D. (2020). 3D approaches to model the tumor microenvironment of pancreatic cancer. Theranostics, 10(11), 5074–5089. https://doi.org/10.7150/thno.42441

116. Breslin, S., & O'Driscoll, L. (2013). Three-dimensional cell culture: The missing link in drug discovery. Drug Discovery Today, 18(5-6), 240-249.

117. Bromma, K., Alhussan, A., Perez, M. M., Howard, P., Beckham, W., & Chithrani, D. B. (2021). Three-Dimensional Tumor Spheroids as a Tool for Reliable Investigation of Combined Gold Nanoparticle and Docetaxel Treatment. Cancers, 13(6), 1465. https://doi.org/10.3390/cancers13061465

118. Kourtis, N., & Tavernarakis, N. (2011). Cellular stress response pathways and ageing: Intricate molecular relationships. EMBO Journal, 30(13), 2520-2531. https://doi.org/10.1038/emboj.2011.162

119. Toulany, M. (2019). Targeting DNA double-strand break repair pathways to improve radiotherapy response. Genes, 10(1), 25. https://doi.org/10.3390/genes10010025

120. Attix, F. H. (2007). Introduction to Radiological Physics and Radiation Dosimetry. VCH.

121. Gibbons, J. P., & Khan, F. M. (2020). Khan's the Physics of Radiation Therapy. Wolters Kluwer.

122. INTERNATIONAL ATOMIC ENERGY AGENCY. (2005). Radiation Oncology Physics. IAEA, Vienna.

123. Pawlicki, T., Scalliet, P., & Huq, M. S. (2017). Hendee's Radiation Therapy Physics. John Wiley and Sons.

124. Kaiser, A., Hillbrand, M., Prost, A., Tanadini-Lang, S., Pavic, M., Adams, A., ... & Weber, D. C. (2019). Proton Therapy Delivery and Its Clinical Application in Select Solid Tumour Malignancies. Journal of Visualized Experiments, (144). https://doi.org/10.3791/58372.

125. Anjali, V. R. (2020). Electrons. In Mallick, S., Rath, G., & Benson, R. (Eds.) Practical Radiation Oncology. Springer, Singapore.

126. Rutenberg, M. S., & Nichols, R. C. (2020). Proton Beam Radiotherapy for Pancreas Cancer. Journal of Gastrointestinal Oncology, 11(1), 166–175. https://doi.org/10.21037/jgo.2019.03.02.

127. Hall, W. A., & Goodman, K. A. (2019). Radiation Therapy for Pancreatic Adenocarcinoma, a Treatment Option That Must Be Considered in the Management of a Devastating Malignancy. Radiation Oncology, 14(1), 114. https://doi.org/10.1186/s13014-019-1277-1.

128. Lin, Y. K., Chang, Y. H., Chen, W. T., ... & Chen, H. H. W. (2018). Intensity-Modulated Radiotherapy with Systemic Chemotherapy Improves Survival in Patients with Nonmetastatic Unresectable Pancreatic Adenocarcinoma: A Propensity Score-Matched, Nationwide, Population-Based Cohort Study. Radiotherapy and Oncology, 129(2), 326–332. https://doi.org/10.1016/j.radonc.2018.07.012.

129. Goto, Y., Nakamura, A., Ashida, R., ... & Ohtsuka, T. (2018). Clinical Evaluation of Intensity-Modulated Radiotherapy for Locally Advanced Pancreatic Cancer. Radiation Oncology, 13. https://doi.org/10.1186/s13014-018-1063-5.

130. Hsieh, M.-C., Chang, W. W., Yu, H. H., ... & Chang, C. L. (2018). Adjuvant Radiotherapy and Chemotherapy Improve Survival in Patients with Pancreatic Adenocarcinoma Receiving Surgery: Adjuvant Chemotherapy Alone Is Insufficient in the Era of Intensity Modulation Radiation Therapy. Cancer Medicine, 7(6), 2328–2338. https://doi.org/10.1002/cam4.1479.

131. Geus, S. W. L. de, Lens, E., Horst, E. v. d., ... & Daams, F. (2017). Stereotactic Body Radiotherapy for Unresected Pancreatic Cancer: A Nationwide Review. Cancer, 123(21), 4158–4167. https://doi.org/10.1002/cncr.30856.

132. Zhong, J., Patel, K., Switchenko, J., ... & Cassidy, R. J. (2017). Outcomes for Patients With Locally Advanced Pancreatic Adenocarcinoma Treated With Stereotactic Body Radiation Therapy Versus Conventionally Fractionated Radiation. Cancer, 123(18), 3486–3493. https://doi.org/10.1002/cncr.30706.

133. Lischalk, J. W., Burke, A., Chew, J., ... & Collins, S. P. (2018). Five-Fraction Stereotactic Body Radiation Therapy (SBRT) and Chemotherapy for the Local Management of Metastatic Pancreatic Cancer. Journal of Gastrointestinal Cancer, 49(2), 116–123. https://doi.org/10.1007/s12029-016-9909-2.

134. Ryan, J. F., Groot, V. P., Rosati, L. M., Hacker-Prietz, A., Narang, A. K., McNutt, T. R., Jackson, J. F., Le, D. T., Jaffee, E. M., Zheng, L., Laheru, D. A., He, J., Pawlik, T. M., Weiss, M. J., Wolfgang, C. L., & Herman, J. M. (2018). Stereotactic Body Radiation Therapy for Isolated Local Recurrence After Surgical Resection of Pancreatic Ductal Adenocarcinoma Appears to be Safe and Effective. Annals of Surgical Oncology, 25(1), 280–289. https://doi.org/10.1245/s10434-017-6134-6

135. Schneider, M., Hackert, T., Strobel, O., & Büchler, M. W. (2021). Technical advances in surgery for pancreatic cancer. The British Journal of Surgery, 108(7), 777–785. https://doi.org/10.1093/bjs/znab133

136. Biagi, J. J., Cosby, R., Bahl, M., Elfiki, T., Goodwin, R., Hallet, J., Hirmiz, K., & Mahmud, A. (2023). Adjuvant Chemotherapy and Radiotherapy in Resected Pancreatic Ductal Adenocarcinoma: A Systematic Review and Clinical Practice Guideline. Current Oncology (Toronto, Ont.), 30(7), 6575–6586. https://doi.org/10.3390/curroncol30070482

137. Springfeld, C., Ferrone, C. R., Katz, M. H. G., Philip, P. A., Hong, T. S., Hackert, T., Büchler, M. W., & Neoptolemos, J. (2023). Neoadjuvant therapy for pancreatic cancer. Nature Reviews. Clinical Oncology, 20(5), 318–337. https://doi.org/10.1038/s41571-023-00746-1

138. Xu, B., Zhou, Y., Pei, Q., Tan, F., Zhao, L., Güngör, C., Wang, D., Li, Y., Liu, W., & Zhou, Z. (2022). The survival impact of palliative radiotherapy on synchronous metastatic pancreatic ductal adenocarcinoma: Metastatic site can serve for radiotherapy-decision. Journal of Cancer, 13(2), 385–392. https://doi.org/10.7150/jca.64800

139. Klement, R. J. (2019). The influence of ketogenic therapy on the 5 R's of radiobiology. International Journal of Radiation Biology, 95(4), 394–407. https://doi.org/10.1080/09553002.2017.1380330

140. Boustani, J., Grapin, M., Laurent, P.-A., Apetoh, L., & Mirjolet, C. (2019). The 6th R of Radiobiology: Reactivation of Anti-Tumor Immune Response. *Cancers*, *11*(6), 860. https://doi.org/10.3390/cancers11060860

141. Kerner, G. S. M. A., et al. (2014). Concurrent Gemcitabine and 3D Radiotherapy in Patients with Stage III Unresectable Non-Small Cell Lung Cancer. Radiation Oncology, 9(1), 190. https://doi.org/10.1186/1748-717X-9-190

142. Kobashigawa, S., et al. (2015). Gemcitabine Induces Radiosensitization Through Inhibition of RAD51-Dependent Repair for DNA Double-Strand Breaks. Anticancer Research, 35(5), 2731-2737.

143. Santis, M. D., et al. (2014). Combined Chemoradiotherapy with Gemcitabine in Patients with Locally Advanced Inoperable Transitional Cell Carcinoma of the Urinary Bladder and/or in Patients Ineligible for Surgery: A Phase I Trial. Annals of Oncology, 25(9), 1789-1794. https://doi.org/10.1093/annonc/mdu209

144. Harrabi, S. B., et al. (2016). S-Phase–Specific Radiosensitization by Gemcitabine for Therapeutic Carbon Ion Exposure *in vitro*. Journal of Radiation Research, 57(2), 110-114. https://doi.org/10.1093/jrr/rrv097

145. Demirci, U., et al. (2015). Radiotherapy Concurrent with Weekly Gemcitabine after Transurethral Tumour Resection in Muscle Invasive Bladder Cancer. Journal of Cancer Research and Therapeutics, 11(4), 704-707

146. Kim, H., et al. (2016). SPARC Independent Delivery of Nab-Paclitaxel without Depleting Tumour Stroma in Patient-Derived Pancreatic Cancer Xenografts. Molecular Cancer Therapeutics, 15(4), 680–88. doi:10.1158/1535-7163.MCT-15-0764.

147. Sen, S., et al. (2018). Phase I Study of Nab-Paclitaxel, Gemcitabine, and Bevacizumab in Patients with Advanced Cancers. British Journal of Cancer, 118(11), 1419–24. doi:10.1038/s41416-018-0068-z.

148. Halozyme Therapeutics. (2020). A Phase 2, Randomized, Multicenter Study of PEGPH20 (PEGylated Recombinant Human Hyaluronidase) Combined With Nab-Paclitaxel Plus Gemcitabine Compared With Nab-Paclitaxel Plus Gemcitabine in Subjects With Stage IV Previously Untreated Pancreatic Cancer. Clinical trial registration, NCT01839487. Retrieved from https://clinicaltrials.gov/ct2/show/NCT01839487.

149. Zeng, S., et al. (2019). Chemoresistance in Pancreatic Cancer. International Journal of Molecular Sciences, 20(18). doi:10.3390/ijms20184504.

150. Bachet, J.-B., et al. (2015). A Randomized Phase II Study of Weekly Nab-Paclitaxel plus Gemcitabine or Simplified LV5FU2 as First-Line Therapy in Patients with Metastatic Pancreatic Cancer: The AFUGEM GERCOR Trial. BMC Cancer, 15. doi:10.1186/s12885-015-1656-4.

151. Giordano, G., et al. (2017). Nano Albumin Bound-Paclitaxel in Pancreatic Cancer: Current Evidences and Future Directions. World Journal of Gastroenterology, 23(32), 5875–86. doi:10.3748/wjg.v23.i32.5875.

152. Von Hoff, D. D., et al. (2013). Increased Survival in Pancreatic Cancer with Nab-Paclitaxel plus Gemcitabine. The New England Journal of Medicine, 369(18), 1691–703. doi:10.1056/NEJMoa1304369.

153. Weaver, B. A. (2014). How Taxol/Paclitaxel Kills Cancer Cells. Molecular Biology of the Cell, 25(18), 2677–81. doi:10.1091/mbc.E14-04-0916.

154. Peronne, L., et al. (2020). Two Antagonistic Microtubule Targeting Drugs Act Synergistically to Kill Cancer Cells. BioRxiv. doi:10.1101/2020.02.06.936849.

155. Serpico, A. F., et al. (2020). Exploiting Immune-Dependent Effects of Microtubule-Targeting Agents to Improve Efficacy and Tolerability of Cancer Treatment. Cell Death & Disease, 11(5). doi:10.1038/s41419-020-2567-0.

156. Senese, S., Lo, Y.-C., Gholkar, A. A., Li, C.-M., Huang, Y., Mottahedeh, J., Kornblum, H. I., Damoiseaux, R., & Torres, J. Z. (2017). Microtubins: A novel class of small synthetic microtubule targeting drugs that inhibit cancer cell proliferation. Oncotarget, 8(61), 104007–104021. https://doi.org/10.18632/oncotarget.21945

157. Field, J. J., Kanakkanthara, A., & Miller, J. H. (2014). Microtubule-targeting agents are clinically successful due to both mitotic and interphase impairment of microtubule function. Bioorganic & Medicinal Chemistry, 22(18), 5050–5059. https://doi.org/10.1016/j.bmc.2014.02.035

158. Risinger, A. L., Peng, J., Rohena, C. C., Aguilar, H. R., Frantz, D. E., & Mooberry, S. L. (2013). The Bat Flower: A Source of Microtubule-Destabilizing and -Stabilizing Compounds with Synergistic Antiproliferative Actions. Journal of Natural Products, 76(10), 1923–1929. https://doi.org/10.1021/np4005079

159. U.S. Food and Drug Administration. (2012). Docetaxel Injection [Reference ID: 3101735]. https://www.accessdata.fda.gov/drugsatfda_docs/label/2012/201525s002lbl.pdf

160. Snyder, J.P., Nettles, J.H., Cornett, B., Downing, K.H., & Nogales, E. (2001). The binding conformation of taxol in beta-tubulin: A model based on electron crystallographic density. Proc. Natl. Acad. Sci. USA, 98, 5312–5316.

161. De Brabander, M., Geuens, G., Nuydens, R., Willebrords, R., & De Mey, J. (1981). Taxol induces the assembly of free microtubules in living cells and blocks the organizing capacity of the centrosomes and kinetochores. Proc. Natl. Acad. Sci. USA, 78, 5608–5612.

162. Paoletti, A., Giocanti, N., Favaudon, V., & Bornens, M. (1997). Pulse treatment of interphasic hela cells with nanomolar doses of docetaxel affects centrosome organization and leads to catastrophic exit of mitosis. J. Cell Sci., 110, 2403–2415.

163. Granger, E., McNee, G., Allan, V., & Woodman, P. (2014). The role of the cytoskeleton and molecular motors in endosomal dynamics. Semin. Cell Dev. Biol., 31, 20–29.

164. Gorodetsky, R., Levdansky, L., Ringel, I., & Vexler, A. (1998). Paclitaxel-induced modification of the effects of radiation and alterations in the cell cycle in normal and tumor mammalian cells. Radiation Research, 150(3), 283–291.

165. Milas, L., Saito, Y., Hunter, N., Milross, C. G., & Mason, K. A. (1996). Therapeutic potential of paclitaxel-radiation treatment of a murine ovarian carcinoma. Radiotherapy and Oncology: Journal of the European Society for Therapeutic Radiology and Oncology, 40(2), 163–170. https://doi.org/10.1016/0167-8140(96)01778-1

166. Almasri, F., Sakarya, E. H., & Karshafian, R. (2023). Radioenhancement with the Combination of Docetaxel and Ultrasound Microbubbles: In Vivo Prostate Cancer. Pharmaceutics, 15(5), 1468. https://doi.org/10.3390/pharmaceutics15051468

167. Chen, R. C., Rosenman, J. G., Hoffman, L. G., Chiu, W.-K., Wang, A. Z., Pruthi, R. S., Wallen, E. M., Crane, J. M., Kim, W. Y., Rathmell, W. K., Godley, P. A., & Whang, Y. E. (2012). Phase I study of concurrent weekly docetaxel, high-dose intensity-modulated radiation therapy (IMRT) and androgen-deprivation therapy (ADT) for high-risk prostate cancer. BJU International, 110(11 Pt B), E721-726. https://doi.org/10.1111/j.1464-410X.2012.11536.x

168. Kodaira, T., Fuwa, N., Furutani, K., Tachibana, H., & Yamazaki, T. (2005). Phase I trial of weekly docetaxel and concurrent radiotherapy for head and neck cancer in elderly patients or patients with complications. Japanese Journal of Clinical Oncology, 35(4), 173–176. https://doi.org/10.1093/jjco/hyi058

169. Biete Solà, A., Marruecos Querol, J., Calvo Manuel, F. A., Verger Fransoy, E., Rovirosa Casino, A., Grau de Castro, J. J., de Las Heras González, M., Ramos Aguerri, A., Palacios Eito, A., Veiras Candal, C., & Solano López, M. V. (2007). Phase II trial: Concurrent radio-chemotherapy with weekly docetaxel for advanced squamous cell carcinoma of head and neck. Clinical & Translational Oncology: Official Publication of the Federation of Spanish Oncology Societies and of the National Cancer Institute of Mexico, 9(4), 244–250. https://doi.org/10.1007/s12094-007-0047-y

170. Khuri, F. R. (2002). Docetaxel for locally advanced or metastatic non-small-cell lung cancer. Current data and future directions as front-line therapy. Oncology (Williston Park, N.Y.), 16(6 Suppl 6), 53–62.

171. Armstrong, A. J., Halabi, S., Healy, P., Lee, W. R., Koontz, B. F., Moul, J. W., Mundy, K., Creel, P., Wood, S., Davis, K., Carducci, M. A., Stein, M., Hobbs, C., Reimer, B., Nguyen, M., Anand, M., Bratt, L., Kim, S., Tran, P. T., … Department of Defense Prostate Cancer Clinical Trials Consortium. (2016). A phase 2 multimodality trial of docetaxel/prednisone with sunitinib followed by salvage radiation therapy in men with PSA recurrent prostate cancer after radical prostatectomy. Prostate Cancer and Prostatic Diseases, 19(1), 100–106. https://doi.org/10.1038/pcan.2015.59

172. Iwata, H., Sato, N., Masuda, N., Nakamura, S., Yamamoto, N., Kuroi, K., Kurosumi, M., Tsuda, H., Akiyama, F., Ohashi, Y., & Toi, M. (2011). Docetaxel followed by fluorouracil/epirubicin/cyclophosphamide as neoadjuvant chemotherapy for patients with primary breast cancer. Japanese Journal of Clinical Oncology, 41(7), 867–875. https://doi.org/10.1093/jjco/hyr081

173. Chen, X.-Y., Yang, H.-W., Chi, S.-M., Yue, L.-L., Ruan, Q., Lei, Z., Zhu, H.-Y., & Zhao, Y. (2021). Solubility and biological activity enhancement of docetaxel via formation of inclusion complexes with three alkylenediamine-modified β-cyclodextrins. RSC Adv., 11, 6292–6303.

174. Bae, Y. H., & Park, K. (2011). Targeted drug delivery to tumors: Myths, reality and possibility. Journal of Controlled Release, 153(3), 198–205. https://doi.org/10.1016/j.jconrel.2011.06.001

175. Chung, J. Y., Thone, M. N., & Kwon, Y. J. (2021). COVID-19 vaccines: The status and perspectives in delivery points of view. Advanced Drug Delivery Reviews, 170, 1–25. https://doi.org/10.1016/j.addr.2020.12.011

176. Miao, L., Zhang, Y., & Huang, L. (2021). MRNA vaccine for cancer immunotherapy. Molecular Cancer, 20, 41. https://doi.org/10.1186/s12943-021-01335-5

177. Baetke, S. C., Lammers, T., & Kiessling, F. (2015). Applications of nanoparticles for diagnosis and therapy of cancer. The British Journal of Radiology, 88(1054), 20150207. https://doi.org/10.1259/bjr.20150207

178. Rautio, J., Kumpulainen, H., Heimbach, T., Oliyai, R., Oh, D., Järvinen, T., & Savolainen, J. (2008). Prodrugs: Design and clinical applications. Nature Reviews. Drug Discovery, 7(3), 255–270. https://doi.org/10.1038/nrd2468

179. Penninckx, S., et al. (2020). Gold nanoparticles as a potent radiosensitizer: A transdisciplinary approach from physics to patient. Cancers, 12(8), 2021. https://doi.org/10.3390/cancers12082021

180. Lawrence, T.S., Blackstock, A.W., & McGinn, C. (2003). The mechanism of action of radiosensitization of conventional chemotherapeutic agents. Seminars in Radiation Oncology, 13, 13-21.

181. Parajuli, R. K., Sakai, M., Parajuli, R., & Tashiro, M. (2022). Development and Applications of Compton Camera—A Review. Sensors, 22(19), Article 19. https://doi.org/10.3390/s22197374

182. Harrison, E., Nicol, J.R., Macias-Montero, M., Burke, G.A., Coulter, J.A., Meenan, B.J., & Dixon, D. (2016). A comparison of gold nanoparticle surface co-functionalization approaches using polyethylene glycol (peg) and the effect on stability, non-specific protein adsorption and internalization. Mater. Sci. Eng. C, 62, 710–718.

183. Su, S., Zuo, X., Pan, D., Pei, H., Wang, L., Fan, C., & Huang, W. (2013). Design and applications of gold nanoparticle conjugates by exploiting biomolecule–gold nanoparticle interactions. Nanoscale, 5, 2589–2599.

184. Townley, H.E., Kim, J., & Dobson, P.J. (2012). *In vivo* demonstration of enhanced radiotherapy using rare earth doped titania nanoparticles. Nanoscale, 4, 5043–5050.

185. Mirjolet, C., Papa, A.L., Crehange, G., Raguin, O., Seignez, C., Paul, C., Truc, G., Maingon, P., & Millot, N. (2013). The radiosensitization effect of titanate nanotubes as a new tool in radiation therapy for glioblastoma: A proof-of-concept. Radiother. Oncol., 108, 136–142.

186. Takahashi, J., & Misawa, M. (2007). Analysis of potential radiosensitizing materials for X-ray-induced photodynamic therapy. Nano Biotechnol., 3, 116–126.

187. Yang, W., Read, P.W., Mi, J., Baisden, J.M., Reardon, K.A., Larner, J.M., Helmke, B.P., & Sheng, K. (2008). Semiconductor nanoparticles as energy mediators for photosensitizer-enhanced radiotherapy. Int. J. Radiat. Oncol. Biol. Phys., 72, 633–635.

188. Le Duc, G., Miladi, I., Alric, C., Mowat, P., Brauer-Krisch, E., Bouchet, A., Khalil, E., Billotey, C., Janier, M., Lux, F., et al. (2011). Toward an image-guided microbeam radiation therapy using gadolinium-based nanoparticles. ACS Nano, 5, 9566–9574.

189. Liu, P., Huang, Z., Chen, Z., Xu, R., Wu, H., Zang, F., Wang, C., & Gu, N. (2013). Silver nanoparticles: A novel radiation sensitizer for glioma? Nanoscale, 5, 11829–11836.

190. González-López, M.A., Gutiérrez-Cárdenas, E.M., Sánchez-Cruz, C., Hernández-Paz, J.F., Pérez, I., Olivares-Trejo, J.J., & Hernández-González, O. (2020). Reducing the effective dose of cisplatin using gold nanoparticles as carriers. Cancer Nanotechnol., 11, 4.

191. Podgorsak, E.B. (2005). Radiation Oncology Physics: A Handbook for Teachers and Students. International Atomic Energy Agency.

192. Retif, P., Pinel, S., Toussaint, M., Frochot, C., Chouikrat, R., Bastogne, T., & Barberi-Heyob, M. (2015). Nanoparticles for radiation therapy enhancement: The key parameters. Theranostics, 5, 1030–1044.

193. Butterworth, K., et al. (2013). Radiosensitization by Gold Nanoparticles: Effective at Megavoltage Energies and Potential Role of Oxidative Stress. Translational Cancer Research, 2(4), 269–79. https://pure.qub.ac.uk, doi:10.3978/j.issn.2218-676X.2013.08.03.

194. Hubbell, J.H., & Seltzer, S.M. (1996). Tables of X-ray Mass Attenuation coefficients and mass energy-absorption coefficients from 1 keV to 20MeV for Elements Z=1-92 and 48 Additional Substances of Dosimetric Interest. National Institute of Standards and Technology, US Department of Commerce.

195. Das, I.J., & Chopra, K.L. (1995). Backscatter dose perturbation in kilovoltage photon beams at high atomic number interfaces. Med. Phys., 22, 767–773.

196. Das, I.J. (1997). Forward dose perturbation at high atomic number interfaces in kilovoltage X-ray beams. Med. Phys., 24, 1781–1787.

197. Incerti, S., et al. (2016). Simulation of Auger Electron Emission from Nanometer-Size Gold Targets Using the Geant4 Monte Carlo Simulation Toolkit. Nuclear Instruments and Methods in Physics Research Section B: Beam Interactions with Materials and Atoms, 372(C). https://www.osti.gov, doi:10.1016/j.nimb.2016.02.005.

198. Chen, Y., Yang, J., Fu, S., & Wu, J. (2020). Gold Nanoparticles as Radiosensitizers in Cancer Radiotherapy. International Journal of Nanomedicine, 15, 9407–9430. https://doi.org/10.2147/IJN.S272902

199. Laprise-Pelletier, M., Simão, T., & Fortin, M.-A. (2018). Gold Nanoparticles in Radiotherapy and Recent Progress in Nanobrachytherapy. Advanced Healthcare Materials, 7(16), e1701460. https://doi.org/10.1002/adhm.201701460.

200. Wang, A.Z., Bagalkot, V., Vasilliou, C.C., Gu, F., Alexis, F., Zhang, L., Shaikh, M., Yuet, K., Cima, M.J., Langer, R., & et al. (2008). Superparamagnetic iron oxide nanoparticle-aptamer bioconjugates for combined prostate cancer imaging and therapy. ChemMedChem, 3, 1311–1315.

201. Wang, H., Mu, X., He, H., & Zhang, X.-D. (2018). Cancer radiosensitizers. Trends Pharmacol. Sci., 39, 24–48.

202. Lin, Y., McMahon, S.J., Scarpelli, M., Paganetti, H., & Schuemann, J. (2014). Comparing gold nano-particle enhanced radiotherapy with protons, megavoltage photons and kilovoltage photons: A monte carlo simulation. Phys. Med. Biol., 59, 7675–7689.

203. Lammel, T., Mackevica, A., Johansson, B.R., & Sturve, J. (2019). Endocytosis, intracellular fate, accumulation, and agglomeration of titanium dioxide (TiO2) nanoparticles in the rainbow trout liver cell line RTL-W1. Environ. Sci. Pollut. Res., 26, 15354–15372. doi:10.1007/s11356-019-04856-1.

204. Dykman, L.A., & Khlebtsov, N.G. (2016). Immunological properties of gold nanoparticles. Chem. Sci., 8, 1719–1735. doi:10.1039/c6sc03631g.

205. Manson, J., Kumar, D., Meenan, B.J., & Dixon, D. (2011). Polyethylene glycol functionalized gold nanoparticles: The influence of capping density on stability in various media. Gold Bull., 44, 99–105. doi:10.1007/s13404-011-0015-8.

206. Cruje, C., & Chithrani, B.D. (2015). Optimization of PEG coated nanoscale gold particles for enhanced radiation therapy. RSC Adv., 5, 101525–101532. doi:10.1039/c5ra19104a.

207. Spadavecchia, J., Movia, D., Moore, C., Maguire, C.M., Moustaoui, H., Casale, S., Volkov, Y., & Prina-Mello, A. (2016). Targeted polyethylene glycol gold nanoparticles for the treatment of pancreatic cancer: From synthesis to proof-of-concept *in vitro* studies. Int. J. Nanomed., 11, 791–822. doi:10.2147/IJN.S97476.

208. Cruje, C., Chithrani, B.D., & Chithrani, D. (2015). Integration of Peptides for Enhanced Uptake of PEGylayed Gold Nanoparticles. J. Nanosci. Nanotechnol., 15, 2125–2131. doi:10.1166/jnn.2015.10321.

209. Wu, P.-H., Onodera, Y., Ichikawa, Y., Rankin, E.B., Giaccia, A.J., Watanabe, Y., Qian, W., Hashimoto, T., Shirato, H., & Nam, J.-M. (2017). Targeting integrins with RGD-conjugated gold nanoparticles in radiotherapy decreases the invasive activity of breast cancer cells. Int. J. Nanomed., 12, 5069–5085. doi:10.2147/ijn.s137833.

210. Biscaglia, F., Ripani, G., Rajendran, S., Benna, C., Mocellin, S., Bocchinfuso, G., Meneghetti, M., Palleschi, A., & Gobbo, M. (2019). Gold Nanoparticle Aggregates Functionalized with Cyclic RGD Peptides for Targeting and Imaging of Colorectal Cancer Cells. ACS Appl. Nano Mater., 2, 6436–6444. doi:10.1021/acsanm.9b01392.

211. Pedrosa, P., Corvo, M. L., Ferreira-Silva, M., Martins, P., Carvalheiro, M. C., Costa, P. M., Martins, C., Martins, L. M. D. R. S., Baptista, P. V., & Fernandes, A. R. (2019). Targeting Cancer Resistance via Multifunctional Gold Nanoparticles. International Journal of Molecular Sciences, 20(21), 5510. https://doi.org/10.3390/ijms20215510

212. Albertini, B., Mathieu, V., Iraci, N., Van Woensel, M., Schoubben, A., Donnadio, A., Greco, S.M.L., Ricci, M., Temperini, A., Blasi, P., & et al. (2019). Tumor targeting by peptide-decorated gold nanoparticles. Mol. Pharm., 16, 2430–2444.

213. Cheng, Z., Li, M., Dey, R., & Chen, Y. (2021). Nanomaterials for cancer therapy: current progress and perspectives. Journal of Hematology & Oncology, 14(1), 85. https://doi.org/10.1186/s13045-021-01096-0

214. Alhussan, A., Bozdoğan, E. P. D., & Chithrani, D. B. (2021). Combining Gold Nanoparticles with Other Radiosensitizing Agents for Unlocking the Full Potential of Cancer Radiotherapy. Pharmaceutics, 13(4), 442. https://doi.org/10.3390/pharmaceutics13040442

215. Chithrani, B.D., Ghazani, A.A., & Chan, W.C.W. (2006). Determining the size and shape dependence of gold nanoparticle uptake into mammalian cells. Nano Lett., 6, 662–668.

216. Yohan, D., Cruje, C., Lu, X., & Chithrani, D.B. (2016). Size-Dependent Gold Nanoparticle Interaction at Nano–Micro Interface Using Both Monolayer and Multilayer (Tissue-Like) Cell Models. Nano-Micro Lett., 8, 44–53. doi:10.1007/s40820-015-0060-6.

217. Amendola, V., & Meneghetti, M. (2009). Size Evaluation of Gold Nanoparticles by UV−vis Spectroscopy. J. Phys. Chem. C, 113, 4277–4285. https://doi.org/10.1021/jp8082425

218. Chithrani, B. D., & Chan, W. C. W. (2007). Elucidating the mechanism of cellular uptake and removal of protein-coated gold nanoparticles of different sizes and shapes. Nano Letters, 7, 1542-1550.

219. Chithrani, D. B. (2010). Intracellular uptake, transport, and processing of gold nanostructures. Molecular Membrane Biology, 27, 299-311.

220. Yang, C., Neshatian, M., Van Prooijen, M., & Chithrani, D.B. (2014). Cancer Nanotechnology: Enhanced Therapeutic Response Using Peptide-Modified Gold Nanoparticles. J. Nanosci. Nanotechnol., 14, 4813–4819. https://doi.org/10.1166/jnn.2014.9280

221. Gao, H., Shi, W., & Freund, L.B. (2005). From The Cover: Mechanics of receptor-mediated endocytosis. Proc. Natl. Acad. Sci. USA, 102, 9469–9474. https://doi.org/10.1073/pnas.0503879102

222. Friedman, L. M., Furberg, C. D., DeMets, D. L., Reboussin, D. M., & Granger, C. B. (2015). *Fundamentals of Clinical Trials*. Springer International Publishing. https://doi.org/10.1007/978-3-319-18539-2.

223. Alhussan, A., Bromma, K., Bozdoğan, E. P. D., Metcalfe, A., Karasinska, J., Beckham, W., Alexander, A. S., Renouf, D. J., Schaeffer, D. F., & Chithrani, D. B. (2021). Investigation of Nano-Bio Interactions within a Pancreatic Tumor Microenvironment for the Advancement of Nanomedicine in Cancer Treatment. Current Oncology (Toronto, Ont.), 28(3), 1962–1979. https://doi.org/10.3390/curroncol28030183

224. Alhussan, A., Bromma, K., Perez, M. M., Beckham, W., Alexander, A. S., Howard, P. L., & Chithrani, D. B. (2021). Docetaxel-Mediated Uptake and Retention of Gold Nanoparticles in Tumor Cells and in Cancer-Associated Fibroblasts. Cancers, 13(13), 3157. https://doi.org/10.3390/cancers13133157

225. Alhussan, A. & Devika, B.C. (2021). Microtubule Targeting in Cancer Treatment. In L.S. Milane & M.M. Amiji (Eds.), Organelle and Molecular Targeting (1st ed.) (pp. 403-419). CRC Press. https://doi.org/10.1201/9781003092773

226. Zhang, X.D., Wu, H.Y., Wu, D., Wang, Y.Y., Chang, J.H., Zhai, Z.B., Meng, A.M., Liu, P.X., Zhang, L.A., & Fan, F.Y. (2010). Toxicologic effects of gold nanoparticles *in vivo* by different administration routes. Int. J. Nanomed., 5, 771–781.

227. Bailly, A.-L., Correard, F., Popov, A., Tselikov, G., Chaspoul, F., Appay, R., Al-Kattan, A., Kabashin, A.V., Braguer, D., & Esteve, M.-A. (2019). *In vivo* evaluation of safety, biodistribution and pharmacokinetics of laser-synthesized gold nanoparticles. Sci. Rep., 9, 1–12. https://doi.org/10.1038/s41598-019-48748-3

228. Khoo, A.M., Cho, S.H., Reynoso, F.J., Aliru, M., Aziz, K., Bodd, M., Yang, X., Ahmed, M.F., Yasar, S., Manohar, N., & others. (2017). Radiosensitization of prostate cancers *in vitro* and *in vivo* to erbium-filtered orthovoltage x-rays using actively targeted gold nanoparticles. Sci. Rep., 7, 18044-18044.

229. Yang, C., Bromma, K., & Chithrani, B. D. (2018). Peptide mediated *in vivo* tumour targeting of nanoparticles through optimization in single and multilayer *in vitro* cell models. Cancers, 10, 84

230. Haiss, W., Thanh, N.T.K., Aveyard, J., & Fernig, D.G. (2007). Determination of size and concentration of gold nanoparticles from UV-Vis spectra. Analytical Chemistry, 79(11), 4215-4221.

231. Berne, B. J., & Pecora, R. (2000). Dynamic Light Scattering: With Applications to Chemistry, Biology, and Physics. Dover Publications.

232. Harris, J. M., & Chess, R. B. (2003). Effect of pegylation on pharmaceuticals. Nature Reviews Drug Discovery, 2(3), 214-221.

233. Jang, I., & Beningo, K. (2019). Integrins, CAFs and Mechanical Forces in the Progression of Cancer. Cancers, 11(5), 721. doi:10.3390/cancers11050721

234. Dominguez, C. X., Müller, S., Keerthivasan, S., Koeppen, H., Hung, J., Gierke, S., Breart, B., Foreman, O., Bainbridge, T. W., Castiglioni, A., et al. (2020). Single-cell rna sequencing reveals stromal evolution into lrrc15 (+) myofibroblasts as a determinant of patient response to cancer immunotherapy. Cancer Discov., 10, 232–253.

235. Kemi, N., Eskuri, M., Herva, A., Leppänen, J., Huhta, H., Helminen, O., Saarnio, J., Karttunen, T. J., & Kauppila, J. H. (2018). Tumour-stroma ratio and prognosis in gastric adenocarcinoma. Br. J. Cancer, 119, 435–439.

236. Graizel, D., Zlotogorski-Hurvitz, A., Tsesis, I., Rosen, E., Kedem, R., & Vered, M. (2020). Oral cancer-associated fibroblasts predict poor survival: Systematic review and meta-analysis. Oral Dis., 26, 733–744.

237. Hosein, A. N., Brekken, R. A., & Maitra, A. (2020). Pancreatic cancer stroma: An update on therapeutic targeting strategies. Nat. Rev. Gastroenterol. Hepatol., 17, 487–505. https://doi.org/10.1038/s41575-020-0300-1.

238. Yang, C., Uertz, J., Yohan, D., & Chithrani, B.D. (2014). Peptide modified gold nanoparticles for improved cellular uptake, nuclear transport, and intracellular retention. Nanoscale, 6(20), 12026–12033. doi:10.1039/c4nr02535k

239. Yang, C., Uertz, J., & Chithrani, D.B. (2016). Colloidal gold-mediated delivery of bleomycin for improved outcome in chemotherapy. Nanomaterials, 6(2), 48.

240. Kim, J.A., Åberg, C., Salvati, A., & Dawson, K.A. (2011). Role of cell cycle on the cellular uptake and dilution of nanoparticles in a cell population. Nat. Nanotechnol., 7, 62–68. https://doi.org/10.1038/nnano.2011.191.

241. Maeda, H.; Fang, J.; Inutsuka, T.; Kitamoto, Y. "Vascular permeability enhancement in solid tumor: Various factors, mechanisms involved and its implications." Int. Immunopharmacol. 2003, 3, 319–328.

242. Goodrich, G. P., Bao, L., Gill-Sharp, K., Sang, K. L., Wang, J., & Payne, J. D. (2010). Photothermal therapy in a murine colon cancer model using near-infrared absorbing gold nanorods. Journal of Biomedical Optics, 15(1), 018001. https://doi.org/10.1117/1.3290817

243. Libutti, S. K., Paciotti, G. F., Byrnes, A. A., Alexander, H. R., Gannon, W. E., Walker, M., Seidel, G. D., Yuldasheva, N., & Tamarkin, L. (2010). Phase I and pharmacokinetic studies of CYT-6091, a novel PEGylated colloidal gold-rhTNF nanomedicine. Clinical Cancer Research: An Official Journal of the American Association for Cancer Research, 16(24), 6139–6149. https://doi.org/10.1158/1078-0432.CCR-10-0978

244. Puvanakrishnan, P., Park, J., Chatterjee, D., Krishnan, S., & Tunnell, J.W. (2012). *In vivo* tumor targeting of gold nanoparticles: Effect of particle type and dosing strategy. Int. J. Nanomed., 7, 1251–1258.

245. Mirjolet, C., Boudon, J., Loiseau, A., Chevrier, S., Boidot, R., Oudot, A., ... & Créhange, G. (2017). Docetaxel-Titanate Nanotubes Enhance Radiosensitivity in an Androgen-Independent Prostate Cancer Model. Int J Nanomedicine, 12, 6357–6364. https://doi.org/10.2147/IJN.S139167.

246. Vale, R. D., & Milligan, R. A. (2000). The way things move: Looking under the hood of molecular motor proteins. Science, 288(5463), 88–95.

247. Barlan, K., & Gelfand, V. I. (2017). Microtubule-based transport and the distribution, tethering, and organization of organelles. Cold Spring Harbor perspectives in biology, 9(3).

248. Shen, Y., Ma, Z., Chen, F., Dong, Q., Hu, Q., Bai, L., & Chen, J. (2015). Effective photothermal chemotherapy with docetaxel-loaded gold nanospheres in advanced prostate cancer. J Drug Target, 23(7), 568-576.

249. Ghalandari, B., Asadollahi, K., Shakerizadeh, A., Komeili, A., Riazi, G., Kamrava, S. K., & Attaran, N. (2019). Microtubule network as a potential candidate for targeting by gold nanoparticle-assisted photothermal therapy. Journal of photochemistry and photobiology B, Biology, 192, 131-140.

250. Gascoigne, K. E., & Taylor, S. S. (2009). How do anti-mitotic drugs kill cancer cells? Journal of cell science, 122(16), 2579-2585.

251. Kim, J., Kim, J., & Rhee, K. (2019). PCNT is critical for the association and conversion of centrioles to centrosomes during mitosis. Journal of Cell Science, 132(6), jcs225789. https://doi.org/10.1242/jcs.225789

252. Loubéry, S., Wilhelm, C., Hurbain, I., Neveu, S., Louvard, D., & Coudrier, E. (2008). Different Microtubule Motors Move Early and Late Endocytic Compartments. Traffic, 9(4), 492–509. https://doi.org/10.1111/j.1600-0854.2008.00704.x

253. Brunsvig, P. F. R., Andersen, A., Aamdal, S., Kristensen, V., & Olsen, H. (2007). Pharmacokinetic analysis of two different docetaxel dose levels in patients with non-small cell lung cancer treated with docetaxel as monotherapy or with concurrent radiotherapy. BMC cancer, 7(1), 197.

254. DiPersio, C. M., & Van De Water, L. (2019). Integrin Regulation of CAF Differentiation and Function. Cancers, 11(5), 715. https://doi.org/10.3390/cancers11050715

255. Desgrosellier, J.S., & Cheresh, D.A. (2010). Integrins in Cancer: Biological Implications and Therapeutic Opportunities. Nature Reviews Cancer, 10, 9–22.

256. Wen, S., et al. (2019). Cancer-Associated Fibroblast (CAF)-Derived IL32 Promotes Breast Cancer Cell Invasion and Metastasis via Integrin B3–P38 MAPK Signalling. Cancer Letters, 442, 320–32. doi:10.1016/j.canlet.2018.10.015

257. Ruddon, R. W. (2007). Cancer biology (4th ed.). New York; Oxford: Oxford University Press.

258. Turkevich, J., Stevenson, P. C., & Hillier, J. (1951). A study of the nucleation and growth processes in the synthesis of colloidal gold. Discussions of the Faraday Society, 11, 55–75.

259. Rahman, A., Rahman, A., Ghann, W., Kang, H-G., & Uddin, J. (2018). Terahertz multispectral imaging for the analysis of gold nanoparticles' size and the number of unit cells in comparison with other techniques. International Journal of Biosensors & Bioelectronics, 4. https://doi.org/10.15406/ijbsbe.2018.04.00118

260. Alhussan, A., Palmerley, N., Smazynski, J., Karasinska, J., Renouf, D. J., Schaeffer, D. F., Beckham, W., Alexander, A. S., & Chithrani, D. B. (2022). Potential of Gold Nanoparticles in Current Radiotherapy Using a Co-Culture Model of Cancer Cells and Cancer Associated Fibroblasts. Cancers, 14(15), Article 15. https://doi.org/10.3390/cancers14153586

261. Alhussan, A., Jackson, N., Calisin, R., Morgan, J., Beckham, W., & Chithrani, D. B. (2023). Utilizing Gold Nanoparticles as Prospective Radiosensitizers in 3D Radioresistant Pancreatic Co-Culture Model. International Journal of Molecular Sciences, 24(15), 12523. https://doi.org/10.3390/ijms241512523

262. Wu, M., Guo, H., Liu, L., Liu, Y., & Xie, L. (2019). Size-dependent cellular uptake and localization profiles of silver nanoparticles. International Journal of Nanomedicine, 14, 4247–4259.

263. Noireaux, J., Grall, R., Hullo, M., Chevillard, S., Oster, C., Brun, E., Sicard-Roselli, C., Loeschner, K., & Fisicaro, P. (2019). Gold Nanoparticle Uptake in Tumor Cells: Quantification and Size Distribution by sp-ICPMS. Separations, 6(3).

264. Kini, S., Bahadur, D., & Panda, D. (2015). Mechanism of Anti-Cancer Activity of Benomyl Loaded Nanoparticles in Multidrug Resistant Cancer Cells. Journal of Biomedical Nanotechnology, 11, 877–889.

265. Wang, B., Matsuoka, S., Carpenter, P. B., & Elledge, S. J. (2002). 53BP1, a Mediator of the DNA Damage Checkpoint. Science, 298, 1435–1438.

266. Kuo, L. J., & Yang, L.-X. (2008). Gamma-H2AX—A novel biomarker for DNA double-strand breaks. *In vivo*, 22, 305–309.

267. Banáth, J. P., Klokov, D., MacPhail, S. H., Banuelos, C. A., & Olive, P. L. (2010). Residual gammaH2AX foci as an indication of lethal DNA lesions. BMC Cancer, 10, 4.

268. Popp, H. D., Brendel, S., Hofmann, W.-K., & Fabarius, A. (2017). Immunofluorescence Microscopy of γH2AX and 53BP1 for Analyzing the Formation and Repair of DNA Double-strand Breaks. Journal of Visualized Experiments, 129, e56617.

269. Han, O., Bromma, K., Palmerley, N., Bido, A. T., Monica, M., Alhussan, A., Howard, P. L., Brolo, A. G., Beckham, W., Alexander, A. S., & Chithrani, D. B. (2022). Nanotechnology Driven Cancer Chemoradiation: Exploiting the Full Potential of Radiotherapy with a Unique Combination of Gold Nanoparticles and Bleomycin. Pharmaceutics, 14(2), 233. https://doi.org/10.3390/pharmaceutics14020233

270. Yang, N., Lode, K., Berzaghi, R., Islam, A., Martinez-Zubiaurre, I., & Hellevik, T. (2020). Irradiated Tumor Fibroblasts Avoid Immune Recognition and Retain Immunosuppressive Functions Over Natural Killer Cells. Frontiers in Immunology, 11, 602530.

271. Nagelkerke, A., Bussink, J., van der Kogel, A. J., Sweep, F. C. G. J., & Span, P. N. (2013). The PERK/ATF4/LAMP3-arm of the unfolded protein response affects radioresistance by interfering with the DNA damage response. Radiotherapy and Oncology, 108, 415–421.

272. Ansems, M., & Span, P. N. (2020). The tumor microenvironment and radiotherapy response; a central role for cancer-associated fibroblasts. Clinical and Translational Radiation Oncology, 22, 90–97.

273. Domogauer, J. D., de Toledo, S. M., Howell, R. W., & Azzam, E. I. (2021). Acquired radioresistance in cancer associated fibroblasts is concomitant with enhanced antioxidant potential and DNA repair capacity. Cell Communication and Signaling, 19, 30.

274. Maia, A., & Wiemann, S. (2021). Cancer-Associated Fibroblasts: Implications for Cancer Therapy. Cancers, 13, 3526.

275. Wang, Z., Tang, Y., Tan, Y., Wei, Q., & Yu, W. (2019). Cancer-associated fibroblasts in radiotherapy: Challenges and new opportunities. Cell Communication and Signaling, 17, 47.

276. Dai, P. L., Du, X., Hou, Y., Li, L., Xia, Y., Wang, L., Chen, H., Chang, L., & Li, W. (2020). Different Proteins Regulated Apoptosis, Proliferation and Metastasis of Lung Adenocarcinoma After Radiotherapy at Different Time. Cancer Management and Research, 12, 2437–2447.

277. Otani, K., Naito, Y., Sakaguchi, Y., Seo, Y., Takahashi, Y., Kikuta, J., Ogawa, K., & Ishii, M. (2016). Cell-cycle-controlled radiation therapy was effective for treating a murine malignant melanoma cell line *in vitro* and *in vivo*. Scientific Reports, 6, 30689.

278. Özgür, E., Kayhan, H., Kismali, G., Senturk, F., Sensoz, M., Ozturk, G. G., & Sel, T. (2021). Effects of radiofrequency radiation on colorectal cancer cell proliferation and inflammation. Turkish Journal of Biochemistry, 46, 525–532.

279. Arafat, W., Zhou, T., Naoum, G. E., & Buchsbaum, D. J. (2015). Targeted radiotherapy potentiates the cytotoxicity of a novel anti-human DR5 monoclonal antibody and the adenovirus encoding soluble TRAIL in prostate cancer. Journal of the Egyptian National Cancer Institute, 27, 205–215.

280. Boncler, M., Rózalski, M., Krajewska, U., Podsędek, A., & Watala, C. (2014). Comparison of PrestoBlue and MTT assays of cellular viability in the assessment of anti-proliferative effects of plant extracts on human endothelial cells. Journal of Pharmacological and Toxicological Methods, 69, 9–16.

281. Räsänen, K., & Herlyn, M. (2012). Paracrine signaling between carcinoma cells and mesenchymal stem cells generates cancer stem cell niche via epithelial-mesenchymal transition. Cancer Discovery, 2, 775–777.

282. Ren, Y., Jia, H.-H., Xu, Y.-Q., Zhou, X., Zhao, X.-H., Wang, Y., Song, X., Zhu, Z.-Y., Sun, T., Dou, Y., et al. (2018). Paracrine and epigenetic control of CAF-induced metastasis: The role of HOTAIR stimulated by TGF-ß1 secretion. Molecular Cancer, 17, 5.

283. Yang, F., Guo, Z., He, C., Qing, L., Wang, H., Wu, J., & Lu, X. (2021). Cancer-associated fibroblasts promote cell proliferation and invasion via paracrine Wnt/IL1β signaling pathway in human bladder cancer. Neoplasma, 68, 79–86.

284. Wu, F., Yang, J., Liu, J., Wang, Y., Mu, J., Zeng, Q., Deng, S., & Zhou, H. (2021). Signaling pathways in cancer-associated fibroblasts and targeted therapy for cancer. Signal Transduction and Targeted Therapy, 6, 218.

285. Wessolly, M., Mairinger, E., Borchert, S., Bankfalvi, A., Mach, P., Schmid, K. W., Kimmig, R., Buderath, P., & Mairinger, F. D. (2022). CAF-Associated Paracrine Signaling Worsens Outcome and Potentially Contributes to Chemoresistance in Epithelial Ovarian Cancer. Frontiers in Oncology, 12, 798680.

286. Kapałczyńska, M., Kolenda, T., Przybyła, W., Zajączkowska, M., Teresiak, A., Filas, V., ... & Lamperska, K. (2018). 2D and 3D Cell Cultures – a Comparison of Different Types of Cancer Cell Cultures. Arch Med Sci, 14(4), 910–919. https://doi.org/10.5114/aoms.2016.63743

287. Jensen, C., & Teng, Y. (2020). Is It Time to Start Transitioning From 2D to 3D Cell Culture? Front. Mol. Biosci., 7. https://doi.org/10.3389/fmolb.2020.00033

288. Melissaridou, S., Wiechec, E., Magan, M., Jain, M. V., Chung, M. K., Farnebo, L., & Roberg, K. (2019). The Effect of 2D and 3D Cell Cultures on Treatment Response, EMT Profile and Stem Cell Features in Head and Neck Cancer. Cancer Cell International, 19(1), 16. https://doi.org/10.1186/s12935-019-0733-1

289. Joseph, J. S., Malindisa, S. T., & Ntwasa, M. (2018). Two-Dimensional (2D) and Three-Dimensional (3D) Cell Culturing in Drug Discovery. IntechOpen. https://doi.org/10.5772/intechopen.81552

290. Zanoni, M., Piccinini, F., Arienti, C., Zamagni, A., Santi, S., Polico, R., Bevilacqua, A., & Tesei, A. (2016). 3D tumor spheroid models for in vitro therapeutic screening: A systematic approach to enhance the biological relevance of data obtained. Scientific Reports, 6, 19103. https://doi.org/10.1038/srep19103

291. Singh, S. K., Abbas, S., Saxena, A. K., Tiwari, S., Sharma, L. K., & Tiwari, M. (2020). Critical role of three-dimensional tumorsphere size on experimental outcome. BioTechniques, 69, 333–338.

292. Liu, T., Han, C., Wang, S., Fang, P., Ma, Z., Xu, L., & Huang, Q. (2018). Cancer-associated fibroblasts: An emerging target of anti-cancer immunotherapy. Journal of Hematology & Oncology, 11, 86.

293. Vaish, U., Jain, T., Are, A. C., & Dudeja, V. (2021). Cancer-Associated Fibroblasts in Pancreatic Ductal Adenocarcinoma: An Update on Heterogeneity and Therapeutic Targeting. International Journal of Molecular Sciences, 22(24), 13408. https://doi.org/10.3390/ijms222413408

294. Tao, L., Huang, G., Song, H., Chen, Y., & Chen, L. (2017). Cancer associated fibroblasts: An essential role in the tumor microenvironment. Oncology Letters, 14(3), 2611–2620. https://doi.org/10.3892/ol.2017.6497

295. Mikhail, A.S., Eetezadi, S., & Allen, C. (2013). Multicellular Tumor Spheroids for Evaluation of Cytotoxicity and Tumor Growth Inhibitory Effects of Nanomedicines *In vitro*: A Comparison of Docetaxel-Loaded Block Copolymer Micelles and Taxotere®. PLoS ONE, 8(6), e62630.

296. Hirschhaeuser, F., & et al. (2010). Multicellular tumor spheroids: An underestimated tool is catching up again. Journal of Biotechnology, 148, 3–15.

297. Albanese, A., Tang, P. S., & Chan WC, W. (2012). The effect of nanoparticle size, shape, and surface chemistry on biological systems. Annual Review of Biomedical Engineering, 14, 1–16.

298. Rosa, S., Connolly, C., Schettino, G., Butterworth, K. T., & Prise, K. M. (2017). Biological mechanisms of gold nanoparticle radiosensitization. Cancer Nanotechnology, 8(1), 2. https://doi.org/10.1186/s12645-017-0026-0

299. Niidome, T., Yamagata, M., Okamoto, Y., Akiyama, Y., Takahashi, H., Kawano, T., Katayama, Y., & Niidome, Y. (2006). PEG-modified gold nanorods with a stealth character for in vivo applications. Journal of Controlled Release: Official Journal of the Controlled Release Society, 114(3), 343–347. https://doi.org/10.1016/j.jconrel.2006.06.017

300. Yao, Y., Zhou, Y., Liu, L., Xu, Y., Chen, Q., Wang, Y., Wu, S., Deng, Y., Zhang, J., & Shao, A. (2020). Nanoparticle-Based Drug Delivery in Cancer Therapy and Its Role in Overcoming Drug Resistance. Frontiers in Molecular Biosciences, 7, 193. https://doi.org/10.3389/fmolb.2020.00193

301. Fröhlich, E. (2018). Comparison of conventional and advanced in vitro models in the toxicity testing of nanoparticles. Artificial Cells, Nanomedicine, and Biotechnology, 46(Suppl 2), 1091–1107. https://doi.org/10.1080/21691401.2018.1479709

302. Guo, J., Wang, S., & Gao, Q. (2023). An integrated overview of the immunosuppression features in the tumor microenvironment of pancreatic cancer. Frontiers in Immunology, 14. https://www.frontiersin.org/articles/10.3389/fimmu.2023.1258538

303. Moore, K. M., Desai, A., Delgado, B. de L., Trabulo, S. M. D., Reader, C., Brown, N. F., Murray, E. R., Brentnall, A., Howard, P., Masterson, L., Zammarchi, F., Hartley, J. A., van Berkel, P. H., & Marshall, J. F. (2020). Integrin αvβ6-specific therapy for pancreatic cancer developed from foot-and-mouth-disease virus. Theranostics, 10(7), 2930–2942. https://doi.org/10.7150/thno.38702

304. Bergonzini, C., Kroese, K., Zweemer, A. J. M., & Danen, E. H. J. (2022). Targeting Integrins for Cancer Therapy—Disappointments and Opportunities. Frontiers in Cell and Developmental Biology, 10. https://www.frontiersin.org/articles/10.3389/fcell.2022.863850

305. Li, Z., Sun, C., & Qin, Z. (2021). Metabolic reprogramming of cancer-associated fibroblasts and its effect on cancer cell reprogramming. Theranostics, 11(17), 8322–8336. https://doi.org/10.7150/thno.62378

306. Suh, J., Kim, D.-H., Lee, Y.-H., Jang, J.-H., & Surh, Y.-J. (2020). Fibroblast growth factor-2, derived from cancer-associated fibroblasts, stimulates growth and progression of human breast cancer cells via FGFR1 signaling. Molecular Carcinogenesis, 59(9), 1028–1040. https://doi.org/10.1002/mc.23233

307. Qiao, Y., Chen, H., Lin, Y., & Huang, J. (2011). Controllable Synthesis of Water-Soluble Gold Nanoparticles and Their Applications in Electrocatalysis and Surface-Enhanced Raman Scattering. Langmuir, 27(17), 11090–11097. https://doi.org/10.1021/la2019154

308. Shen, C.-C., Hsu, S., Chang, K.-B., Yeh, C.-A., Chang, H.-C., Tang, C.-M., Yang, Y.-C., Hsieh, H.-H., & Hung, H.-S. (2021). Physical Gold Nanoparticle-Decorated Polyethylene Glycol-Hydroxyapatite Composites Guide Osteogenesis and Angiogenesis of Mesenchymal Stem Cells. Biomedicines, 9(11), 1632. https://doi.org/10.3390/biomedicines9111632

309. Liao, L., Liu, J., Dreaden, E. C., Morton, S. W., Shopsowitz, K. E., Hammond, P. T., & Johnson, J. A. (2014). A convergent synthetic platform for single-nanoparticle combination cancer therapy: Ratiometric loading and controlled release of cisplatin, doxorubicin, and camptothecin. Journal of the American Chemical Society, 136(16), 5896–5899. https://doi.org/10.1021/ja502011g

310. Tiwari, H., Rai, N., Singh, S., Gupta, P., Verma, A., Singh, A. K., Kajal, Salvi, P., Singh, S. K., & Gautam, V. (2023). Recent Advances in Nanomaterials-Based Targeted Drug Delivery for Preclinical Cancer Diagnosis and Therapeutics. Bioengineering, 10(7), Article 7. https://doi.org/10.3390/bioengineering10070760

311. Liang, G., Jin, X., Zhang, S., & Xing, D. (2017). RGD peptide-modified fluorescent gold nanoclusters as highly efficient tumor-targeted radiotherapy sensitizers. Biomaterials, 144, 95–104. https://doi.org/10.1016/j.biomaterials.2017.08.017

312. Alhussan, A., Jackson, N., Eaton, S., Santos, N. D., Barta, I., Zaifman, J., Chen, S., Tam, Y. Y. C., Krishnan, S., & Chithrani, D. B. (2022). Lipid-Nanoparticle-Mediated Delivery of Docetaxel Prodrug for Exploiting Full Potential of Gold Nanoparticles in the Treatment of Pancreatic Cancer. Cancers, 14(24), 6137. https://doi.org/10.3390/cancers14246137

313. Alhussan, A., Calisin, R., Jackson, N., Morgan, J., Chen, S., Tam, Y. Y. C., Beckham, W., Krishnan, S., & Chithrani, D. (2023). A Synergetic Approach Utilizing Nanotechnology, Chemotherapy, and Radiotherapy for Pancreatic Cancer Treatment. Precision Nanomedicine, November, 1157–1172. https://doi.org/10.33218/001c.90447

314. Meel, R.; Chen, S.; Zaifman, J.; Kulkarni, J.A.; Zhang, X.R.S.; Tam, Y.K.; Bally, M.B.; Schiffelers, R.M.; Ciufolini, M.A.; Cullis, P.R., et al. (2021). Modular Lipid Nanoparticle Platform Technology for siRNA and Lipophilic Prodrug Delivery. Small, 17, 2103025.

315. Cho, S.; Yoon, Y.-R. (2018). Understanding the pharmacokinetics of prodrug and metabolite. Transl. Clin. Pharmacol., 26(1), 1–5.

316. Van Der Meel, R.; Sulheim, E.; Shi, Y.; Kiessling, F.; Mulder, W.J.M.; Lammers, T. (2019). Smart cancer nanomedicine. Nat. Nanotechnol., 14, 1007–1017.

317. Markovic, M.; Ben-Shabat, S.; Dahan, A. (2020). Prodrugs for Improved Drug Delivery: Lessons Learned from Recently Developed and Marketed Products. Pharmaceutics, 12, 1031.

318. Jing, F.; Guo, Q.; Xu, W.; Qu, H.; Sui, Z. (2018). Docetaxel prodrug self-assembled nanosystem: Synthesis, formulation and cytotoxicity. Bioorganic Med. Chem. Lett., 28, 826–830.

319. Li, Y.; Chen, X.; Ji, J.; Li, L.; Zhai, G. (2021). Redox-responsive nanoparticles based on Chondroitin Sulfate and Docetaxel prodrug for tumor targeted delivery of Docetaxel. Carbohydr. Polym., 255, 117393.

320. Kulkarni, J.A.; Witzigmann, D.; Thomson, S.B.; Chen, S.; Leavitt, B.R.; Cullis, P.R.; van der Meel, R. (2021). The current landscape of nucleic acid therapeutics. Nat. Nanotechnol., 16, 630–643.

321. Barenholz, Y. (2012). Doxil®—The first FDA-approved nano-drug: Lessons learned. J. Control. Release Off. J. Control Release Soc., 160, 117–134.

322. Alfayez, M., Kantarjian, H., Kadia, T., Ravandi-Kashani, F., & Daver, N. (2020). CPX-351 (vyxeos) in AML. Leukemia & Lymphoma, 61(2), 288–297. https://doi.org/10.1080/10428194.2019.1660970

323. Xu, S., Olenyuk, B.Z., Okamoto, C.T., & Hamm-Alvarez, S.F. (2012). Targeting receptor-mediated endocytotic pathways with nanoparticles: Rationale and advances. Advances in Drug Delivery Reviews, 65, 121–138.

324. Oh, N., & Park, J.-H. (2014). Endocytosis and exocytosis of nanoparticles in mammalian cells. International Journal of Nanomedicine, 9(Suppl. S1), 51–63.

325. Bromma, K., Dos Santos, N., Barta, I., Alexander, A., Beckham, W., Krishnan, S., & Chithrani, D. B. (2022). Enhancing nanoparticle accumulation in two dimensional, three dimensional, and xenograft mouse cancer cell models in the presence of docetaxel. Sci. Rep., 12, 13508.

326. Booij, T. H., Price, L. S., & Danen, E. H. J. (2019). 3D Cell-Based Assays for Drug Screens: Challenges in Imaging, Image Analysis, and High-Content Analysis. Slas Discovery, 24(6), 615–627. https://doi.org/10.1177/2472555219830087

327. Xiang, S., Sarem, M., Shah, S., & Shastri, V. P. (2018). Liposomal Treatment of Cancer Cells Modulates Uptake Pathway of Polymeric Nanoparticles by Altering Membrane Stiffness. Small (Weinheim an Der Bergstrasse, Germany), 14(14), e1704245. https://doi.org/10.1002/smll.201704245

328. Feng, X., Xiong, X., & Ma, S. (2022). Docetaxel-Loaded Novel Nano-Platform for Synergistic Therapy of Non-Small Cell Lung Cancer. Frontiers in Pharmacology, 13, 832725. https://doi.org/10.3389/fphar.2022.832725

329. Yang, L., Gong, L., Wang, P., Zhao, X., Zhao, F., Zhang, Z., Li, Y., & Huang, W. (2022). Recent Advances in Lipid Nanoparticles for Delivery of mRNA. Pharmaceutics, 14(12), 2682. https://doi.org/10.3390/pharmaceutics14122682

330. Khlebtsov, N., & Dykman, L. (2011). Biodistribution and toxicity of engineered gold nanoparticles: A review of in vitro and in vivo studies. Chemical Society Reviews, 40(3), 1647–1671. https://doi.org/10.1039/c0cs00018c

331. Jain, S., Hirst, D. G., & O'Sullivan, J. M. (2012). Gold nanoparticles as novel agents for cancer therapy. The British Journal of Radiology, 85(1010), 101–113. https://doi.org/10.1259/bjr/59448833

332. Steinberg, G., & Fuchs, U. (2004). The role of microtubules in cellular organization and endocytosis in the plant pathogen Ustilago maydis. Journal of Microscopy, 214(Pt 2), 114–123. https://doi.org/10.1111/j.0022-2720.2004.01319.x

333. Hu, J., Chen, L., Lu, Z., Yao, H., Hu, Y., Feng, L., Pang, Y., Wu, J.-Q., Yu, Z., & Chen, W.-H. (2023). Design, Synthesis and Antitumor Activity of Novel Selenium-Containing Tepotinib Derivatives as Dual Inhibitors of c-Met and TrxR. Molecules (Basel, Switzerland), 28(3), 1304. https://doi.org/10.3390/molecules28031304

334. Krueger, S. A., Wilson, G. D., Piasentin, E., Joiner, M. C., & Marples, B. (2010). THE EFFECTS OF G2-PHASE ENRICHMENT AND CHECKPOINT ABROGATION ON LOW-DOSE HYPER-RADIOSENSITIVITY. International Journal of Radiation Oncology, Biology, Physics, 77(5), 10.1016/j.ijrobp.2010.01.028. https://doi.org/10.1016/j.ijrobp.2010.01.028

335. Guo, M., Sun, Y., & Zhang, X.-D. (2017). Enhanced Radiation Therapy of Gold Nanoparticles in Liver Cancer. Applied Sciences, 7(3), Article 3. https://doi.org/10.3390/app7030232

336. Tan, J., Cho, T. J., Tsai, D.-H., Liu, J., Pettibone, J. M., You, R., Hackley, V. A., & Zachariah, M. R. (2018). Surface Modification of Cisplatin-complexed Gold Nanoparticles and its Influence on Colloidal Stability, Drug Loading and Release. Langmuir : The ACS Journal of Surfaces and Colloids, 34(1), 154–163. https://doi.org/10.1021/acs.langmuir.7b02354

337. Wu, R., Zhang, Z., Wang, B., Chen, G., Zhang, Y., Deng, H., Tang, Z., Mao, J., & Wang, L. (2020). Combination Chemotherapy of Lung Cancer – Co-Delivery of Docetaxel Prodrug and Cisplatin Using Aptamer-Decorated Lipid–Polymer Hybrid Nanoparticles. Drug Design, Development and Therapy, 14, 2249. https://doi.org/10.2147/DDDT.S246574

338. Zhu, S., Oremo, J. A., Li, S., Zhen, M., Tang, Y., & Du, Y. (2014). Synergistic Antitumor Activities of Docetaxel and Octreotide Associated with Apoptotic-Upregulation in Castration-Resistant Prostate Cancer. PLOS ONE, 9(3), e91817. https://doi.org/10.1371/journal.pone.0091817

339. Xu, M., McCanna, D. J., & Sivak, J. G. (2015). Use of the viability reagent PrestoBlue in comparison with alamarBlue and MTT to assess the viability of human corneal epithelial cells. Journal of Pharmacological and Toxicological Methods, 71, 1–7. https://doi.org/10.1016/j.vascn.2014.11.003

340. Ma, H., Yuelin, W., Zhang, W., Zhang, H., Miao, Z., & Zhuang, C. (2021). Radiosensitization of human pancreatic cancer by piperlongumine analogues. Chinese Chemical Letters, 32, 1197-1201.

341. Jamieson, E. R., & Lippard, S. J. (1999). Structure, recognition, and processing of cisplatin-DNA adducts. Chemical Reviews, 99, 2467–2498.

342. Lippard, S. J. (1982). New chemistry of an old molecule: Cis-[Pt(NH3)2Cl2]. Science, 218, 1075–1082.

343. Rosenberg, B., VanCamp, L., Trosko, J. E., & Mansour, V. H. (1969). Platinum compounds: A new class of potent antitumour agents. Nature, 222, 385–386.

344. Rosenberg, B., & VanCamp, L. (1970). The successful regression of large solid sarcoma 180 tumors by platinum compounds. Cancer Research, 30, 1799–1802.

345. Kociba, R. J., Sleight, S. D., & Rosenberg, B. (1970). Inhibition of dunning ascitic leukemia and walker 256 carcinosarcoma with cis-diamminedichloroplatinum (NSC-119875). Cancer Chemotherapy Reports, 54, 325–328.

346. Keys, H. M., Bundy, B. N., Stehman, F. B., Muderspach, L. I., Chafe, W. E., Suggs, C. L., 3rd, Walker, J. L., & Gersell, D. (1999). Cisplatin, radiation, and adjuvant hysterectomy compared with radiation and adjuvant hysterectomy for bulky stage ib cervical carcinoma. The New England Journal of Medicine, 340, 1154–1161.

347. Loehrer, P. J., & Einhorn, L. H. (1984). Drugs five years later. Cisplatin. Annals of Internal Medicine, 100, 704–713.

348. Morris, M., Eifel, P. J., Lu, J., Grigsby, P. W., Levenback, C., Stevens, R. E., Rotman, M., Gershenson, D. M., & Mutch, D. G. (1999). Pelvic radiation with concurrent chemotherapy compared with pelvic and para-aortic radiation for high-risk cervical cancer. The New England Journal of Medicine, 340, 1137–1143.

349. Rose, P. G., Bundy, B. N., Watkins, E. B., Thigpen, J. T., Deppe, G., Maiman, M. A., Clarke-Pearson, D. L., & Insalaco, S. (1999). Concurrent cisplatin-based radiotherapy and chemotherapy for locally advanced cervical cancer. The New England Journal of Medicine, 340, 1144–1153.

350. Bosl, G. J., & Motzer, R. J. (1997). Testicular germ-cell cancer. The New England Journal of Medicine, 337, 242–253

351. Andrews, P. A., Velury, S., Mann, S. C., & Howell, S. B. (1988). Cis-diamminedichloroplatinum(II) accumulation in sensitive and resistant human ovarian carcinoma cells. Cancer Research, 48, 68–73.

352. Eljack, N. D., Ma, H.-Y. M., Drucker, J., Shen, C., Hambley, T. W., New, E. J., Friedrich, T., & Clarke, R. J. (2014). Mechanisms of cell uptake and toxicity of the anticancer drug cisplatin. Metallomics, 6, 2126–2133.

353. Cohen, G. L., Bauer, W. R., Barton, J. K., & Lippard, S. J. (1979). Binding of cis-and trans-dichlorodiammineplatinum(II) to DNA: Evidence for unwinding and shortening of the double helix. Science, 203, 1014–1016.

354. Macquet, J.-P., & Butour, J.-L. (1978). Modifications of the DNA secondary structure upon platinum binding: A proposed model. Biochimie, 60, 901–914.

355. Siu, L. L. M., & Malcolm, J. (2005). Pharmacology of anticancer drugs. In I. Tannock, R. Hill, R. Bristow, & L. Harrington (Eds.), The Basic Science Oncology (pp. 322–348). McGraw-Hill: Toronto, ON, Canada.

356. Sorenson, C. M., & Eastman, A. (1988). Influence of cis-diamminedichloroplatinum(II) on DNA synthesis and cell cycle progression in excision repair proficient and deficient Chinese hamster ovary cells. Cancer Research, 48, 6703–6707.

357. Sorenson, C. M., & Eastman, A. (1988). Mechanism of cis-diamminedichloroplatinum(II)-induced cytotoxicity: Role of G2 arrest and DNA double-strand breaks. Cancer Research, 48, 4484–4488.

358. Sorenson, C. M., Barry, M. A., & Eastman, A. (1990). Analysis of events associated with cell cycle arrest at G2 phase and cell death induced by cisplatin. Journal of the National Cancer Institute, 82, 749–755.

359. Cui, L., Tse, K., Zahedi, P., Harding, S. M., Zafarana, G., Jaffray, D. A., & Bristow, R. G. (2014). Hypoxia and cellular localization influence the radiosensitizing effect of gold nanoparticles (AuNPs) in breast cancer cells. Radiation Research, 182, 475–488.

360. Hanigan, M. H., & Devarajan, P. (2003). Cisplatin nephrotoxicity: Molecular mechanisms. Cancer Therapy, 1, 47–61.

361. Yang, C., Bromma, K., Sung, W., Schuemann, J., & Chithrani, D. (2018). Determining the radiation enhancement effects of gold nanoparticles in cells in a combined treatment with cisplatin and radiation at therapeutic megavoltage energies. Cancers, 10, 150.

362. Cui, L., Her, S., Dunne, M., & Borst, G. R. (2017). Significant radiation enhancement effects by gold nanoparticles in combination with cisplatin in triple negative breast cancer cells and tumor xenografts. Radiation Research, 187, 147–160.

363. Comenge, J., Sotelo, C., Romero, F., Gallego, O., Barnadas, A., Parada, T. G.-C., Domínguez, F., & Puntes, V. F. (2012). Detoxifying antitumoral drugs via nanoconjugation: The case of gold nanoparticles and cisplatin. PLoS ONE, 7, e47562.

364. Estrella, V., Chen, T., Lloyd, M., Wojtkowiak, J., Cornnell, H. H., Ibrahim-Hashim, A., Bailey, K., Balagurunathan, Y., Rothberg, J. M., Sloane, B. F., et al. (2013). Acidity generated by the tumor microenvironment drives local invasion. Cancer Research, 73, 1524–1535.

365. Georgelin, T., Bombard, S., Siaugue, J. M., & Cabuil, V. (2010). Nanoparticle-mediated delivery of bleomycin. Angewandte Chemie International Edition, 49, 8897–8901.

366. Emerich, D. F., & Thanos, C. G. (2007). Targeted nanoparticle-based drug delivery and diagnosis. Journal of Drug Targeting, 15, 163–183.

367. Groneberg, D. A., Giersig, M., Welte, T., & Pison, U. (2006). Nanoparticle-based diagnosis and therapy. Current Drug Targets, 7, 643–648.

368. Duncan, B., Kim, C., & Rotello, V. M. (2010). Gold nanoparticle platforms as drug and biomacromolecule delivery systems. Journal of Controlled Release, 148, 122–127.

369. Ferrari, M. (2005). Cancer nanotechnology: Opportunities and challenges. Nature Reviews Cancer, 5, 161–171.

370. Lavan, D. A., McGuire, T., & Langer, R. (2003). Small-scale systems for in vivo drug delivery. Nature Biotechnology, 21, 1184–1191.

371. Homayoni, H., Menon, J. U., & Nguyen, K. T. (2014). Chitosan-based nanoparticles for drug delivery. Review of Nanoscience and Nanotechnology, 3, 133–148.

372. Bindhani, B. K., Parida, U. K., Biswal, S. K., Panigrahi, A. K., & Nayak, P. L. (2013). Gold nanoparticles and their biomedical applications. Review of Nanoscience and Nanotechnology, 2, 247–260.

373. Ghosh, P., Han, G., De, M., Kim, C. K., & Rotello, V. M. (2008). Gold nanoparticles in delivery applications. Advanced Drug Delivery Reviews, 60, 1307–1315.

374. Paciotti, G. F., Zhao, J., Cao, S., Brodie, P. J., Tamarkin, L., Huhta, M., ... & Kingston, D. G. I. (2016). Synthesis and evaluation of paclitaxel-loaded gold nanoparticles for tumor-targeted drug delivery. Bioconjugate Chemistry, 27, 2646–2657.

375. Kumthekar, P., Ko, C. H., Paunesku, T., Dixit, K., Sonabend, A. M., Bloch, O., Tate, M., Schwartz, M., Zuckerman, L., Lezon, R., Lukas, R. V., Jovanovic, B., McCortney, K., Colman, H., Chen, S., Lai, B., Antipova, O., Deng, J., Li, L., … Stegh, A. H. (2021). A first-in-human phase 0 clinical study of RNA interference-based spherical nucleic acids in patients with recurrent glioblastoma. Science Translational Medicine, 13(584), eabb3945. https://doi.org/10.1126/scitranslmed.abb3945

376. Rastinehad, A. R., Anastos, H., Wajswol, E., Winoker, J. S., Sfakianos, J. P., Doppalapudi, S. K., Carrick, M. R., Knauer, C. J., Taouli, B., Lewis, S. C., Tewari, A. K., Schwartz, J. A., Canfield, S. E., George, A. K., West, J. L., & Halas, N. J. (2019). Gold nanoshell-localized photothermal ablation of prostate tumors in a clinical pilot device study. Proceedings of the National Academy of Sciences of the United States of America, 116(37), 18590–18596. https://doi.org/10.1073/pnas.1906929116

377. Connor, E. E., Mwamuka, J., Gole, A., Murphy, C. J., & Wyatt, M. D. (2005). Gold nanoparticles are taken up by human cells but do not cause acute cytotoxicity. Small, 1, 325–327.

378. Male, K. B., Lachance, B., Hrapovic, S., Sunahara, G., & Luong, J. H. T. (2008). Assessment of cytotoxicity of quantum dots and gold nanoparticles using cell-based impedance spectroscopy. Analytical Chemistry, 80, 5487–5493.

379. Faridounnia, M., Folkers, G. E., & Boelens, R. (2018). Function and Interactions of ERCC1-XPF in DNA Damage Response. Molecules, 23, 3205.

380. McHugh, P., Spanswick, V. J., & Hartley, J. A. (2001). Repair of DNA interstrand crosslinks: Molecular mechanisms and clinical relevance. Lancet Oncology, 2, 483-490.

381. Ahmad, A., Robinson, A. R., Duensing, A., van Drunen, E., Beverloo, H. B., Weisberg, D. B., ... & Niedernhofer, L. J. (2008). ERCC1-XPF endonuclease facilitates DNA double-strand break repair. Molecular and Cellular Biology, 28, 5082-5092.

382. McNeil, E. M., & Melton, D. W. (2012). DNA repair endonuclease ERCC1-XPF as a novel therapeutic target to overcome chemo-resistance in cancer therapy. Nucleic Acids Research, 40, 9990-10004.

383. Weilbeer, C., Jay, D., Donnelly, J. C., Gentile, F., Karimi-Busheri, F., Yang, X., ... & et al. (2022). Modulation of ERCC1-XPF Heterodimerization Inhibition via Structural Modification of Small Molecule Inhibitor Side-Chains. Frontiers in Oncology, 12, 819712.

384. Elmenoufy, A. H., Gentile, F., Jay, D., Karimi-Busheri, F., Yang, X., Soueidan, O. M., ... & et al. (2019). Targeting DNA Repair in Tumor Cells via Inhibition of ERCC1–XPF. Journal of Medicinal Chemistry, 62, 7684-7696.

385. Jordheim, L. P., Barakat, K. H., Heinrich-Balard, L., Matera, E.-L., Cros-Perrial, E., Bouledrak, K., ... & et al. (2013). Small molecule inhibitors of ERCC1-XPF protein-protein interaction synergize alkylating agents in cancer cells. Molecular Pharmacology, 84, 12-24.

386. Vignaux, P. A., Lane, T. R., Puhl, A. C., Hau, R. K., Wright, S. H., Cherrington, N. J., & Ekins, S. (2023). Transporter Inhibition Profile for the Antivirals Tilorone, Quinacrine and Pyronaridine. ACS Omega, 8(13), 12532–12537. https://doi.org/10.1021/acsomega.3c00724

387. Rahn, J. J., Rowley, B., Lowery, M. P., Della Coletta, L., Limanni, T., Nairn, R. S., & Adair, G. M. (2011). Effects of varying gene targeting parameters on processing of recombination intermediates by ERCC1–XPF. DNA Repair, 10, 188-198.

388. Kuraoka, I., Kobertz, W., Ariza, R., Biggerstaff, M., Essigmann, J., & Wood, R. (2000). Repair of an Interstrand DNA Cross-link Initiated by ERCC1-XPF Repair/Recombination Nuclease. Journal of Biological Chemistry, 275, 26632-26636.

389. Ghosalkar, J., Sonawane, V., Pisal, T., Achrekar, S., Pujari, R., Chugh, A., Shastry, P., & Joshi, K. (2022). Prostate Apoptosis Response-4 (Par-4): A Novel Target in Pyronaridine-Induced Apoptosis in Glioblastoma (GBM) Cells. Cancers, 14, 3198.

390. Zhong, Z.-H., Yi, Z.-Y., Zhao, Y.-D., Wang, J., Jiang, Z.-B., Xu, C., Xie, Y.-J., He, Q.-D., Tong, Z.-Y., Yao, X.-J., & et al. (2022). Pyronaridine induces apoptosis in non-small cell lung cancer cells by upregulating death receptor 5 expression and inhibiting epidermal growth factor receptor. Chemical Biology Drug Design, 99, 83–91.

391. Jackson, N., Alhussan, A., Bromma, K., Jay, D., Donnelly, J. C., West, F. G., Lavasanifar, A., Weinfeld, M., Beckham, W., & Chithrani, D. B. (2022). Repurposing Antimalarial Pyronaridine as a DNA Repair Inhibitor to Exploit the Full Potential of Gold-Nanoparticle-Mediated Radiation Response. *Pharmaceutics*, *14*(12), 2795. https://doi.org/10.3390/pharmaceutics14122795

392. Xue, Y., Li, X., Li, H., & Zhang, W. (2014). Quantifying thiol–gold interactions towards the efficient strength control. Nature Communications, 5, 4348.

393. Libutti, S. K. (2006, May - 2009, April). A Phase I Trial of TNF-Bound Colloidal Gold (CYT-6091) by Intravenous Administration in Subjects with Advanced Solid Organ Malignancies. Identifier: NCT00356980. https://www.clinicaltrials.gov/study/NCT00356980

394. Rosenberg, S. A. (2006, December - 2009, August). An Evaluation of the Tissue Distribution and the Selective Tumor Trafficking of TNF-Bound Colloidal Gold (CYT-6091) Following Intravenous Administration in Subjects with Primary and Metastatic Cancer Undergoing Surgical Resection. Identifier: NCT00436410. https://www.clinicaltrials.gov/study/ NCT00436410

395. Nanospectra Biosciences, Inc. (2008, April - 2014, August). Pilot Study of AuroLase(tm) Therapy in Refractory and/or Recurrent Tumors of the Head and Neck. Identifier: NCT00848042. https://www.clinicaltrials.gov/study/ NCT00848042

396. Nanospectra Biosciences, Inc. (2016, February - 2020, October). MRI/US Fusion Imaging and Biopsy in Combination With Nanoparticle Directed Focal Therapy for Ablation of Prostate Tissue. Identifier: NCT02680535. https://www.clinicaltrials.gov/study/ NCT02680535

397. Conte, M., & Cauda, V. (2022). Multimodal Therapies against Pancreatic Ductal Adenocarcinoma: A Review on Synergistic Approaches toward Ultimate Nanomedicine Treatments. Advanced Therapeutics, 5(11), 2200079. https://doi.org/10.1002/adtp.202200079

398. Lakshmanan, I., Marimuthu, S., Chaudhary, S., Seshacharyulu, P., Rachagani, S., Muniyan, S., Chirravuri-Venkata, R., Atri, P., Rauth, S., Nimmakayala, R. K., Siddiqui, J. A., Gautam, S. K., Shah, A., Natarajan, G.,

Parte, S., Bhyravbhatla, N., Mallya, K., Haridas, D., Talmon, G. A., … Batra, S. K. (2022). Muc16 depletion diminishes KRAS-induced tumorigenesis and metastasis by altering tumor microenvironment factors in pancreatic ductal adenocarcinoma. Oncogene, 41(48), 5147–5159. https://doi.org/10.1038/s41388-022-02493-6

399. Bhatia, R., Siddiqui, J. A., Ganguly, K., Thompson, C. M., Cannon, A., Aithal, A., Perumal, N., Maurya, S. K., Li, X., Cox, J. L., Gurumurthy, C. B., Rachagani, S., Jain, M., Nasser, M. W., Batra, S. K., & Kumar, S. (2023). Muc4 loss mitigates epidermal growth factor receptor activity essential for PDAC tumorigenesis. Oncogene, 42(10), 759–770. https://doi.org/10.1038/s41388-022-02587-1

400. Luan, Z., Morimoto, Y., Fushimi, A., Yamashita, N., Suo, W., Bhattacharya, A., Hagiwara, M., Jin, C., & Kufe, D. (2022). MUC1-C dictates neuroendocrine lineage specification in pancreatic ductal adenocarcinomas. Carcinogenesis, 43(1), 67–76. https://doi.org/10.1093/carcin/bgab097

401. Yamaguchi, K., Enjoji, M., & Tsuneyoshi, M. (1991). Pancreatoduodenal carcinoma: A clinicopathologic study of 304 patients and immunohistochemical observation for CEA and CA19-9. Journal of Surgical Oncology, 47(3), 148–154. https://doi.org/10.1002/jso.2930470303

402. Li, Y., Hong, Y. K., Wang, X., Pandit, H., Zheng, Q., Yu, Y., Shi, X., Chen, Y., Tan, M., Pulliam, Z., Bhutiani, N., Lin, A., Badach, J., Zhang, P., & Martin, R. C. (2022). Epigenetic modulation enhances immunotherapy for pancreatic ductal adenocarcinoma. Clinical & Translational Immunology, 11(12), e1430. https://doi.org/10.1002/cti2.1430

403. Klemke, L., Fehlau, C. F., Winkler, N., Toboll, F., Singh, S. K., Moll, U. M., & Schulz-Heddergott, R. (2021). The Gain-of-Function p53 R248W Mutant Promotes Migration by STAT3 Deregulation in Human Pancreatic Cancer Cells. Frontiers in Oncology, 11, 642603. https://doi.org/10.3389/fonc.2021.642603

404. Gjertsen, M. K., Buanes, T., Rosseland, A. R., Bakka, A., Gladhaug, I., Soreide, O., Eriksen, J. A., Moller, M., Baksaas, I., Lothe, R. A., ... & others. (2001). Intradermal ras peptide vaccination with granulocyte-macrophage colony-stimulating factor as adjuvant: Clinical and immunological responses in patients with pancreatic adenocarcinoma. International Journal of Cancer, 92(3), 441–450.

405. Hardacre, J. M., Mulcahy, M., Small, W., Talamonti, M., Obel, J., Krishnamurthi, S., Rocha-Lima, C. S., Safran, H., Lenz, H. J., & Chiorean, E. G. (2013). Addition of algenpantucel-L immunotherapy to standard adjuvant therapy for pancreatic cancer: A phase 2 study. Journal of Gastrointestinal Surgery, 17(1), 94–100, discussion p. 100-101.

406. Yan, J., Pankhong, P., Shin, T. H., Obeng-Adjei, N., Morrow, M. P., Walters, J. N., Khan, A. S., Sardesai, N. Y., & Weiner, D. B. (2013). Highly optimized DNA vaccine targeting human telomerase reverse transcriptase stimulates potent antitumor immunity. Cancer Immunology Research, 1(3), 179–189.

407. Park, A. K., Fong, Y., Kim, S.-I., Yang, J., Murad, J. P., Lu, J., Jeang, B., Chang, W.-C., Chen, N. G., Thomas, S. H., Forman, S. J., & Priceman, S. J. (2020). Effective combination immunotherapy using oncolytic viruses to deliver CAR targets to solid tumors. Science Translational Medicine, 12(559), eaaz1863. https://doi.org/10.1126/scitranslmed.aaz1863

408. Li, B., Chan, H. L., & Chen, P. (2019). Immune Checkpoint Inhibitors: Basics and Challenges. Current Medicinal Chemistry, 26(17), 3009–3025. https://doi.org/10.2174/0929867324666170804143706

409. Kroemer, G., Galluzzi, L., Kepp, O., & Zitvogel, L. (2013). Immunogenic cell death in cancer therapy. Annual Review of Immunology, 31, 51–72. https://doi.org/10.1146/annurev-immunol-032712-100008

410. Kroemer, G., Galassi, C., Zitvogel, L., & Galluzzi, L. (2022). Immunogenic cell stress and death. Nature Immunology, 23(4), 487–500. https://doi.org/10.1038/s41590-022-01132-2

411. Ahmed, A., & Tait, S. W. G. (2020). Targeting immunogenic cell death in cancer. Molecular Oncology, 14(12), 2994–3006. https://doi.org/10.1002/1878-0261.12851

412. Chen, K. T. J., Anantha, M., Leung, A. W. Y., Kulkarni, J. A., Militao, G. G. C., Wehbe, M., Sutherland, B., Cullis, P. R., & Bally, M. B. (2020). Characterization of a liposomal copper(II)-quercetin formulation suitable for parenteral use. Drug Delivery and Translational Research, 10(1), 202–215. https://doi.org/10.1007/s13346-019-00674-7

413. Zaheer, J., Kim, H., Lee, Y.-J., Kim, J. S., & Lim, S. M. (2019). Combination Radioimmunotherapy Strategies for Solid Tumors. International Journal of Molecular Sciences, 20(22), Article 22. https://doi.org/10.3390/ijms20225579

414. Aghanejad, A., Bonab, S. F., Sepehri, M., Haghighi, F. S., Tarighatnia, A., Kreiter, C., Nader, N. D., & Tohidkia, M. R. (2022). A review on targeting tumor microenvironment: The main paradigm shift in the mAb-based immunotherapy of solid tumors. *International Journal of Biological Macromolecules*, *207*, 592–610. https://doi.org/10.1016/j.ijbiomac.2022.03.057

415. Parakh, S., Lee, S. T., Gan, H. K., & Scott, A. M. (2022). Radiolabeled Antibodies for Cancer Imaging and Therapy. *Cancers*, *14*(6), 1454. https://doi.org/10.3390/cancers14061454

416. Rousseau, J., Lau, J., & Bénard, F. (2022). Radiolabeled Antibodies for Cancer Radioimmunotherapy. In S. Harsini, A. Alavi, & N. Rezaei (Eds.), *Nuclear medicine and immunology* (pp. 297–345). Springer International Publishing.

417. Picozzi, V.J.; Ramanathan, R.K.; Lowery, M.A.; Ocean, A.J.; Mitchell, E.P.; O'Neil, B.H.; Guarino, M.J.; Conkling, P.R.; Cohen, S.J.; Bahary, N.; et al. Feasibility and results of a randomized phase Ib study of fractionated 90Y-clivatuzumab tetraxetan in patients with metastatic pancreatic cancer having two or more prior therapies. J. Clin. Oncol. 2014, 32, 4026.

418. Wegener, W. (2013, December - 2016, November). Phase 3 Trial of 90Y-Clivatuzumab Tetraxetan & Gemcitabine vs Placebo & Gemcitabine in Metastatic Pancreatic Cancer (PANCRIT®-1). Identifier: NCT01956812. https://www.clinicaltrials.gov/study/ NCT01956812.

419. Sultana, A., Shore, S., Raraty, M. G., Vinjamuri, S., Evans, J. E., Smith, C. T., Lane, S., Chauhan, S., Bosonnet, L., Garvey, C., et al. (2009). Randomised Phase I/II trial assessing the safety and efficacy of radiolabelled anti-carcinoembryonic antigen I131KAb201 antibodies given intra-arterially or intravenously in patients with unresectable pancreatic adenocarcinoma. BMC Cancer, 9, 66.

420. Vives, J., & Batlle-Morera, L. (2020). The challenge of developing human 3D organoids into medicines. Stem Cell Research & Therapy, 11(1), 72. https://doi.org/10.1186/s13287-020-1586-1

421. Tiriac, H., Belleau, P., Engle, D. D., Plenker, D., Deschênes, A., Somerville, T. D. D., Froeling, F. E. M., Burkhart, R. A., Denroche, R. E., Jang, G.-H., Miyabayashi, K., Young, C. M., Patel, H., Ma, M., LaComb, J. F., Palmaira, R. L. D., Javed, A. A., Huynh, J. C., Johnson, M., … Tuveson, D. A. (2018). Organoid Profiling Identifies Common Responders to Chemotherapy in Pancreatic Cancer. Cancer Discovery, 8(9), 1112–1129. https://doi.org/10.1158/2159-8290.CD-18-0349

422. Driehuis, E., van Hoeck, A., Moore, K., Kolders, S., Francies, H. E., Gulersonmez, M. C., Stigter, E. C. A., Burgering, B., Geurts, V., Gracanin, A., Bounova, G., Morsink, F. H., Vries, R., Boj, S., van Es, J., Offerhaus, G. J. A., Kranenburg, O., Garnett, M. J., Wessels, L., … Clevers, H. (2019). Pancreatic cancer organoids recapitulate disease and allow personalized drug screening. Proceedings of the National Academy of Sciences of the United States of America, 116(52), 26580–26590. https://doi.org/10.1073/pnas.1911273116

423. Baghban, R., Roshangar, L., Jahanban-Esfahlan, R., Seidi, K., Ebrahimi-Kalan, A., Jaymand, M., Kolahian, S., Javaheri, T., & Zare, P. (2020). Tumor microenvironment complexity and therapeutic implications at a glance. Cell Communication and Signaling, 18(1), 59. https://doi.org/10.1186/s12964-020-0530-4

424. Moreira, L., Bakir, B., Chatterji, P., Dantes, Z., Reichert, M., & Rustgi, A. K. (2018). Pancreas 3D Organoids: Current and Future Aspects as a Research Platform for Personalized Medicine in Pancreatic Cancer. Cellular and Molecular Gastroenterology and Hepatology, 5(3), 289–298. https://doi.org/10.1016/j.jcmgh.2017.12.004

425. Sharma, R., Restan Perez, M., da Silva, V. A., Thomsen, J., Bhardwaj, L., Andrade, T. A. M., Alhussan, A., & Willerth, S. M. (2023). 3D bioprinting complex models of cancer. *Biomaterials Science*, *11*(10), 3414–3430. https://doi.org/10.1039/d2bm02060b

426. Bejoy, A. M., Makkithaya, K. N., Hunakunti, B. B., Hegde, A., Krishnamurthy, K., Sarkar, A., Lobo, C. F., Keshav, D. V. S., G, D., S, D. D., Mascarenhas, S., Chakrabarti, S., Kalepu, S. R. R. D., Paul, B., & Mazumder, N. (2021). An insight on advances and applications of 3d bioprinting: A review. Bioprinting, 24(e00176). https://doi.org/10.1016/j.bprint.2021.e00176

427. Datta, P., Dey, M., Ataie, Z., Unutmaz, D., & Ozbolat, I. T. (2020). 3D bioprinting for reconstituting the cancer microenvironment. NPJ Precision Oncology, 4, 18. https://doi.org/10.1038/s41698-020-0121-2

428. Augustine, R., Kalva, S. N., Ahmad, R., Zahid, A. A., Hasan, S., Nayeem, A., McClements, L., & Hasan, A. (2021). 3D Bioprinted cancer models: Revolutionizing personalized cancer therapy. Translational Oncology, 14(4), 101015. https://doi.org/10.1016/j.tranon.2021.101015

429. Hou, S., Tiriac, H., Sridharan, B. P., Scampavia, L., Madoux, F., Seldin, J., Souza, G. R., Watson, D., Tuveson, D., & Spicer, T. P. (2018). Advanced Development of Primary Pancreatic Organoid Tumor Models for High-Throughput Phenotypic Drug Screening. Slas Discovery, 23(6), 574–584. https://doi.org/10.1177/2472555218766842

430. Langer, E. M., Allen-Petersen, B. L., King, S. M., Kendsersky, N. D., Turnidge, M. A., Kuziel, G. M., Riggers, R., Samatham, R., Amery, T. S., Jacques, S. L., Sheppard, B. C., Korkola, J. E., Muschler, J. L., Thibault, G., Chang, Y. H., Gray, J. W., Presnell, S. C., Nguyen, D. G., & Sears, R. C. (2019). Modeling Tumor Phenotypes In Vitro with Three-Dimensional Bioprinting. Cell Reports, 26(3), 608-623.e6. https://doi.org/10.1016/j.celrep.2018.12.090

431. Hakobyan, D., Médina, C., Dusserre, N., Stachowicz, M.-L., Handschin, C., Fricain, J.-C., Guillermet-Guibert, J., & Oliveira, H. (2020). Laser-assisted 3D bioprinting of exocrine pancreas spheroid models for cancer initiation study. Biofabrication, 12(3), 035001. https://doi.org/10.1088/1758-5090/ab7cb8

432. Okada, S., Vaeteewoottacharn, K., & Kariya, R. (2019). Application of Highly Immunocompromised Mice for the Establishment of Patient-Derived Xenograft (PDX) Models. Cells, 8(8), 889. https://doi.org/10.3390/cells8080889

433. Abdolahi, S., Ghazvinian, Z., Muhammadnejad, S., Saleh, M., Asadzadeh Aghdaei, H., & Baghaei, K. (2022). Patient-derived xenograft (PDX) models, applications and challenges in cancer research. Journal of Translational Medicine, 20(1), 206. https://doi.org/10.1186/s12967-022-03405-8

434. Huang, L., Bockorny, B., Paul, I., Akshinthala, D., Frappart, P.-O., Gandarilla, O., Bose, A., Sanchez-Gonzalez, V., Rouse, E. E., Lehoux, S. D., Pandell, N., Lim, C. M., Clohessy, J. G., Grossman, J., Gonzalez, R., Del Pino, S. P., Daaboul, G., Sawhney, M. S., Freedman, S. D., … Muthuswamy, S. K. (2020). PDX-derived organoids model in vivo drug response and secrete biomarkers. JCI Insight, 5(21), e135544, 135544. https://doi.org/10.1172/jci.insight.135544

435. Torres, M. P., Rachagani, S., Souchek, J. J., Mallya, K., Johansson, S. L., & Batra, S. K. (2013). Novel Pancreatic Cancer Cell Lines Derived from Genetically Engineered Mouse Models of Spontaneous Pancreatic Adenocarcinoma: Applications in Diagnosis and Therapy. PLoS ONE, 8(11), e80580. https://doi.org/10.1371/journal.pone.0080580

436. Herreros-Villanueva, M., Hijona, E., Cosme, A., & Bujanda, L. (2012). Mouse models of pancreatic cancer. World Journal of Gastroenterology, 18(12), 1286–1294. https://doi.org/10.3748/wjg.v18.i12.1286

APPENDIX

Supplementary section S1: GNPs DF and HIS Images

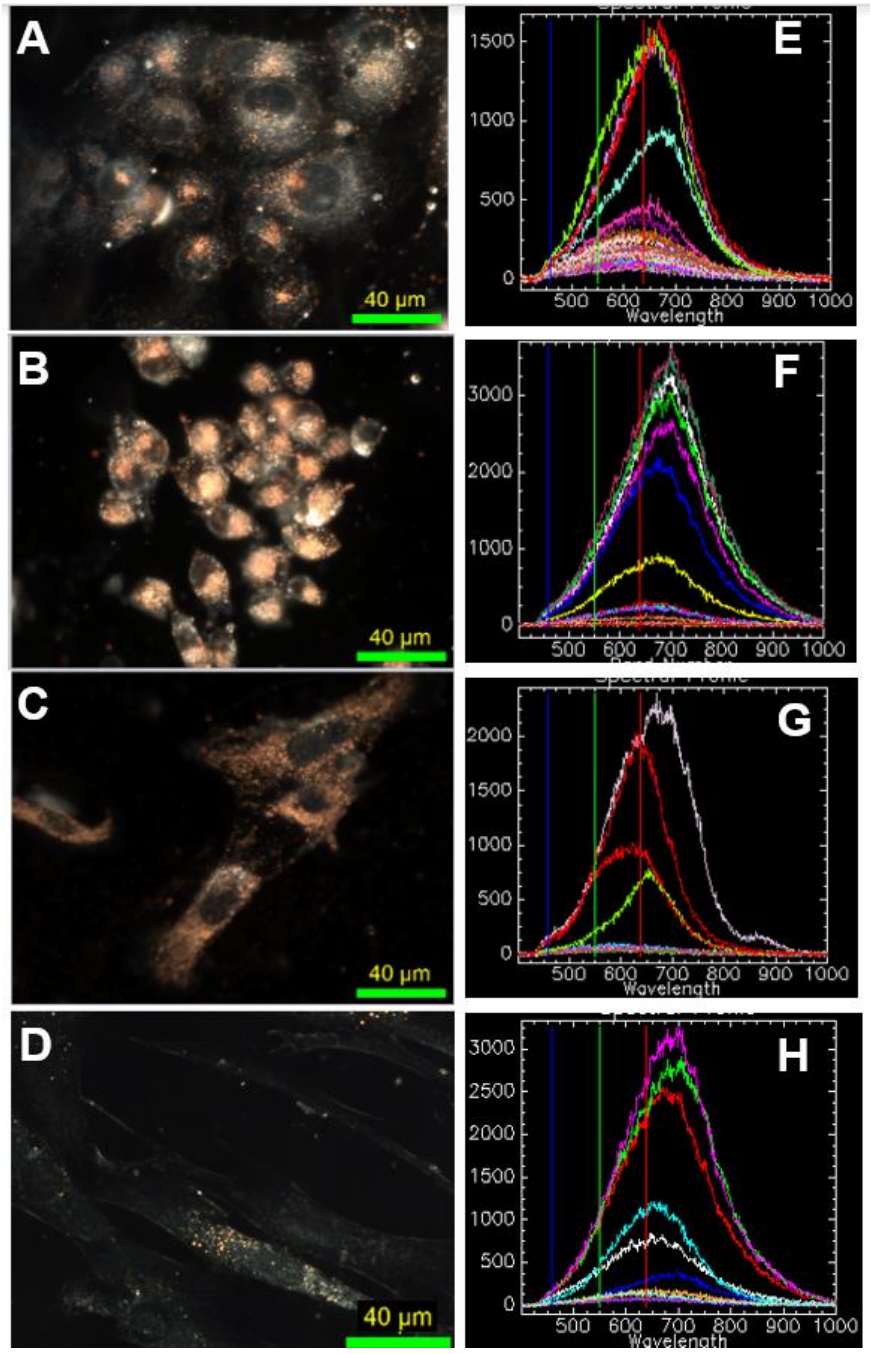

Figure S1.1 GNPs Endocytosis 24 h post incubation. Visualization of intracellular NP distribution in PANC-1 (**A**), Mia PaCa-2 (**B**), CAFs (**C**) and NFs (**D**) using DF. (**E**–**H**) HSI spectra collected from GNP clusters (bright specs) in images from A to D. Scale bar is 40 µm. Reproduced with permission from open access Creative Common license [222].

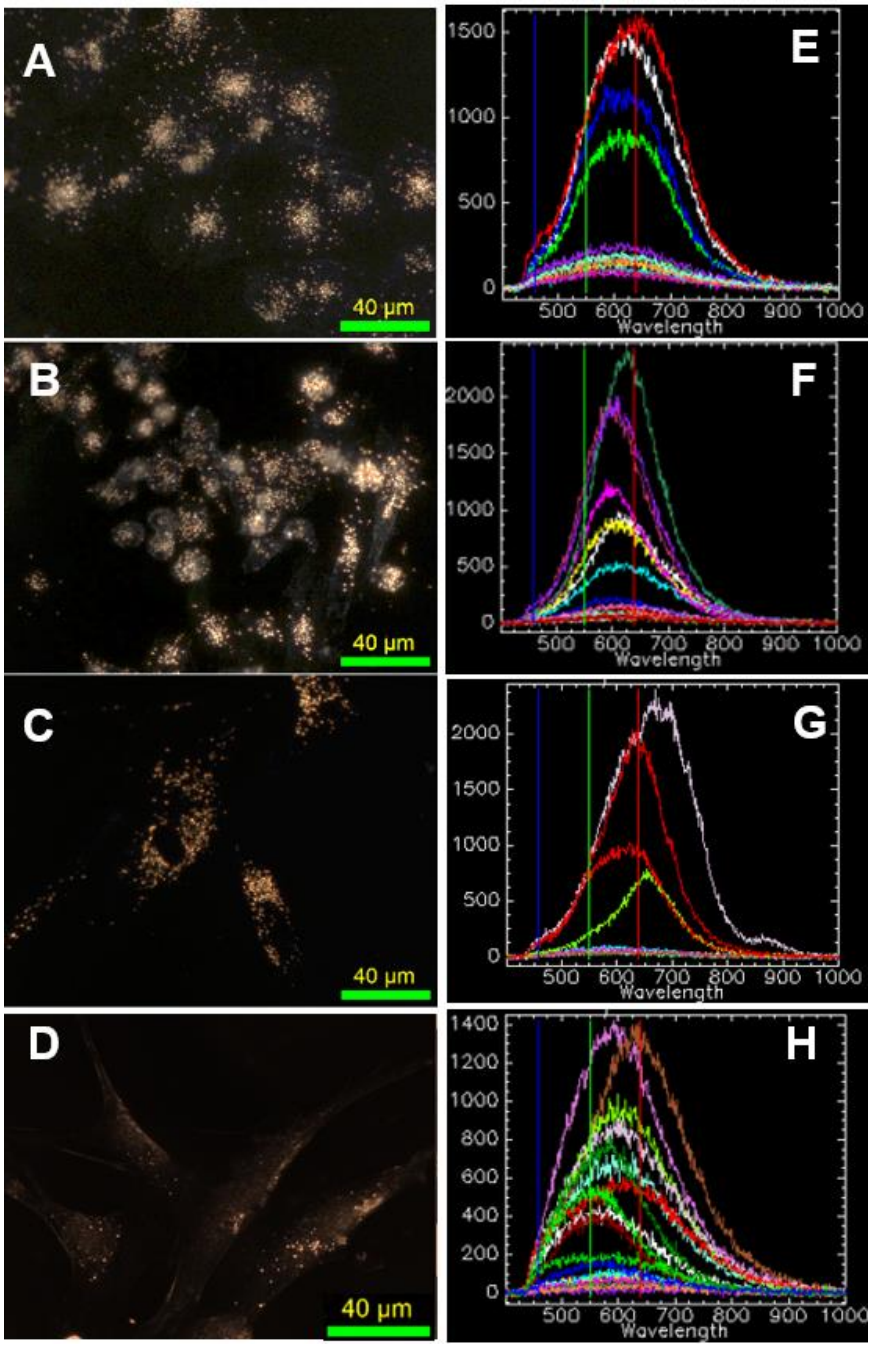

Figure S1.2 GNPs Exocytosis 48 h post incubation. Visualization of intracellular NP distribution in PANC-1 (**A**), Mia PaCa-2 (**B**), CAFs (**C**) and NFs (**D**) using DF. (**E**–**H**) HSI spectra collected from GNP clusters (bright specs) in images from A to D. Scale bar is 40 µm. Reproduced with permission from open access Creative Common license [222].

Supplementary section S2: DTX effect on tumor cells and CAFs.

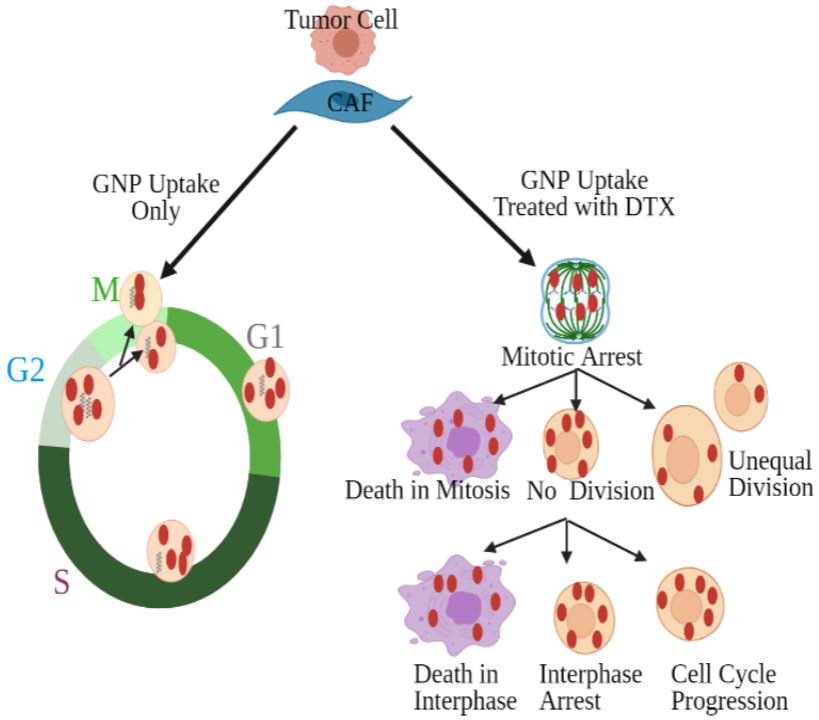

Figure S2 An illustration showing normal cell division (**left**) vs. the effect of DTX on cell division (**right**). Reproduced with permission from open access Creative Common license [223].

Supplementary section S3: MT network and distribution of NPs in tumor cells (HeLa)

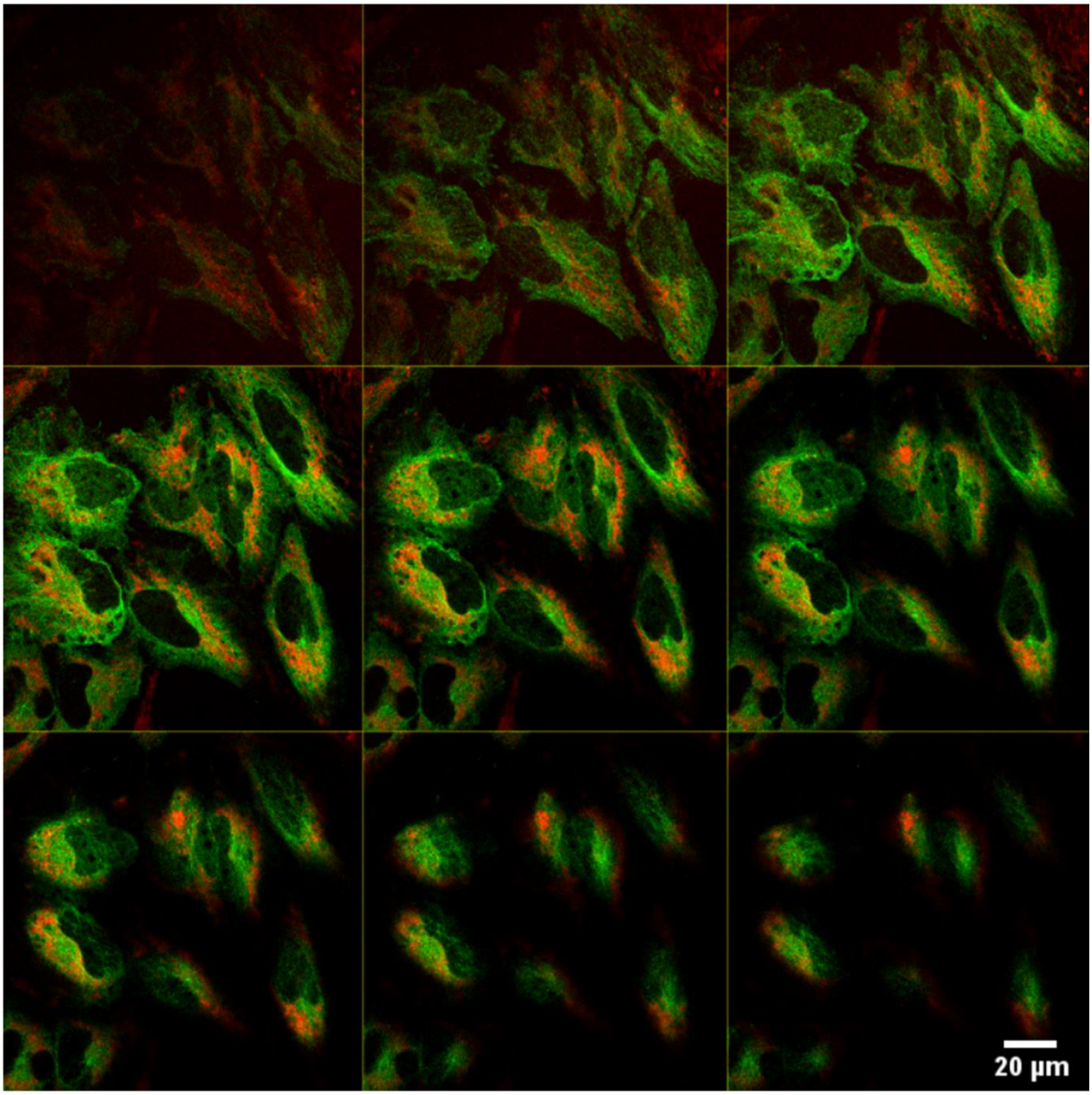

Figure S3.1 MT network and distribution of NPs in HeLa cells across many planes of a cell. Vesicles containing GNPs and MT network are marked in red and green, respectively. Scale bar is 20 µm. Reproduced with permission from open access Creative Common license [223].

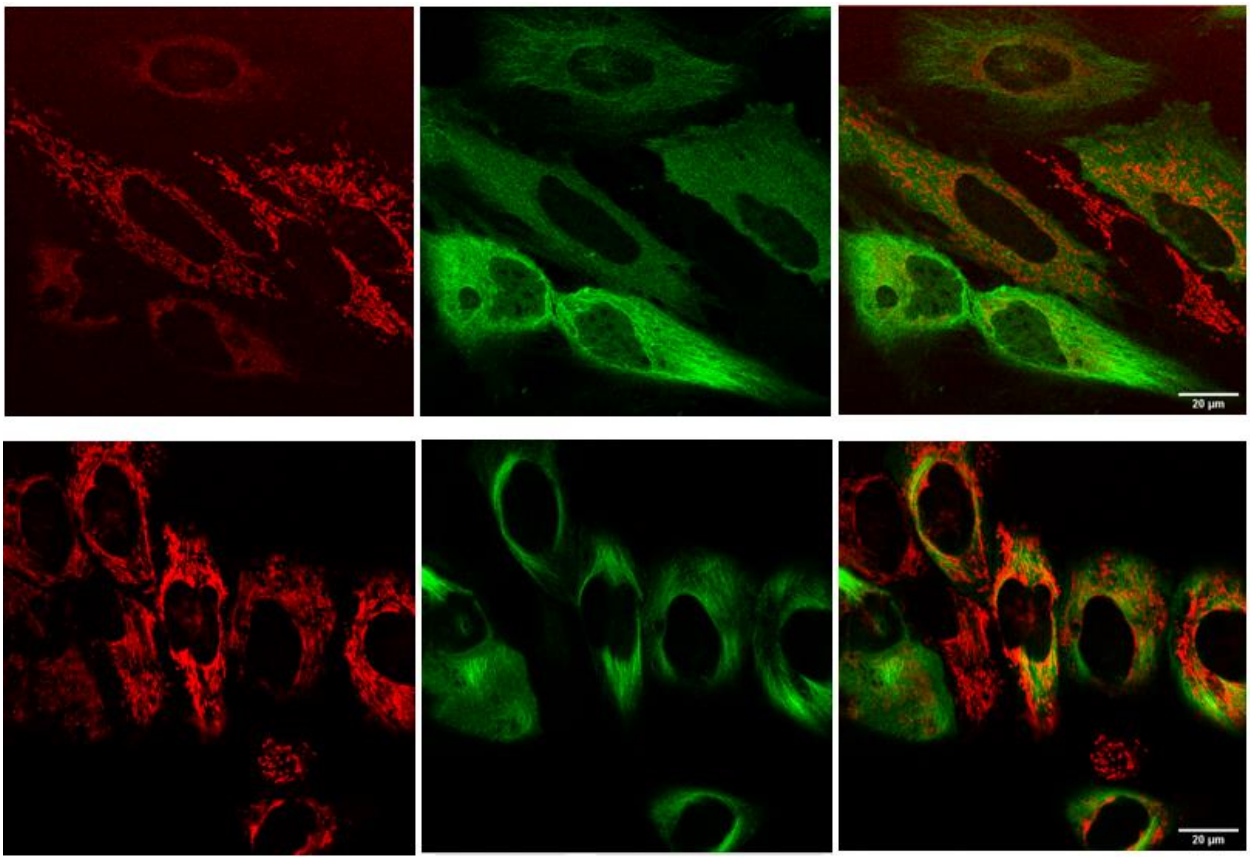

Figure S3.2 MT network and distribution of NPs for control cells (top panel) and cells treated with 50 nM DTX (bottom panel). Scale bar is 20 µm. Vesicles containing GNPs and MT network are marked in red and green, respectively. Reproduced with permission from open access Creative Common license [223].

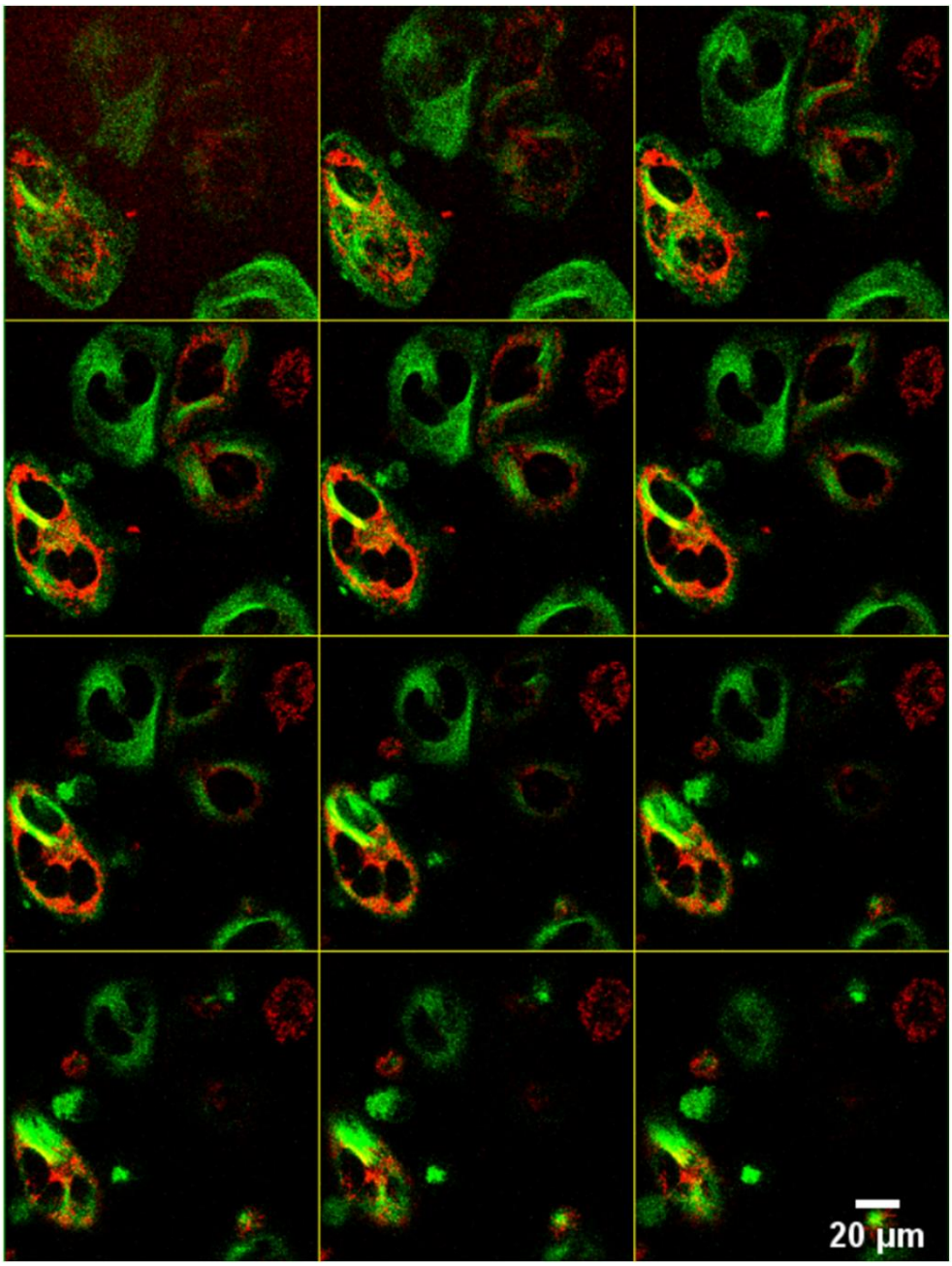

Figure S3.3 MT network and distribution of NPs across many planes of a cell treated with 50 nM DTX. Scale bar is 20 µm. Vesicles containing GNPs and MT network are marked in red and green, respectively. Reproduced with permission from open access Creative Common license [223].

Supplementary Section S4: MT network and distribution of NPs in CAFs

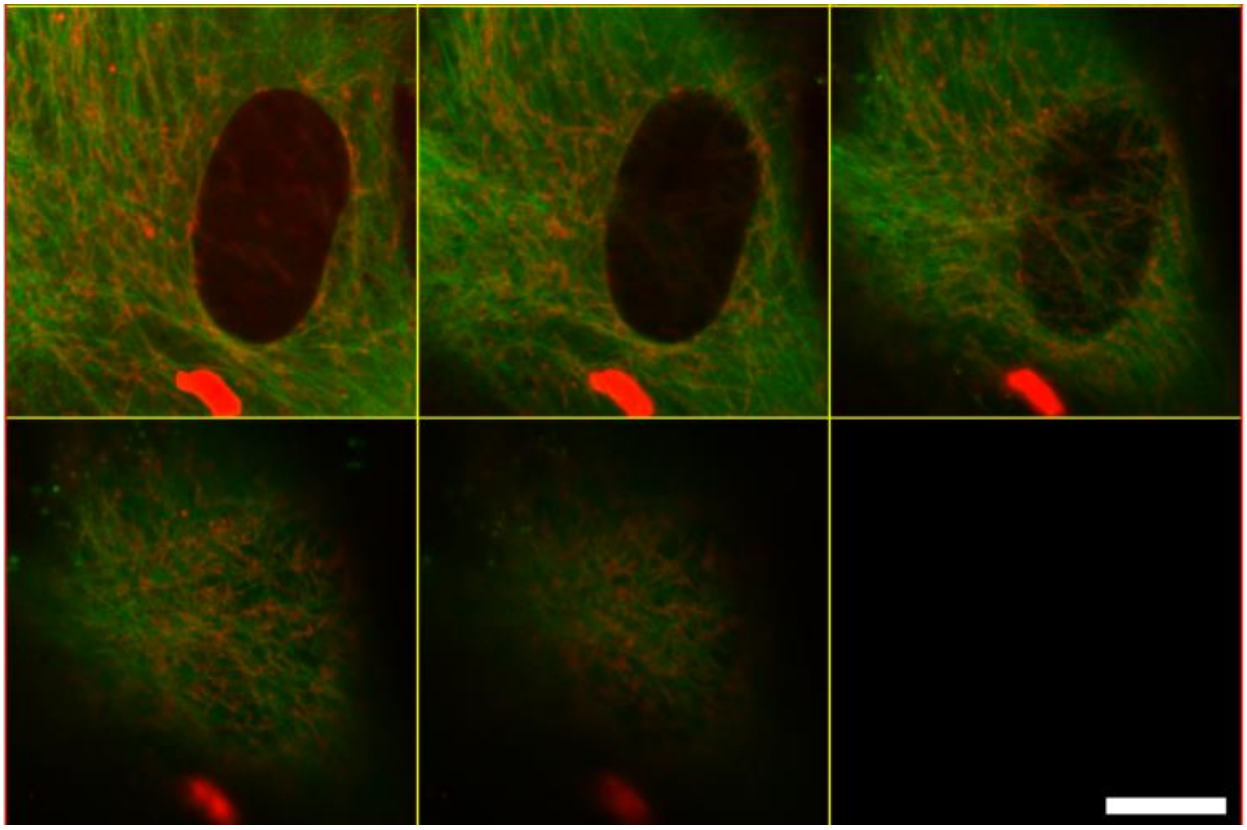

Figure S4.1 MT network and distribution of NPs in CAFs across many planes of a cell. Scale bar is 20 μm. Vesicles containing GNPs and MT network are marked in red and green, respectively. Reproduced with permission from open access Creative Common license [223].

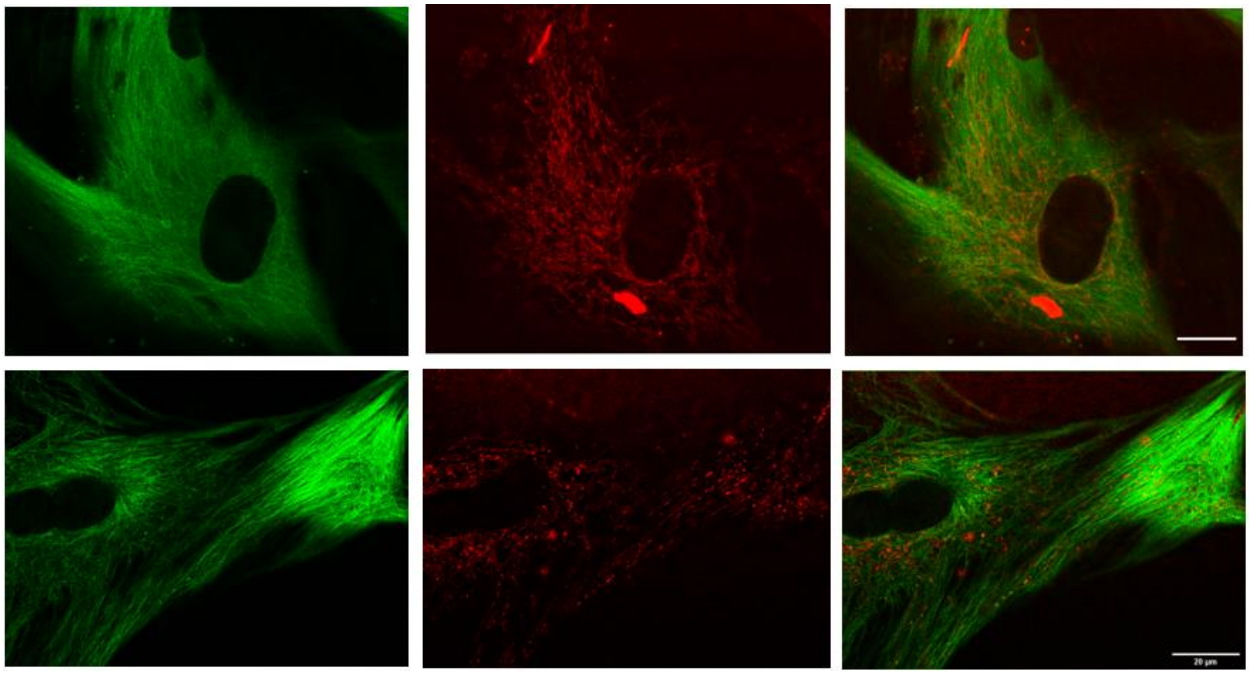

Figure S4.2 MT network and distribution of NPs for control cells (top panel) and cells treated with 50 nM DTX (bottom panel). Scale bar is 20 μm. Vesicles containing GNPs and MT network are marked in red and green, respectively. Reproduced with permission from open access Creative Common license [223].

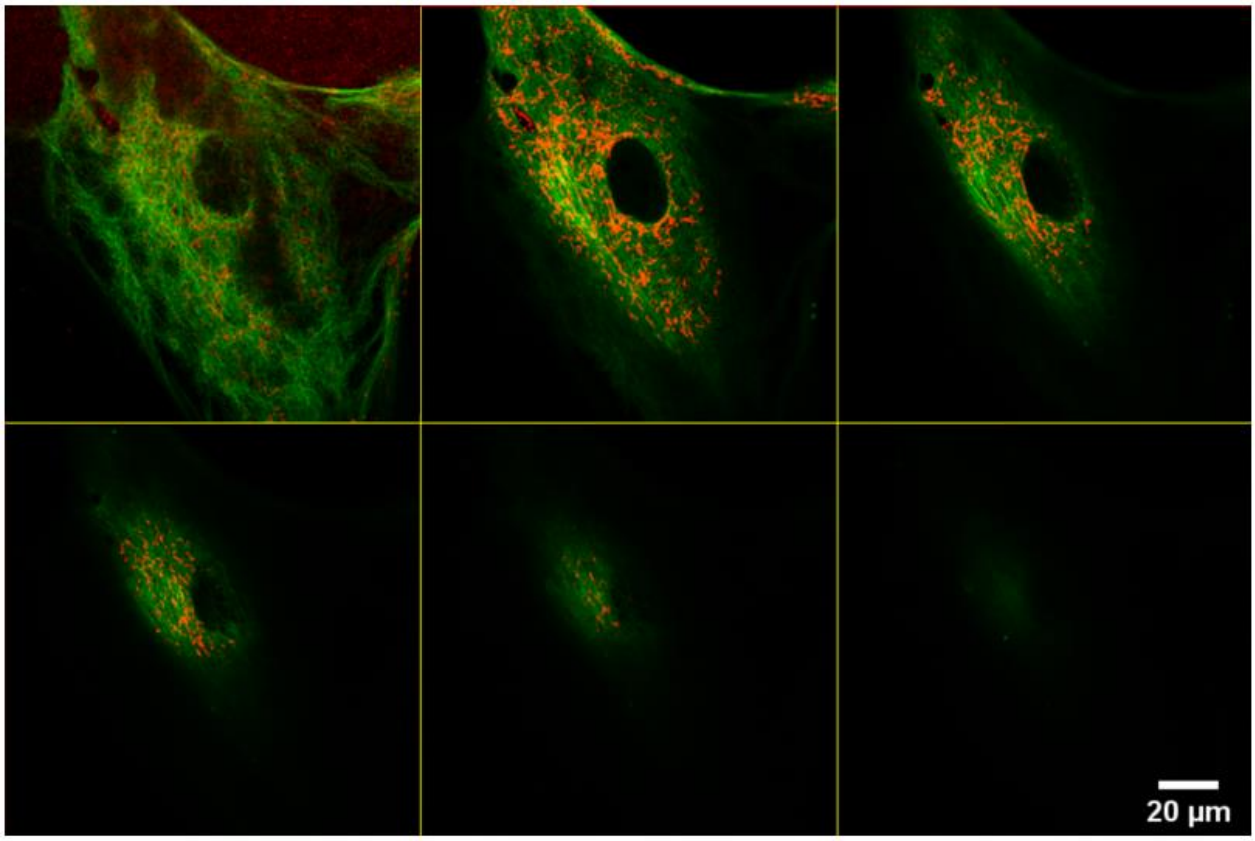

Figure S4.3 MT network and distribution of NPs across many planes of a cell treated with 50 nM DTX. Scale bar is 20 µm. Vesicles containing GNPs and MT network are marked in red and green, respectively. Reproduced with permission from open access Creative Common license [223].

Supplementary Section S5: Transmission Electron Microscopy of GNPs

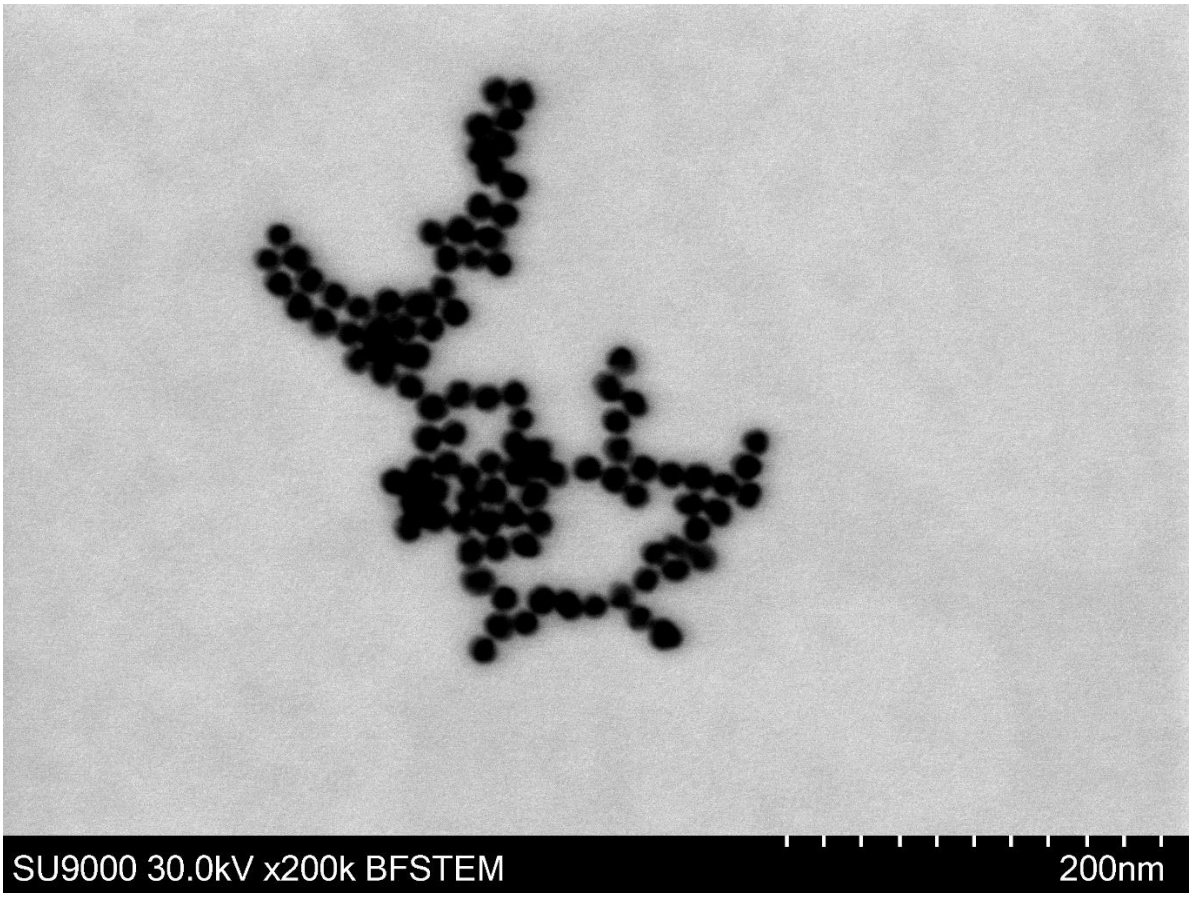

Figure S5.1 TEM image of GNPs.

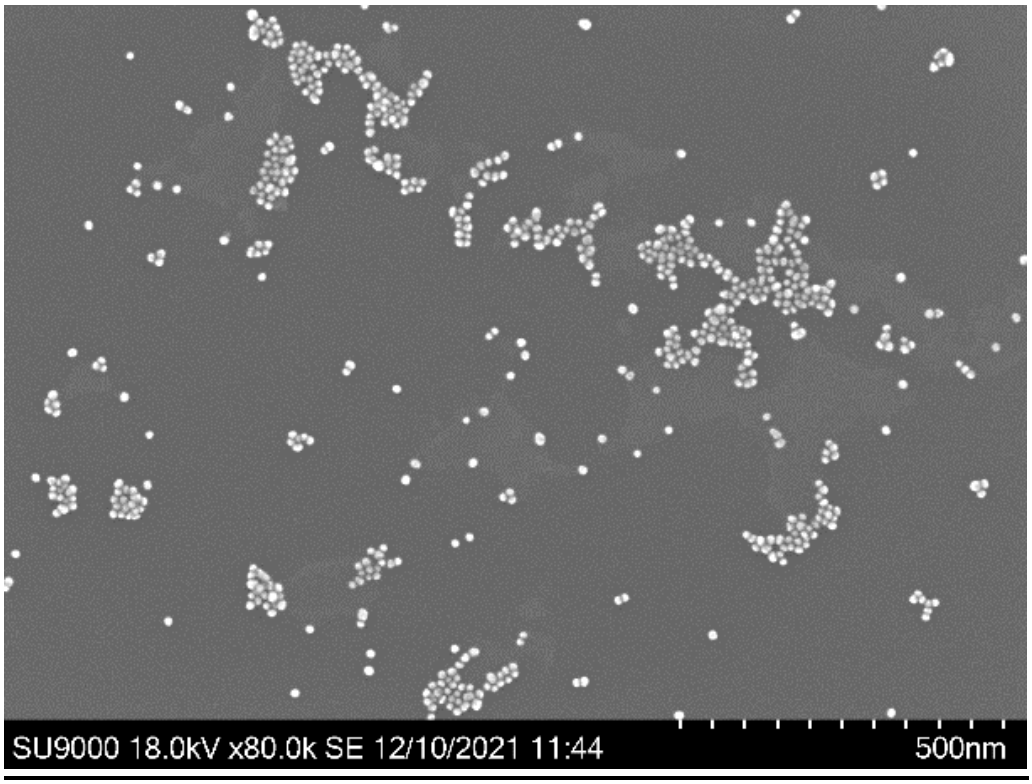

Figure S5.2 TEM image of as-made GNPs.

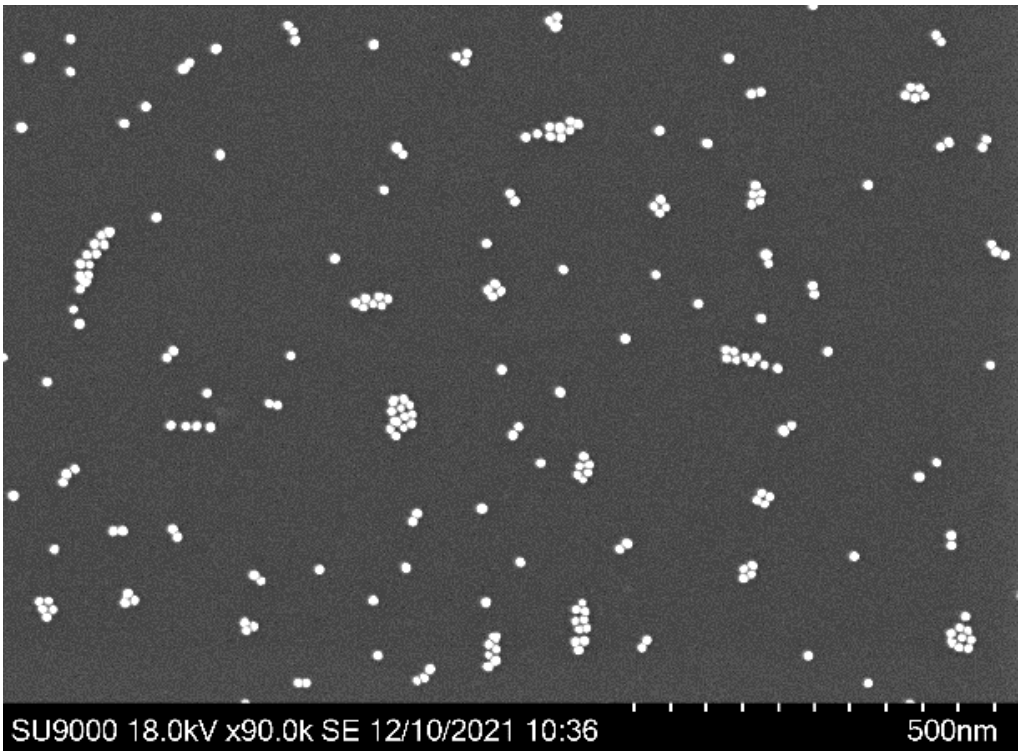

Figure S5.3 TEM image of $GNP_{PEG\text{-}RGD}$.

Supplementary Section S6: Magnetic Beads Separation Method

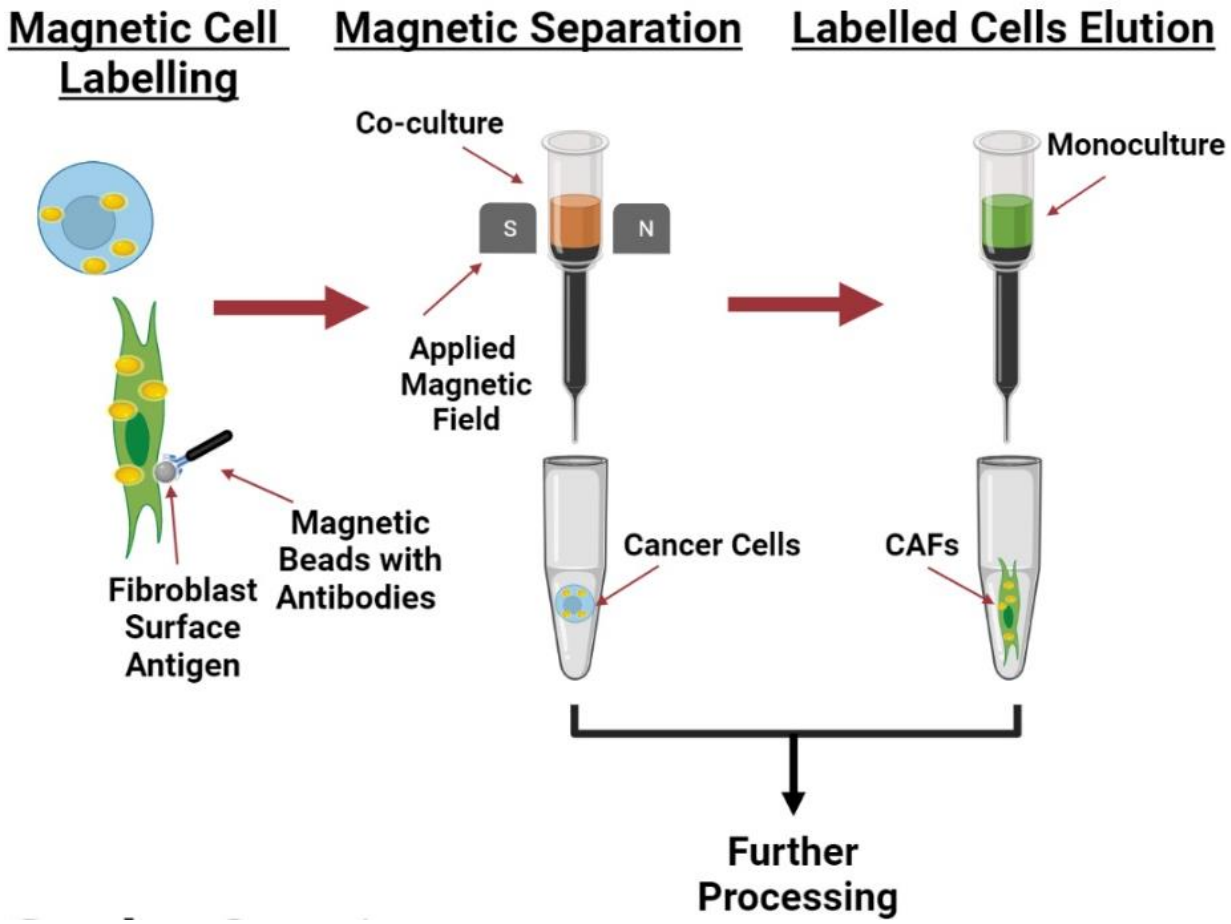

Figure S6.1 Magnetic Beads Separation method. The co-culture of MIA PaCa-2and CAFs was stained with fibroblasts surface antigens that attached to CAFs. The co-culture was then washed with magnetic beads with antibodies that link up with the surface fibroblast surface antigen. The cell co-culture tube is then hooked up to a magnet and is washed multiple times, during which the CAFs will be attracted to the magnet and will stay in the tube, whereas MIA PaCa-2 will be collected in a new tube. The CAFs tube is then moved away from the magnetic field and the cells are washed and collected in a new tube. Reproduced with permission from open access Creative Common license [259].

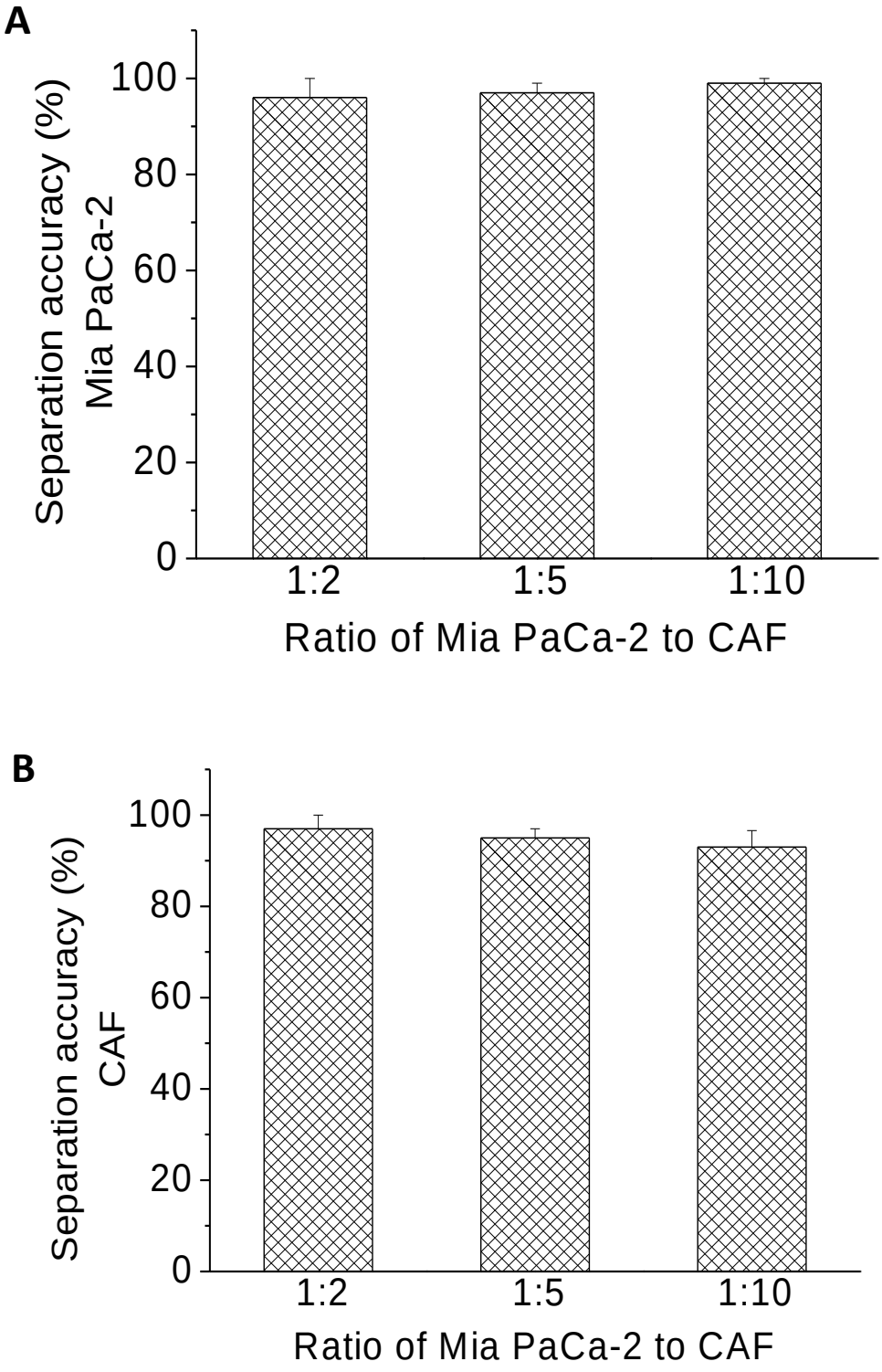

Figure S6.2 Efficiency of the cell separation method. The percentage of Mia-Paca-2 and CAFs post-separation in three different ratios. **(A)** Separation accuracy of MIA PaCa-2. **(B)** Separation accuracy of CAFs. Reproduced with permission from open access Creative Common license [259].

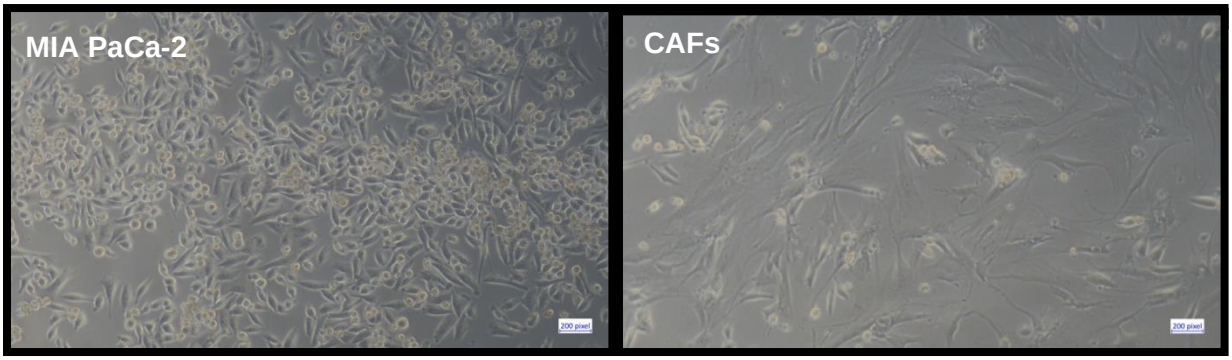

Figure S6.3 Phase contrast microscope of Mia-Paca-2 and CAFs post-separation. Reproduced with permission from open access Creative Common license [259].

Supplementary Section S7: GNPs Uptake DF Images

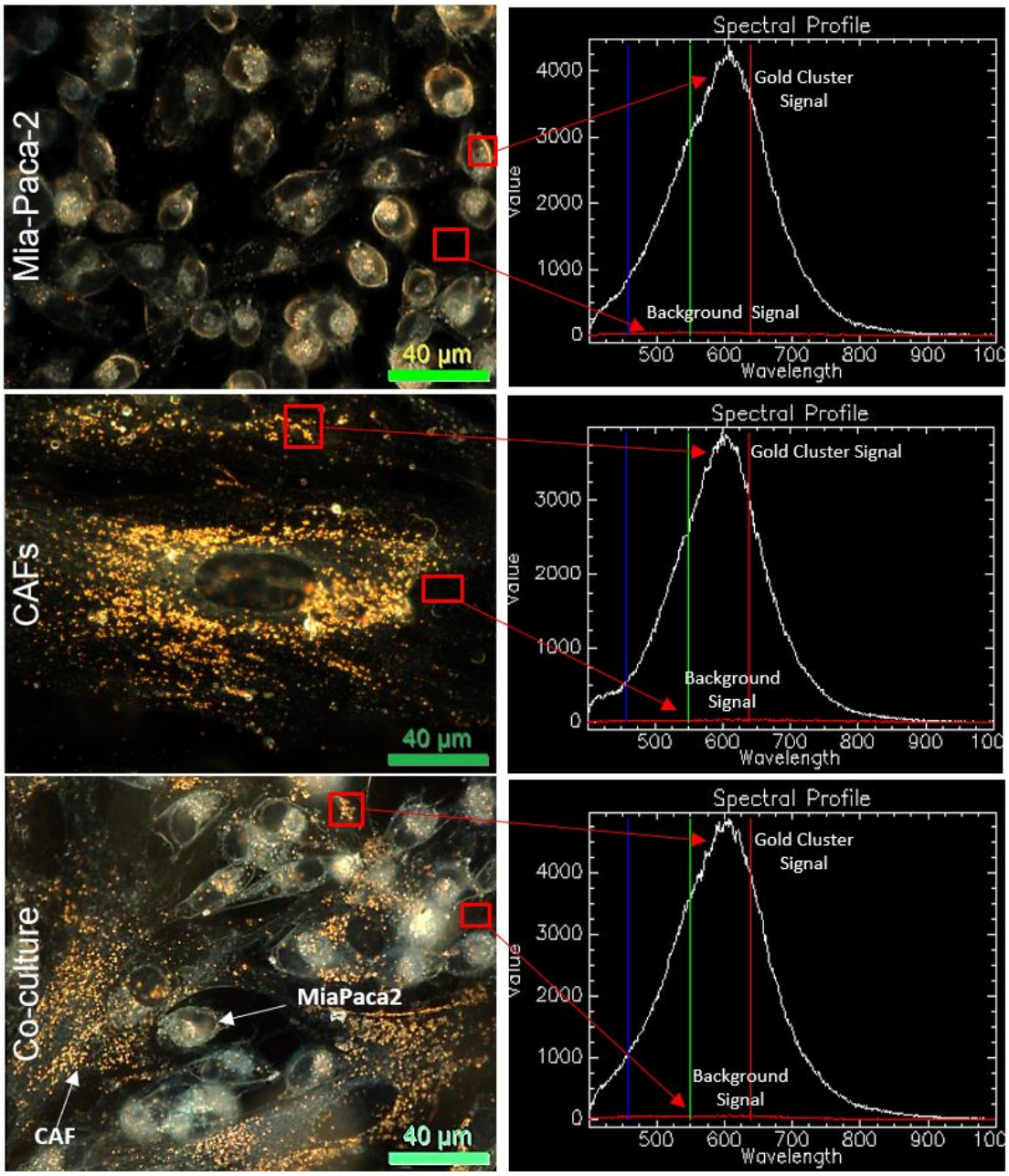

Figure S7.1 GNPs uptake in cancer cells and CAFs in monoculture vs. co-culture. GNP distribution in monoculture MIA PaCa-2 (first row), monoculture CAFs (second row), and co-culture of CAFs & MIA PaCa-2with 2:1 ratio (third row) using DF microscopy (first column) and using HIS (second column) which shows a spectrum collected from GNP clusters (white spectrum) vs. background (red spectrum). Scale bars are 40 µm. Reproduced with permission from open access Creative Common license [259].

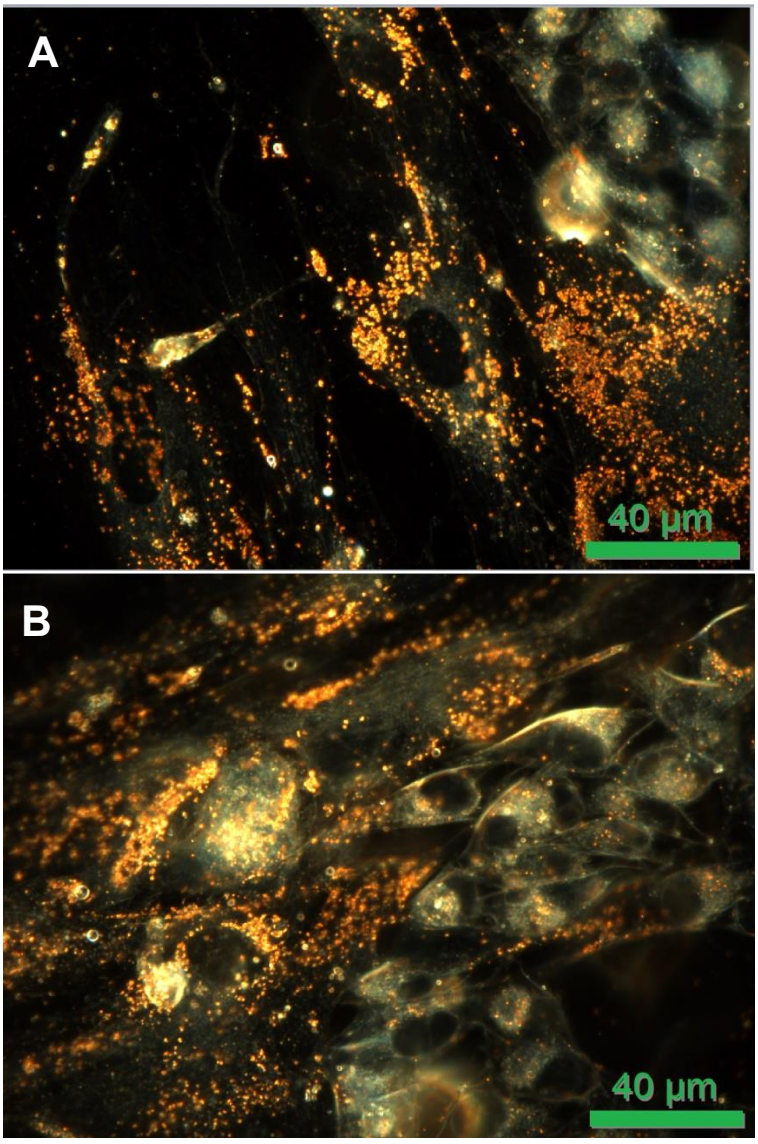

Figure S7.2 DF Images of GNPs Uptake. **(A)** Using a ratio of 5:1 CAFs to cancer cells. **(B)** Using 10:1 ratio of CAFs to cancer cells. Scale bar: 40 µm. Reproduced with permission from open access Creative Common license [259].

Supplementary Section S8: DNA DSB in Co-Culture.

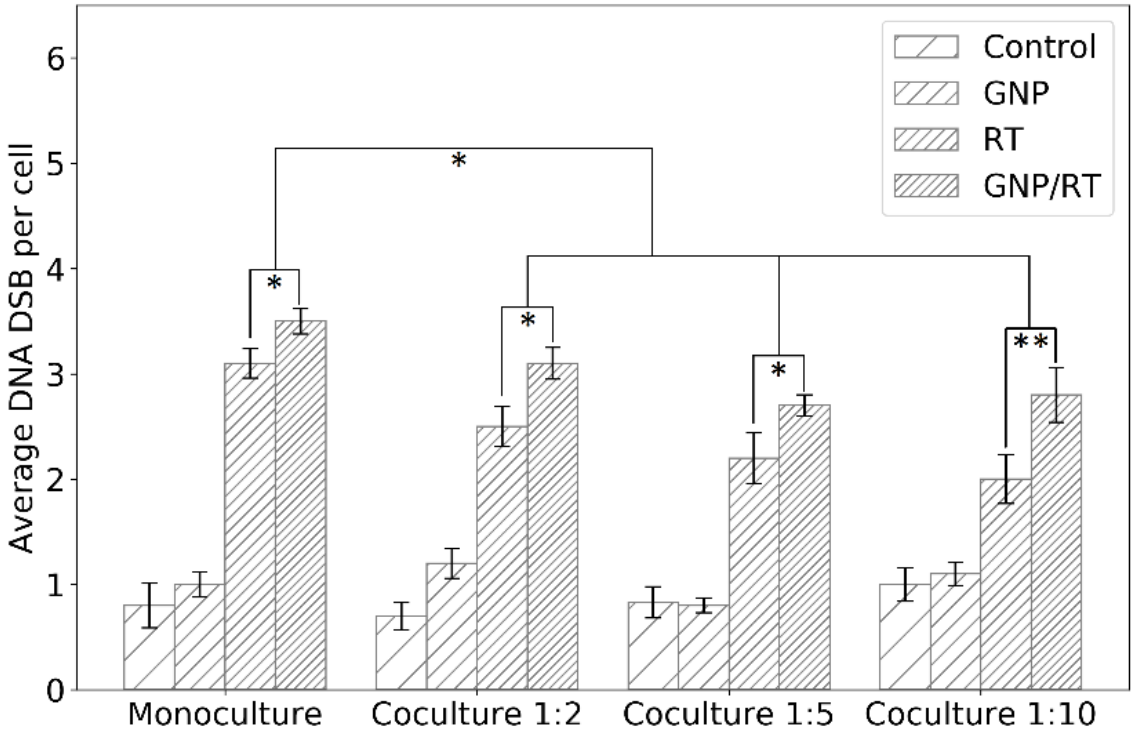

Figure S8.1 DNA DSB damage in CAFs. Average number of DNA DSB damage per cell in CAFs in monoculture vs. in co-culture ($n = 3$). * indicates $p < 0.05$, ** indicates $p < 0.01$. Reproduced with permission from open access Creative Common license [259].

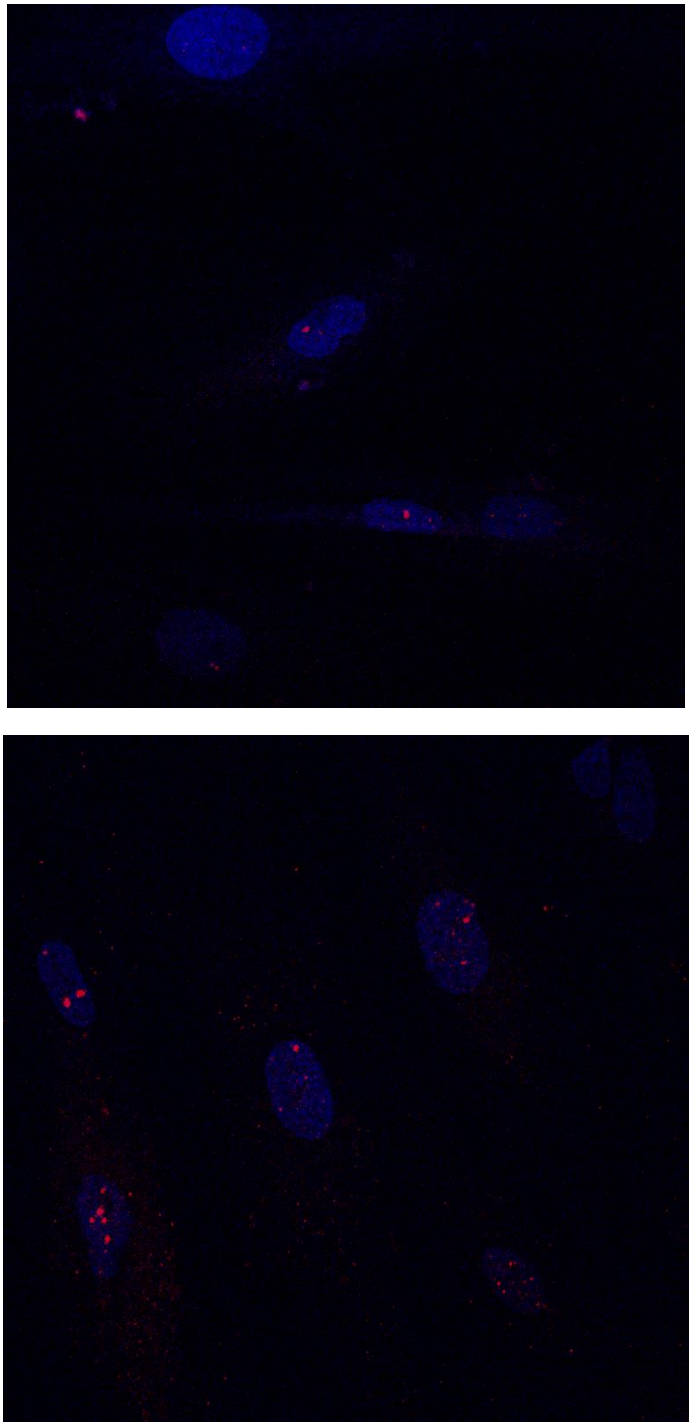

Figure S8.2 Confocal microscopy images of repair protein γ-H2AX in the nucleus of CAFs. **(A)** Irradiated cells. **(B)** Irradiated cells with GNP. Red dots correspond to DNA DSB damages and the blue stains are the cell nuclei. Reproduced with permission from open access Creative Common license [259].

Supplementary Section S9: Cell Proliferation in Co-Culture.

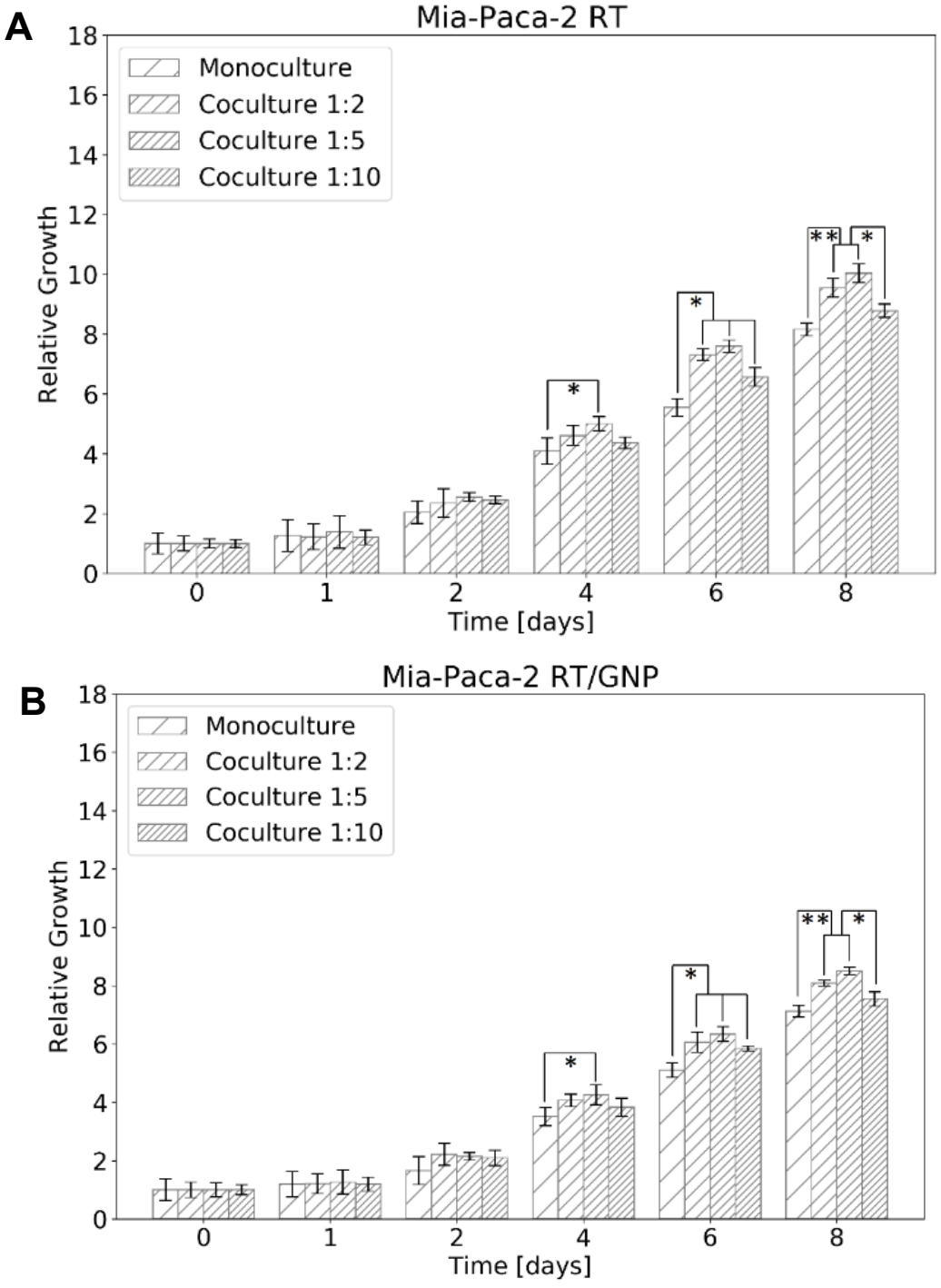

Figure S9.1 Proliferation assay for Mia-Paca-2. (**A**) Irradiated 2 Gy. (**B**) Dosed with GNP and irradiated 2 Gy. * indicates $p < 0.05$, ** indicates $p < 0.01$. Reproduced with permission from open access Creative Common license [259].

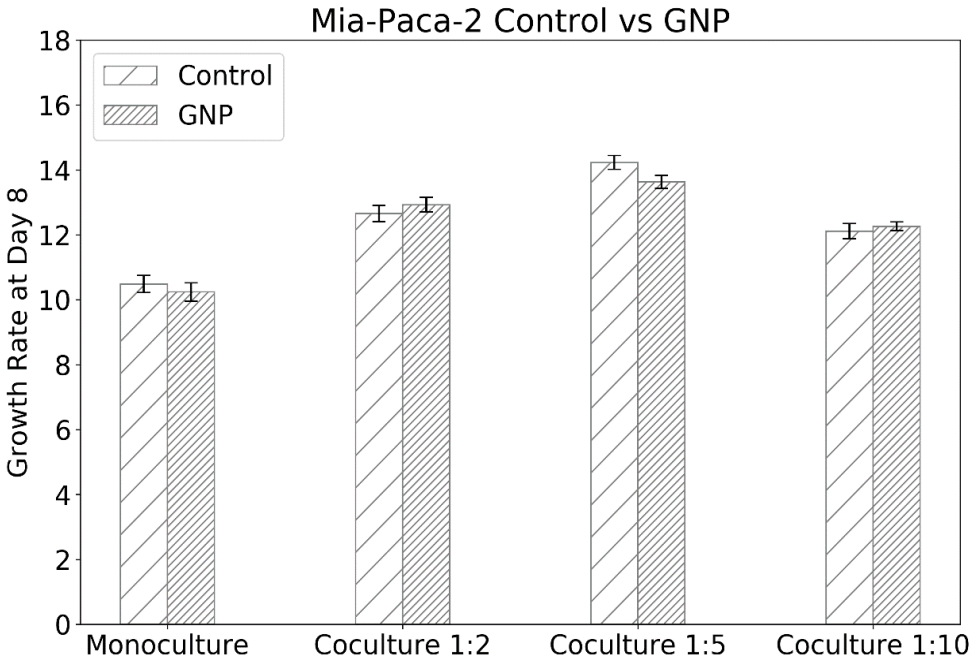

Figure S9.2 Proliferation assay for Mia-Paca-2. Comparison of control vs. GNP at the end of the experiment. Reproduced with permission from open access Creative Common license [259].

Supplementary Section S10: Monoculture Spheroids.

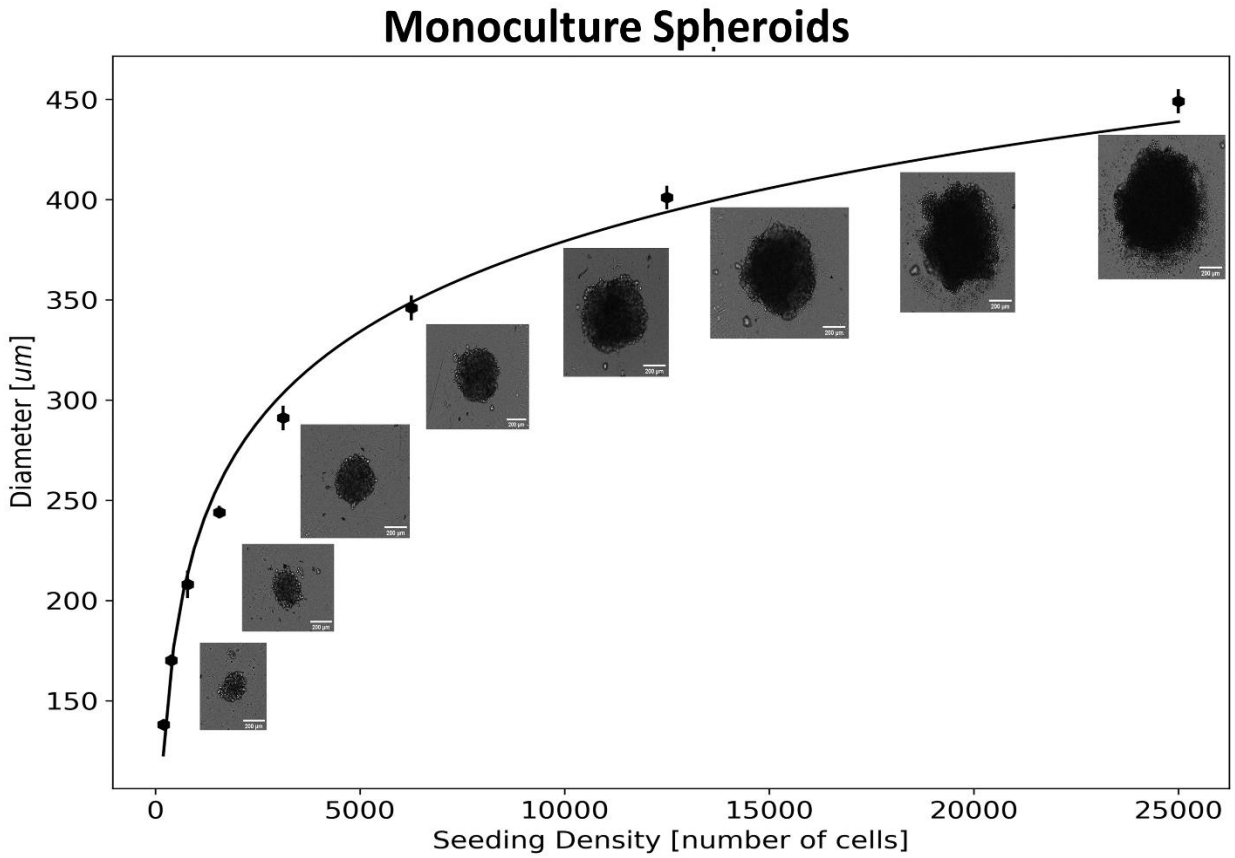

Figure S10 Characterizing pancreatic cancer 3D spheroid size. The size of the spheroids for MIA PaCa-2 monoculture under different initial cell count seeding. The scale bar is 200 μm. Reproduced with permission from open access Creative Common license [260].

Supplementary Section S11: GNPs Characterization

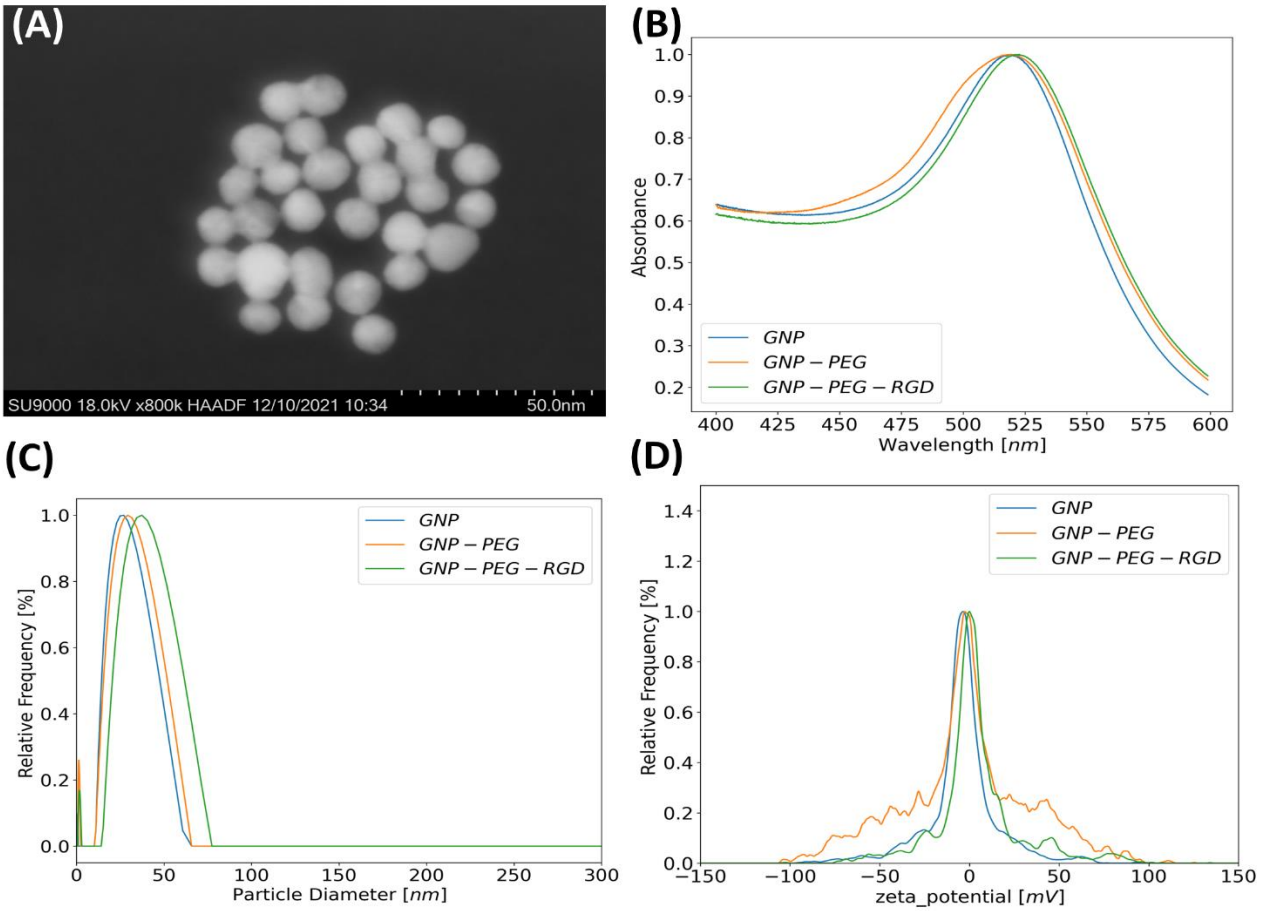

(E)

	Peak Wavelength (nm)	Hydrodynamic Diameter (nm)	Zeta Potential (mV)
GNP	519.15 ± 0.05	14.30 ± 1.46	−13.22 ± 2.89
GNP+PEG	520.05 ± 0.05	20.82 ± 2.01	−3.61 ± 1.22
GNP+PEG+RGD	524.35 ± 0.05	28.44 ± 3.79	0.82 ± 0.82

Figure S11 GNPs characterization. **(A)** HAADF STEM image of GNPs **(B)** UV–visible absorption spectra of GNPs, GNP_{PEG}, and $GNP_{PEG\text{-}RGD}$. **(C)** The hydrodynamic diameter of GNPs, GNP_{PEG}, and $GNP_{PEG\text{-}RGD}$. **(D)** The ζ-potential of GNPs, GNP_{PEG}, and $GNP_{PEG\text{-}RGD}$**. (E)** A table outlines the peak absorption wavelength, hydrodynamic diameter, and mean ζ-potential for GNPs, GNP_{PEG}, and $GNP_{PEG\text{-}RGD}$. Reproduced with permission from open access Creative Common license [260].

Supplementary Section S12: GNPs in Spheroids Confocal Images

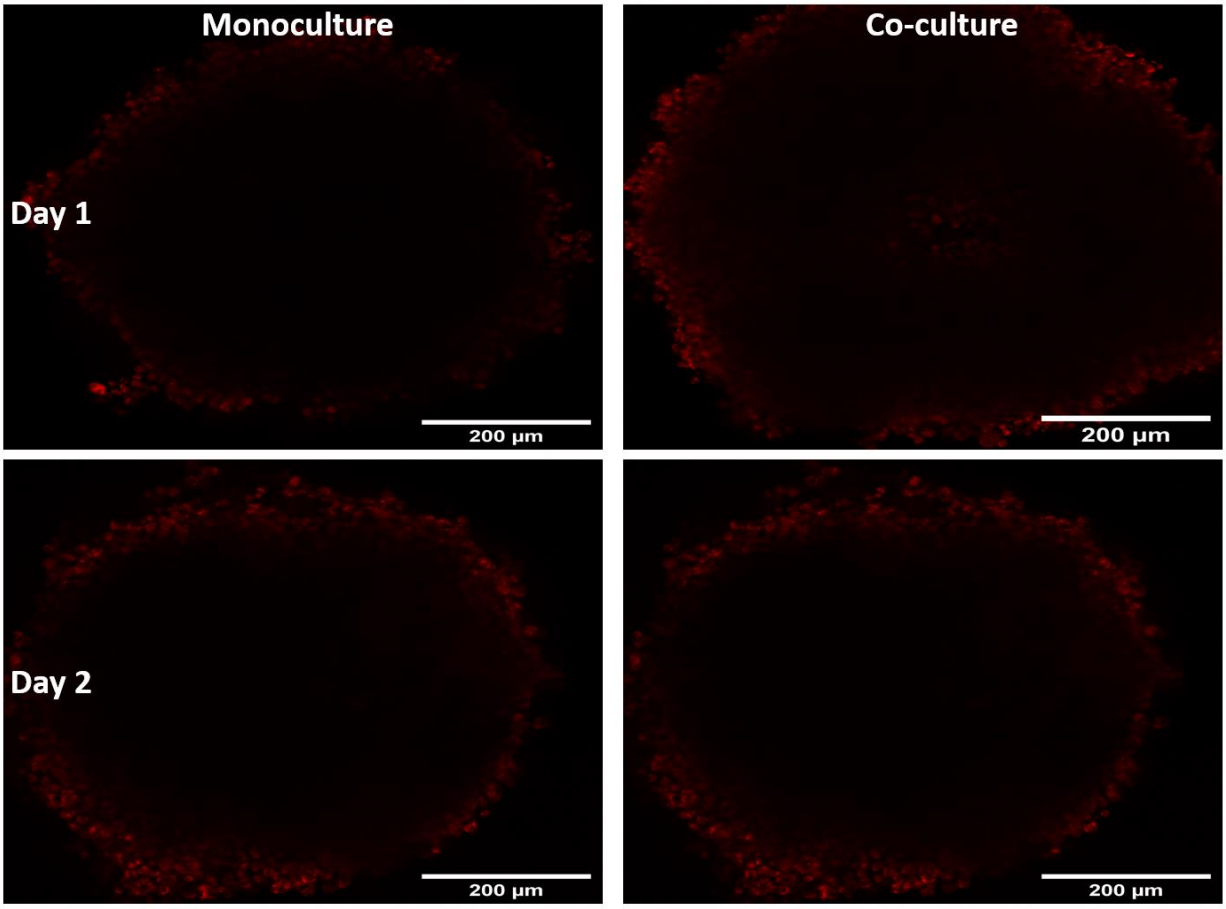

Figure S12 Confocal Images of GNPs', in red, for day 1 and day 2 in MIA PaCa-2 monoculture spheroids and CAF-98 to MIA PaCa-2 (5:1) co-culture spheroids. Scale bar: 200 µm. Reproduced with permission from open access Creative Common license [260].

Supplementary Section S13: Spheroids Proliferation

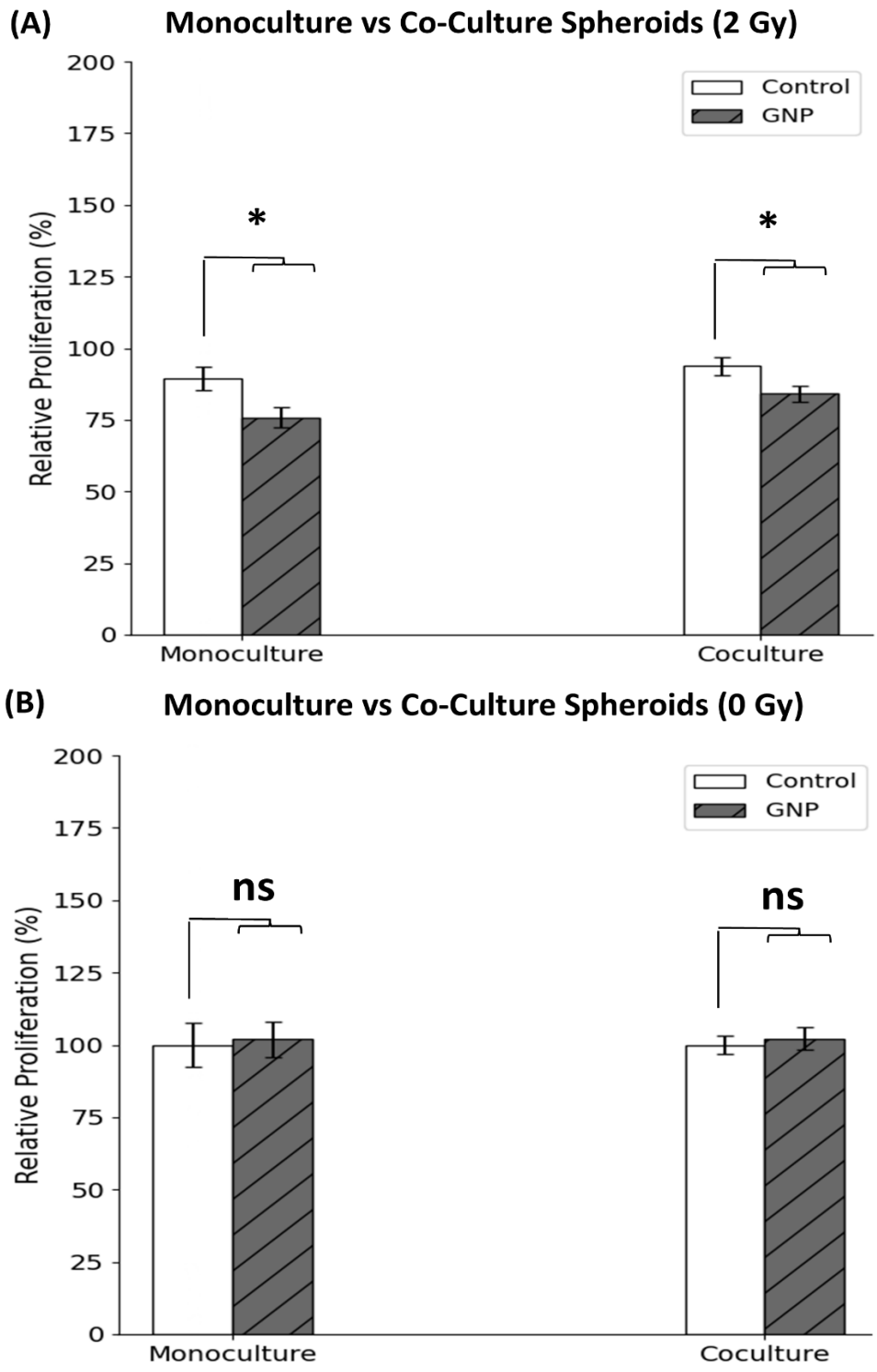

Figure S13 Monoculture vs co-culture spheroids proliferation post-treatment with radiation. **(A-B)** Irradiated spheroids **(A)** and non-irradiated spheroids **(B)** relative cell proliferation at day 14 post-treatment. ns indicates non-significance, * indicates $p < 0.05$. Reproduced with permission from open access Creative Common license [260].

Supplementary Section S14: DNA DSB Mapping in 2D Monoculture vs 2D Co-culture

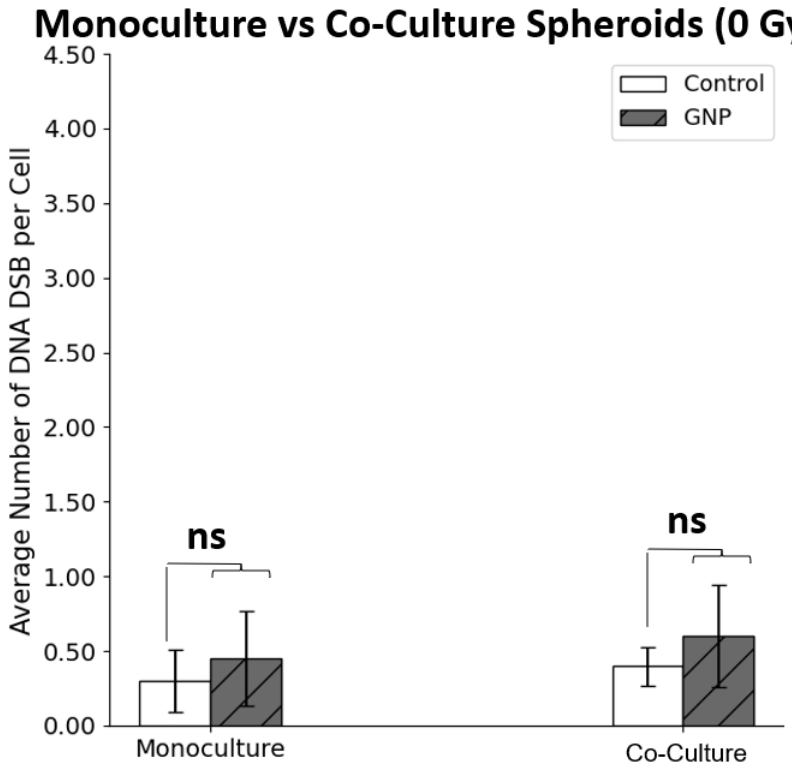

Figure S14.1 The average number of DNA DSB per cell in 2D monoculture and 2D co-culture without radiation. ns indicates non-significance. Reproduced with permission from open access Creative Common license [260].

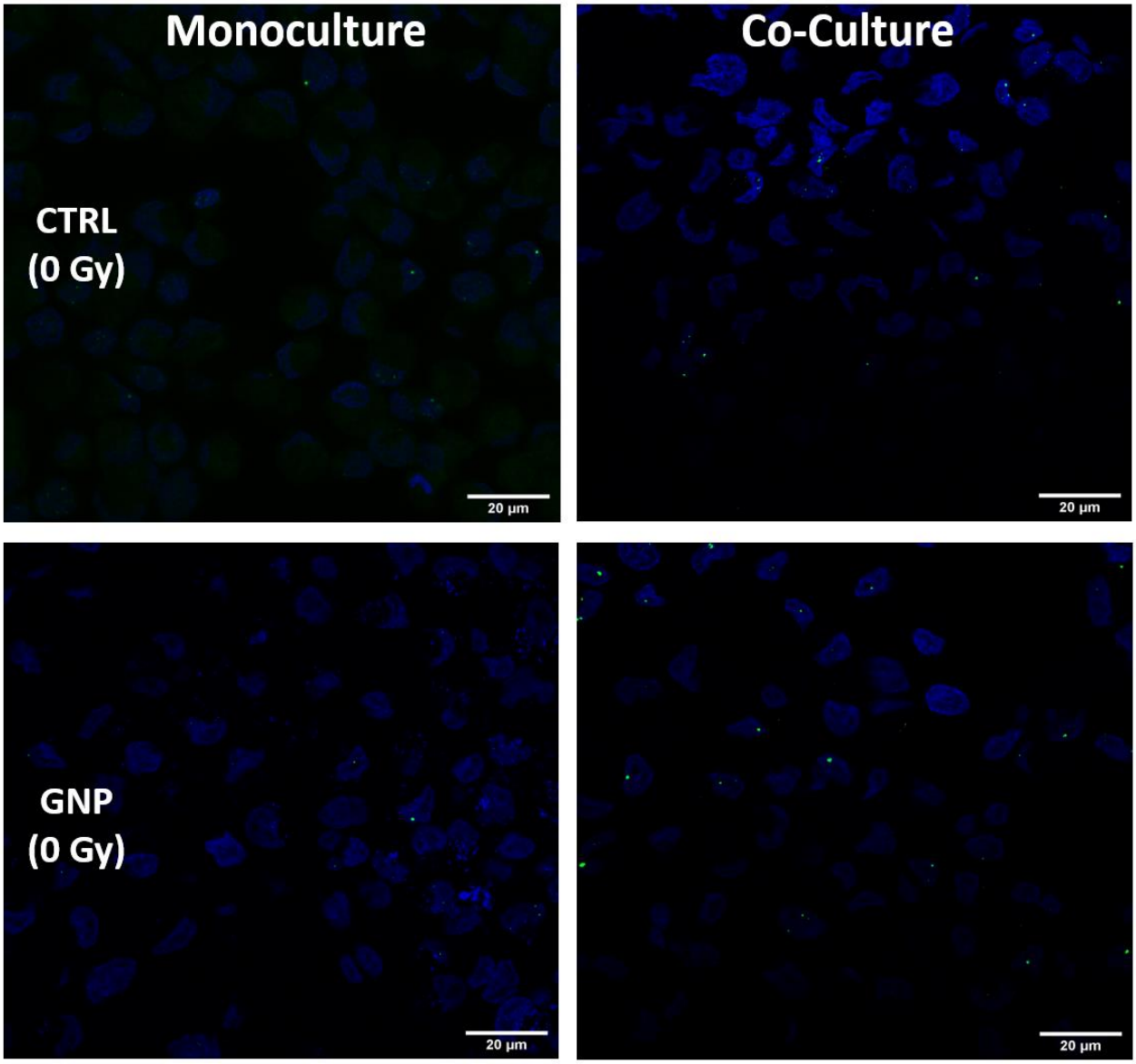

Figure S14.2 Confocal microscopy images of repair protein 53BP1 in the nucleus of monoculture MIA PaCa-2 and in co-culture of MIA PaCa-2 and CAF-98 without radiation. The cell nuclei are stained blue, while the green dots indicate DNA DSB damage. Scale bar: 20 µm. Reproduced with permission from open access Creative Common license [260].

Supplementary Section S15: RT Set-up

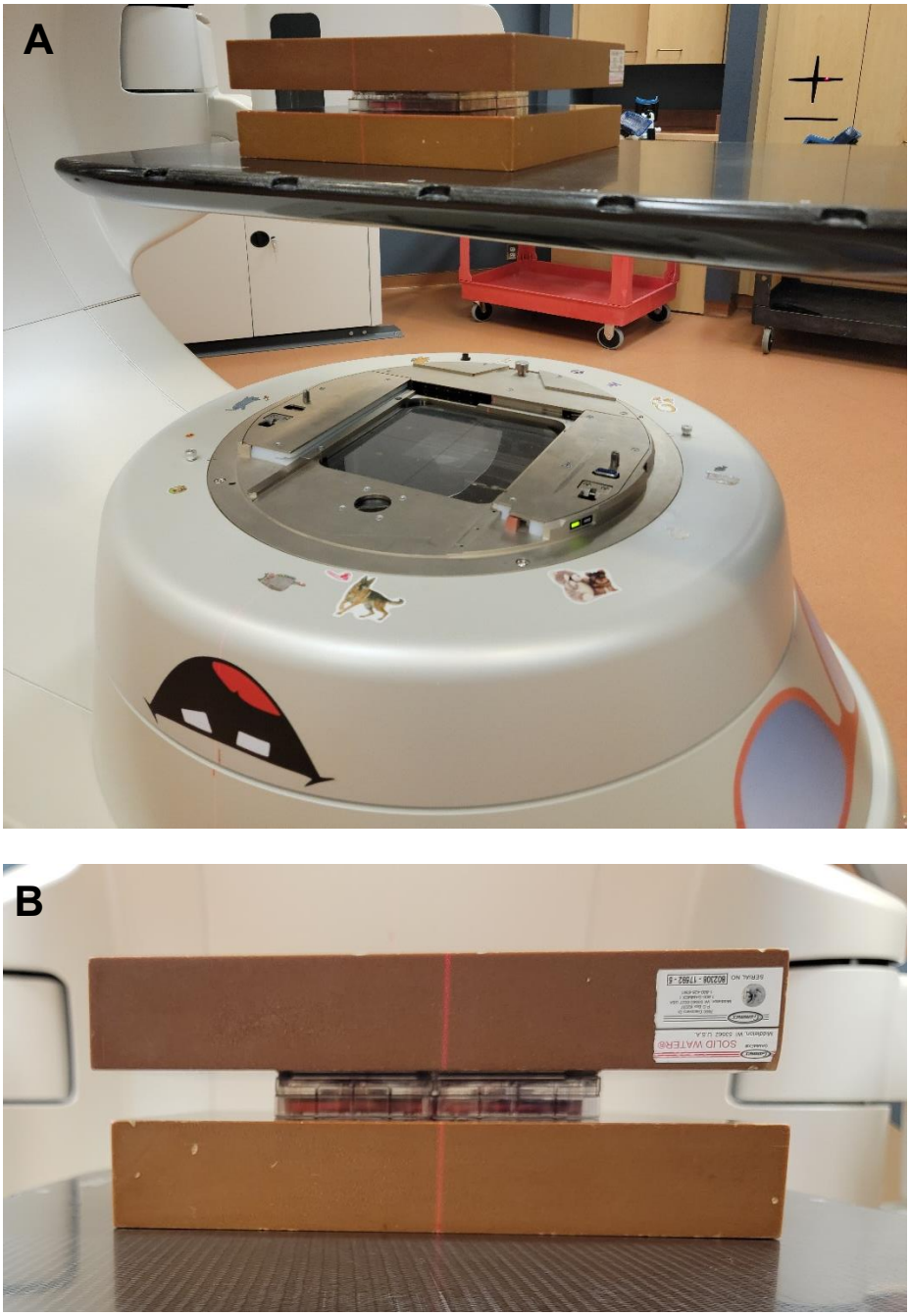

Figure S15 RT Set-up for *in vitro* experiments. **(A)** Showing linear accelerator. **(B)** Close-up view.

Supplementary Section S16: GNPs and LNPs Characterization

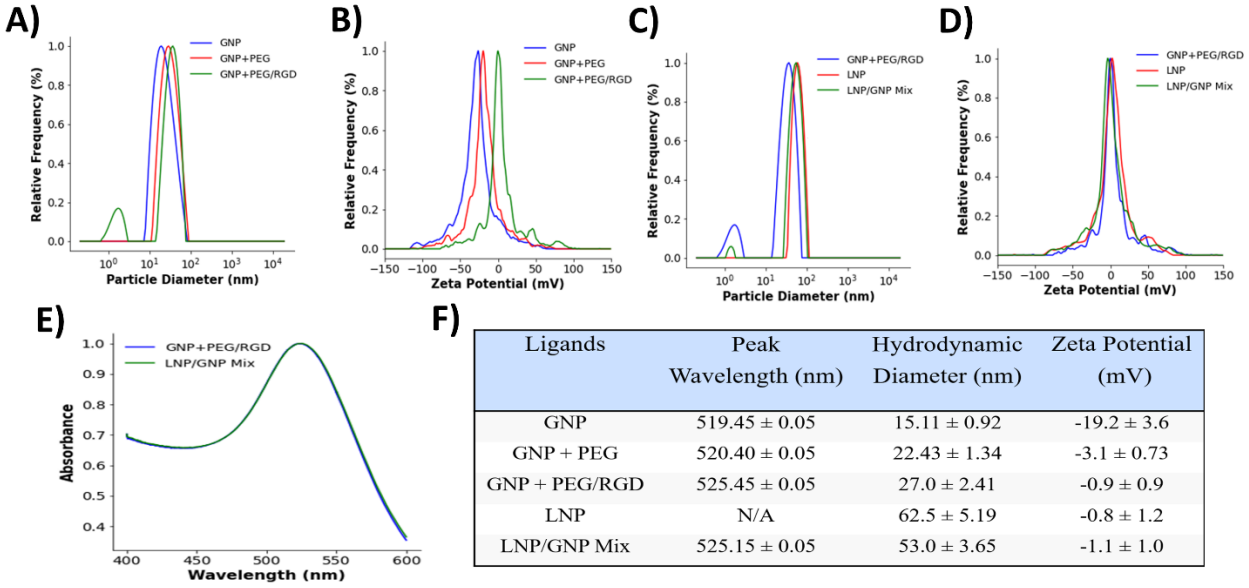

Ligands	Peak Wavelength (nm)	Hydrodynamic Diameter (nm)	Zeta Potential (mV)
GNP	519.45 ± 0.05	15.11 ± 0.92	-19.2 ± 3.6
GNP + PEG	520.40 ± 0.05	22.43 ± 1.34	-3.1 ± 0.73
GNP + PEG/RGD	525.45 ± 0.05	27.0 ± 2.41	-0.9 ± 0.9
LNP	N/A	62.5 ± 5.19	-0.8 ± 1.2
LNP/GNP Mix	525.15 ± 0.05	53.0 ± 3.65	-1.1 ± 1.0

Figure S16 Characterization of GNPs and LNPs. (**A-B**) Hydrodynamic diameter and ζ-potential measurements of pure GNPs, GNP_{PEG}, and $GNP_{PEG\text{-}RGD}$, respectively. (**C-D**) Hydrodynamic diameter and ζ-potential measurements of $GNP_{PEG\text{-}RGD}$, $LNP_{DTX\text{-}P}$, and $LNP_{DTX\text{-}P}$/ $GNP_{PEG\text{-}RGD}$, respectively. **(E)** UV–Visible absorption spectra of $GNP_{PEG\text{-}RGD}$ and $LNP_{DTX\text{-}P}$/ $GNP_{PEG\text{-}RGD}$. **(F)** Summary of peak absorption wavelength, hydrodynamic diameter, and mean ζ-potential for pure GNPs, GNP_{PEG}, $GNP_{PEG\text{-}RGD}$, LNP_{DTX} and $LNP_{DTX\text{-}P}$/ $GNP_{PEG\text{-}RGD}$. Reproduced with permission from open access Creative Common license [311].

Supplementary Section S17: DF Tumour Tissue Images

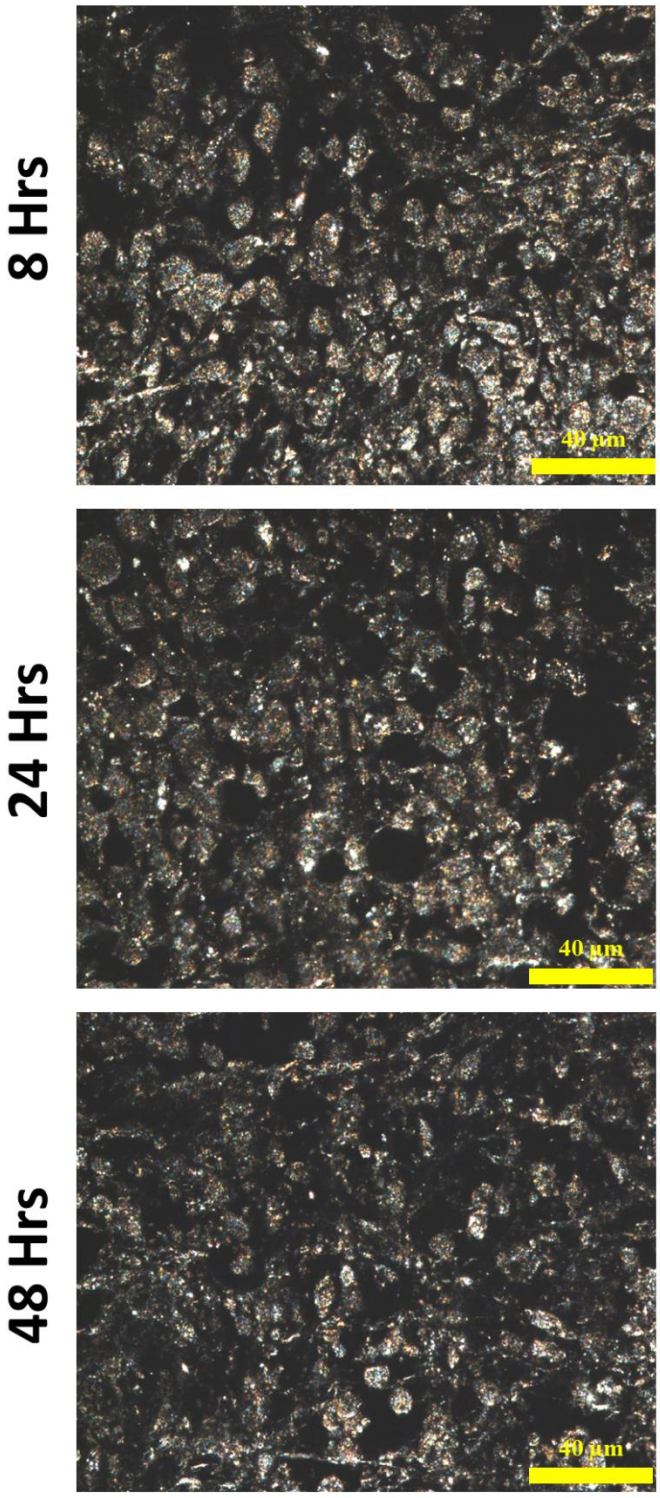

Figure S17 DF images of 4 µm sections of tumour tissues treated with $LNP_{DTX\text{-}2}$. Scale bar: 40 µm. Reproduced with permission from open access Creative Common license [311].

Supplementary Section S18: Images of Organs H&E

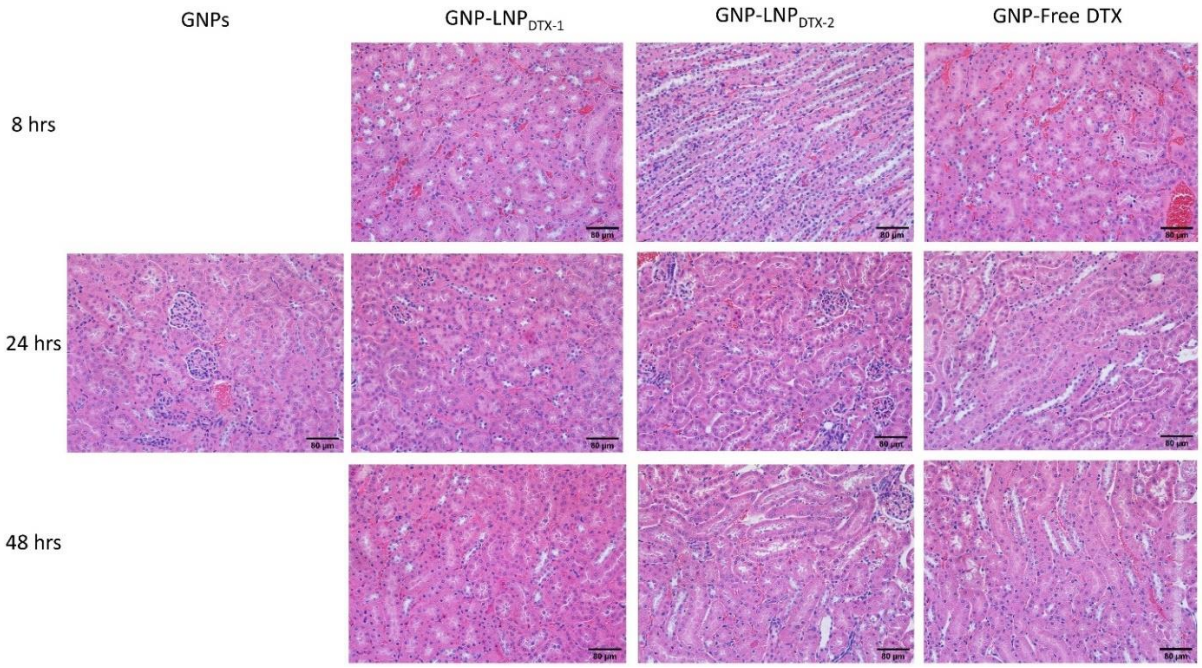

Figure S18.1 Haematoxylin and eosin-stained sections of kidneys 0 h, 24 h, and 48 h after dosing with the drugs and GNPs. Scale bar: 80 µm. Reproduced with permission from open access Creative Common license [311].

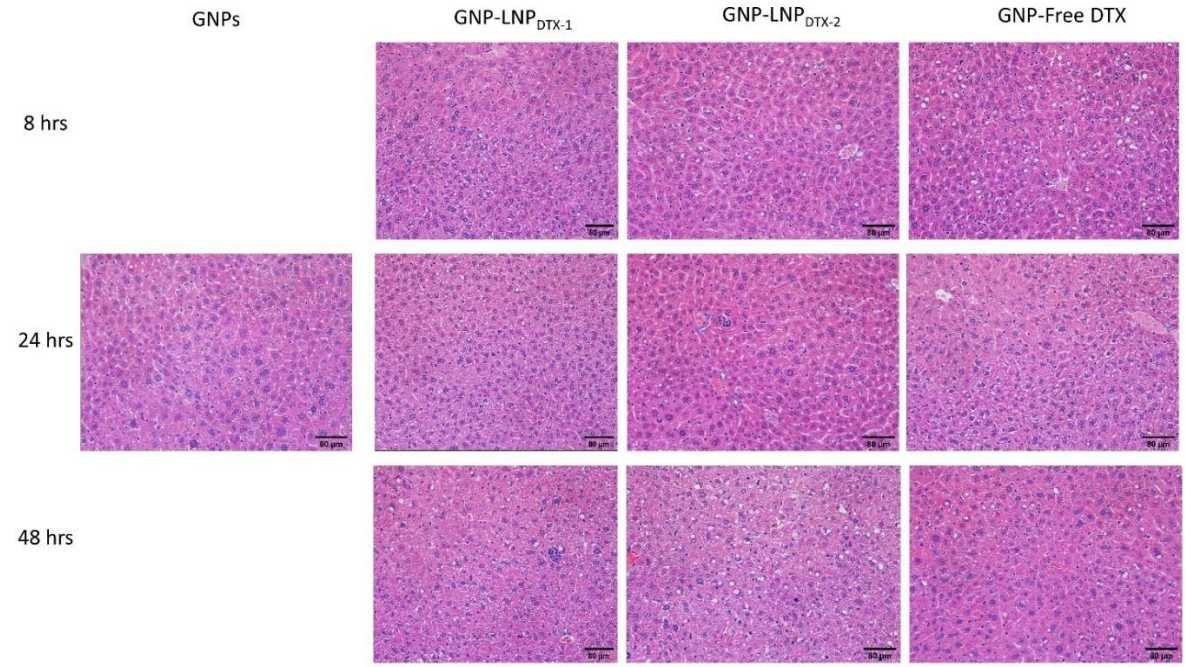

Figure S18.2 Haematoxylin and eosin-stained sections of liver 0 h, 24 h, and 48 h after dosing with the drugs and GNPs. Scale bar: 80 µm. Reproduced with permission from open access Creative Common license [311].

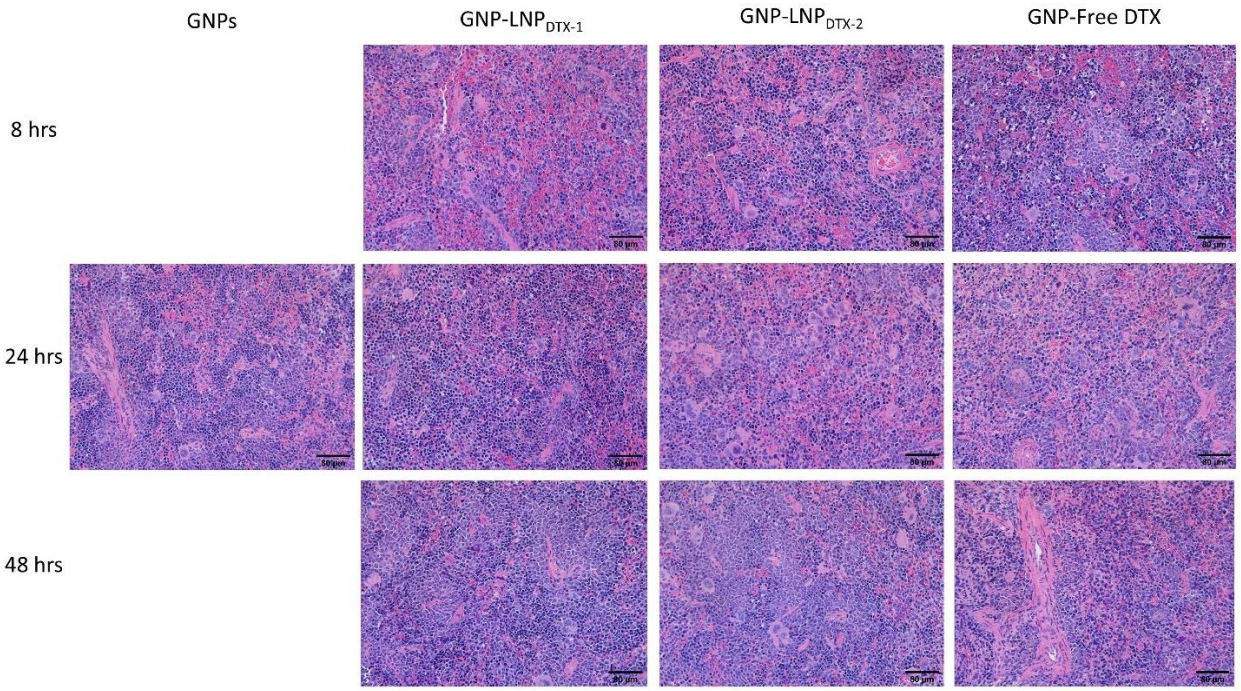

Figure S18.3 Haematoxylin and eosin-stained sections of spleen 0 h, 24 h, and 48 h after dosing with the drugs and GNPs. Scale bar: 80 μm. Reproduced with permission from open access Creative Common license [311].

Supplementary Section S19: Organs DF Images

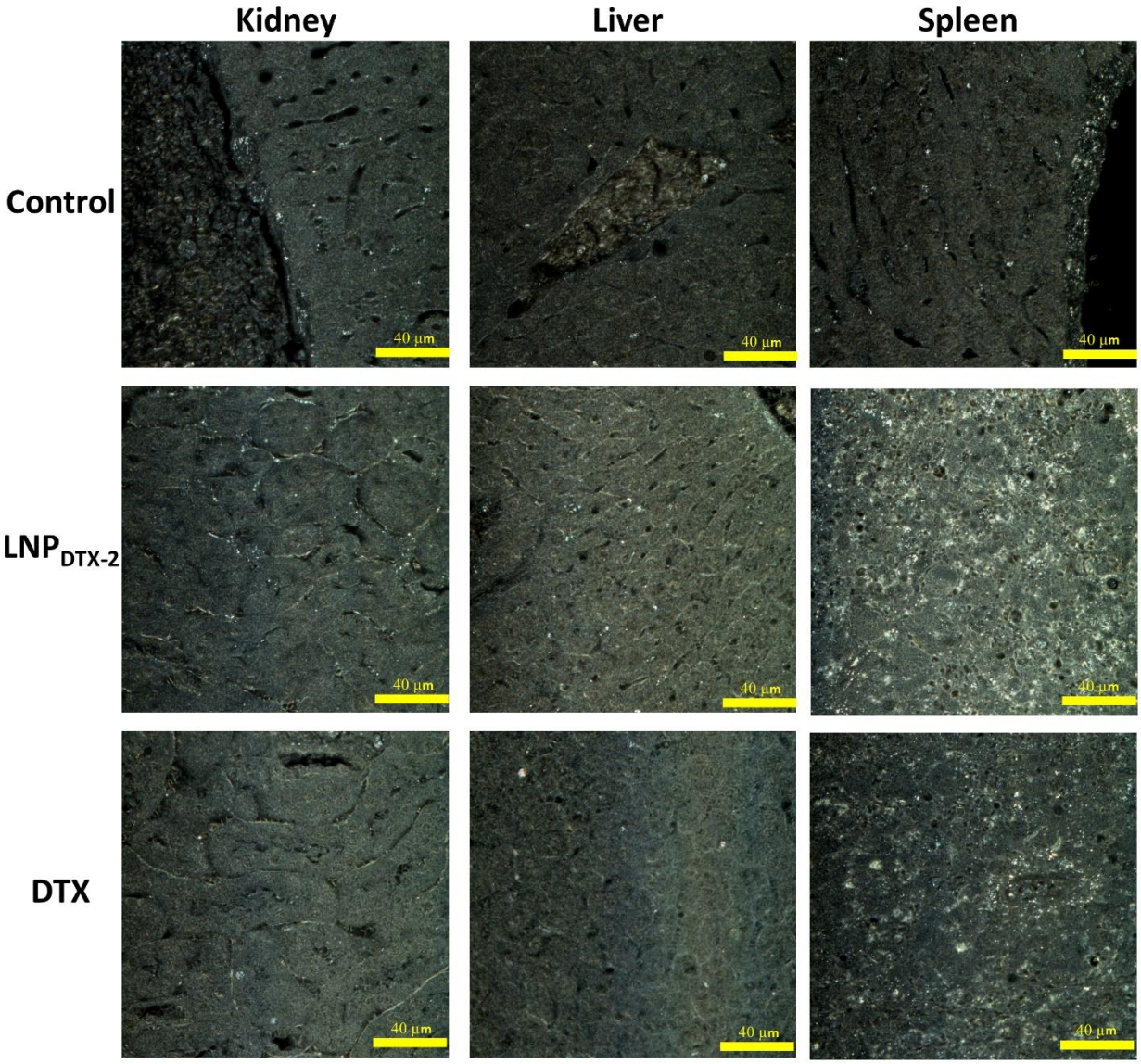

Figure S19 DF images of 4 µm sections of kidney, liver, and spleen, for control samples, LNP_{DTX-2} treated samples, and free DTX treated samples, 24 h post treatment, respectively. Scale bar: 40 µm. Reproduced with permission from open access Creative Common license [311].

Supplementary Section S20: GNPs Uptake & Retention

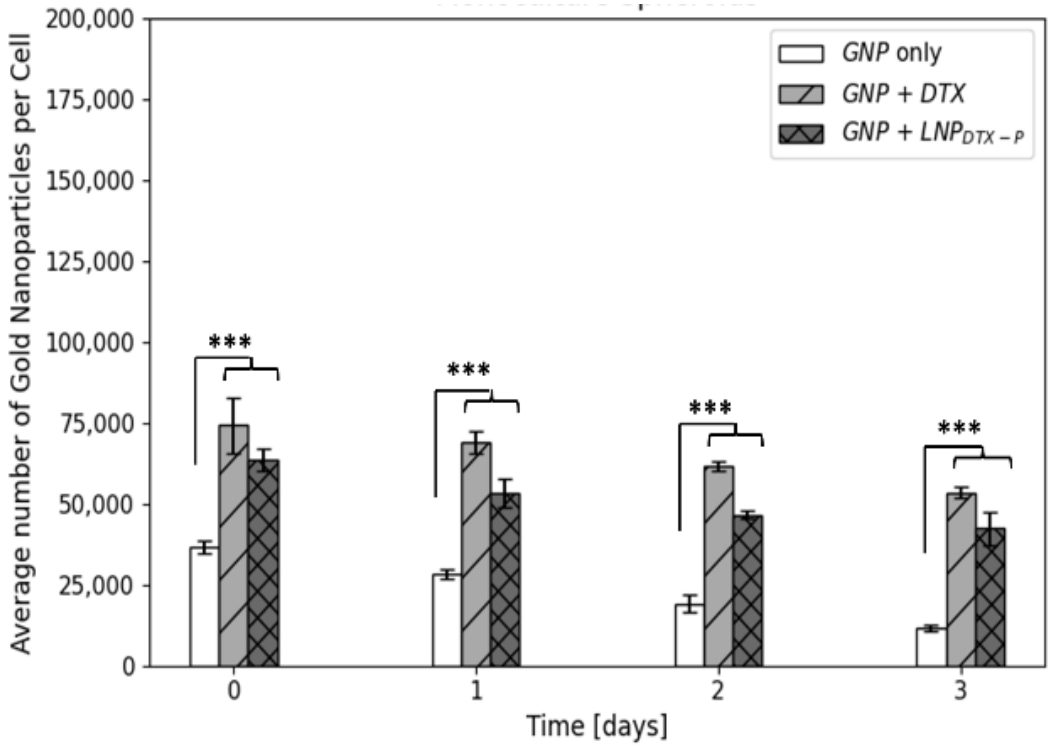

Figure S20.1 GNP uptake and retention in pancreatic cancer spheroids. Quantification of uptake of 7.5 µg/ml of GNPs into MIA PaCa-2 monoculture spheroids dosed with only GNPs, GNPs + DTX, and GNPs + LNP_{DTX-P}, as measured using ICP-MS. ******* indicates $p < 0.001$.

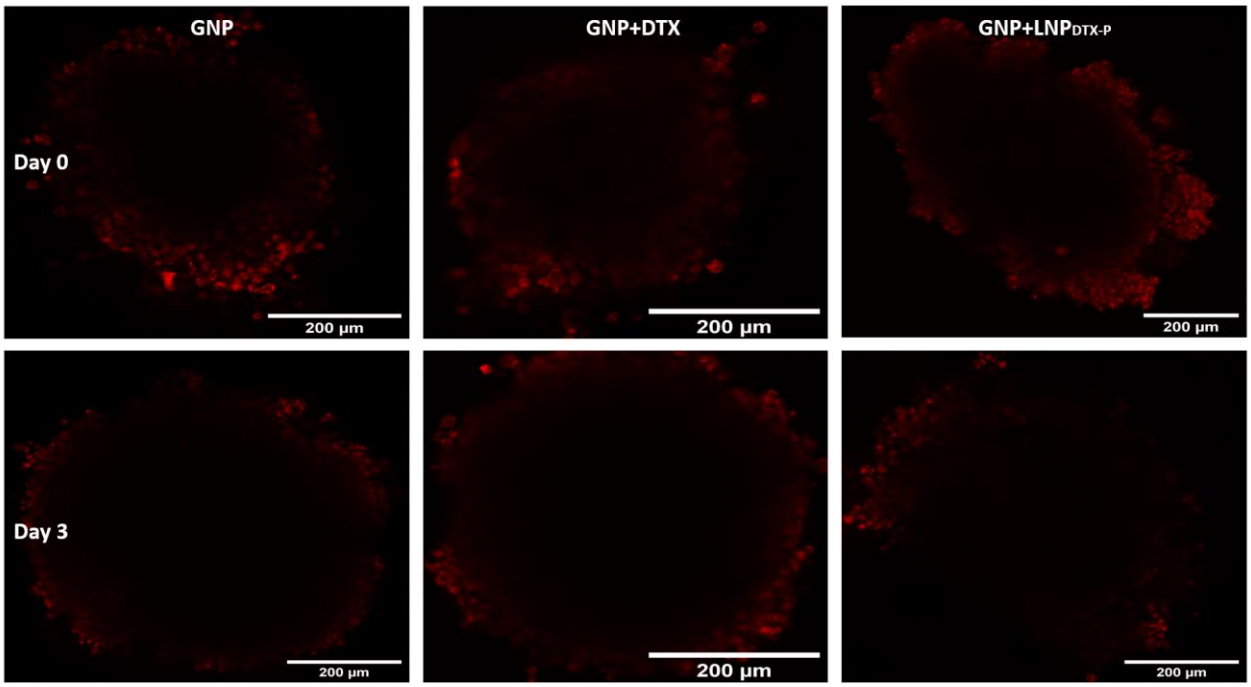

Figure S20.2 Confocal Images of GNPs', in red, uptake, and retention in day 0 and day 3 days in MIA PaCa-2 monoculture spheroids dosed with only GNPs (first column), GNPs + DTX (second column), and GNPs + $LNP_{DTX\text{-}P}$ (third column). Scale bar: 200 µm.

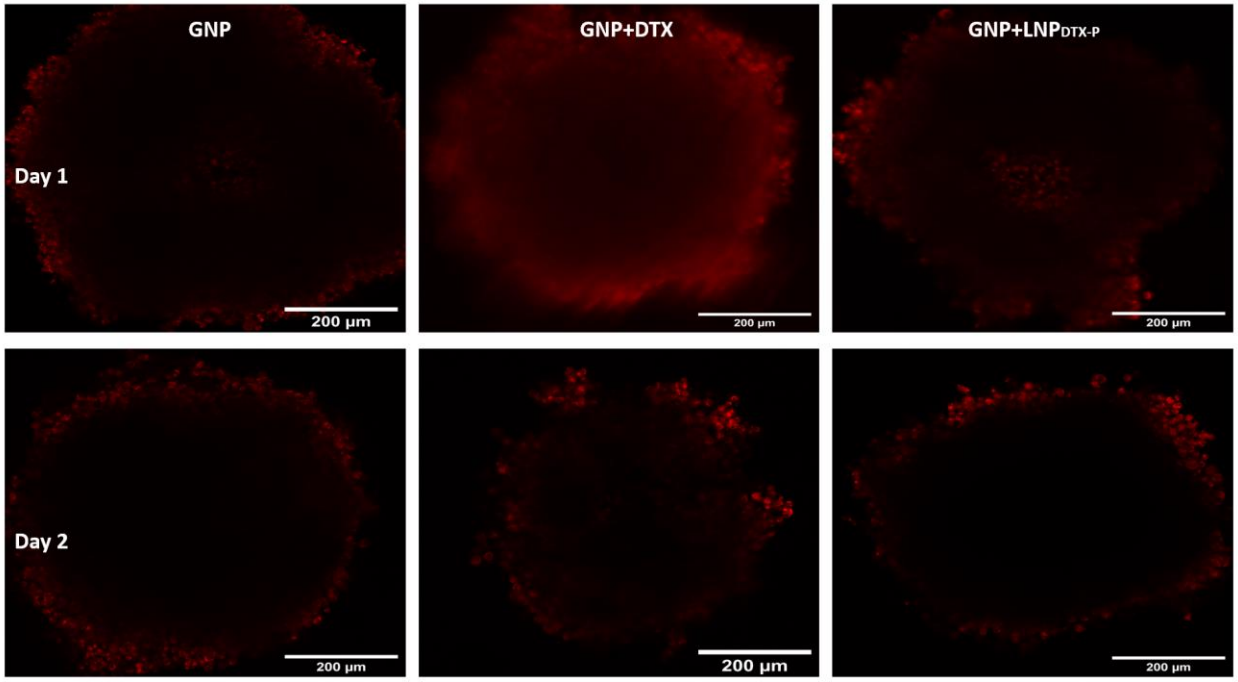

Figure S20.3 Confocal Images of GNPs', in red, uptake, and retention in day 1 and day 2 days in CAF-98 to MIA PaCa-2 (5:1) co-culture spheroids dosed with only GNPs (first column), GNPs + DTX (second column), and GNPs + $LNP_{DTX\text{-}P}$ (third column). Scale bar: 200 µm. Reproduced with permission from open access Creative Common license [312].

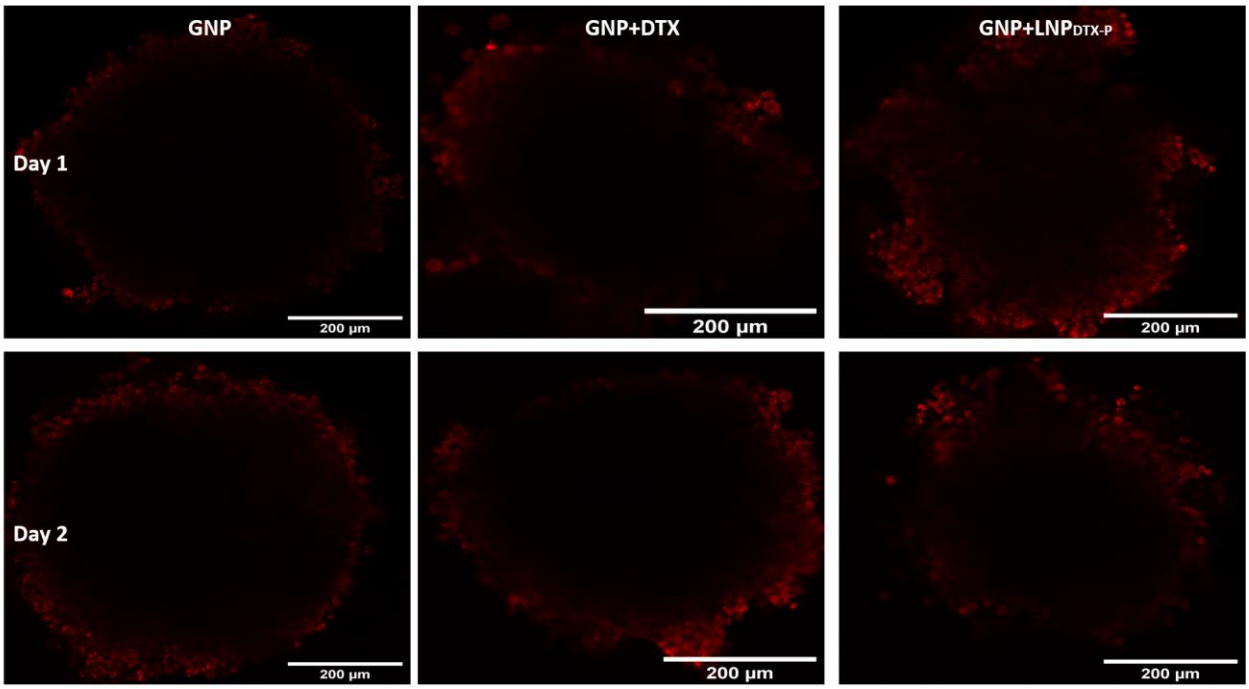

Figure S20.4 Confocal Images of GNPs', in red, uptake, and retention in day 1 and day 2 days in MIA PaCa-2 monoculture spheroids dosed with only GNPs (first column), GNPs + DTX (second column), and GNPs + $LNP_{DTX\text{-}P}$ (third column). Scale bar: 200 µm.

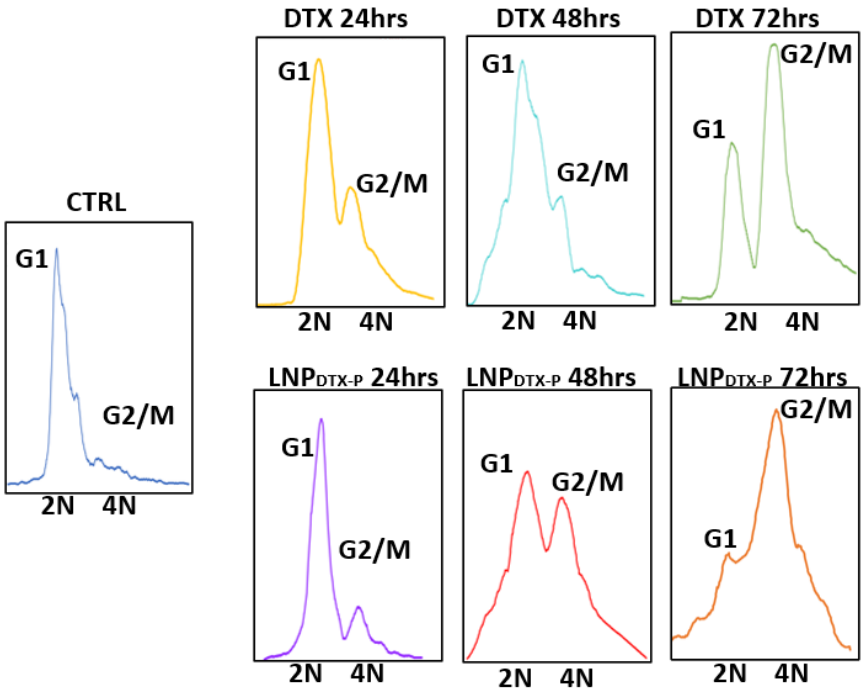

Figure S20.5 Cell cycle data of monoculture spheroids cells using DTX and $LNP_{DTX\text{-}P}$ over 3 days.

Supplementary Section S21: Spheroid Size

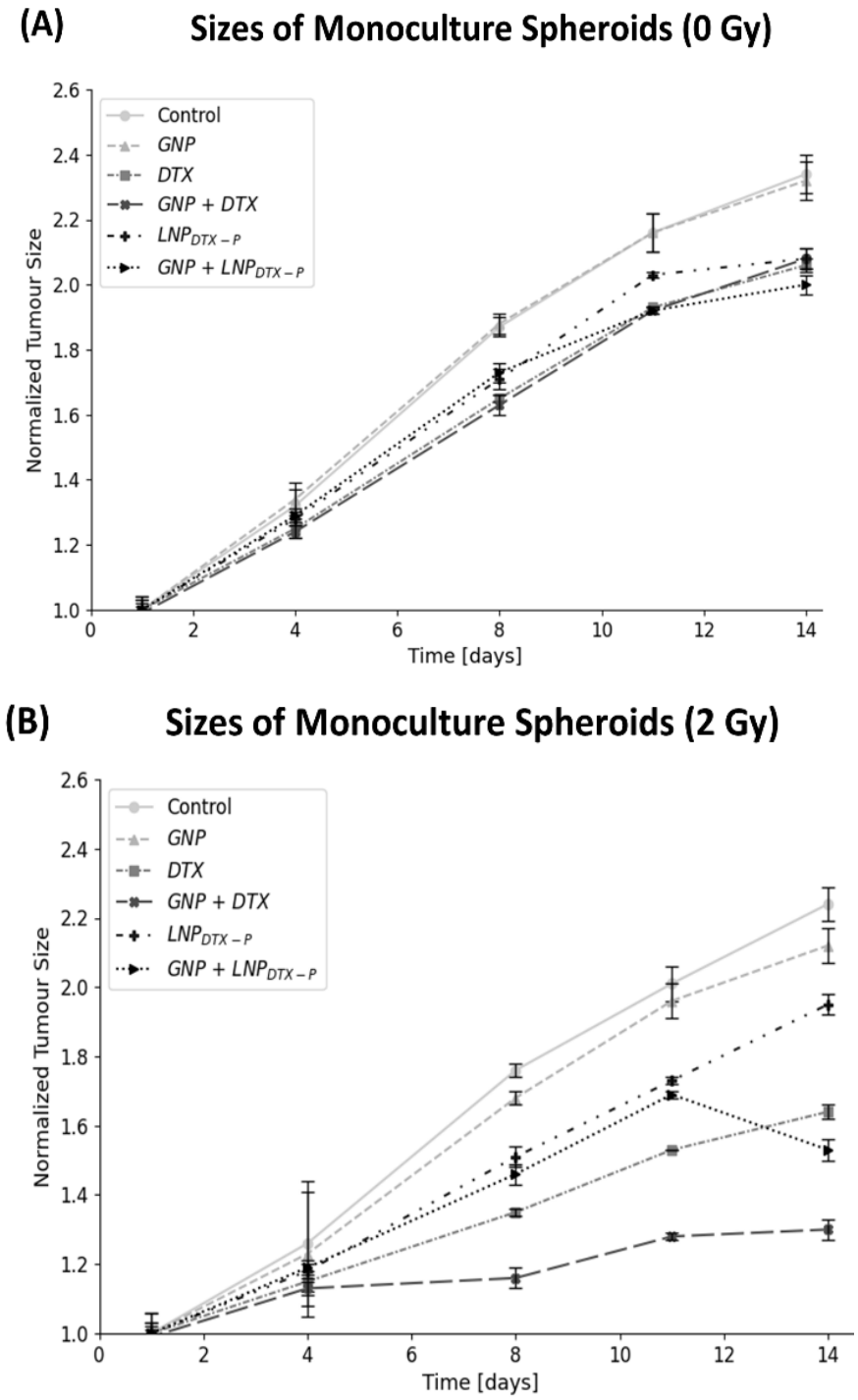

Figure S21.1 Monoculture spheroids sizes post-treatment with radiation/drug. **(A–B)** Normalized spheroids sizes over 14 days post-treatment: **(A)** 0 Gy, **(B)** 2 Gy.

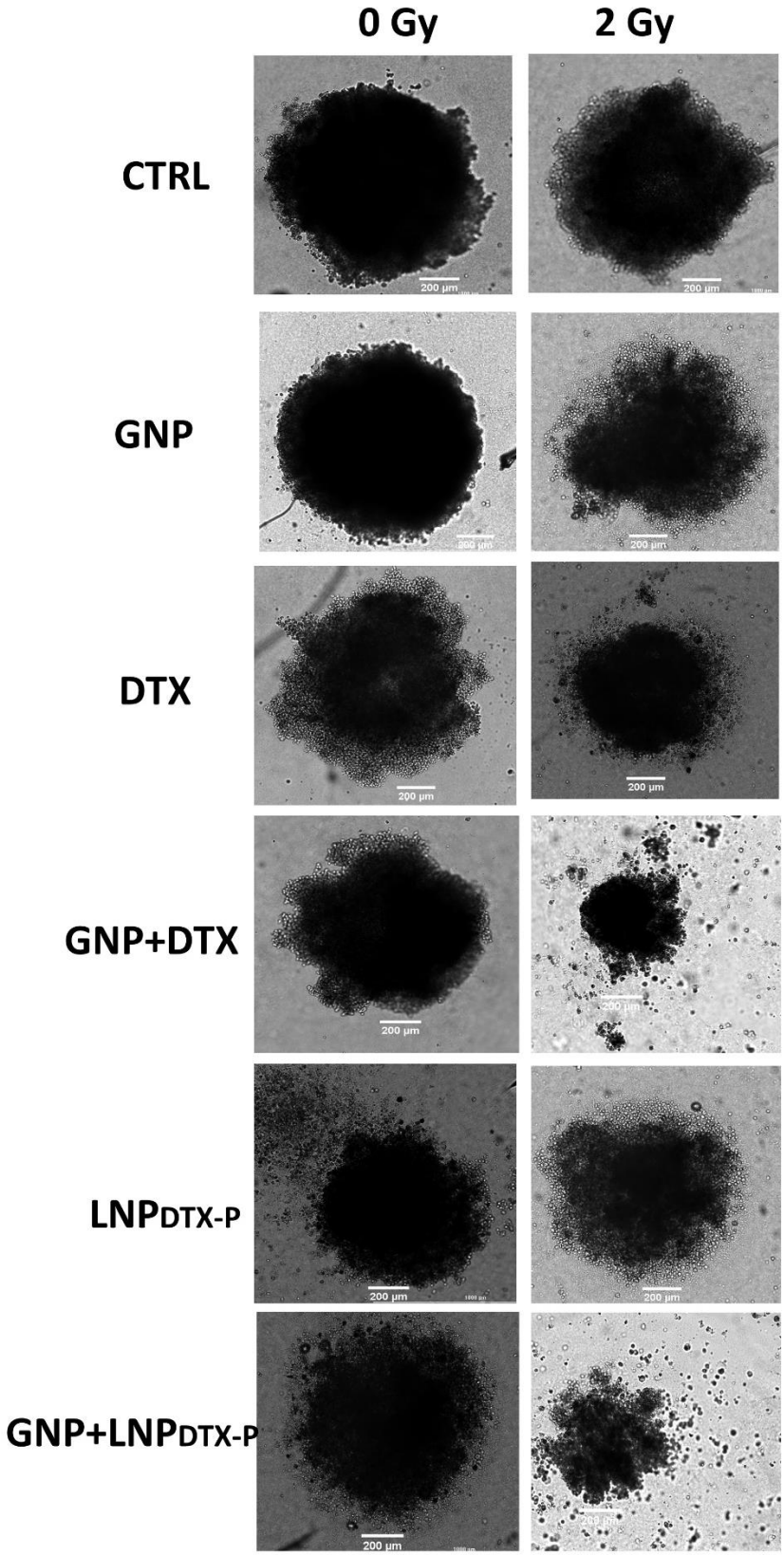

Figure S21.2 Bright-Field images of monoculture spheroids taken 14 days post-treatment. Scale bar: 200 µm.

Supplementary Section S22: Cell Proliferation

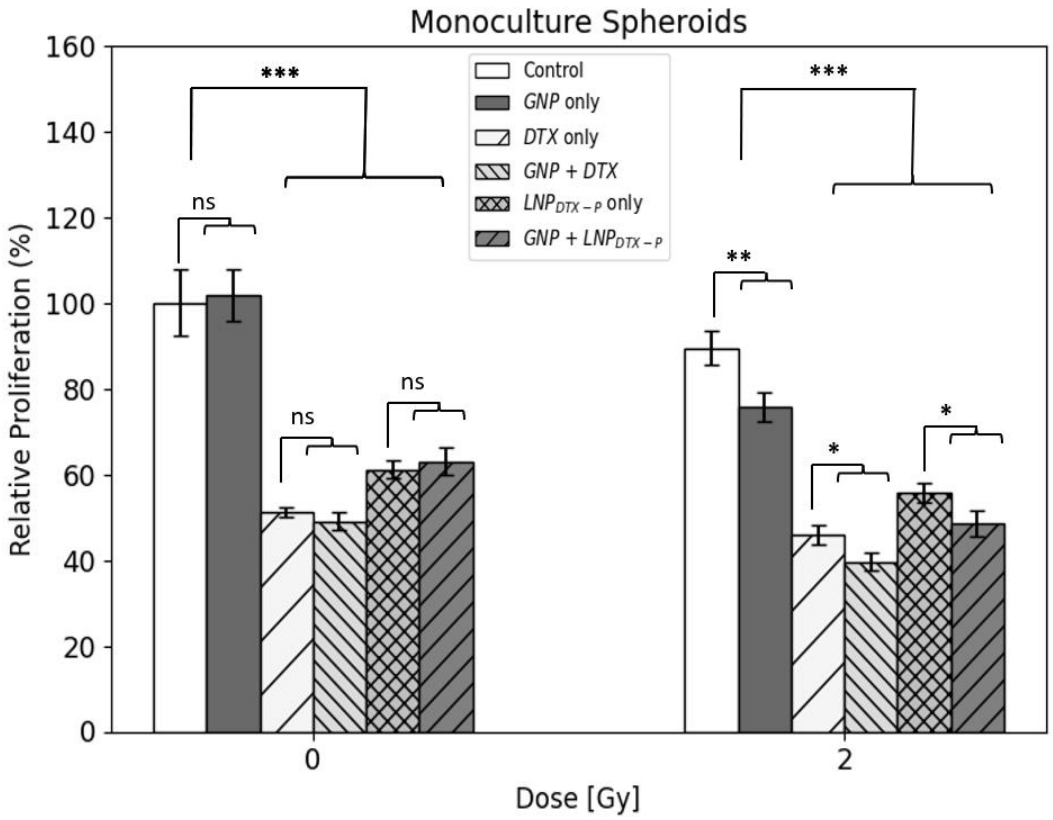

Figure S22 Monoculture spheroids relative cell proliferation at day 14 post-treatment. ns indicates non-significance, * indicates $p < 0.05$, ** indicates $p < 0.01$, *** indicates $p < 0.001$.

Supplementary Section S23: DNA DSB in Monoculture vs Co-culture

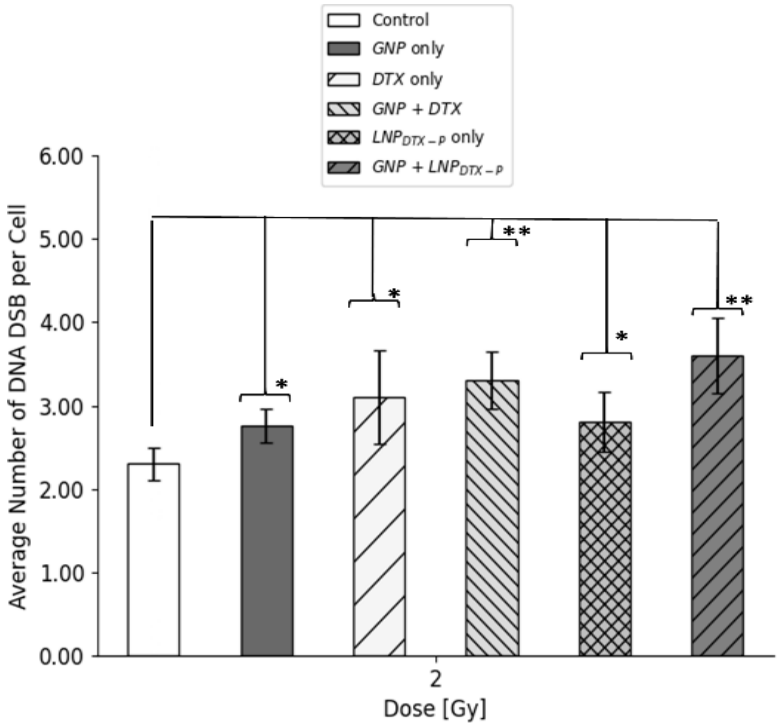

Figure S23.1 The average number of DNA DSB per cell in 2D monoculture with radiation following treatments with different agents**.** * indicates $p < 0.05$, ** indicates $p < 0.01$.

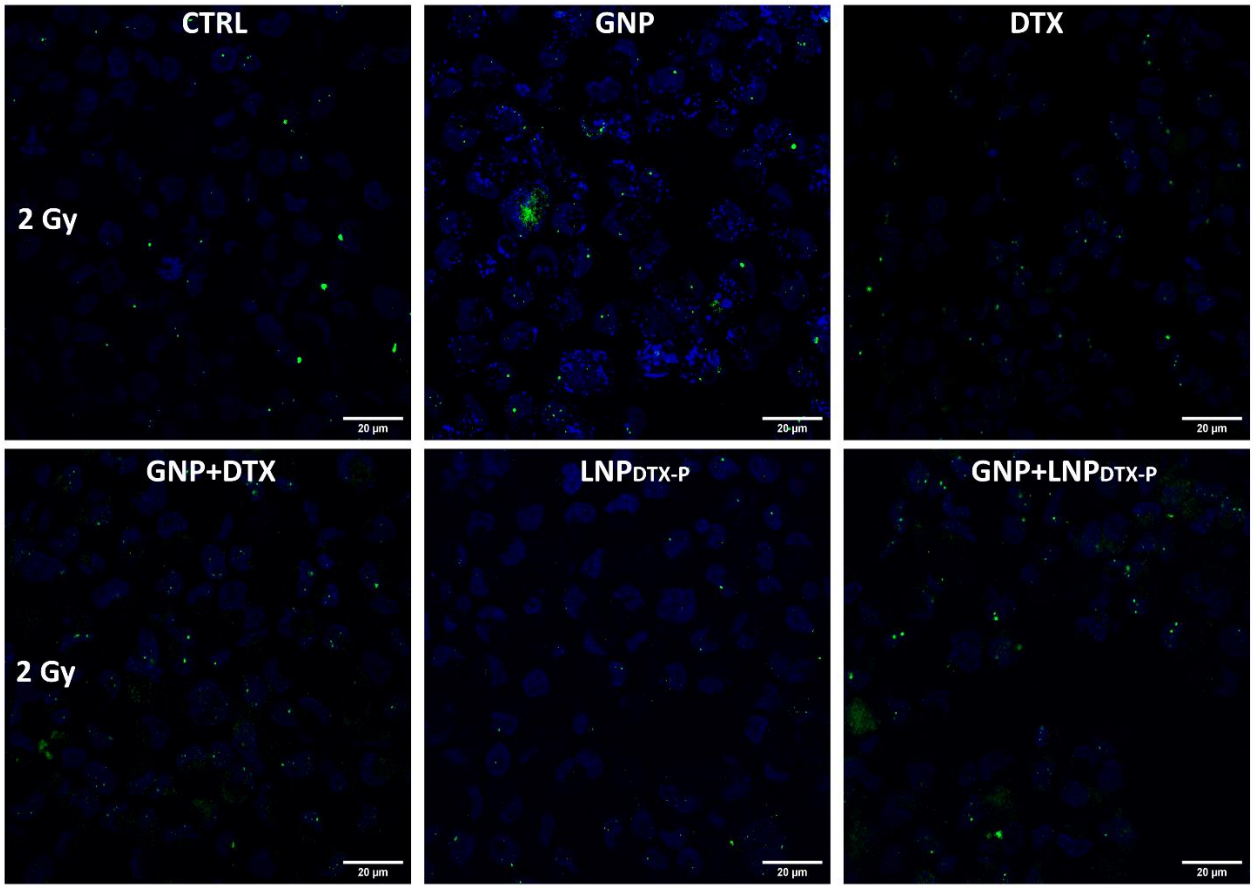

Figure S23.2 Confocal microscopy images of repair protein 53BP1 in the nucleus of irradiated monocultures of MIA PaCa-2. The cell nuclei are stained blue, while the green dots indicate DNA DSB damage. Scale bar: 20 µm.

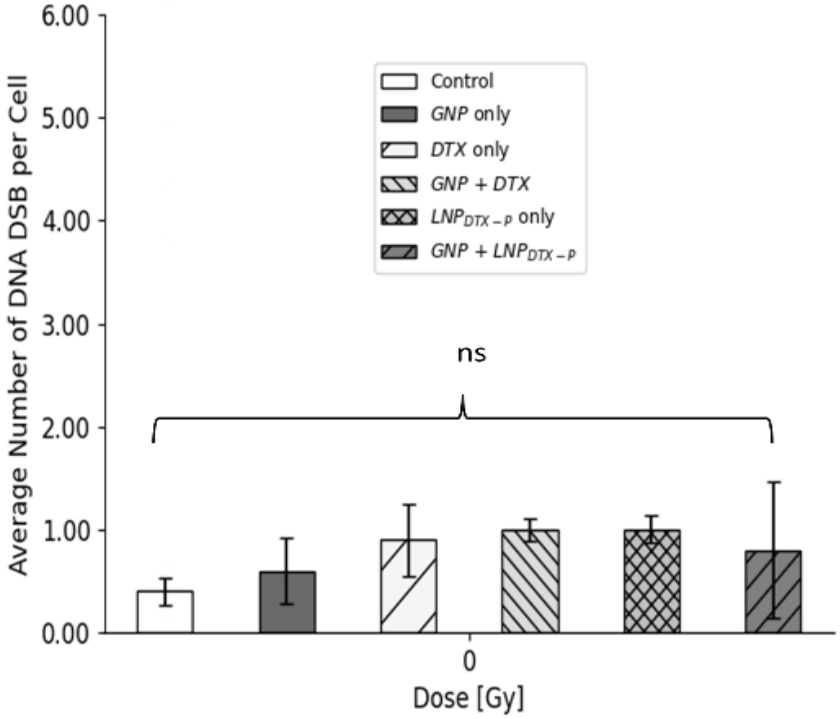

Figure S23.3 The average number of DNA DSB per cell in 2D co-culture without radiation following treatments with different agents**.** ns indicates non-significance. Reproduced with permission from open access Creative Common license [312].

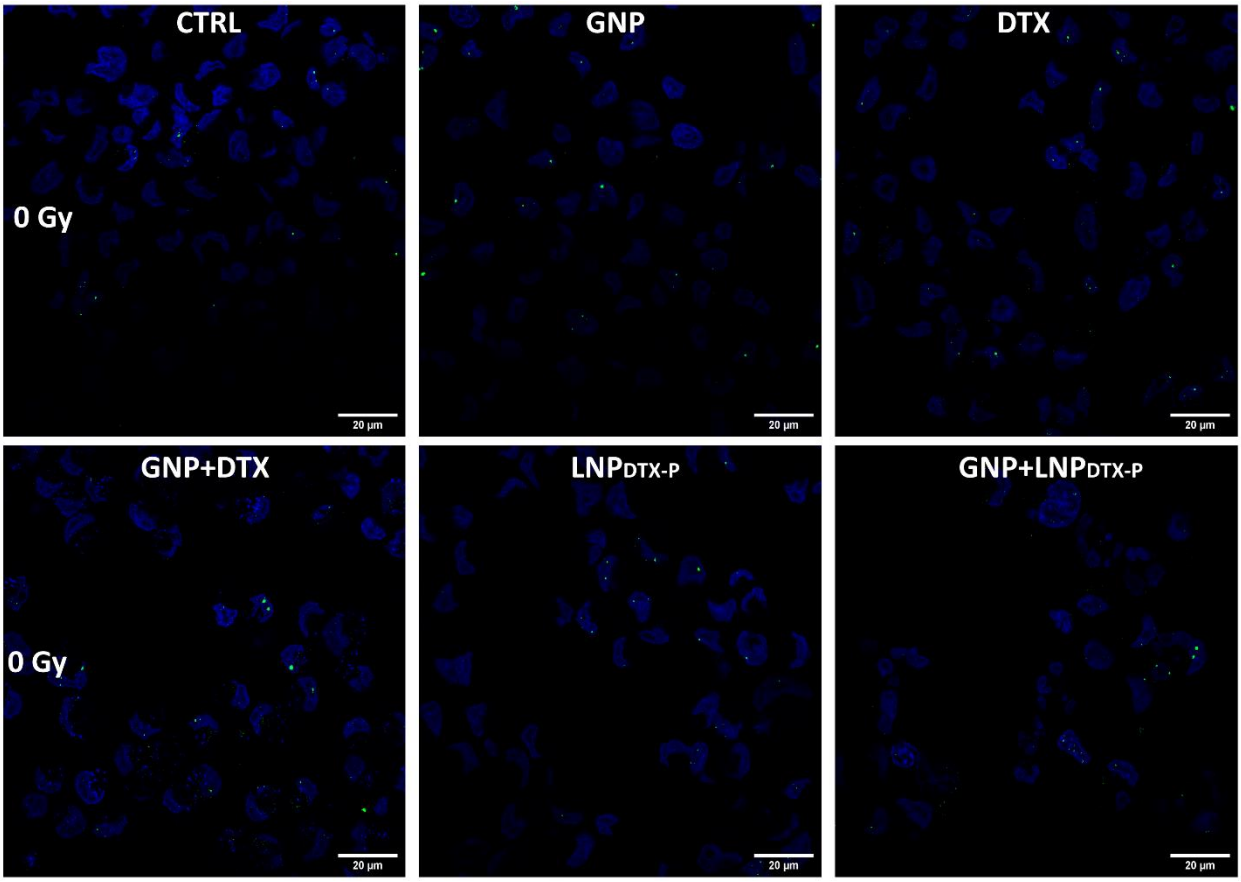

Figure S23.4 Confocal microscopy images of repair protein 53BP1 in the nucleus of non-irradiated co-cultures of MIA PaCa-2 and CAF-98. The cell nuclei are stained blue, while the green dots indicate DNA DSB damage. Scale bar: 20 µm. Reproduced with permission from open access Creative Common license [312].

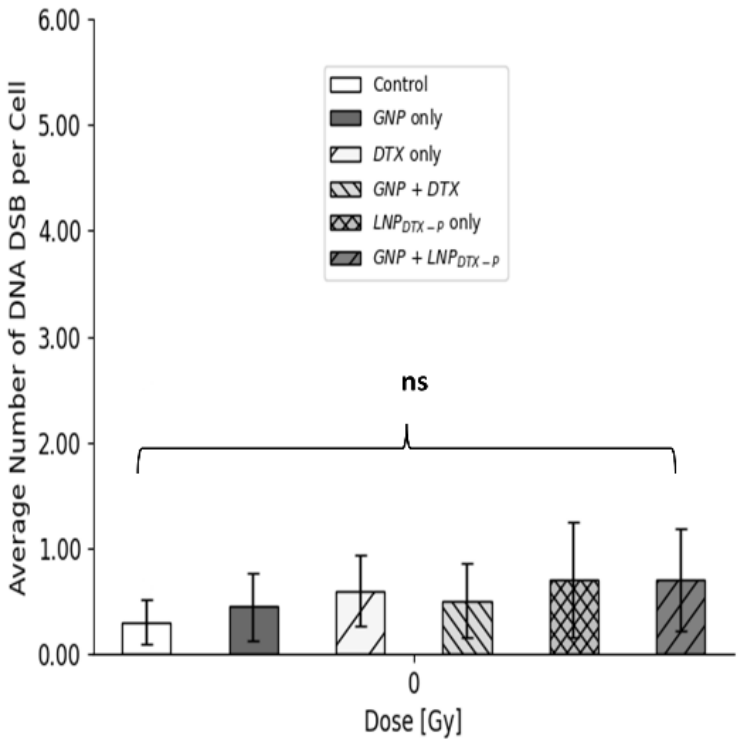

Figure S23.5 2D monoculture DNA DSB mapping. The average number of DNA DSB per cell in 2D monoculture without radiation following treatments with different agents**.** ns indicates non-significance.

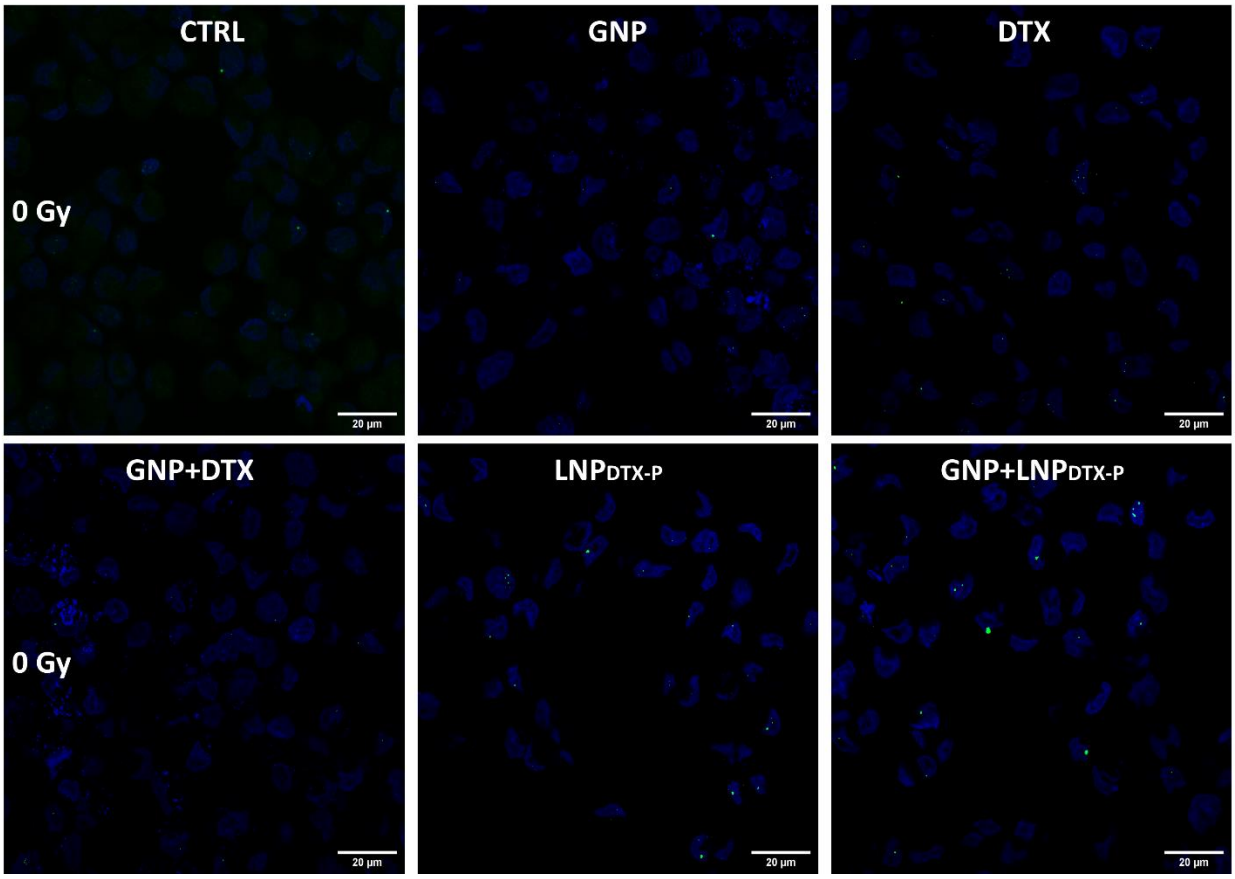

Figure S23.6 Confocal microscopy images of repair protein 53BP1 in the nucleus of non-irradiated monocultures of MIA PaCa-2. The cell nuclei are stained blue, while the green dots indicate DNA DSB damage. Scale bar: 20 µm.

Supplementary Section S24: Monoculture GNPs & LNP_{DTX-P} with RT vs 5/10 Gy

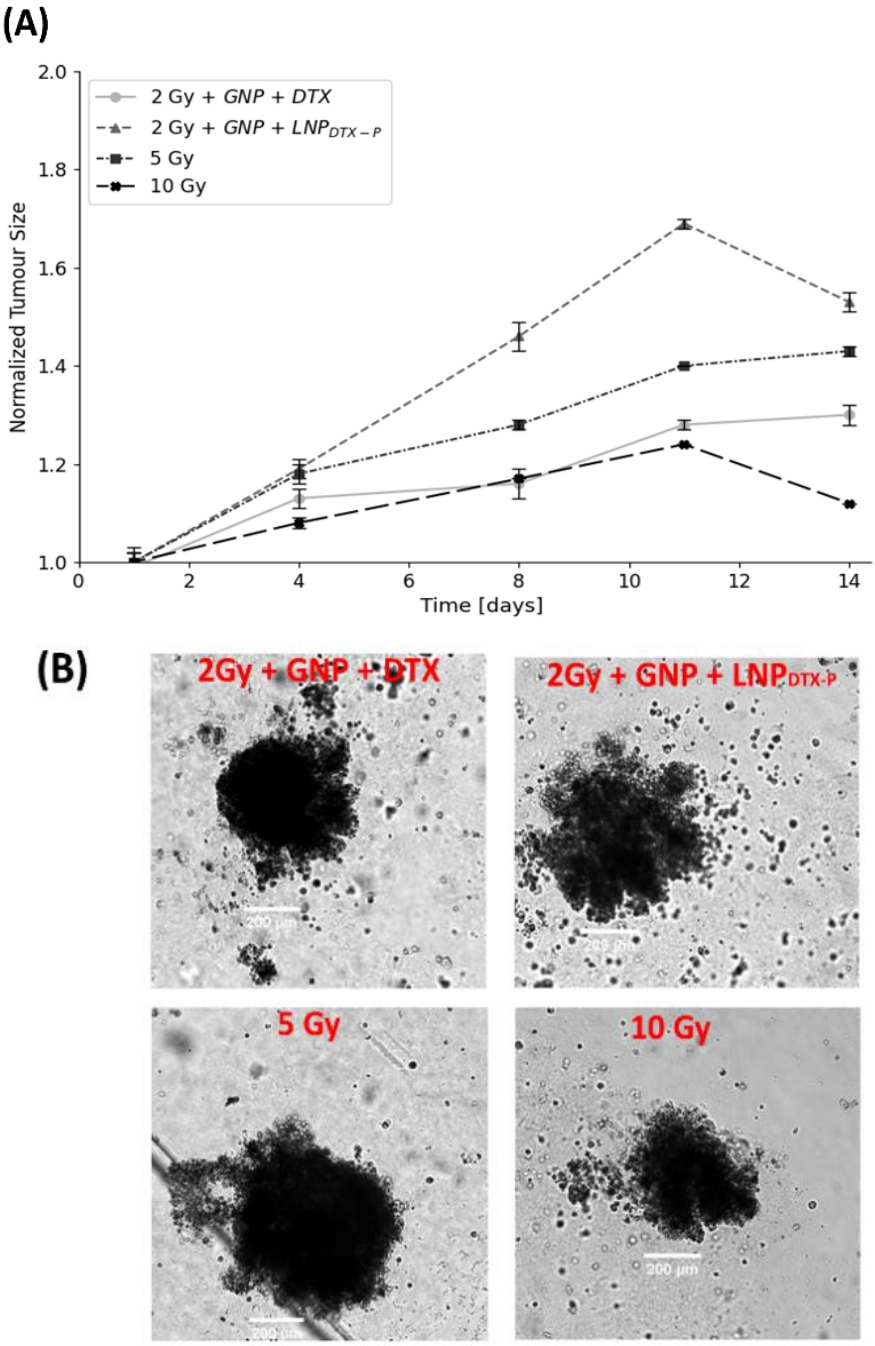

Figure S24.1 Irradiated Monoculture spheroids sizes and DNA damage post-treatment. **(A)** Normalized irradiated monoculture spheroids sizes over 14 days post-treatment. **(B)** Bright-Field images of irradiated monoculture spheroids taken 14 days post-treatment. Scale bar: 200 µm.

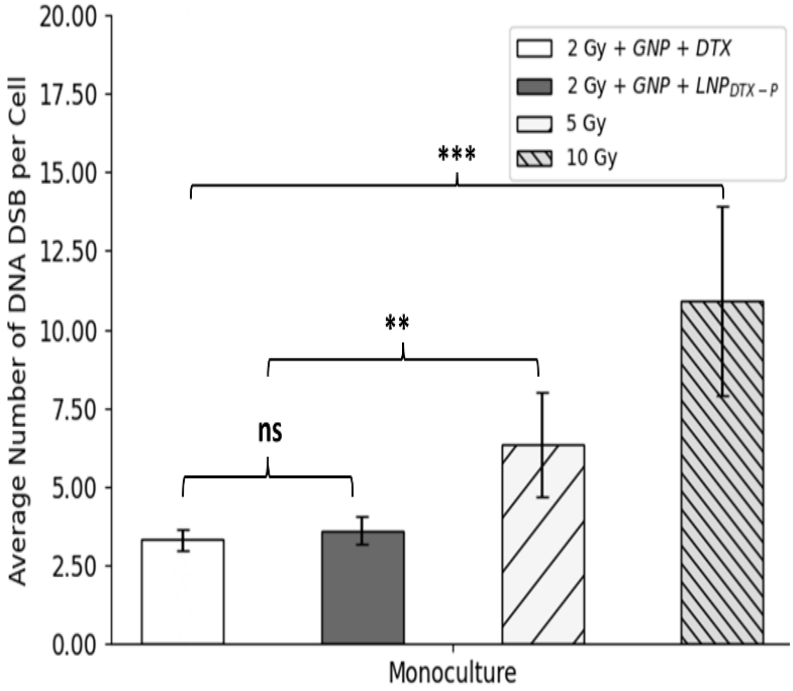

Figure S24.2 Irradiated 2D monoculture showing the average number of DNA DSB per cell. ns indicates non-significance, ** indicates $p < 0.01$, *** indicates $p < 0.001$.

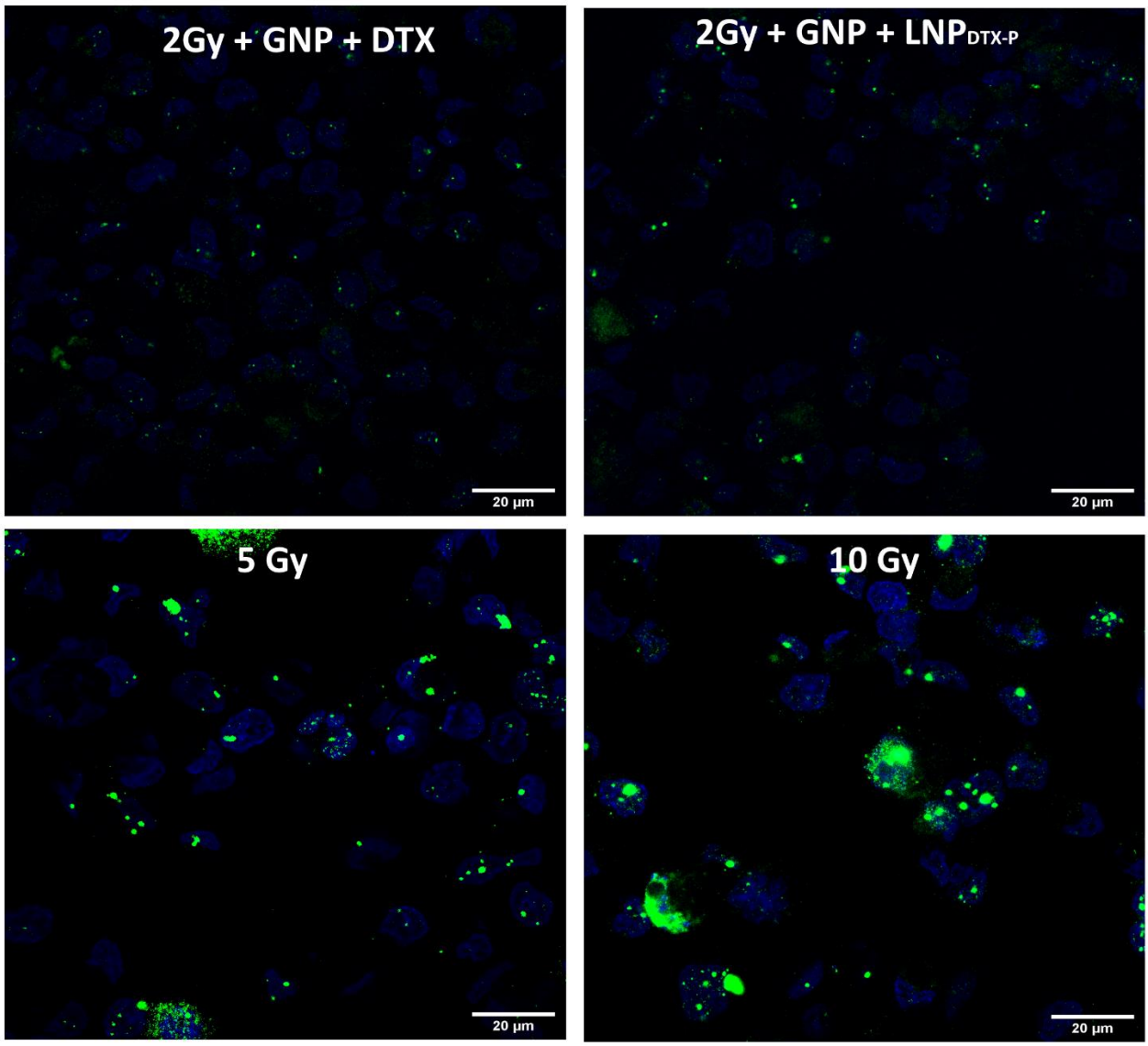

Figure S24.3 Confocal images of repair protein 53BP1 in the nucleus of monoculture MIA PaCa-2. Scale bar: 20 µm. The cell nuclei are stained blue, while the green dots indicate DNA DSB damage.

Supplementary Section S25: Proliferation GNPs & LNP_{DTX-P} with RT vs 5/10 Gy

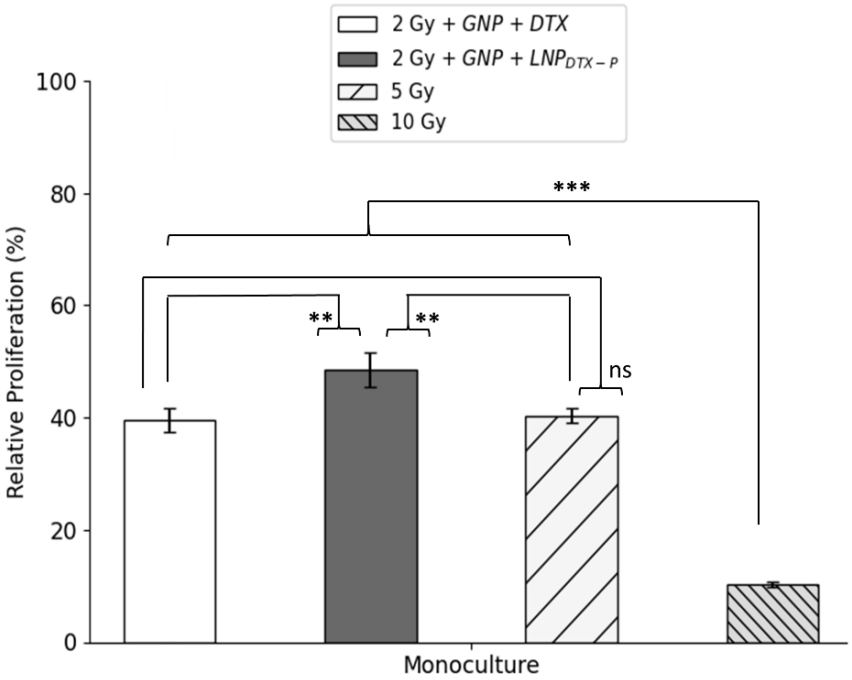

Figure S25 Monoculture spheroids relative cell proliferation at day 14 post-treatment. ns indicates non-significance, ** indicates $p < 0.01$, *** indicates $p < 0.001$.

Supplementary Section S26: DTX Prodrug Synthesis

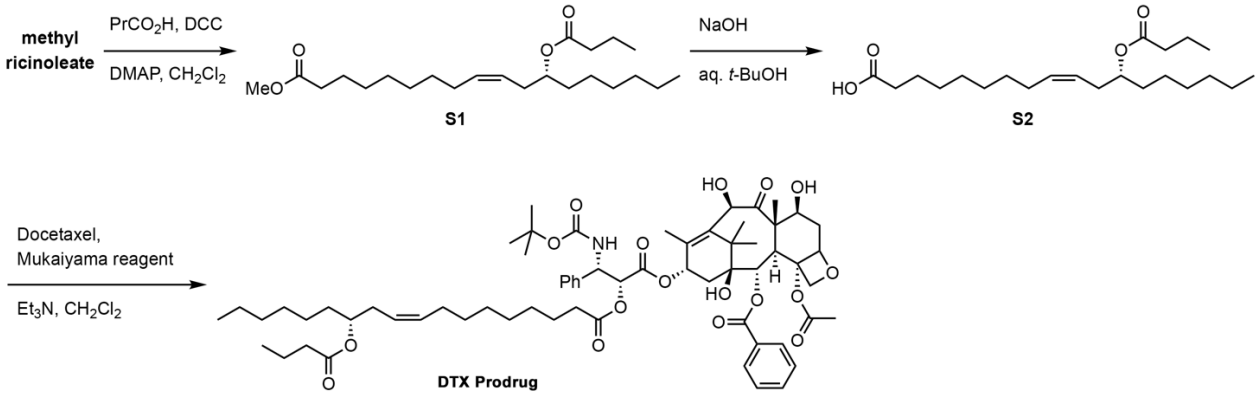

Figure S26 Synthetic scheme for Docetaxel (DTX) prodrug. Reproduced with permission from open access Creative Common license [311].

Methyl (*R*,*Z*)-12-(butyryloxy)octadec-9-enoate (S1): Butanoic acid (1.22 mL, 13.2 mmol) was added to an ice-cold CH_2Cl_2 (24 mL) solution of DCC (2.72 g, 13.2 mmol) in a round bottom flask under argon and the ice bath was removed. After 20 min, the ice bath was replaced, methyl ricinoleate (3.75 g, 12.0 mmol) and DMAP (2.20 g, 18.0 mmol) were added and the resultant was allowed to warm up over 14 h. The reaction mixture was diluted with hexanes, filtered through Celite® and concentrated on a rotary evaporator. The crude was resuspended in hexanes, washed with aqueous 1 M HCl (2 × 50 mL), aqueous 1 M NaOH (2 × 50 mL), H_2O (1 × 50 mL), brine, dried over Na_2SO_4 and concentrated on a rotary evaporator to afford a clear, colourless oil as desired diester **S1** (4.31 g, 94% yield), which was used without further purification.

(*R*,*Z*)-12-(Butyryloxy)octadec-9-enoic acid (S2): Aqueous 2.0 M KOH (5.35 mL, 10.7 mmol) was added to a room temperature *t*-BuOH (35 mL) solution of methyl ester **S1** (4.30 g, 11.2 mmol) in a round bottom flask under argon and stirred for 14 h. The reaction mixture was adjusted to pH <2 by addition of aqueous 6 M HCl and extracted with hexanes (3 × 50 mL). The combined organic extracts were washed with aqueous 1 M HCl (1 × 50 mL), brine, dried over Na_2SO_4 and concentrated on a rotary evaporator. The crude was purified by flash column chromatography (95:5:0→80:15:5→60:30:10 hexanes-EtOAc-MeOH) to afford a clear, colourless oil as desired carboxylic acid **S2** (3.02 g, 77% yield based on KOH).

Docetaxel Prodrug: Triethylamine (0.17 mL, 1.25 mmol), followed by Mukaiyama reagent (166 mg, 0.65 mmol), was added to a CH_2Cl_2 (5 mL) suspension of docetaxel (404 mg, 0.50 mmol) and carboxylic acid **S2** (0.55, 1.10 mmol) and the resultant stirred for 14 h. The reaction mixture was concentrated on a rotary evaporator and purified by flash column chromatography (80:20→50:50 hexanes-EtOAc) to afford a clear, colourless oil as desired docetaxel prodrug (262 mg, 45% yield). Analytic TLC was carried out with Merck silica gel 60 plates with fluorescent indicator; spots were visualized with UV light, iodine vapour or permanganate stain. The structure and purity of all final compounds were ascertained by NMR spectroscopy (^1H at 300 MHz, ^{13}C at 75 MHz, recorded at ambient temperature in $CDCl_3$).